



Study of supersymmetric signals with *R*-parity violation in ATLAS at LHC

Emma Torr3 Pastor

Dirigida por
Vasiliki Mitsou y Salvador Mart3 i Garcia
Tutor: Jos3 Ros Pallares

Doctorado en F3sica
Diciembre 2012

Facultat de F3sica
Departament de F3sica Te3rica
Universitat de Val3ncia Estudi General

La Dra. **Vasiliki A. Mitsou** y el Dr. **Salvador Martí i Gracia**

CERTIFICAN:

Que la presente memoria, "**Study of supersymmetric signals with R -parity violation at ATLAS/LHC**", ha sido realizada bajo nuestra dirección en el *Departamento de Física Teórica* de la *Universitat de València* por Emma Torró Pastor y constituyete su tesis para optar al grado de doctora en Física por la *Universitat de València*.

Y para que conste, firmamos el presente Certificado en Burjassot a 19 de Diciembre de 2012.



Dra. Vasiliki A. Mitsou



Dr. Salvador Martí i Gracia

Contents

1	Introduction	1
1.1	The Standard Model	1
1.1.1	Limitations of the Standard Model	2
1.1.2	Beyond the Standard Model theories	3
1.2	The LHC and the ATLAS detector	5
1.3	Searches for SUSY in the ATLAS detector	5
1.4	Experimental constraints on RPV SUSY scenarios	6
2	Experimental framework	7
2.1	The Large Hadron Collider (LHC)	7
2.2	The LHC experiments	11
2.2.1	A Toroidal LHC ApparatuS (ATLAS)	12
2.2.2	Compact Muon Solenoid (CMS)	13
2.2.3	LHCb	14
2.2.4	A Large Ion Collider Experiment (ALICE)	15
2.3	ATLAS	16
2.3.1	Inner Detector	17
2.3.2	Calorimeters	19
2.3.3	Muon system	20
2.3.4	Forward detectors	21
2.3.5	Trigger system	22
2.3.6	Object reconstruction in ATLAS	23
2.4	LHC Computing GRID	30
3	Theoretical framework	31
3.1	Supersymmetry	31
3.1.1	Introduction	31
3.1.2	Formal description of SUSY	34
3.1.3	MSSM	39
3.1.4	mSUGRA	43
3.2	R -parity violation (RPV)	44
3.2.1	Bilinear R -parity violation (bRPV)	46
4	Monte Carlo analysis	51
4.1	Introduction	51
4.2	Analysis strategy	52
4.3	Simulated samples	53
4.3.1	Signal samples	53

4.3.2	SM samples	58
4.4	Trigger and preselection	58
4.4.1	Analysis at 7 TeV	59
4.4.2	Analysis at 10 TeV	61
4.4.3	Analysis at 14 TeV	62
4.5	SM background suppression	63
4.5.1	Analysis at 7 TeV	64
4.5.2	Analysis at 10 TeV	69
4.5.3	Analysis at 14 TeV	71
4.5.4	Conclusions on the SM background suppression	71
4.6	Combinatorial background study	73
4.6.1	Analysis at 7 TeV	74
4.6.2	Analysis at 10 TeV	81
4.7	Invariant mass of muon+jets	84
4.8	Systematic uncertainties	85
4.9	Conclusion	86
5	Searches for bRPV SUSY with 2011 ATLAS data	89
5.1	Analysis overview	90
5.1.1	Signal regions	91
5.1.2	Control regions	91
5.1.3	Background determination in the signal regions	92
5.1.4	Results interpretation	93
5.1.5	Motivation of analysis setup	93
5.2	Samples: data, bRPV and backgrounds	94
5.2.1	Data	94
5.2.2	MC background	94
5.2.3	bRPV grid	95
5.3	Definition of objects	96
5.3.1	Jets and b -jets	96
5.3.2	Electrons	97
5.3.3	Muons	98
5.3.4	Missing transverse energy (E_T^{miss})	99
5.3.5	Pile-up treatment	99
5.3.6	Liquid Argon (LAr) hole veto	99
5.4	Trigger and preselection	99
5.4.1	Triggers	100
5.4.2	Event preselection	100
5.5	Event selection	102
5.5.1	Definition of signal regions	102
5.5.2	QCD background estimation	109
5.5.3	W and top background estimation	110
5.5.4	Initial and final state radiation	112
5.5.5	Contamination from cosmic events	112
5.5.6	SUSY signal	114
5.5.7	Comparison between bilinear RPV and RPC SUSY	125
5.6	Results	127
5.6.1	Fit setup	127
5.6.2	Summary of transfer function values	128

5.6.3	Fit results	128
5.6.4	Impact of systematic uncertainties	129
5.6.5	Limits on visible cross sections and discovery p -values	129
5.7	Conclusions	132
6	AtFast-II validation for SUSY	135
6.1	Introduction	135
6.2	AtFast-II description	136
6.3	Validation setup	136
6.4	Object definition	139
6.5	Results	140
6.5.1	Description of objects	140
6.5.2	Description of event selection efficiencies	145
6.6	Summary and proposal	146
7	Conclusions	149
8	Epilogue	153
8.1	Analysis follow up.	153
9	Resumen en castellano	157
9.1	Introducción	157
9.1.1	El LHC y el detector ATLAS	157
9.1.2	Supersimetría	158
9.2	Análisis con muestras de Monte Carlo	160
9.2.1	Definición de la señal	160
9.2.2	Trigger y preselección	161
9.2.3	Supresión del fondo del SM	162
9.2.4	Estudio sobre el fondo combinatorio	164
9.2.5	Masa invariante muón+jets y conclusión	165
9.3	Búsqueda de $bRPV$ -SUSY con datos de ATLAS de 2011	167
9.3.1	Regiones de señal y de control	167
9.3.2	Muestras: datos, fondos del SM y $bRPV$	168
9.3.3	Trigger y preselección	169
9.3.4	Selección de sucesos	170
9.3.5	Resultados	172
9.3.6	Conclusiones	174
9.4	Validación de AF-II para SUSY	175
9.4.1	Resultados	175
9.4.2	Propuesta	176
9.5	Conclusiones	176
9.6	Seguimiento del análisis	177
A	Monte Carlo sample details	179
A.1	SUSY production processes	179
A.2	Monte Carlo signal samples for the 1muon+2jets analyses	179
A.3	Monte Carlo SM samples for the one-lepton analysis	181

B Backup plots for the 10 TeV and 14 TeV analyses	183
B.1 Event selection: SM background for the 10 TeV analysis	183
B.2 Event selection: SM background for the 14 TeV analysis	184
B.3 Combinatorial background study for the 10 TeV analysis	185
C Combinatorial background study for different p_T^μ thresholds	187
D Further details on the comparison RPC versus $bRPV$	189
E OS muon + electron cut flow details	195
Bibliography	199

Chapter 1

Introduction

Supersymmetry (SUSY) [1] is one of the most promising theories providing a solution for many of the current open questions in the Standard Model (SM) [2]. Among the several possible scenarios that SUSY presents, there is a particularly interesting one due to its relation with neutrino physics. In this model the spontaneous breaking of R -parity (see Section 1.1.2) gives vacuum expectation values (vevs) to neutrinos, providing a “vev-seesaw” mechanism that leads to neutrino masses (see Section 3.2.1). Below the scale of these vevs, R -parity breaking is explicit through bilinear lepton number violating terms. The same parameters that induce neutrino masses and mixings are responsible for the decay of the lightest supersymmetric particle (LSP).

In this thesis two studies have been developed in order to search for a proof on the existence or not of SUSY with bilinear R -parity violation (bRPV) in Nature, within the accessible mass range. The first part of the thesis is devoted to the determination of the discovery potential of the bRPV model in the ATLAS detector at the Large Hadron Collider (LHC) [3,4] and to the possible measurement of the LSP mass, at three different working centre-of-mass energies for the LHC of $\sqrt{s} = 7, 10$ and 14 TeV. Since one of the characteristics of this model is the presence of muons in a large percentage of events (see Chapter 4) and by high jet multiplicity, the optimal approach for its search is to consider one muon and several jets in the final state. In this case, a search implying one muon and two jets is presented using Monte Carlo (MC) simulated samples of bRPV-SUSY and SM background. This work is documented in the ATLAS Internal Note in Ref. [91]. The second part of the thesis is an inclusive search for bRPV with real ATLAS data taken from 2011 LHC collisions at 7 TeV, considering a grid of points in the bRPV parameter space. In this analysis, final states containing one muon and at least three or four jets are selected. After taking into account all possible sources of uncertainties, no significant excess of events has been observed over the expected SM background. This has led to the first hadron colliders exclusion limits set on bRPV models, which has been published in Physical Review D [113] and documented in detail in the ATLAS Internal Note in Ref. [114]

1.1 The Standard Model

The Standard Model of High Energy Physics provides the current most accurate description of the Elementary Particle Physics phenomenology. It has been tested up to the TeV scale with remarkably successful results by experiments such as LEP [5], Tevatron [6], ATLAS [7–9] and

CMS [10], with the Higgs boson being the only remaining piece to be discovered ¹⁾. These experiments also give clear hints of additional structure, pointing to some New Physics (NP) beyond the SM [13].

1.1.1 Limitations of the Standard Model

There is a 17 orders of magnitude gap between the highest physical scale tested, the spontaneous electroweak symmetry breaking scale ($\Lambda_{\text{EW}} \sim O(100 \text{ GeV})$) and the next known physical scale, the Planck mass ($M_{\text{P}} \sim O(10^{19} \text{ GeV})$) [14]. There are several limitations which the SM is unable to cover if it is to be valid up to the Planck mass. Some of them are outlined below.

1. **Hierarchy problem.** The Higgs boson is the only scalar field in the SM, which makes it special in that loop corrections to scalar fields squared masses are quadratically divergent: they are proportional to the squared cut-off of the theory, Λ^2 . This is known as the *hierarchy problem*.
2. **Matter-antimatter asymmetry.** The observed asymmetry between matter and antimatter in the Universe have not been explained so far within the framework of the SM. *CP* violation in the SM predicts matter and antimatter not to behave in the exact same way. Still, some additional mechanism would be needed to explain the amazing dominance of matter over antimatter in the Universe.
3. **Neutrino masses.** Neutrinos are massless particles in the SM. However, it is experimentally known that this is not the case, and lower limits on their masses have been set [15,16].
4. **Cosmological consideration.** It is estimated that only $\sim 4\%$ of the Universe density is made of baryonic matter. The rest of the universe is composed of $\sim 24\%$ Dark Matter (DM) and $\sim 72\%$ Dark Energy [17], for neither of which the SM provides any explanation nor suitable candidates.
5. **Grand Unification.** Unification of all the fundamental interactions is an attractive concept. In the SM, strong and electroweak interactions are described independently and their running coupling constants do not get unified at any higher energy. A Grand Unifying Theory (GUT) [18,19] would make these two interactions to converge in one universal gauge coupling defined at the grand unification scale.
6. **The fermion mass hierarchy problem.** The existence of three fermion families has been experimentally tested. Nevertheless, the SM gives no prediction on the number of fermion generations. Furthermore, there is no explanation or prediction of their masses, which are observed to have hierarchical pattern spanning over six orders of magnitude between the top quark and the electron, or the difference even greater between these two and the neutrinos, which are lighter still by many orders of magnitude.
7. **Gravity.** Even though it is one of the fundamental forces of Nature, it is not included in the SM.

Thus, it seems clear that the SM is not the ultimate Theory, but an effective field theory which is able to explain Nature with great accuracy up to a certain energy scale beyond which it will need to be extended or included in a more complete theory. Several theories have been developed in this direction, such as Supersymmetry, theories involving extra dimensions like String Theories [20] or technicolor [21]. Among them, Supersymmetry is one of the best motivated.

¹⁾During the writing of this thesis, the ATLAS and CMS experiments announced the observation of a particle with mass at 125 – 126 GeV compatible with the SM Higgs boson [11,12]

1.1.2 Beyond the Standard Model theories

Several beyond the Standard Model theories have been developed involving higher symmetries of one form or another or new spatial dimensions. Some examples of the most ambitious such theories are outlined in the following.

- **Supersymmetry**

Supersymmetry [1] is one of the most promising approaches providing a solution for some of the current problems of the Standard Model. It is the maximal possible extension of the Lorentz group. Through its generators Q , Q^\dagger , it relates particles with the same quantum numbers, differing by $\pm 1/2$ unit of spin:

$$Q|\text{boson}\rangle = |\text{fermion}\rangle, \quad Q|\text{fermion}\rangle = |\text{boson}\rangle.$$

This implies that every SM particle has a superpartner with the same quantum numbers except for the spin. If SUSY is actually a symmetry of Nature, it must be a broken one so that superpartners masses are higher than those of the SM particles.

An important characteristic of SUSY is that it predicts a Higgs mass free of quadratically divergent quantum corrections due to the cancellation—to all orders in perturbation theory—of each of such divergent terms by the analogous term for the superpartner. Another attractive aspect is that it predicts grand unification at a scale $M_{\text{GUT}} \simeq O(10^{16} \text{ GeV})$ [18] since the running of the couplings is affected by the inclusion of the supersymmetric particles. Most of the scenarios considered within SUSY assume the conservation of both baryon and total lepton number in order to avoid a (relatively) fast proton decay. This scenario is referred to as R -parity conserving SUSY. R -parity is a quantum number defined as

$$P_R = (-1)^{3(B-L)+2s} \tag{1.1}$$

where B stands for Baryon number, L for Lepton number and s for spin.

In the case of R -parity being conserved, the lightest supersymmetric particle is neutral and stable, becoming an ideal Dark Matter candidate. Nevertheless this assumption can be relaxed in several ways. In the case that R -parity is not conserved there are still some possibilities for DM candidates such as the gravitino [22] or the axino [23]. Furthermore, in the case of R -parity violation (RPV) through the bilinear term (see Section 3.2.1), neutrinos acquire mass in a natural way. Hence, Supersymmetry is a very complete theory, able to solve many of the above mentioned limitations of the SM. A detailed description of SUSY is available in Chapter 3.

From the experimental point of view, the decays of supersymmetric particles, such as squarks and gluinos, would involve cascades which, if R -parity is conserved, always contain two stable LSPs. As the LSP would interact only weakly with the detector, the experiment would measure a significant missing transverse energy, E_T^{miss} , in the final state. In the case R -parity is not conserved, the LSP would decay into SM particles. The rest of the cascade would result in a number of leptons and jets.

- **Extra dimensions**

Several new models propose the existence of extra dimensions [24] containing additional space dimensions on top of the usual 4-dimensional manifold, while gravity can propagate through all the dimensions. Then in these models, the observed weakness of the

gravitational interaction (compared to the others) is not fundamental but a mere consequence of the existence of such extra dimensions. Moreover, these extra dimensions are assumed to be curled up, such that their small size explains why they would be invisible to us.

Extra dimensions may become detectable at very high energies. One possible experimental signature could lead to the emission of gravitons which escape into extra dimensions and therefore generate E_T^{miss} or miniature black-hole production with spectacular decays involving democratic productions of fundamental final states such as jets, leptons, photons, neutrinos and W and Z bosons [25]. Also Kaluza-Klein excitations may appear, which manifest themselves as Z -like resonances with $O(\text{TeV})$ separations in mass.

• Little Higgs

Little Higgs models [26] are based on the idea that the Standard-Model-like Higgs boson is a pseudo-Goldstone boson arising from some spontaneous global symmetry breaking at the TeV energy scale. This idea arose from the observation that, if certain global symmetries are broken only by the interplay between two or more coupling constants, then the Higgs-mass-squared is free from quadratic divergences at one loop. However, these cancellations do not continue in higher orders, unlike the case of supersymmetry. This “collective” symmetry breaking is the essential ingredient in little Higgs theories, which are weakly-coupled extensions of the SM describing physics up at an energy scale ~ 10 TeV. Such models necessarily predict the existence of additional particles. The spectrum of new particles varies somewhat from one little Higgs model to another, but all of them predict at least one vector-like quark at the TeV scale, along with extra gauge bosons and scalars.

• Two-Higgs-doublets model

The minimal version of the Standard Model contains one complex Higgs doublet, resulting in one physical neutral CP -even Higgs boson after electroweak symmetry breaking. However, the SM is not likely to be the ultimate theory and some theories (such as supersymmetry) have been developed containing a scalar Higgs sector corresponding to that of a two-Higgs-doublet model (2HDM) [27].

There are two possible cases for general 2HDM. In the first case, there is no energy range for which the effective low-energy theory contains only one light Higgs boson. In the second case, one CP -even neutral Higgs boson is significantly lighter than the other Higgs bosons of the model. In particular, in the so-called decoupling limit [28] where the mass scale of the heavier Higgs bosons is much higher than the mass of the lightest Higgs and all dimensionless Higgs self-coupling parameters $\lambda_i \lesssim O(1)$, the properties of the lightest Higgs boson are nearly indistinguishable from those of the SM Higgs boson.

All these theories are subject of extensive searches in the LHC. Apart from the already mentioned ones, other signatures belonging to NP will be investigated with the ATLAS data from LHC collisions. New heavy gauge bosons W' and Z' bosons could be accessible for masses up to several TeV. Anomalous high-mass di-jet production and searches for flavour-changing neutral currents and lepton flavour violation may also open a window onto New Physics. The LHC has been constructed and is currently in operation at CERN, the European Laboratory for Particle Physics near Geneva.

1.2 The LHC and the ATLAS detector

The Large Hadron Collider is currently the largest ever built particle accelerator and collider. It is situated at CERN near Geneva, in the existing 26.7 km round tunnel that was constructed between 1984 and 1989 for the Large Electron-Positron Collider (LEP) [5].

The LHC aims to discover the Higgs boson, to perform precision measurements of the Standard Model parameters and to reveal the Physics beyond it, with proton-proton collisions with centre-of-mass energies of up to $\sqrt{s} = 14$ TeV. In addition to the huge Physics program with pp collisions, the LHC is also designed to study physics of strongly interacting matter and the quark-gluon plasma by colliding heavy ions (Pb) with an energy of 2.8 TeV per nucleon.

Most of the interesting processes to be studied in the LHC are expected to have very small cross sections and hence a huge number of collisions is needed in order to get enough statistics in the physics analyses. This is the main reason for the formidable luminosity ($\mathcal{L} = 10^{34} \text{ cm}^{-2}\text{s}^{-1}$) and resulting interaction rate the LHC is designed to obtain.

Installed at the LHC there are two general purpose experiments, ATLAS [7–9] and CMS [10], both aiming to explore the above mentioned Physics. ATLAS is a general purpose experiment whose design has been optimised to be sensitive to a wide range of physics signatures in order to fully exploit the discovery potential of the hadron collider. It is composed of different sub-detectors, each of them specialised in the identification of a specific type of particle. The Inner Detector ensures a robust pattern recognition, precise vertex measurements and, with the help of a solenoid magnet, good momentum determination. The Electromagnetic Calorimeter is used for the identification and energy measurements of electrons and photons. The Hadronic Calorimeter measures hadronic jets and missing energy. The Muon Spectrometer is designed for muon detection and momentum identification. The whole detector is embedded in a toroidal magnet which generates strong bending power to ensure a proper measure of all particle features.

The LHC started working in a stable mode at the end of 2010 and so far it has released 5.61 fb^{-1} of integrated luminosity for $\sqrt{s} = 7$ TeV collisions and over 19 fb^{-1} of integrated luminosity for $\sqrt{s} = 8$ TeV collisions. The ATLAS detector is having a really good response and it has collected 5.25 fb^{-1} of integrated luminosity for $\sqrt{s} = 7$ TeV data and about 18 fb^{-1} of integrated luminosity for $\sqrt{s} = 8$ TeV data with excellent detector conditions.

A more detailed description of the LHC and its larger experiments follows in Chapter 2.

1.3 Searches for SUSY in the ATLAS detector

Supersymmetry is one of the best motivated extensions of the Standard Model, so its study is one of the primary goals of the Large Hadron Collider. If SUSY exists at the TeV scale, there are good perspectives for discovering SUSY particles at the LHC.

Standard searches for generic SUSY involve R -parity conservation, implying that sparticles must be produced in pairs and that the lightest sparticle (LSP) must be stable. The LSP is a supersymmetric candidate for dark matter, and should presumably have neither electric charge nor color charge; otherwise, it would bind to regular matter and form anomalous heavy nuclei that have never been observed [29]. It is the weakly-interacting nature of the LSP that provides the classic supersymmetric signature of missing (transverse) energy, giving signatures involving $E_{\text{T}}^{\text{miss}}$, jets, and possibly leptons.

Different strategies are designed for the search of a wide spectrum of possible signatures arising in different SUSY models. There is an endless list of analyses covering many configurations of final states (e.g. different number of leptons, photons, including or not b -tagged jets, etc. as well as specific searches for non-standard SUSY including electron-muon resonances,

long-lived R-hadrons, displaced vertices, etc.) the results of which can be found in the ATLAS SUSY Public Results Webpage [30].

All these searches are possible thanks to the simulation of the corresponding scenarios for particular sets of points in the parameter space. Since large numbers of signal points must be studied, these scans are in some cases based on fast, parameterised detector simulation which will be discussed in Chapter 6.

1.4 Experimental constraints on *RPV* SUSY scenarios

Several exclusion results on *RPV* signatures from high-energy experiments are available, leading to constraints fulfilled by sufficiently high LSP masses (see e.g. Ref. [31] for searches at LEP or Ref. [32] discussing *RPV* searches at the Tevatron). Other *RPV* searches are based on HERA results [33], results from Belle/Babar [34] or neutrino laboratories and astrophysics data [35]. It should also be noted that there have been new constraints on sparticle masses assuming trilinear *RPV* couplings λ_{123} or λ_{122} by the ATLAS [36–38] and CMS [39] collaborations. Since these results are based on different assumptions and lead to other decay modes of the LSP, there is no direct effect on the analyses performed for this thesis. Nevertheless and as it will be commented in Chapter 4, some similarities between different *RPV* scenarios make it possible to reinterpret results based on *bRPV* within a trilinear *RPV* context. The impact of bounds from neutrinoless double beta decay or rare leptonic decays for *bRPV* is discussed in Ref. [?,101], and an extensive discussion on the constraints on the size of *RPV* couplings from Cosmology and Astrophysics including the proton decay can be found in Ref. [?]. All these constraints have been taken into account for this work.

Chapter 2

Experimental framework

2.1 The Large Hadron Collider (LHC)

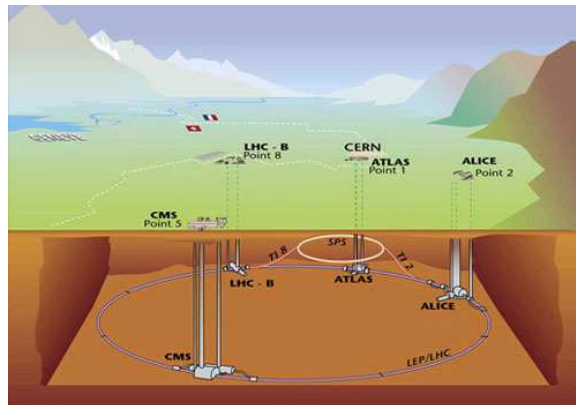


Figure 2.1: Drawing of the LHC and the experiments therein.

The Large Hadron Collider (LHC) [3,4] is currently the largest ever built particle accelerator and collider. It is placed at the European Laboratory for Particle Physics (CERN) near Geneva, in the existing 26.7 km round tunnel that was constructed for the Large Electron-Positron Collider (LEP) [5].

The prime motivation of the LHC is to shed light on the mathematical consistency of the Standard Model at energy scales above 1 TeV. It should perform precision measurements of the already known phenomenology and elucidate the nature of electroweak symmetry breaking for which the Higgs mechanism is presumed to be responsible. It also aims at revealing the Physics beyond the SM, with proton-proton (pp) collisions with centre-of-mass energies of up to 14 TeV. It will lead to the investigation of various alternatives to the SM which invoke new symmetries, new forces or new constituents. Furthermore, there are high hopes for discoveries that could pave the way toward a unified theory.

In addition to the huge Physics program with pp collisions, the LHC is also designed to study physics of strongly interacting matter and the quark-gluon plasma by colliding heavy ions (Pb) with an energy of 2.8 TeV per nucleon.

Most of the interesting processes to be studied in the LHC are expected to have very small cross sections and hence a huge number of collisions is needed in order to get enough statistics in the physics analyses. This is the main reason for the formidable luminosity ($\mathcal{L} = 10^{34} \text{ cm}^{-2}\text{s}^{-1}$) and resulting interaction rate the LHC is designed to obtain. In addition, the higher the LHC energy reaches, the larger the spectrum of possible processes generated to be investigated is. The exploration of rare events in the LHC collisions therefore requires both high beam energies and high beam intensities.

The number of a certain physics process events generated in the LHC collisions is given by:

$$N_{\text{process}} = L \sigma_{\text{process}}, \quad (2.1)$$

where σ_{process} is the cross section for the process under study and L the integrated luminosity which is defined by

$$L = \int \mathcal{L} dt, \quad (2.2)$$

where \mathcal{L} is the machine instantaneous luminosity. The machine luminosity depends only on the beam parameters, such as the number of bunches per beam (each beam has an internal structure as they are arranged in bunches), the number of particles per bunch, the revolution frequency and the beam size at the interaction point (IP).

Theoretically, the luminosity can be increased by increasing both the number of particles per bunch and the number of bunches, and by reducing the intersection area between them. Nevertheless, this is hard to achieve in practice since the major limitation comes from beam-to-beam effects when particles are close to the interaction point. The proton bunch creates a hugely non-linear electromagnetic field which modifies the trajectory of particles from their ideal orbits. The force on the particle is proportional to the number of protons on the bunch, and limits the bunch intensity to $O(10^{11})$ protons.

The considerable amount of Bremsstrahlung radiation for the required high energies, excludes the use of electrons in this collider. In addition, the high beam intensity required for a luminosity of $\mathcal{L} = 10^{34} \text{ cm}^{-2}\text{s}^{-1}$ excludes the use of anti-proton beams, and hence excludes the particle-anti-particle collider configuration of a common vacuum and magnet system for both circulating beams, as used for example in the Tevatron.

The LHC magnets have to accelerate two beams of equally charged particles but in opposite directions and there are obvious room constraints. To bend the trajectory of the 7 TeV proton beams along the LHC tunnel, a magnetic field of up to a 8.33 Tesla is generated by 1232 superconducting dipole magnets. The tunnel has eight straight sections and eight arcs and lies between 45 m and 170 m below the surface sloping towards the Léman lake. In the arcs it has an internal diameter of 3.7 m, which makes it extremely difficult to install two completely separate proton rings. This hard limit on space led to the adoption of the twin-bore magnet design, that consists of two sets of coils and beam channels within the same mechanical structure and cryostat. The disadvantage of the twin-bore design is that the rings are magnetically coupled, which adversely affects flexibility. This is why the Superconducting Super Collider (SSC) [40] was designed with separate rings with counter-rotating beams. The coils are made of niobium-titanium (NbTi) which is a material that allows to reach the superconducting regime when it is at 1.9 K [4]. In addition, 392 quadrupolar magnets are used to focus and correct the beams. There are also sextupole, octupole and decapole magnets mainly for compensating the systematic non-linearities.

The LHC is therefore designed as a proton-proton collider with separate magnet fields and vacuum chambers in the main arcs and with common sections only at the insertion regions (IR) where the experimental detectors are located. Together with the large number of bunches (with a nominal number of 2808 for each proton beam), and a nominal bunch spacing of 25 ns, the long common beam pipe implies 34 parasitic collision points at each experimental insertion region. For four experimental IRs, this implies a total of 136 unwanted collision points. Dedicated crossing angle orbit bumps separate the two LHC beams left and right from the IP in order to avoid collisions at these parasitic collision points.

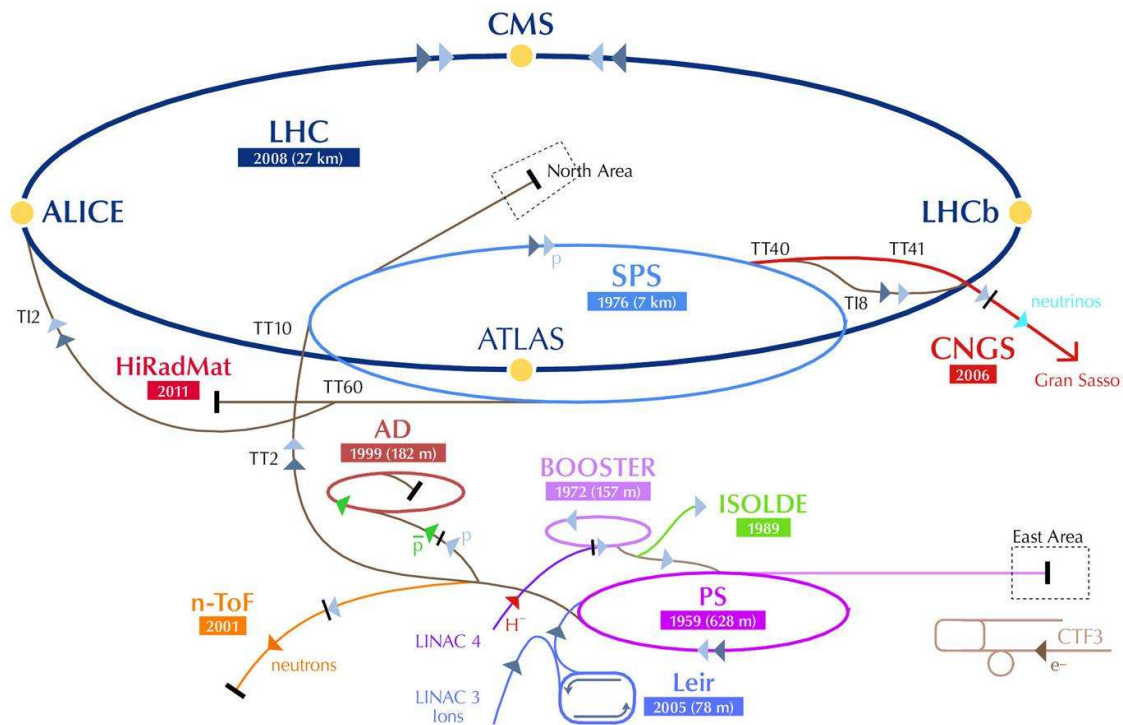


Figure 2.2: Schematic layout of the CERN accelerator complex (not to scale).

The LHC is linked through two transfer tunnels to the CERN accelerator complex, which is used as injector (see Figure 2.2). Protons are generated at the LINAC2 linear accelerator and sent to the Proton Synchrotron Booster (PSB) where the energy is increased to 1.4 GeV. In the Proton Synchrotron (PS) they are accelerated up to 25 GeV before the SPS accelerates the beam to 450 GeV and injects it into the LHC.

In order to obtain the design instantaneous luminosity, the machine went through a series of intermediate steps. At the first phase the machine ran with a luminosity ranging from $3 \times 10^{28} \text{ cm}^{-2}\text{s}^{-1}$ up to $2 \times 10^{31} \text{ cm}^{-2}\text{s}^{-1}$. A second phase with a luminosity of $10^{32} \text{ cm}^{-2}\text{s}^{-1}$ followed and at the end of the 2011 data-taking period a luminosity of $3.65 \times 10^{33} \text{ cm}^{-2}\text{s}^{-1}$ was achieved with an integrated luminosity of 5.61 fb^{-1} delivered at a centre-of-mass energy of $\sqrt{s} = 7 \text{ TeV}$.

During 2012 the LHC is producing collisions at $\sqrt{s} = 8 \text{ TeV}$ with $\sim 19 \text{ fb}^{-1}$ collected so far with a peak luminosity of $7.7 \times 10^{33} \text{ cm}^{-2}\text{s}^{-1}$. Starting from February 2013, a 20-month long shutdown is scheduled, mainly for maintenance and technical consolidation of the machine performance and some concerning experiment issues. After that, from 2014 on, operation is expected with an increase of its energy from the current energy of 8 TeV to 13 TeV or 14 TeV reaching the nominal luminosity of $10^{34} \text{ cm}^{-2}\text{s}^{-1}$, with few hundreds inverse femptobarns of integrated luminosity, and a bunch-crossing time of 25 ns, i.e. at a rate of 40 MHz. In 2018 the LHC phase I will end and a shutdown is scheduled with the goal of reaching a high luminosity of $2 \times 10^{34} \text{ cm}^{-2}\text{s}^{-1}$. In the period 2019 - 2021 the high luminosity LHC (HL-LHC) phase will take place, collecting data at $\sqrt{s} = 14 \text{ TeV}$. The last shutdown is scheduled for 2022-2023 at HL-LHC with the goal of reaching $5 \times 10^{34} \text{ cm}^{-2}\text{s}^{-1}$.

With respect to the LHC running with Pb-Pb nuclei collisions for the year 2011, a peak luminosity of $L = 5.1 \times 10^{26} \text{ cm}^{-2}\text{s}^{-1}$ was reached with collisions at $\sqrt{s_{NN}} = 2.76 \text{ TeV}$.

The data considered in the search performed in this thesis (see Chapter 5) were delivered by the LHC and collected by the ATLAS detector during 2011 at $\sqrt{s} = 7 \text{ TeV}$. The magnificent behaviour of the LHC and the ATLAS experiment during that year can be seen in Figure 2.3, where the total luminosity delivered by the LHC and collected by ATLAS during 2011 can be seen for proton-proton collisions (left) and for heavy ions (right).

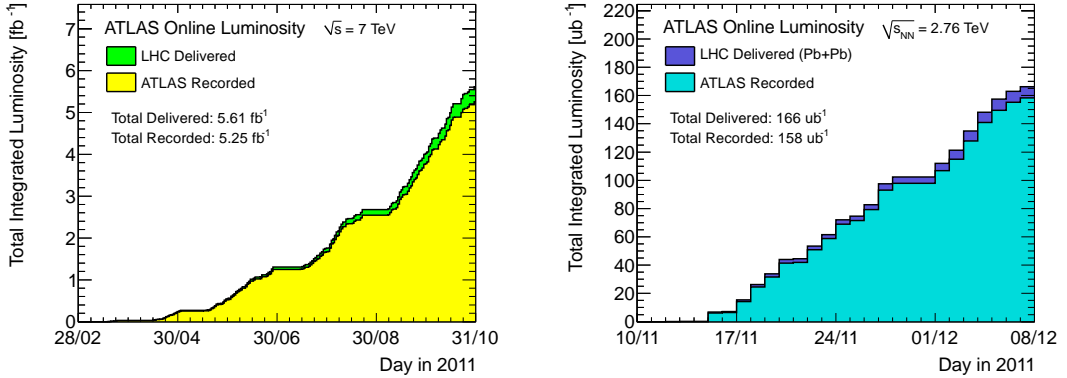


Figure 2.3: Luminosity delivered by the LHC and collected by ATLAS during 2011 for proton-proton (left) and Pb-Pb (right) collisions.

The LHC and the ATLAS detector have had a magnificent performance since they started delivering and collecting data in 2010. To get a visual image of the spectacular improvement of the LHC and the ATLAS experiment performances, the cumulative luminosity versus day delivered to ATLAS during stable beams and for pp collisions is shown in Figure 2.4. This is shown for 2010 (green), 2011 (red) and 2012 (blue) running.

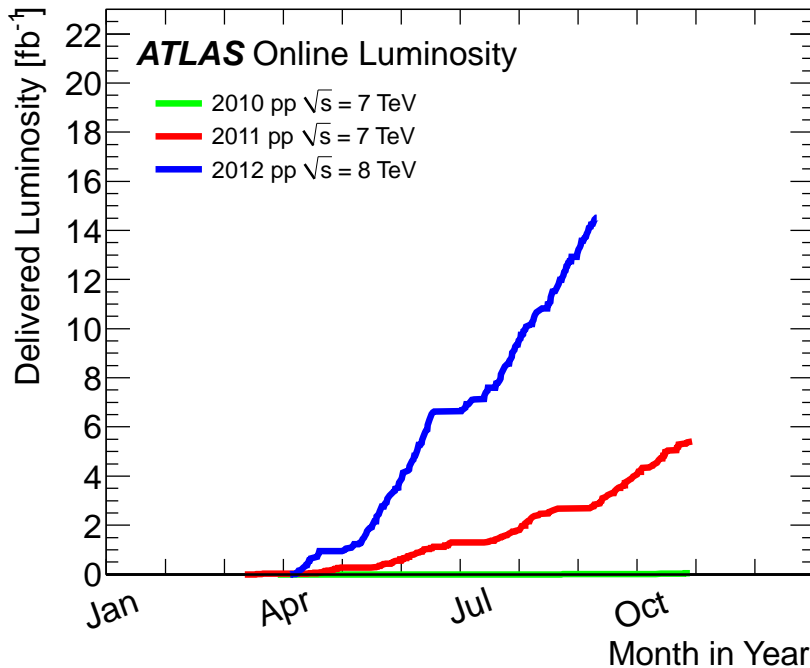


Figure 2.4: Delivered luminosity versus time for 2010, 2011, 2012 (pp data only).

2.2 The LHC experiments

Installed at the LHC there are two high-luminosity general-purpose experiments, ATLAS [7–9] and CMS [10], both aiming at a peak luminosity of $\mathcal{L} = 10^{34} \text{ cm}^{-2}\text{s}^{-1}$ for proton-proton operation. There are also two low-luminosity experiments: LHCb [41] for B -physics, aiming at a peak luminosity of $\mathcal{L} = 10^{32} \text{ cm}^{-2}\text{s}^{-1}$, and TOTEM [42] (integrated into CMS) for the detection of protons from elastic scattering at small angles, aiming at a peak luminosity of $\mathcal{L} = 10^{29} \text{ cm}^{-2}\text{s}^{-1}$.

In addition to the proton beams, the LHC operates with ion beams. The LHC has one heavy-ion dedicated experiment, ALICE [43], collecting data at a peak luminosity of $\mathcal{L} = 10^{27} \text{ cm}^{-2}\text{s}^{-1}$ with Pb-Pb nuclei collisions.

Placed at ± 140 m away from the ATLAS interaction point, the LHCf experiment [44] is installed. Its purpose is to study forward production of neutral particles in proton-proton collisions at extremely low angles, providing input to the many air-shower Monte Carlo codes currently used for modelling cosmic rays interactions in the Earth atmosphere.

A seventh experiment is being developed to be installed at the LHC. The MoEDAL [45] (Monopole and Exotics Detector at the LHC) project's prime motivation is to directly search for the Magnetic Monopole or Dyon and other highly ionising Stable (or pseudo-stable) Massive Particles (SMPs) at the LHC.

In the following, a general description of the four main LHC experiments is presented.

2.2.1 A Toroidal LHC Apparatus (ATLAS)

ATLAS [7–9] is a general-purpose experiment for high luminosity (up to $10^{34} \text{ cm}^{-2}\text{s}^{-1}$). Its design has been optimised to be sensitive to a wide range of physics signatures in order to fully exploit the discovery potential of the hadron collider. The experiment will perform high precision measurements on SM parameters and the Higgs boson search. It has also been designed to be able to account for several new physics processes that may be expected at the TeV scale. The ATLAS detector is nominally forward-backward symmetric with respect to the interaction point. It is the largest LHC detector, with 46 m length, 25 m diameter and weighting 7000 tons. The overall ATLAS detector layout is shown in Figure 2.5.

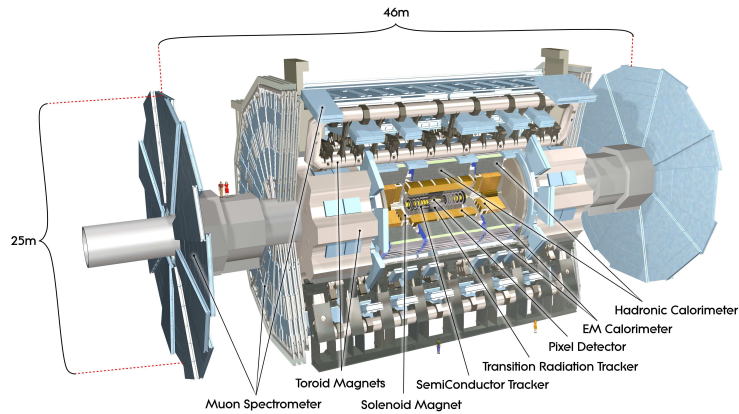


Figure 2.5: Layout of the ATLAS experiment.

It comprises three main subsystems: tracking system, calorimeters and muon detectors, all embedded in a magnetic field generated by a solenoidal and a toroidal magnet. They are arranged in a cylindrical barrel with two end-caps, following the usual particle detector scheme that aims at an hermetic coverage. From the inside out:

- **The Inner Detector (ID)**, together with the solenoidal magnet, ensures a robust pattern recognition and momentum determination, precise vertex measurements, electron identification, and electron-pion separation.
- **The Electromagnetic Calorimeter (ECAL)** for the identification and energy measurements of electrons and photons. The high granularity of the detector elements allows to work with excellent performance in terms of energy and position resolution.
- **The Hadronic Calorimeter (HCAL)** for the measurements of hadronic jets and missing transverse energy (E_T^{miss}).
- **The Muon Spectrometer**, a stand-alone tracking device for muon detection including high precision tracking chambers and trigger chambers with very fast response.
- **An air-core toroid magnet system**, generating strong bending power in a large volume.

In order to select events of interest, a three-level trigger system is used achieving a total rate reduction from approximately 4×10^{10} events per second to a rate of about 200 events/s.

The ATLAS detector will be described in more detail in Section 2.3.

2.2.2 Compact Muon Solenoid (CMS)

CMS [10] is the other general-purpose experiment for high luminosity and it has the same discovery potential as ATLAS although its hardware and software design are different. It is smaller than ATLAS, with a length of 21.6 m, a diameter of 14.6 m, although heavier with a total weight of 12500 tons. The most important difference with respect to the ATLAS detector is given by the choice of the magnetic field configuration for the measurement of the momentum of muons. It has the same general cylindrical structure as ATLAS, but different magnets geometry. The 13 m long, 6 m inner diameter, 4 T superconducting solenoid, providing a large bending power (12 T m), sits at the core of the CMS detector, and drives the final detector design and layout, which is shown on Figure 2.6.

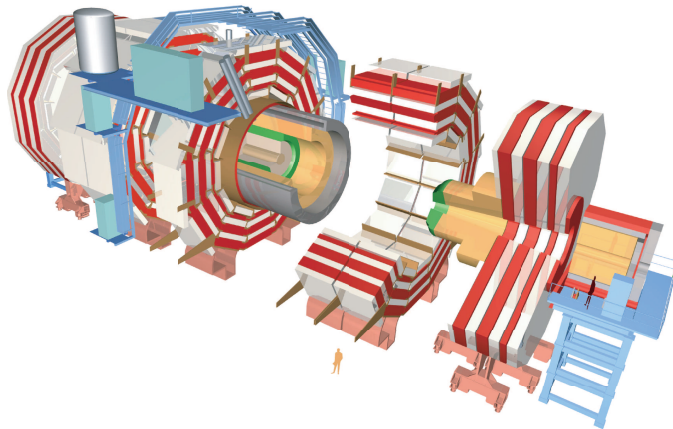


Figure 2.6: Layout of the CMS experiment.

The bore of the magnetic coil is large enough to accommodate inside:

- **The inner tracker**, with silicon microstrip detectors, which provide the required granularity and precision and silicon pixel detectors placed close to the interaction region to improve the measurement of the impact parameter of charged-particle tracks, as well as the position of secondary vertices.
- **The electromagnetic calorimeter (ECAL)**, with a coverage in pseudorapidity up to $|\eta| < 3.0$. A preshower system is installed in front of the ECAL endcap for π^0 rejection.
- **The hadron calorimeter (HCAL)**, surrounding the ECAL, with coverage a pseudorapidity of up to $|\eta| < 5.0$. This central calorimetry is complemented by a tail-catcher in the barrel region ensuring that hadronic showers are sampled with nearly 11 hadronic interaction lengths.

The coil is surrounded by a massive iron return yoke with the inserted **muon system**, covering most of the 4π solid angle, composed of muon chambers, consisting of several layers of aluminium drift tubes (DT) in the barrel region and cathode strip chambers (CSC) in the endcap region where the muon rate and the neutron background are higher.

Forward sampling calorimeters extend the pseudorapidity coverage to high values ($|\eta| < 5$) assuring very good hermeticity, full geometric coverage for the measurement of the transverse energy in the event. An even higher forward coverage is obtained with additional dedicated calorimeters and with the TOTEM [42] tracking detectors.

2.2.3 LHCb

The LHC is a B -hadrons factory, thanks to the high $b\bar{b}$ cross section in pp collisions at high energies. LHCb [41] is a low luminosity experiment ($10^{32} \text{ cm}^{-2}\text{s}^{-1}$) aimed to make precision studies of CP asymmetries and of rare decays in B -meson systems.

The LHCb detector is a single-arm spectrometer stretching for 20 metres along the beam pipe and with a forward angular coverage from approximately 10 mrad to 300 (250) mrad in the bending (non-bending) plane, defined by the magnetic field. Its subdetectors are stacked behind each other like books on a shelf. The choice of the detector geometry is justified by the fact that at high energies both the b - and \bar{b} -hadrons are predominantly produced in the same forward or backward cone. The layout of the LHCb spectrometer can be seen in Figure 2.7.

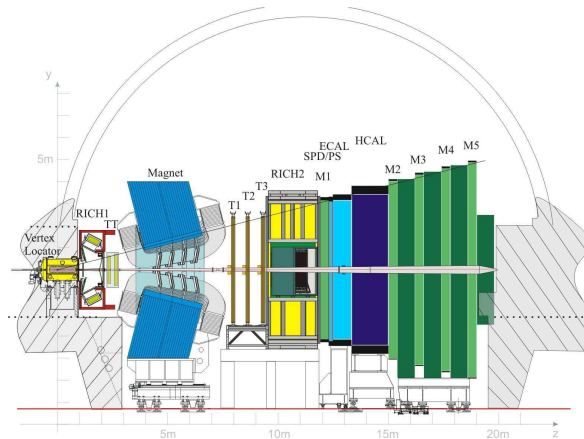


Figure 2.7: Layout of the LHCb experiment.

The LHCb is composed of:

- **The vertex locator (VELO)**, comprising a silicon detector providing precise information on the production and decay vertices of b -hadrons, and a pile-up veto counter used as a Level-0 trigger to suppress events containing multiple pp interactions in a single bunch-crossing.
- **The Tracker System**, partially inside a dipole magnet, is upstream of the spectrometer magnet, between the VELO and the calorimeters. It provides charged particles reconstruction and momentum measurements in addition to Level-1 and higher-level triggers.
- **Two Ring Imaging Cherenkov counters**, in charge of particle identification to achieve excellent $\pi - K$ separation for low (RICH1) and high (RICH2) momentum charged particles, and Hybrid Photon Detectors.
- **The calorimeter system**, whose main purpose is the identification of electrons and hadrons and the measure of their position and energy. It is composed of a Preshower Detector (SPD/PS) to reject the high backgrounds of charged pions, an electromagnetic calorimeter (ECAL) for efficient π^0 reconstruction and a hadron calorimeter (HCAL).
- **The muon detection system**, composed of five stations (M1-M5) placed downstream of the magnet along the beam axis.
- **A spectrometer magnet** providing an integrated field of 4 T m.

2.2.4 A Large Ion Collider Experiment (ALICE)

With heavy ions at a centre-of-mass energy of about 5.5 TeV, the LHC is the only machine that can reach and even extend the energy range probed by cosmic ray nucleus-nucleus collisions.

ALICE [43] is a heavy-ion detector which focuses on QCD, designed to address the physics of strongly interacting matter and the quark-gluon plasma at extreme values of energy density and temperature in nucleus-nucleus collisions. It works at a peak luminosity of $10^{27} \text{ cm}^{-2}\text{s}^{-1}$ for nominal Pb-Pb ion operation. Its overall dimensions are $16 \times 26 \times 26 \text{ m}^3$ with a weight of 10000 tons. It consists of a central barrel and a forward muon spectrometer as seen in Figure 2.8. The central part is embedded in a large magnet with a weak solenoid field of 0.5 T.

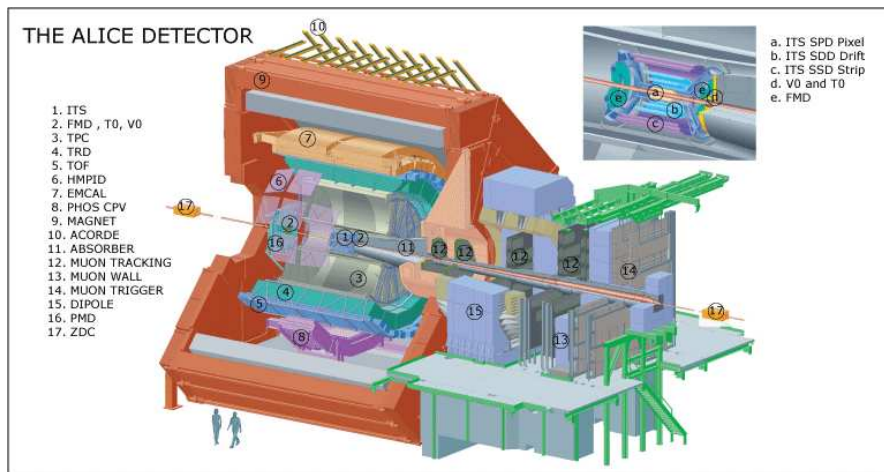


Figure 2.8: Layout of the ALICE experiment.

From the inside out, it is composed of:

- **The Inner Tracking System (ITS)**, aimed to the secondary vertex reconstruction of charm and hyperon decays, particle identification and tracking of low-momentum particles. It is formed by six layers of high-resolution detectors in the barrel, made of pixel and silicon drift detectors in the inner layers and silicon micro-strips in the outer ones.
- **A cylindrical Time-Projection Chamber (TPC)**, with a radius covering from $r \approx 90 \text{ cm}$ to $r \approx 250 \text{ cm}$. It gives an efficient and robust tracking and it serves for electron identification with momenta up to $\sim 2.5 \text{ GeV}$.
- **A large area for particle identification (PID)**. An array of Time-of-Flight (TOF) counters measure a momentum range limited to a few times the average p_T (more than 97% of all charged particles are below $p_T = 2 \text{ GeV}$) and π, K, p separation better than 3σ . A second system is optimised for the detection of high- p_T particles.
- **The electromagnetic calorimeters (PHOS and EMCal)**, single-arm high-resolution electromagnetic calorimeters to measure prompt photons, π^0 and η mesons.
- **The forward muon detector**, consisting of a complex arrangement of absorbers, a large dipole magnet (3 T m) and fourteen planes of tracking and triggering chambers located up to 14 m from the interaction point. It is designed to cover the complete spectrum of heavy quark resonances, with a mass resolution sufficient to separate all states.

2.3 ATLAS

The Large Hadron Collider (LHC) at CERN promises a major step forward in the understanding of the fundamental nature of matter. The ATLAS experiment is a general-purpose detector for the LHC, whose design was steered by the need to accommodate the wide spectrum of possible physics signatures covering the exploration of the TeV mass scale where ground-breaking discoveries are expected. Main investigation interests focus on the electroweak symmetry breaking mechanism and the search for the Higgs boson as well as high-precision measurements of the Standard Model parameters and the search for Physics beyond it.

Very small cross sections are expected for many of the interesting processes to be investigated. As a result, the LHC is designed to achieve a huge luminosity and consequently a very high interaction rate. The LHC will produce a total rate of 10^9 inelastic events per second at design luminosity. This leads to a number of formidable experimental challenges as it implies that, at the design luminosity, about 23 inelastic collisions per bunch crossing on the average will be superimposed on the event of interest. The total proton-proton cross section at $\sqrt{s} = 14$ TeV to be collected by ATLAS is expected to be roughly 100 mb.

Viewed in this context, these benchmark physics goals can be turned into a set of general requirements for the ATLAS detector.

- The detector requires fast, radiation-hard electronics and sensor elements. At nominal operation, a collision is expected every 25 ns. High-granularity detectors with good time resolution, resulting in low occupancy, can reduce the possible bunch crossings pile-up, avoiding the products of an interaction to be confused with the products of another one. The resulting millions of detector electronic channels require very good synchronisation.
- Large acceptance in pseudorapidity with almost full azimuthal angle coverage is required to achieve the highest hermeticity.
- Good charged-particle momentum resolution and reconstruction efficiency in the inner tracker are essential. Secondary vertices reconstruction in the vertex detectors is needed for offline tagging of τ -leptons and b -jets and potential long-lived particles predicted by some NP models.
- Very good electromagnetic calorimetry for electron and photon identification and measurements, complemented by hadronic calorimetry for accurate jet and missing transverse energy measurements.
- Good muon identification and momentum resolution over a wide range of momenta as well as charge determination.
- Highly efficient triggering is needed to achieve an acceptable event rate.

The ATLAS detector has been designed to be able to identify all kind of particles arising from the proton-proton collisions at the LHC. It is composed of several subdetectors placed in concentric cylinders each of which aims at detecting and reconstructing a particular feature of the particles to be detected. In the following, a brief description of each of the subdetectors is presented. A complete report on the design, construction and performance of the ATLAS detector can be found in Ref. [9].

2.3.1 Inner Detector

The ATLAS Inner Detector (ID) [46] is designed to provide pattern recognition and excellent momentum resolution for charged tracks with $p_T > 0.5$ GeV within the pseudorapidity¹⁾ range $|\eta| < 2.5$. It is the main instrument for the reconstruction and measurement of fermions, b-quark jets and tau-lepton tagging (complementary to that of the calorimeters) and primary and secondary vertices from the pp collisions at the LHC.

The order of 1000 tracks every 25 ns within $|\eta| < 2.5$ will need to be reconstructed by the ID at the LHC design luminosity. This induces a very high track and vertex density and hence the necessity for a high-precision measurement in the ID to disentangle each of the tracks and vertices. In order to reconstruct primary vertices, the ID needs to be as close to the interaction point as possible. It surrounds the LHC beam pipe which has a radius of 36 mm.

The ID layout, as shown in Figure 2.9, reflects the performance requirements. The ID is composed of four main parts: two precision tracker detectors made of silicon—the Pixel and the Semi-Conductor Tracker—and the Transition-Radiation Tracker made of straw tubes. In the outer part of the ID there is the central solenoid which immerses the ID in a 2T magnetic field.

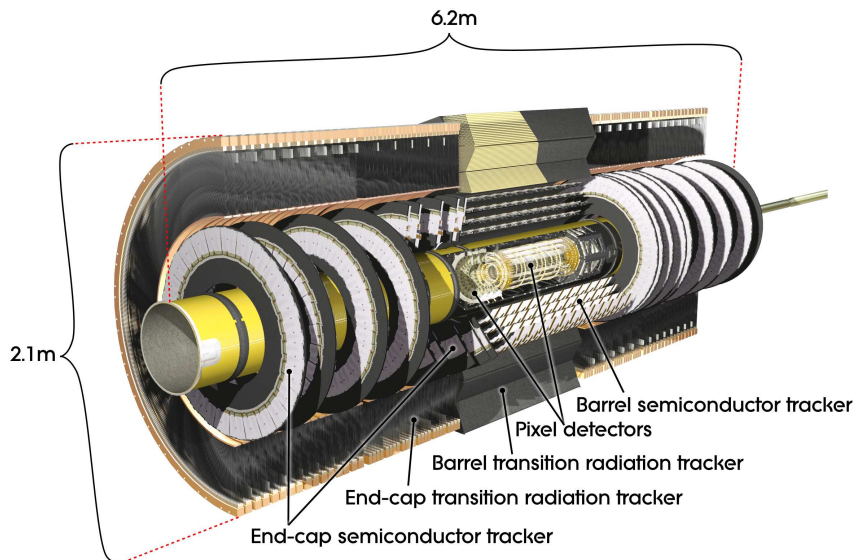


Figure 2.9: Layout of the ATLAS Inner Detector.

To maintain an adequate noise performance in the high-radiation environment the ID works in, the silicon sensors must be kept at low temperature, approximately -10°C . In contrast, the TRT is designed to operate at room temperature. In order to monitor the position of the detector elements, charged tracks are used and, for the SCT, laser interferometric monitoring. The ATLAS Inner Detector tracking system has been aligned for the analysis of the LHC $\sqrt{s} = 7$ TeV pp collision data taken during 2010 and 2011. For details on the alignment procedure, see Ref. [47]. The effect of the detector material on object reconstruction is also well understood. For a study on this effect, see Ref. [48].

¹⁾In the right-handed ATLAS coordinate system, the pseudorapidity η is defined as $\eta = -\ln[\tan(\theta/2)]$, where the polar angle θ is measured with respect to the LHC beamline. The azimuthal angle ϕ is measured with respect to the x -axis, which points towards the centre of the LHC ring. The z -axis is parallel to the anti-clockwise beam viewed from above. Transverse momentum and energy are defined as $p_T = p \sin \theta$ and $E_T = E \sin \theta$, respectively.

From the inside out, it is composed of the following subdetectors:

- **Pixel Detector**

The Pixel [49] is the inner-most subdetector. It is based on silicon sensors and aims at the precision measurements of tracks and vertices at small radii. It has a structure formed by three layers of concentric cylinders in the barrel and three end-cap disks per side perpendicular to the beam axis. All pixel modules are identical, with the minimum pixel size on a sensor being $50 \times 400 \mu\text{m}^2$. Secondary vertex reconstruction and measurement performance is enhanced by the inner-most layer of the pixel system, called "vertexing layer", at a radius of about 5 cm.

- **Semi-Conductor Tracker**

The Semi-Conductor Tracker (SCT) surrounds the Pixel detector. As the pixels, it is based on silicon sensors and aims at the precision measurements of tracks. It has a structure formed by four layers of concentric cylinders in the barrel and nine end-cap disks per side perpendicular to the beam axis. In the barrel region [50], small-angle stereo strips measure R and ϕ coordinates. Each side of a detector module consists of two 6.4 cm long, daisy-chained sensors with a strip pitch of $80 \mu\text{m}$. In the end-cap region [51], the detectors have a set of strips running radially and a set of stereo strips. The mean pitch of the strips is also approximately $80 \mu\text{m}$.

The radiation dose has important consequences for the sensors of both Pixel and SCT detectors. The required operating voltage depends on that irradiation.

- **Transition Radiation Tracker**

The Transition Radiation Tracker (TRT) [52] is next to the SCT and it is devoted to larger radii measurements. It is composed of 4 mm diameter straw tubes filled with a xenon-based gas mixture. In the barrel region the tubes are placed in straw planes parallel to the beam axis. In the end-caps the tubes are arranged radially in wheels in straw planes. The straw hits contribute significantly to the momentum measurements, since the lower precision per point compared to the silicon modules is compensated by the large number of hit measurements and longer measured track length.

- **Solenoid**

The solenoid extends over a length of 5.3 m with a diameter of 2.5 m. and immerses the ID in a 2T magnetic field with the function of making the measurement of particle charge and momenta possible.

Details on the subdetectors characteristics can be found in Table 2.1.

Table 2.1: Sensitive extension and accuracies of the ID subdetectors.

	Pixel		SCT		TRT	
$ \eta $ coverage	2.5		2.5		2.0	
	Barrel	End Caps	Barrel	End Caps	Barrel	End Caps
Radius (mm)	50.5 – 122.5	88.8 – 149.6	299 – 514	275 – 560	563 – 1066	644 – 1004
Length (mm)	0 – 400.5	495 – 650	0 – 749	839 – 2735	0 – 712	839 – 2710
($R - \phi$) accuracy (μm)	10	10	17	17	130 per straw tube	
z accuracy (μm)	115	115 (in R)	580	580 (in R)	–	
Average hits/track	3 pixel layers		4 space points		30 hits	

2.3.2 Calorimeters

Calorimeters are the main instrument for E_T^{miss} measurements and for the reconstruction of a large energy ranged jets, electrons and photons, for which different techniques are required. They need to completely retain electromagnetic and hadronic showers and to prevent hadrons from reaching the muon spectrometer (“punch-through”). A total thickness of 11 interaction lengths (λ) has been shown to be sufficient to reduce punch-through well below the irreducible level of prompt or decay muons. The layout of the Calorimeters is shown in Figure 2.10.

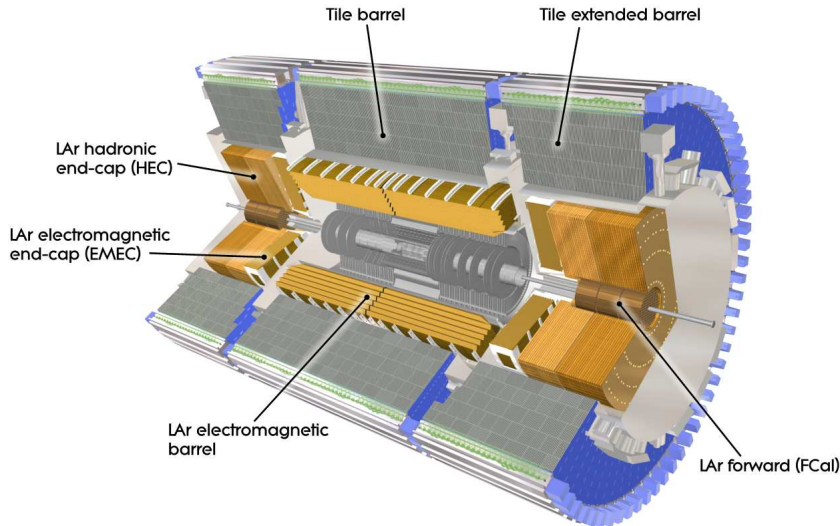


Figure 2.10: Layout of the ATLAS Calorimeters.

- **Liquid Argon Electromagnetic Calorimeter**

The Liquid Argon (LAr) [53] Electromagnetic Calorimeter is a lead-LAr detector with an accordion structure with kapton electrodes and lead absorber plates. It is divided into a barrel, covering $|\eta| < 1.475$ and two end-caps, covering $1.375 < |\eta| < 3.2$ (although precision measurements are restricted to the range $|\eta| < 2.5$), each of these parts located in their own cryostat. It shares the vacuum vessel with the solenoid in order to save two vacuum walls. The total thickness of the calorimeter is greater than 22 radiation lengths (X_0) in the barrel and greater than $24 X_0$ in the end-caps.

For $|\eta| < 1.8$, a presampler detector is used to correct for the energy lost by electrons and photons upstream of the calorimeter.

- **Hadronic Calorimeter**

The Hadronic Calorimeter [54] is composed of three main parts:

- **The Tile Calorimeter (TileCal)**, placed directly outside the EM calorimeter envelope, is a sampling calorimeter using steel as the absorber and scintillating tiles as the active material. It is composed of a barrel covering $|\eta| < 1.0$ and a thickness of 1.8λ and two extended barrels with $0.8 < |\eta| < 1.7$ and 3.3λ thick. The total radial extension of the TileCal ranges from an inner radius of 2.28 m to an outer radius of 4.25 m.

- **The LAr hadronic end-cap calorimeter (HEC)** is located directly behind the Electro-magnetic Calorimeter end-cap, covering the region $1.5 < |\eta| < 3.2$. It is composed of two independent wheels per end-cap, and it shares the same LAr cryostat as the EM end-caps. Each wheel is divided into two segments in depth, for a total of four layers per end-cap. It covers a radial extension from 0.475 m to 2.03 m.
- **The LAr forward calorimeter (FCal)** is integrated into the end-cap cryostats, providing uniformity of the calorimeter coverage and reduced background radiation level in the muon spectrometer, covering the range $3.1 < |\eta| < 4.9$. It is approximately 10λ deep and consists of three modules in each end-cap. The first one, made of copper, is optimised for electromagnetic measurements. The other two, made of tungsten, are optimised to measure the energy of hadronic interactions.

The approximate 10λ of active calorimeter combined with the large η coverage, provides good resolution for high energy jets and a good measurement of the E_T^{miss} .

2.3.3 Muon system

Only a tiny fraction of the LHC collisions that the ATLAS experiment detects, correspond to interesting Standard Model processes and an even smaller fraction may be associated to New Physics. Muons, especially those with high- p_T and those that are isolated from other activity in the detector, are much more common in these interesting events than in the background, and thus provide important means to identify such events.

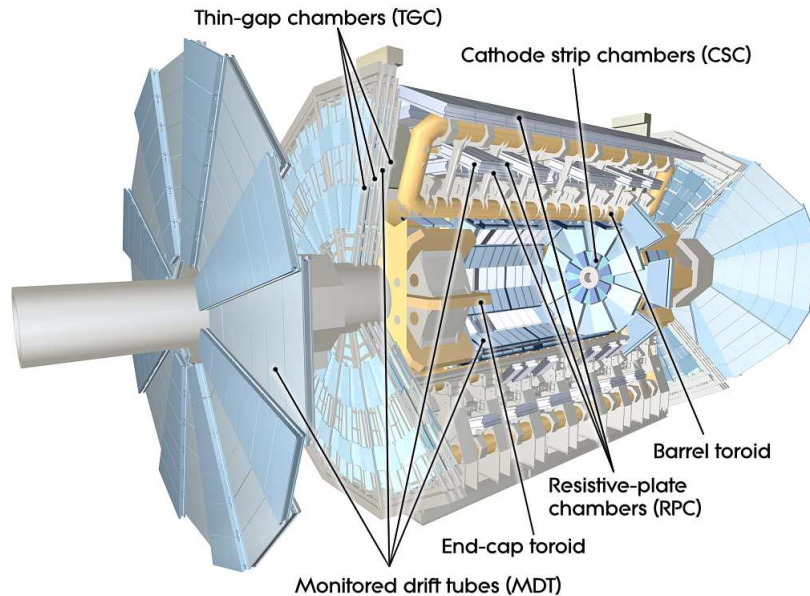


Figure 2.11: Layout of the ATLAS Muon System.

The ATLAS detector has been designed to provide efficient muon identification and precise momentum measurement over a wide range of momentum. The primary detector system built to achieve this objective is the muon spectrometer [55], shown in Figure 2.11. It is based on the magnetic deflection of muon tracks in the large superconducting air-core toroid magnets,

instrumented with separate trigger and high-precision tracking chambers. The muon spectrometer comprises three subsystems:

- **Superconducting coils**

The magnets system [56] provides a toroidal magnetic field whose performance in terms of bending power varies as a function of η and ϕ . Each of the three toroids consists of eight coils assembled radially and symmetrically around the beam axis. Over the range $|\eta| < 1.4$, magnetic bending is provided by the large barrel toroid, with a bending power of 1.5 to 5.5 T m. For $1.6 < |\eta| < 2.7$, two smaller end-cap magnets inserted into both ends of the barrel toroid give a bending power of 1 to 7.5 T m. Over $1.4 < |\eta| < 1.6$, usually referred to as the transition region, magnetic field is provided by a combination of barrel and end-cap fields. This magnet configuration provides a field which is mostly orthogonal to the muon trajectories and minimises the degradation of resolution due to multiple scattering.

- **Precision detectors**

These detectors are located in three widely-separated stations at increasing distance from the collision region. In the barrel region, tracks are measured in chambers arranged in three cylindrical layers around the beam axis; in the transition and end-cap regions, the chambers are installed in planes perpendicular to the beam, also in three layers. Over most of the η -range, a precision measurement of the track coordinates in the principal bending direction of the magnetic field is provided by Monitored Drift Tubes (MDT). In the innermost plane over $2 < |\eta| < 2.7$, Cathode Strip Chambers (CSC) with higher granularity are used to withstand the demanding rate and background conditions. The measurement precision in each layer is typically better than $100 \mu\text{m}$. The cathode strip chambers additionally provide a rough (1 cm) measurement of the ϕ -coordinate.

- **The trigger system**

Resistive Plate Chambers (RPC) in the barrel and Thin Gap Chambers (TGP) in the end-caps provide similarly rough measurements of η and ϕ . The trigger chambers for the muon spectrometer provide bunch-crossing identification, well-defined p_T thresholds and measure the muon coordinate in the direction orthogonal to that determined by the precision-tracking chambers.

High- p_T muons typically traverse all three stations obtaining good resolution and efficiency.

2.3.4 Forward detectors

Three smaller detector systems cover the ATLAS very forward region. At ± 17 m from the interaction point lies LUCID (LUminosity measurement using Cerenkov Integrating Detector), detecting inelastic pp scattering in the forward direction, and acting as the main online relative-luminosity monitor for ATLAS.

The second detector is the Zero-Degree Calorimeter (ZDC). Located at ± 140 m from the interaction point, where the LHC beam-pipe is divided into two separate pipes, plays a key role in determining the centrality of heavy-ion collisions.

The third system is ALFA (Absolute Luminosity For ATLAS), located at ± 240 m. It consists of scintillating fibre trackers located inside Roman pots which are designed to approach as close as 1 mm to the beam.

2.3.5 Trigger system

At design luminosity the general-purpose detectors will observe a rate of approximately 1 bunch-crossing (BC) every 25 ns (40 MHz) with an average of 20 interactions per BC. The online event selection process (trigger) must reduce this huge rate of 8×10^8 events per second to a rate of about 4000 events/s for storage and subsequent analysis, rejecting QCD processes while maintaining high efficiency for low cross section interesting physics processes that may include new physics. Decisions must be taken every 25 ns during normal LHC operations at the design luminosity of $10^{34} \text{cm}^{-2} \text{s}^{-1}$.

The ATLAS trigger is composed of three levels of event selection (Level 1 [57], Level 2 and Event Filter, referred to as the High Level Trigger or HLT [58] together with the Level 2), each of them refining the decisions made at the previous level.

- **Level 1 (L1)** is hardware-based. It receives data at the full LHC bunch crossing rate of 40 MHz and uses a limited amount of the total detector information in order to make a decision within $2.5 \mu\text{s}$ to reduce the output rate to 75 kHz.

The L1 trigger decision is based on the multiplicities and energy thresholds of electromagnetic clusters, jets and hadronic τ -leptons, missing transverse energy and total transverse energy of L1 objects observed in the trigger towers of the LAr and TileCal sub-systems. The measurement of trajectories in the muon trigger detectors are also used, where the input to the trigger decision is the multiplicity for various muon p_T thresholds.

Every L1 trigger configuration can be prescaled by a factor N , where only 1 in N events is selected and passed to the HLT for further consideration.

- **Level 2 (L2)** is based on software algorithms. The L1 output is passed to L2 as input to provide an additional rejection to reduce the output rate from 75 kHz down to 2 kHz.

A seed is constructed for each trigger accepted by L1 that consists of a p_T threshold and an $\eta - \phi$ position. The L2 algorithms use this seed to construct a region-of-interest (RoI) window around it. The L2 algorithms then use the RoI to selectively analyse the associated fine-grained sub-detector data for that $\eta - \phi$ position, including reconstructed tracks from the Inner Detector and more optimal calibrations to provide results with improved resolution.

- **Event Filter (EF)** is also based on software algorithms. The EF receives events accepted by L2 at a rate of 2 kHz and must provide the additional rejection to reduce the output rate to $\sim 200 - 400$ Hz with an event size of approximately 1.3 Mbyte, compatible with offline computing power and storage capacity. An average processing time of 4 s per event is available to achieve this rejection.

Each L2 trigger that has been accepted can be used to seed a sequence of EF algorithms that provide a more refined and complete analysis.

Trigger selections must be adaptable to the changing beam conditions while preserving the interesting physics and satisfying varying detector requirements. As the LHC ramps up to its design luminosity, the use of higher p_T thresholds, isolation criteria and tighter selections at HLT become necessary to reduce the background rates while achieving selection of interesting physics with high efficiency, maintaining the output Event Filter rates at about 200 Hz. However, many of the L1 thresholds are retained providing common points of comparison across luminosity regimes.

2.3.6 Object reconstruction in ATLAS

In order to recognise the processes originated in the pp collisions at the LHC and registered by the ATLAS detector, reconstruction and identification is needed for all kinds of particles: electrons and photons, high- p_T and isolated muons, tau-leptons decaying to hadrons and jets in a wide range of p_T . High quality and highly efficient reconstruction of all these kinds of particles is crucial in the searches for new phenomena. A very good measurement of the missing transverse energy, E_T^{miss} , is also essential for many physics studies in ATLAS.

In the following a basic explanation on how these objects are reconstructed and measured in ATLAS is given for each kind of object. Further details can be found in Ref. [8].

2.3.6.1 Tracking and vertexing

The track and vertex reconstruction is performed mainly in the Inner Detector, where the reconstruction algorithms [59] allow for several processes such as track extrapolation, track fitting including material corrections and vertex fitting and are logically sub-divided into three stages:

1. **A pre-processing stage**, in which the raw data from the pixel and SCT detectors are converted into clusters, the SCT clusters are transformed into space-points and the TRT raw timing information is translated into calibrated drift circles.
2. **A track-finding stage**, in which the high granularity of the pixel and SCT detectors is exploited in order to find prompt tracks originating from the vicinity of the interaction region. This is done in two steps:

First, the **inside-out algorithm** starts from 3-point seeds in the silicon detectors (in the three pixel layers and the first SCT layer) and then extends throughout the SCT to form track candidates. Next, these candidates are fitted and extended into the TRT to associate drift-circle information in a road around the extrapolation. Finally, the extended tracks are refitted with the full information of all three detectors. The inside-out algorithm is the baseline algorithm designed for the efficient reconstruction of primary charged particles²⁾

In a second stage, a complementary track-finding strategy, called **back-tracking**, searches for unused track segments in the TRT. Such segments are extended inwards by adding silicon hits. Back-tracking is designed to improve the tracking efficiency for secondaries, which are particles produced in the interactions of primaries, from conversions or decays of long-lived particles.

Finally tracks with a TRT segment but no extension into the silicon detectors are referred to as TRT-standalone tracks.

3. **A post-processing stage**, in which a dedicated vertex finder is used to reconstruct primary vertices. These are reconstructed using an iterative vertex finding algorithm [60]. Vertex seeds are obtained from the z -position at the beamline of reconstructed tracks. An iterative χ^2 fit is made using the seed and nearby tracks. Tracks displaced by more than 7σ from the vertex are used to seed a new vertex and the procedure is repeated until no additional vertices can be found. The beam spot position is used as a three-dimensional constraint. During reconstruction, vertices are required to contain at least two tracks, but for the studies in Section 5, vertices are required to have at least five tracks for robustness.

²⁾Primary particles are defined as particles with a mean lifetime greater than 3×10^{-11} s directly produced in a pp interaction or from the subsequent decays or interactions of particles with a lifetime shorter than 3×10^{-11} s.

After the track is fitted, corrections at later stages can be applied, like calibration corrections of the pattern recognition, to correct for module deformations or to resolve hit-association ambiguities. This is followed by algorithms dedicated to the reconstruction of photon conversions and of secondary vertices.

2.3.6.2 Electrons and photons

The ATLAS detector must be able to identify efficiently electrons and photons within a large energy range, and to measure their energies with a linearity better than 0.5%.

The standard reconstruction of an electromagnetic object is based on clusters reconstructed in the electromagnetic calorimeter and then, the inner detector information determines whether the object is a photon — either converted or unconverted — or an electron. The optimal cluster size depends on the particle type being reconstructed: electrons need larger clusters than photons due to their larger interaction probability in the upstream material and also due to the fact that they bend in the magnetic field.

For each of the reconstructed clusters, algorithms try to find a matching track with momentum compatible with the cluster energy. In the case that more than one track matches the same seed cluster, tracks with silicon hits have priority over tracks without silicon hits, the latter tracks being viewed as more likely to belong to electrons originating from photon conversions.

For every cluster energy, the reconstruction looks for the presence of an associated conversion. An electron candidate is created if a matched track is found and no conversion is flagged. Otherwise, the candidate is classified as a photon. This early classification allows for applying different corrections to electron and photon candidates. It is the starting point of a more refined identification based largely on shower shapes [6,7].

The energy is computed as a weighted average between the cluster energy and the track momentum. The ϕ and η directions are taken from the corresponding track parameters unless the track contains no silicon hits, in which case the ϕ position is taken from the track and the η is provided by cluster η -pointing.

Three levels of selection are defined for electrons:

1. **Loose Electrons.** This selection performs a simple electron identification based only on limited information from the calorimeters. Cuts are applied on the hadronic leakage (ratio of E_T in the first layer of the hadronic calorimeter to E_T of the EM cluster and the ratio of E_T in the hadronic calorimeter to E_T of the EM cluster) and on shower-shape variables. This set of cuts provides excellent identification efficiency, but low background rejection.
2. **Medium Electrons.** In addition to the loose requirements, this set of cuts improves the quality by adding cuts on the strips in the first layer of the EM calorimeter (for the rejection of $\pi^0 \rightarrow \gamma\gamma$ decays) and on the tracking variables. The medium cuts increase the jet rejection by a factor of 3-4 with respect to the loose cuts, while reducing the identification efficiency by $\sim 10\%$.
3. **Tight Electrons.** In addition to the cuts used in the medium set, further or tighter cuts are applied on the tracking variables. Furthermore, electron candidates matching to reconstructed photon conversions are rejected. An additional energy isolation cut can be applied to the cluster, using all cell energies within a cone of $\Delta R < 0.2$ around the electron candidate. This set of cuts provides, in general, the highest isolated electron identification and the highest rejection against jets.

2.3.6.3 Muons

The ATLAS detector is optimised for muon identification with an efficiency greater than 95% and a momentum resolution better than 3% over a wide transverse momentum. Muons are independently reconstructed in the Inner Detector and the muon spectrometer (MS).

The current ATLAS base line reconstruction includes two families of algorithms, both aiming at the association of tracks found in the MS with the corresponding ID track. The muon spectrometer is the outermost subdetector of the ATLAS detector, beginning after the muon has traversed 100 radiation lengths of material. Hence, a parameterisation of energy loss in the calorimeters is used for the muon momenta determination. These families of algorithms are referred to as:

- **Staco:** It involves three algorithms: Muonboy, Staco and MuTag. The track is built starting with Muonboy identifying “regions of activity” (ROA) in the MS. Track segments are reconstructed in the ROA for every muon station and they are combined to form muon candidates, which are finally fitted through the full MS system. Then Staco applies a Statistical COmbination of the two independent measurements, MS and ID. Only those combinations with a match χ^2 lower than certain threshold are accepted as muon combined tracks. The MuTag algorithm has been developed to tag low- p_T muons. It starts from ID tracks, extrapolates them to the MS and tries to match them with a segment reconstructed in these stations not yet associated with a combined track [61].
- **Muid:** The corresponding algorithms are Moore, Muid Standalone and MuGirl. The track reconstruction starts with Moore, which reconstructs tracks in the MS. It looks for ROA, constructs a path by matching the segments in each plane and makes a global fit of hits along the path. Then Muid Standalone extrapolates tracks from Moore back to the IP. Tracks are matched according to the same χ^2 as in Staco and finally, a new fit to all hits along this combined path is performed [62]. MuGirl is the analogous algorithm to MuTag. It performs a search for segments and tracks in the MS using an ID track as seed.

ATLAS employs a variety of strategies for identifying and reconstructing muons and each strategy includes one algorithm of each family. Muon identification can be performed in several ways:

1. **Standalone muons.** This is the most direct approach with MS information only. The direction of flight and the impact parameter of the muon at the IP are determined by extrapolating (taking into account the multiple scattering) the spectrometer track back to the beam line. The Staco-family algorithm, Muonboy, assigns energy loss based on the material crossed in the calorimeter. On the Muid side, Moore additionally makes use of the calorimeter energy measurements if they are significantly larger than the most likely value and the muon appears to be isolated.
Very low momentum muons (around a few GeV) may be difficult to reconstruct by standalone algorithms because they do not penetrate to the outermost stations. On the other hand, muons produced in the calorimeter, e.g. from π and K decays, are likely to be found in the standalone reconstruction.
- * **Inner detector muons.** Space points identified in the pixel and microstrip detectors are linked to form track seeds in the inner four layers. Tracks are found by extending these seeds to add measurements from the outer layers.
2. **Combined muons.** Combined muons are found by matching standalone muons to nearby inner detector tracks and then combining the measurements from the two systems. The match χ^2 is used to decide which pairs are retained.

3. **Segment-tagged muons.** The spectrometer tagging algorithms propagate all ID tracks with sufficient momentum out to the first station of the MS and search for nearby segments. If a segment is sufficiently close to the predicted track position, then the ID track is tagged as corresponding to a muon.

There is an important difference in the way these algorithms are run in the standard reconstruction chain. MuGirl [63] considers all ID tracks and re-does segment finding in the region around the track. MuTag [61] only makes use of ID tracks and MS segments not used by the general Staco algorithm.

4. **Calorimeter-tagged muons.** A trajectory in the inner detector is identified as a muon if the associated energy depositions in the calorimeters are compatible with the hypothesis of a minimum ionising particle.

* **Merging muons.** The muon finding efficiency (and fake rate) may be increased by including muons found by multiple algorithms. Special care is taken to remove overlaps, i.e. cases where the same muon is identified by two or more algorithms.

2.3.6.4 Tau leptons

Tau leptons decay hadronically in 64.8% of all cases predominately to pions, while in 17.8% (17.4%) of the cases they decay to an electron (muon) [14]. Because of their short lifetime, it is very difficult to separate τ leptons decaying to electrons or muons from prompt electrons and muons, and τ identification therefore focuses on reconstructing hadronically decaying τ leptons, τ_h . These are categorised by the number of charged decay products, observed as the number of tracks or prongs. Hadronic one-prong decays are the most common ($BR = 49.5\%$) followed by 3-prong decays ($BR = 15.2\%$) [14]. The small fraction (0.1%) of five-prong decays is usually too hard to detect in a jet environment.

Their reconstruction at hadron colliders remains a very difficult task in terms of distinguishing interesting events from background processes dominated by QCD multi-jet production. τ_h leptons are distinguished from QCD jets on the basis of low track multiplicities contained in a narrow cone, characteristics of the track system and the shapes of the calorimetric showers. Isolation from the rest of the event is required both in the inner detector and the calorimeter. Another related challenge is providing efficient triggering for these events while keeping trigger rates at manageable levels.

τ_h leptons are reconstructed starting from either calorimeter or track seeds [9]. *Track-seeded candidates* have a seeding track with $p_T > 6$ GeV satisfying some quality criteria. *Calorimeter-seeded candidates* consist of calorimeter jets reconstructed with the anti- k_T algorithm [64] starting from topological clusters (topoclusters) [65]. The candidate is required to have $p_T > 10$ GeV. The p_T of the τ candidate is further adjusted by applying multiplicative factors derived from MC studies, in order to reconstruct the p_T of signal τ leptons accurately.

The reconstruction of τ candidates provides very little rejection against QCD jet backgrounds. Rejection comes from a separate identification step and is usually based on several discriminating variables. Identification methods for τ candidates include selections based on simple cuts, boosted decision trees, and projective likelihood methods [66].

Three alternative identification methods have been studied to discriminate tau leptons from QCD jets and other two identification methods to reject electrons mis-identified as tau leptons. For a signal identification efficiency of $\approx 50\%$, rejection factors in the range 50-200 for jets and 50-1000 for electrons are achieved [67].

2.3.6.5 Jets

High quality jet reconstruction is an important feature for almost all physics analyses. Typically, an absolute systematic uncertainty of better than 1% on the jet energy scale is desirable for precision physics.

All jets are composed of constituents. The obvious way to obtain a jet is to gather those components and to calculate the jet p_T by adding their four-momenta. There is no universal jet finder for all topologies of interest. For example, the measurement of the inclusive QCD cross sections requires wide jets to capture the hard scattered parton kinematics. On the other hand, to find jets in very busy final states like possible SUSY signatures, narrow jets are preferred. For this reason several jet reconstruction tools have been developed. The most commonly used ones in ATLAS are seeded fixed cone finders, and sequential combination algorithms.

1. Fixed cone jet finder in ATLAS

This kind of algorithm aims at gathering energy in a geometric cone, whose radius R_{cone} is a key parameter of the algorithm, together with the seed p_T threshold. In the ATLAS cone jet finder the seed threshold is $p_T > 1$ GeV and a narrow ($R_{\text{cone}} = 0.4$) and a wide ($R_{\text{cone}} = 0.7$) cone jet options are available.

It starts by ordering all input objects in decreasing p_T . If the object with the highest p_T is above the threshold it is considered a seed and all objects within $\Delta R = \sqrt{\Delta\eta^2 + \Delta\phi^2} < R_{\text{cone}}$ are combined with it. A new direction is calculated from the four-momenta inside the cone and a new cone is centred around it. This process is repeated until the direction of the cone is stable and the object is called a jet. Then the next seed is taken from the input list and the same iterative procedure is repeated. This continues until no more seeds are available. This algorithm is not infrared safe (soft particles between two particles belonging to the same jet could affect the recombination of these two particles into a jet) and thus cannot be used in NLO QCD calculations. This can be partly recovered by introducing a split and merge step after the jet formation is done. A Seedless Infrared Safe Cone (SISCone) algorithm is also available for ATLAS.

2. Sequential recombination algorithms

These algorithms are based upon pair-wise clustering of the initial constituents. For every pair of objects i, j , the quantities d_{ij} and d_{iB} are defined for a given value of n [9]:

$$\begin{aligned} d_{ij} &= \min(p_{Ti}^{2n}, p_{Tj}^{2n}) \frac{(\Delta R)_{ij}^2}{R^2}, \\ d_{iB} &= p_{Ti}^{2n}. \end{aligned} \quad (2.3)$$

The d_{ij} is the distance between two objects, and d_{iB} is the distance between the object and the beam. Thus, the variable R is a parameter of the algorithm setting the resolution at which jets are resolved from each other as compared to the beam. A list of all d_{ij} and d_{iB} is compiled and its minimum, d_{\min} , is found. If d_{\min} is a d_{ij} , the corresponding objects i and j are combined into a new object using four-momentum recombination and the list is remade. If d_{\min} is a d_{iB} , the object i is considered to be a complete jet by itself and removed from the list. This procedure is repeated until the list is empty. This means that all original input objects end up to be either part of a jet or to be jets by themselves and, contrary to the cone algorithms described earlier, no objects are shared between jets. For large values of R , the d_{ij} are smaller and thus more merging takes place before jets are complete, and viceversa. Default configurations in ATLAS are $R = 0.4$ for narrow and $R = 0.6$ for wide jets. This procedure is infrared safe.

The variable n takes different values for different algorithms:

- **k_T algorithm:** $n = 1$.
Objects with low- p_T are merged first, like inverting the splitting in the parton shower which tends to be ordered in p_T . The final merge for a jet is the hardest component, and information about the jet substructure can be extracted in the merging process.
- **Anti- k_T algorithm:** $n = -1$ [64].
This means that in the vicinity $\Delta R < R$ of a hard object, all softer objects will be merged with the harder one in order of their closeness in ΔR . For hard objects within $\Delta R < R$ of each other, a single jet will be formed containing all objects within their vicinity.

ATLAS has developed several jet calibration schemes [8], all of them starting from the measured calorimeter energy (the most important system for jet reconstruction) at the electromagnetic (EM) energy scale, which measures the energy deposited by electromagnetic showers. In the simplest scheme (EM+JES) the jet calibration is derived as a simple correction relating the calorimeters response to the true jet energy. More sophisticated schemes exploit the topology of the calorimeter energy depositions to correct for calorimeter non-compensation and other jet reconstruction effects.

2.3.6.6 b -tagged jets

The ability to identify jets containing b -hadrons is important for the high- p_T physics program of ATLAS detector. Exploiting the relatively long lifetime and high mass of b -flavoured hadrons, offers the best performance to identify (tag) such jets. This can be done using different methods:

1. Impact-parameter-based algorithms.

The IP3D [68,69] algorithm uses a likelihood ratio technique in which input variables are compared to predefined distributions for both the b - and light jets, obtained from MC simulation. The distributions in this case are two-dimensional histograms of the signed transverse impact parameter (i.e. the distance between the IP and the point of closest approach to it) significance and longitudinal impact parameter significance of tracks.

2. Secondary-vertex-based algorithms.

Lifetime-based b -tagger algorithms reconstruct a secondary vertex (SV) from all the tracks associated to the jet which are displaced from the primary vertex (PV). In the SV0 algorithm [70], a jet is considered as tagged if the decay length significance of the reconstructed SV with respect to the PV is above a certain value. For further discrimination, the high-performance tagging algorithm SV1 [69] takes advantage of some vertex properties.

3. Decay chain reconstruction with the JetFitter algorithm.

The JetFitter algorithm exploits the topology of weak b - and c -hadron decays inside the jet. A Kalman filter is used to give an approximated flight path for the b -hadron. The discrimination between b -, c - and light jets is usually based on a likelihood using similar variables as in the SV1 tagging algorithm. Alternatively, a Neural Networks based discriminator can be used to separate b -, c - from light jets.

These algorithms can be easily combined: the weights of the individual tagging algorithms are simply summed up. The combination JetFitter+IP3D is based on artificial neural network techniques giving rise to a complex algorithm called **JetFitterCombNN**. These algorithms and their performance are described in detail in Ref. [9,71].

2.3.6.7 Missing Transverse Energy (E_T^{miss})

A very good measurement of the missing transverse energy, E_T^{miss} , is essential for many physics studies in ATLAS. Events with large E_T^{miss} are expected to be the key signature for new physics such as Supersymmetry and extra dimensions.

The E_T^{miss} in ATLAS is primarily reconstructed from energy deposits in the calorimeter and muon tracks. Apart from the hard scattering process of interest, many other sources, such as the underlying event, multiple interactions and pile-up, lead to energy deposits and/or muon tracks. Classifying the energy deposits into various types and calibrating them accordingly is the essential key for an optimal E_T^{miss} measurement. Other important requirement on the measurement of E_T^{miss} is to minimise the impact of limited detector coverage, finite detector resolution, presence of dead or inactive transition regions and different sources of noise that produce fake missing transverse energy, $E_{T,\text{Fake}}^{\text{miss}}$.

Two algorithms for reconstruction and calibration are implemented in the ATLAS software (see Ref. [9] for details). The first one is Cell-based, where the E_T^{miss} reconstruction and calibration is done starting from the energy deposited in calorimeter cells. The other one is Object-based, where the E_T^{miss} reconstruction is done from the reconstructed, classified and calibrated objects and from the energy outside of them. The performance of the two of them is similar.

1. Cell-based E_T^{miss} reconstruction

The Cell-based E_T^{miss} reconstruction includes contributions from transverse energy deposits in the calorimeters, corrections for energy loss in the cryostat and measured muons:

$$E_{x,y,\text{Final}}^{\text{miss}} = -(E_{x,y,\text{Muon}} + E_{x,y,\text{Cryo}} + E_{x,y,\text{Calo}}). \quad (2.4)$$

The E_T^{miss} muon term

The $E_{T,\text{Muon}}$ term is calculated from the momenta of measured muons. The E_T^{miss} resolution is only marginally affected by the muon term, due to the good resolution of the MS.

The E_T^{miss} cryostat term

The thickness of the cryostat between the LAr electromagnetic calorimeter and the tile hadronic calorimeter is about half an interaction length where hadronic showers can lose energy. The E_T^{miss} reconstruction recovers this loss of energy in the cryostat using the correlation of energies between the last layer of the LAr and the first layer of the TileCal.

The E_T^{miss} calorimeter term

The total transverse energy in the calorimeters, $E_{T,\text{Calo}}$, is calculated from the scalar sum of E_T of all TopoCells³⁾. The straightforward result obtained, gives a large shift in the E_T^{miss} scale of about 30% with respect to the True E_T^{miss} . This systematic shift is reduced after a dedicated calibration according to the cell classification, and a global calibration of all calorimeter cells using the H1-like or Local-Hadronic calibration schemes.

Refined calibration of the E_T^{miss} calorimeter term

Calorimeter cells are associated with a parent reconstructed and identified high- p_T object, in a chosen order: electrons, photons, muons, hadronically decaying τ -leptons, b -jets and light jets. Refined calibration of the object is then used in E_T^{miss} to replace the initial global calibration cells. Throughout this process, the sharing of energy of cells owned by two different TopoClusters is taken into account and the overlap removal is done at cell level in order to avoid double counting of cells in the E_T^{miss} calculation.

³⁾TopoCells are the cells that constitute a TopoCluster, which is a 3-dimensional topological calorimeter cluster

Once the cells are associated with categories of objects, the refined contribution to E_T^{miss} is calculated as:

$$E_{x,y,\text{RefCalo}}^{\text{miss}} = -(E_{x,y,\text{RefElec}} + E_{x,y,\text{RefTau}} + E_{x,y,\text{Refbjets}} + E_{x,y,\text{RefJets}} + E_{x,y,\text{RefMuon}} + E_{x,y,\text{RefOut}}), \quad (2.5)$$

where each term is calculated from the negative of the sum of calibrated cells inside a specific object and $E_{x,y,\text{RefOut}}$ is calculated from the cells in TopoClusters which are not included in the reconstructed objects.

The final E_T^{miss} calculated with this refined term for the calorimeter is referred to as $E_{T,\text{RefFinal}}^{\text{miss}}$.

2. Object-based E_T^{miss} reconstruction

The Object-based algorithm starts from the reconstructed, calibrated and classified high p_T objects ($e/\gamma, \mu, \tau, \text{jets}$) in the event. Each TopoCluster is allowed to be included only once by the first object that it is associated with it. Once the clusters belonging to electrons, photons, muons and taus are removed from the event record, hadronic jets above a certain threshold are identified. TopoCells not forming part of any of the above high p_T objects are classified as low p_T deposits from charged and neutral pions and calibrated accordingly.

A E_T^{miss} algorithm for the ATLAS triggers is also available. The E_T^{miss} L1 calorimeter triggers look for “jet elements”, formed by summing over trigger towers. If the L1 E_T^{miss} components pass certain thresholds, the event is saved as a given RoI. Then, the L2 algorithm uses the calorimeter information in the RoI and applies a correction for L2 muon objects. The EF algorithm sums all calorimeter cells, applies a hadronic calibration and takes the muon contribution into account.

2.4 LHC Computing GRID

In addition to the experiments, there is another key element in the LHC that makes the data storage and analysis possible: the Grid computing system.

The LHC produces roughly 15 PB of raw data annually, around 3.2 PB/year of which are produced by the ATLAS experiment. Moreover, processed data and Monte Carlo (MC) production need to be stored and analysed as well. This amount of data to be stored, together with the fact that over 6000 scientists spread over the World need to access them for analysis almost simultaneously, implies a great challenge. This goal has been resolved using the grid technology, a distributed data storage and computing infrastructure for the entire community which behaves in a stable and efficient way. The project is split into three Grid Flavours: LHC Computing Grid (LCG) [72] in Europe, NorduGrid/ARC [73] in the European Nordic countries and Open Science Grid (OSG) [74] in the US. The LHC distributed computing model is based on a hierarchy of sites called Tiers. CERN acts as the unique Tier 0 centre, recording on tape all data provided by the experiments in the LHC. After the initial processing, these data are distributed to a series of eleven Tier 1 centres located all over the World, keeping a double copy of all data. Tier 2 sites consist of one or several collaborating computing facilities, which can store sufficient data and provide adequate computing power for specific analysis tasks. They are designed to fulfil two main tasks: on one hand they are used for the Monte Carlo production and data processing and on the other hand they serve as storage elements for both MC and LHC data, which they receive Tier 1 centres. The current computing model is evolving to a mesh model where different Tier 2 sites can transfer data among themselves. Physics analyses are performed in the Tier 3 facilities, thought of as computing resources that can be composed of from a single laptop to huge local clusters. The defining philosophy of this model is the idea that jobs should be run in the site where the requested data are, avoiding this way long data transmissions.

Chapter 3

Theoretical framework

3.1 Supersymmetry

3.1.1 Introduction

The Standard Model of Particle Physics [75] provides the current most accurate description of the Elementary Particle Physics phenomenology. It has been experimentally tested up to the TeV scale with remarkably successful results. Nevertheless, there are pieces of evidence pointing to some New Physics (NP) beyond the SM such as the existence of Dark Matter, the matter-antimatter asymmetry, the neutrino masses, or the hierarchy problem. Thus, the SM needs to be extended or included in a more complete theory. Several theories have been developed in this direction among which Supersymmetry (SUSY) [1] is one of the most favoured.

SUSY was defined in the early 70's as the invariance of the theory under the interchange of fermions and bosons. Since it involves spin operators, if it holds in Nature, it is part of the quantum structure of Space and Time. In fact, according to the Haag-Lopuszanski-Sohnius extension of the Coleman-Mandula theorem [76,77], it is the only allowed transformation of the Lorentz group which is not already included in the SM.

During the first few years of its development (Wess-Zumino, 1974 [78]) it was a purely intellectual theory with no physical applications until people began to realise that SUSY might indeed solve many of the abovementioned problems:

- It provides a way to understand how the **EW $SU(2) \times U(1)$ symmetry is broken**, including the Higgs mechanism [79].
- In the case of R -parity conservation (to be explained later on), it **provides a natural candidate to Dark Matter (DM)** [29]: the lightest supersymmetric particle (LSP), which would need to be neutral, weakly interacting, massive and stable (a WIMP). Even in the case R -parity is violated there is still the possibility for a DM candidate such as the gravitino [22,23].
- **It is a Grand Unification Theory.** Including sparticles in the Renormalisation Group Equations (RGEs) for the gauge couplings of the Standard Model would permit them to unify at a very high energy scale [18, 19], whereas unification does not occur if only the Standard Model particles are included in the RGEs. Figure 3.1 (from [1]) shows a comparison of the inverse gauge couplings RG evolution in the SM and in a certain SUSY scenario.

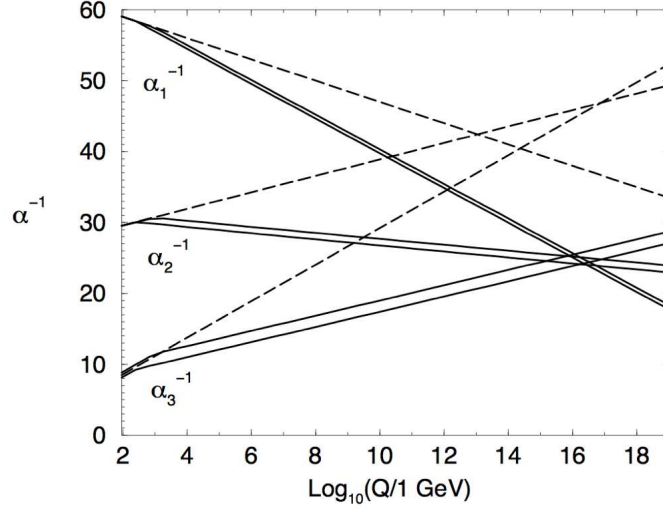


Figure 3.1: RG evolution of the inverse gauge couplings $\alpha_i^{-1}(Q)$ in the Standard Model (dashed lines) and the MSSM (solid lines). In the MSSM case, the sparticle mass thresholds are varied between 250 GeV and 1 TeV, and $\alpha_3(m_Z)$ between 0.113 and 0.123. Two-loop effects are included.

- **It stabilises the Higgs mass.** The Higgs boson is in charge of giving mass to all massive particles in the SM after the EW symmetry is spontaneously broken. If the Higgs boson is light, i.e. of the order of the electro-weak scale, the present electro-weak vacuum would be destabilised by divergent radiative corrections, that can be cancelled if the SM is supplemented by additional scalar particles [80]. This is automatic in SUSY.

The SM Higgs field is a complex scalar, ϕ , with a classical potential:

$$V = -\mu^2 \phi^\dagger \phi + \frac{\lambda_H}{4} (\phi^\dagger \phi)^2, \quad (3.1)$$

$$\phi = \begin{pmatrix} \phi^+ \\ \phi^0 \end{pmatrix},$$

where λ_H is the Higgs self-interaction coupling and $\mu^2 > 0$, otherwise spontaneous EW-symmetry breaking would not be possible.

This potential has its minimum at:

$$|\phi| = \frac{\sqrt{2}\mu}{\sqrt{\lambda_H}} \equiv \frac{v}{\sqrt{2}}, \quad (3.2)$$

where $v \equiv 2\mu/\sqrt{\lambda_H}$ is interpreted as the expectation value of the quantum field ϕ^0 in the quantum vacuum (vacuum expectation value, vev) at least at tree level, and it is related to the W^\pm and Z^0 boson masses through the relations:

$$m_{W^\pm} = \frac{vg}{2} \sim 80 \approx \text{GeV}, \quad (3.3)$$

$$m_{Z^0} = \frac{v}{2} \sqrt{g^2 + g'^2} = \frac{m_{W^\pm}}{\cos \theta_W} \sim 91 \approx \text{GeV},$$


where g and g' are the EW gauge couplings and θ_w is the Weinberg angle.

The first term in the Higgs potential Eq. (3.1) can be taken as the Higgs mass term:

$$m_H = \sqrt{2}\mu = v \sqrt{\frac{\lambda_H}{2}}. \quad (3.4)$$

If the Higgs potential is to be treated perturbatively ($\lambda_H \lesssim O(1)$) and taking into account the experimental value of $v = 246$ GeV [1], the Higgs mass needs to be of the order of $O(100$ GeV).

The second term in the Higgs potential is quartic in the Higgs field and gives a quadratically divergent correction to the Higgs-squared-mass, as shown in Figure 3.2:



$$\sim \lambda_H \int_0^{\Lambda_{uv}} d^4k \frac{1}{k^2 - m_H^2} \sim \lambda_H \Lambda_{uv}^2 \quad (3.5)$$

Figure 3.2: Scalar one-loop quantum correction to the Higgs squared-mass.

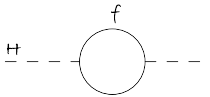
The parameter Λ_{uv} is the cut-off of the theory, an upper limit up to which the SM would be valid and beyond which the existence of NP is hypothesised. Adding this contribution to the Higgs “bare mass”, the physical μ parameter turns out to be:

$$\mu_{\text{physical}}^2 = \mu^2 - \lambda_H \Lambda_{uv}^2. \quad (3.6)$$

There are several solutions to this equation:

- $O(\mu^2) \sim O(\lambda_H \Lambda_{uv}^2)$: the “bare mass” is of the same order as the cut-off of the theory. This is the so-called *Fine Tuning* problem, meaning that the value of the bare mass needs to be set to the same scale as the new physics scale.
- Solutions like the Little Higgs theory [26], where the Higgs boson is a pseudo-Goldstone boson arising from some global symmetry breaking at the TeV scale, or technicolor [21], where SUSY breaking occurs “dynamically” as a result of a new strong interacting sector with a mass scale in the TeV region and scalar states formed as fermion-antifermion bound states.
- The divergent term $\lambda_H \Lambda_{uv}^2$ is somehow cancelled.

Concerning the last option, consider the interaction of the Higgs with a SM fermion through the Yukawa coupling λ_f , displayed in Figure 3.3:



$$\sim -|\lambda_f|^2 \Lambda_{uv}^2 \quad (3.7)$$

Figure 3.3: Fermionic one-loop quantum correction to the Higgs squared-mass.

This diagram would give a contribution to the Higgs squared-mass which would exactly cancel the divergent term in Eq. (3.5), provided that $\lambda_H = |\lambda_f|^2$. This condition is naturally given by Supersymmetry, as it will be seen in the following. It is worth noting that this kind of quadratic divergences affect only the scalar sector. The rest of masses in the SM get logarithmic corrections in Λ_{uv} , thus avoiding the fine-tuning problem.

3.1.2 Formal description of SUSY

The conservation of basic symmetries in Physics has been proven to be very successful. The Haag-Lopuszanski-Sohnius extension of the Coleman-Mandula theorem [76, 77] states that no further transformations of the Lorentz group can exist besides the four-momentum space-time translations (generated by P_μ) and the angular momentum transformations (generated by the antisymmetric tensor $M_{\mu\nu}$), except for objects transforming as spinors. This is exactly the kind of symmetry that SUSY proposes.

SUSY is defined as a symmetry relating fermions and bosons in such a way that every particle in the SM gets a supersymmetric partner (sparticle) with exactly the same quantum numbers and couplings except for the spin, that varies in $\pm 1/2$. This way, the relation $\lambda_H = |\lambda_t|^2$ automatically holds, not only at tree-level but also at any order in perturbation theory, and the Higgs mass is free of quadratic divergences.

The generator of such transformations must be a spinor, Q , fulfilling the equations:

$$Q |\text{Boson}\rangle = |\text{Fermion}\rangle; \quad Q |\text{Fermion}\rangle = |\text{Boson}\rangle, \quad (3.8)$$

$$\begin{aligned} \{Q, Q^\dagger\} &= \sigma_\mu P^\mu, \\ \{Q, Q\} &= \{Q^\dagger, Q^\dagger\} = 0, \\ [\sigma_\mu P^\mu, Q] &= [\sigma_\mu P^\mu, Q^\dagger] = 0. \end{aligned} \quad (3.9)$$

As usual, σ_μ are the 2×2 Pauli matrices.

In theories involving CP violation, like the SM, Eq. (3.9) properly define the SUSY algebra.

The single-particle states of a supersymmetric theory fall into irreducible representations of the supersymmetric algebra, called supermultiplets. Each supermultiplet contains the same number of fermionic and bosonic degrees of freedom (d.o.f.), called superpartners of each other. Because of the commutation of Q with the gauge transformations generators, particles inhabiting the same irreducible supermultiplet must have the same electric charge, weak isospin and color d.o.f. They must also have the same mass since Q commutes with P^μ as well.

There are several supermultiplet composition possibilities but in this thesis only two of them will be used:

- Chiral or matter or scalar supermultiplet, where all fermions in the SM and the Higgs boson live. It contains one Weyl fermion (ψ) and one complex scalar field (ϕ).
- Gauge or vector supermultiplet, where all gauge vector bosons of the SM live. It contains one massless spin-1 vector (A) and one massless Weyl fermion (λ).

In a supersymmetric field theory, the interactions and masses of all particles are determined by their gauge transformation properties and by the superpotential W . By construction, W has to be an analytic function of the superfields, single objects that contain all of the bosonic and fermionic fields within the corresponding supermultiplet: $\Phi_i \supset (\phi_i, \psi_i)^1$. The only renormalisable terms allowed are of the form [2]:

$$W = L^i \Phi_i + \frac{1}{2} M^{ij} \Phi_i \Phi_j + \frac{1}{6} y^{ijk} \Phi_i \Phi_j \Phi_k \quad (3.10)$$

¹From now on, superfields will be denoted with a hat and supersymmetric particles, with a tilde. For example, H_u denotes the spin-0 higgs doublet, \tilde{H}_u denotes its supersymmetric partner and \hat{H}_u denotes the Higgs superfield containing the two previous ones.

- L^i is only allowed if Φ_i is a gauge singlet. The scenario used in this work is based on the Minimal Supersymmetric Model (MSSM) containing the minimum field and interaction content that is able to reproduce the known phenomenology, described in Section 3.1.3. There are no such terms in the MSSM, so L^i terms will not be taken into account.
- M^{ij} is the symmetric mass matrix. Its entries can only be non-zero for supermultiplets Φ_i, Φ_j that transform under the gauge group in representations that are conjugate of each other.
- y^{ijk} are the dimensionless Yukawa couplings of a scalar and two fermions. They can only be non-zero when Φ_i, Φ_j, Φ_k transform in representations that can combine to form a singlet. y^{ijk} must be symmetric under the interchange of any of its indices. Hence, for each term of the form $y^{ijk}\phi_i\psi_j\psi_k$ there must also exist $y^{ijk}\phi_j\psi_i\psi_k$ and $y^{ijk}\phi_k\psi_i\psi_j$.

In a given theory, only a subset of the parameters L^i, M^{ij}, y^{ijk} is allowed to be non-zero. This condition is determined by the requirements of gauge invariance for the given supermultiplet content of the theory.

Because of the structure of supersymmetric theories — only terms analytic in the complex scalar fields allowed — up-type (down-type) quarks can only interact and get masses through a $Y = +1/2$ ($-1/2$) Higgs supermultiplet. As a result, two Higgs doublets are needed in SUSY: $H_u = (H_u^+, H_u^0)$ and $H_d = (H_d^0, H_d^-)$. A second reason for this need of two Higgs doublet can be found in the gauge anomaly cancellation. In the SM the gauge anomaly is cancelled due to the null sum of all left-handed Weyl fermionic d.o.f. third component of the hypercharge.

$$Tr[T_3^2 Y] = Tr[Y_3] = 0 \quad (3.11)$$

This cancellation would be spoiled if only a Higgs supermultiplet with $Y = +1/2$ or $Y = -1/2$ was considered.

Once the superpotential is defined, its derivatives $W^i = \delta W / \delta \Phi_i$ and $W^{ij} = \delta^2 W / \delta \Phi_i \delta \Phi_j$ can be used to write a lagrangian containing the chiral and gauge supermultiplets necessary to reproduce the SM phenomenology and which is invariant under supersymmetric transformations:

$$\begin{aligned} L_{\text{inv}} = & -D^\mu \phi^{*i} D_\mu \phi_i + i\psi^{\dagger i} \bar{\sigma}^\mu D_\mu \psi_i - \frac{1}{2}(W^{ij}\psi_i\psi_j + W_{ij}^*\psi^{\dagger i}\psi^{\dagger j}) - W_i^* W^i \\ & - \frac{1}{4}F_{\mu\nu}^a F^{\mu\nu a} + i\lambda^{\dagger a} \bar{\sigma}^\mu D_\mu \lambda^a - \sqrt{2}g(\phi^* T^a \psi)\lambda^a - \sqrt{2}g\lambda^{\dagger a}(\psi^\dagger T^a \phi) - \frac{1}{2}\sum_a g_a^2(\phi^* T^a \phi)^2. \end{aligned} \quad (3.12)$$

The gauge supermultiplets are formed by the massless Weyl fermion gauginos λ^a and the massless gauge boson fields A_μ^a that are included in the $F_{\mu\nu}^a$ currents, defined as in the SM in terms of the gauge coupling g and the totally antisymmetric structure constants f^{abc} , that define the gauge symmetry group together with its generators, the hermitian matrices $(T^a)_j^i$ satisfying $[T^a, T^b] = if^{abc}T^c$:

$$F_{\mu\nu}^a = \partial_\mu A_\nu^a - \partial_\nu A_\mu^a + gf^{abc}A_\mu^b A_\nu^c \quad (3.13)$$

Covariant derivatives have been included in the lagrangian instead of regular derivatives

for the complete lagrangian to be invariant under supersymmetry transformations:

$$\begin{aligned}
X &\rightarrow X + \delta X; & (X = \phi_i, \psi_i, W_i, A_\mu^a, \lambda_\alpha^a, D^a), & \tag{3.14} \\
\delta\phi_i &= \epsilon\psi_i, \\
\delta(\psi_i)_\alpha &= -i(\sigma^\mu\epsilon^\dagger)_\alpha D_\mu\phi_i - \epsilon_\alpha W_i, \\
\delta W_i &= i\epsilon^\dagger\bar{\sigma}^\mu D_\mu\psi_i - \sqrt{2}g(T^a\phi)_i\epsilon^\dagger\lambda^{\dagger a}, \\
\delta A_\mu^a &= -\frac{1}{\sqrt{2}}(\epsilon^\dagger\bar{\sigma}_\mu\lambda^a + \lambda^{\dagger a}\bar{\sigma}_\mu\epsilon), \\
\delta\lambda_\alpha^a &= \frac{i}{2\sqrt{2}}(\sigma^\mu\bar{\sigma}^\nu\epsilon)_\alpha F_{\mu\nu}^a + \frac{1}{\sqrt{2}}\epsilon_\alpha D^a, \\
\delta D^a &= \frac{i}{\sqrt{2}}(-\epsilon^\dagger\bar{\sigma}^\mu D_\mu\lambda^a + D_\mu\lambda^{\dagger a}\bar{\sigma}^\mu\epsilon),
\end{aligned}$$

where ϵ is an infinitesimal, anticommuting, two-component Weyl fermion object parameterising the supersymmetry transformation. In general, global supersymmetry is considered ($\partial_\mu\epsilon^\mu = 0$) unless gravity is included. In that case, as it is in the mSUGRA model that will be presented later, local supersymmetry takes places.

D^a is an auxiliary field fulfilling the equation of motion $D^a = -g(\phi^*T^a\phi)$, once the gauge supermultiplets are coupled to chiral supermultiplets.

And the covariant derivatives are defined as:

$$\begin{aligned}
D_\mu\phi_i &= \partial_\mu\phi_i - igA_\mu^a(T^a\phi)_i, & \tag{3.15} \\
D_\mu\phi^{*i} &= \partial_\mu\phi^{*i} + igA_\mu^a(\phi^*T^a)^i, \\
D_\mu\psi_i &= \partial_\mu\psi_i - igA_\mu^a(T^a\psi)_i, \\
D_\mu\lambda^a &= \partial_\mu\lambda^a + gf^{abc}A_\mu^b\lambda^c.
\end{aligned}$$

In Eq. (3.12), the superpotential W and its derivatives give rise to interaction terms between the scalar ϕ_i and fermionic ψ_i members of chiral supermultiplets. Discarding the singlet terms, it is defined as:

$$\begin{aligned}
W &= \frac{1}{2}M^{ij}\Phi_i\Phi_j + \frac{1}{6}y^{ijk}\Phi_i\Phi_j\Phi_k, & \tag{3.16} \\
W^i &= \frac{\delta W}{\delta\Phi_i} = M^{ij}\Phi_j + \frac{1}{2}y^{ijk}\Phi_j\Phi_k, \\
W^{ij} &= \frac{\delta^2 W}{\delta\Phi_i\delta\Phi_j} = M^{ij} + y^{ijk}\Phi_k.
\end{aligned}$$

When developing the lagrangian L_{inv} the following terms arise:

$$L_{\text{inv}} = -D^\mu \phi^{*i} D_\mu \phi_i + i\psi^{\dagger i} \bar{\sigma}^\mu D_\mu \psi_i \quad (3.17)$$

$$-\frac{1}{2}(M^{ij}\psi_i\psi_j + M_{ij}^*\psi^{\dagger i}\psi^{\dagger j}) \quad (3.18)$$

$$-\frac{1}{2}(y^{ijk}\Phi_i\psi_j\psi_k + y_{ijk}^*\Phi^i\psi^{\dagger j}\psi^{\dagger k}) \quad (3.19)$$

$$-(M^{ij}M_{il}^*\Phi_j\Phi^{*l}) \quad (3.20)$$

$$+\frac{1}{2}M^{ij}y_{ilm}^*\Phi_j\Phi^{*l}\Phi^{*m} + \frac{1}{2}M_{ij}^*y^{ilm}\Phi^{*j}\Phi_l\Phi_m \quad (3.21)$$

$$+\frac{1}{4}y^{ijk}y_{ilm}^*\Phi_j\Phi_k\Phi^{*l}\Phi^{*m}) \quad (3.22)$$

$$-\frac{1}{4}F_{\mu\nu}^a F^{\mu\nu a} - i\lambda^{\dagger a} \bar{\sigma}^\mu D_\mu \lambda^a \quad (3.23)$$

$$-\sqrt{2}g(\phi^* T^a \psi)\lambda^a - \sqrt{2}g\lambda^{\dagger a}(\psi^\dagger T^a \phi) \quad (3.24)$$

$$-\frac{1}{2}\sum_a g_a^2(\phi^* T^a \phi)^2. \quad (3.25)$$

Listed below is the information each of these terms provide:

- (3.17): kinematic terms for fermions and scalars in chiral supermultiplets (see Figure 3.4).

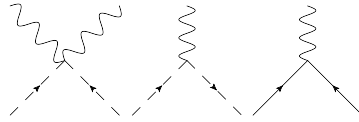


Figure 3.4: Standard interactions between gauge bosons and fermion or scalar fields that must occur in any gauge theory because of the form of the covariant derivative; they come from Eqs. (3.15) inserted in the kinetic part of the Lagrangian Eq. (3.17).

- (3.18): mass terms for fermions in chiral supermultiplets.
- (3.19): interaction terms for two fermions and one scalar from chiral supermultiplets (see Figure 3.5).

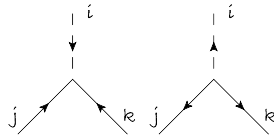


Figure 3.5: The dimensionless non-gauge interaction vertices in a supersymmetric theory: scalar-fermion-fermion Yukawa interaction y^{ijk} and its complex conjugate interaction.

- (3.20): mass terms for scalars in chiral supermultiplets. Note that the mass matrix is the same as for fermions, so that scalars and fermions in the same supermultiplets get the same masses, as they must when SUSY is an exact symmetry.
- (3.21): interaction terms for three scalars in chiral supermultiplets (see Figure 3.6).

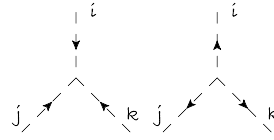


Figure 3.6: Supersymmetric dimensionful couplings: (scalar)³ interaction vertex $M^{ij}y_{ilm}^*$ and its conjugate interaction.

- (3.22): interaction terms for four scalars in chiral supermultiplets. The relation between y^{ijk} and y_{ijk}^* is exactly of the type needed to cancel the quadratic divergences in scalar masses quantum corrections (see Figure 3.7).

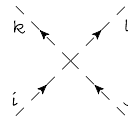


Figure 3.7: The dimensionless non-gauge interaction vertices in a supersymmetric theory: quartic scalar interaction $y^{ijk}y_{ilm}^*$.

- (3.23): kinematic terms for gauge supermultiplets fields (see Figure 3.8).

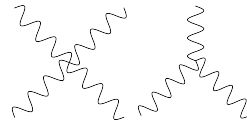


Figure 3.8: Interactions of gauge bosons, which derive from the first term in Eq. (3.23), when the gauge group is non-Abelian, for example for $SU(3)_C$ color and $SU(2)_L$ weak isospin.

- (3.24): interaction terms for scalar-fermion-gaugino (see Figure 3.9).

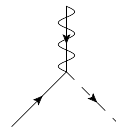


Figure 3.9: Coupling of a gaugino to a chiral fermion and a complex scalar.

- (3.25): 4-scalar interaction terms (see Figure 3.10).

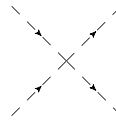


Figure 3.10: (scalar)⁴ interaction.

If SUSY was an exact symmetry, supersymmetric partners of SM components would have already been discovered. The fact that this is not the case indicates that, if SUSY exists, it has to be broken in a way such that the relation $\lambda_H = |\lambda_t|^2$ holds in the broken theory.

Various scenarios have been proposed to explain how SUSY breaking is realised. Spontaneous symmetry breaking is the most elegant mechanism to obtain such a result, however, it is not known how spontaneous breaking occurs in SUSY. One alternative to obtain phenomenological observables for SUSY searches is to keep a part of the lagrangian invariant under supersymmetric transformations (L_{inv}) and parameterise our ignorance by adding a new part, L_{soft} , that explicitly breaks SUSY through soft (of positive mass dimension) terms, and which do not compromise the cancellations in the scalar mass divergences:

$$L_{\text{SUSY}} = L_{\text{inv}} + L_{\text{soft}}. \quad (3.26)$$

The most general lagrangian that explicitly breaks SUSY at low energy scale with soft terms (excluding negligible terms and tadpoles for single fields) is [2]:

$$L_{\text{soft}} = -\left(\frac{1}{2}M_a\lambda^a\lambda^a + \frac{1}{6}a^{ijk}\phi_i\phi_j\phi_k + \frac{1}{2}b^{ij}\phi_i\phi_j\right) + c.c. - (m^2)_i^j\phi_i^*\phi_j. \quad (3.27)$$

This soft lagrangian respects all SM gauge symmetries, which forbid mass terms for SM non-scalar particles. However, mass-terms for gauginos (M^a) and scalar fields ($(m^2)_i^j$) are gauge-invariant so they are always allowed by symmetries (while a^{ijk} and b^{ij} may be not) and give mass to all sparticles. Hence, the soft lagrangian explicitly breaks SUSY when including such mass terms.

As a conclusion, masses for all known massive particles (SM) are protected by gauge symmetries and can only come from EW-symmetry breaking (EWSB). On the opposite, their superpartners' mass terms are gauge invariant and can be included in the theory (explicitly breaking SUSY), allowing them to be heavier.

The terms in L_{soft} have been proven to be free of quadratic divergences in the scalar mass quantum corrections to all orders in perturbation theory.

Using an argument analogue to the one used to estimate the upper value of the SM Higgs mass in Eq. (3.4), the largest mass scale associated with the soft terms, m_{soft} , can be derived:

$$m_{\text{soft}} \sim 1 \text{ TeV}. \quad (3.28)$$

3.1.3 MSSM

As it was stated previously, SUSY theories interactions and masses are determined by their gauge transformation properties and by the superpotential W , in which only a subset of the parameters L^i, M^{ij}, y^{ijk} in Eq. (3.10) can be non-zero. In the Minimal Supersymmetric Model (MSSM) [?], this subset is chosen to include the minimal content to produce a phenomenologically viable, gauge invariant model. The superpotential that gives these conditions is:

$$W_{\text{MSSM}}^{\text{inv}} = \hat{u}_{y_u}\widehat{Q}\widehat{H}_u - \hat{d}_{y_d}\widehat{Q}\widehat{H}_d - \hat{e}_{y_e}\widehat{L}\widehat{H}_d + \mu\widehat{H}_u\widehat{H}_d. \quad (3.29)$$

At this point, the need to include two types of Higgs doublets becomes very clear, besides the anomaly cancellation: the $\bar{u}QH_u$ Yukawa term will end up giving mass to the up-type quarks. In order to give mass to the down-type quarks, a $\bar{d}QH_u^*$ term would be necessary, but since the superpotential must be analytic in the scalar fields, such term is forbidden by the structure of supersymmetry. Hence, a second type of Higgs boson is needed to give masses to the down-type quarks through the terms $\bar{d}QH_d$.

The MSSM particle content can be found in Tables 3.1 and 3.2 and it defines the scalar, fermionic, gauge and gaugino fields to be taken into account in the lagrangian defined by Eq. (3.12):

$$\begin{aligned}
\phi &= \tilde{Q}, \tilde{u}, \tilde{d}, \tilde{L}, \tilde{e}, H_u, H_d, \\
\psi &= Q, \bar{u}, \bar{d}, L, \bar{e}, \tilde{H}_u, \tilde{H}_d, \\
A &= g, W^{\pm,0}, B^0, \\
\lambda &= \tilde{g}, \tilde{W}^{\pm,0}, \tilde{B}^0.
\end{aligned} \tag{3.30}$$

Table 3.1: Chiral supermultiplets in the MSSM.

Names	Superfield	spin 0	spin 1/2	SU(3) _C , SU(2) _L , U(1) _Y
squarks, quarks (× 3 families)	\widehat{Q}	$(\tilde{u}_L \tilde{d}_L)$	$(u_L d_L)$	$(\mathbf{3}, \mathbf{2}, \frac{1}{6})$
	\hat{u}	\tilde{u}_R^*	u_R^\dagger	$(\bar{\mathbf{3}}, \mathbf{1}, -\frac{2}{3})$
	\hat{d}	\tilde{d}_R^*	d_R^\dagger	$(\bar{\mathbf{3}}, \mathbf{1}, \frac{1}{3})$
sleptons, leptons (× 3 families)	\widehat{L}	$(\tilde{\nu} \tilde{e}_L)$	(νe_L)	$(\mathbf{1}, \mathbf{2}, -\frac{1}{2})$
	\hat{e}	\tilde{e}_R^*	e_R^\dagger	$(\mathbf{1}, \mathbf{1}, \mathbf{1})$
Higgs, higgsinos	\widehat{H}_u	$(H_u^+ H_u^0)$	$(\tilde{H}_u^+ \tilde{H}_u^0)$	$(\mathbf{1}, \mathbf{2}, +\frac{1}{2})$
	\widehat{H}_d	$(H_d^0 H_d^-)$	$(\tilde{H}_d^0 \tilde{H}_d^-)$	$(\mathbf{1}, \mathbf{2}, -\frac{1}{2})$

Table 3.2: Gauge supermultiplets in the MSSM.

Names	spin 1/2	spin 1	SU(3) _C , SU(2) _L , U(1) _Y
gluino, gluon	\tilde{g}	g	$(\mathbf{8}, \mathbf{1}, \mathbf{0})$
winos, W bosons	$\tilde{W}^\pm \tilde{W}^0$	$W^\pm W^0$	$(\mathbf{1}, \mathbf{3}, \mathbf{0})$
bino, B boson	\tilde{B}^0	B^0	$(\mathbf{1}, \mathbf{1}, \mathbf{1})$

Besides the $L_{\text{MSSM}}^{\text{inv}}$, determined by the superpotential Eq. (3.29), the MSSM contains a lagrangian explicitly breaking SUSY. The corresponding version of Eq. (3.27) for the MSSM is:

$$\begin{aligned}
L_{\text{MSSM}}^{\text{soft}} &= -\frac{1}{2}(M_3 \tilde{g}^a \tilde{g}^a + M_2 \tilde{W}^a \tilde{W}^a + M_1 \tilde{B} \tilde{B}) \\
&\quad -(\tilde{u}_a \tilde{Q} H_u + \tilde{d}_a \tilde{Q} H_d + \tilde{e}_a \tilde{L} H_d) \\
&\quad -\tilde{Q}^\dagger m_{\tilde{Q}}^2 \tilde{Q} - \tilde{L}^\dagger m_{\tilde{L}}^2 \tilde{L} - \tilde{u}_a^2 \tilde{u}^\dagger - \tilde{d}_a^2 \tilde{d}^\dagger - \tilde{e}_a^2 \tilde{e}^\dagger \\
&\quad -m_{H_u}^2 H_u^* H_u - m_{H_d}^2 H_d^* H_d \\
&\quad -(b H_u H_d + c.c.).
\end{aligned} \tag{3.31}$$

This $L_{\text{MSSM}}^{\text{soft}}$ introduces 105 new free parameters including masses, phases and mixing angles [81], although many of them are very restricted and experimentally constrained [82]. This huge number of parameters gets very much reduced if one accepts some way to spontaneously break SUSY at a high energy scale.

3.1.3.1 Mass spectrum

In the SM, masses of all particles are determined by the Higgs vev and the corresponding gauge or Yukawa couplings. In SUSY there are two Higgs doublets that get vevs after EWSB and masses of all particles are given by a combination of these two vevs: Let v_u be the H_u^0 vev and v_d be the H_d^0 vev. Then:

$$v_u^2 + v_d^2 = v^2 = \frac{4m_Z^2}{g'^2 + g^2} \approx (246 \text{ GeV})^2. \quad (3.32)$$

A useful parameter can be defined whose value is not fixed by present experiments:

$$\tan\beta = \frac{v_u}{v_d}. \quad (3.33)$$

The discussion of the sparticle masses is complicated by the mixing phenomena: after symmetry breaking, mixing will in general occur between any fields which have the same color, charge and spin.

1. Higgs.

Two doublets of complex scalar fields give a number of eight d.o.f. in the Higgs sector. After EWSB, three of these d.o.f. are absorbed into the pseudo-goldstone Z^0 and W^\pm bosons. The remaining five d.o.f. form five Higgs fields: two CP -even neutral fields (h^0 and H^0 , with $m_{h^0} < m_{H^0}$), one CP -odd neutral field (A^0) and two charged fields (H^\pm).

The masses of H^0 , A^0 and H^\pm can be arbitrarily large, but h^0 mass is limited by the experimental value of m_{Z^0} . At leading order, the inequality $m_{h^0} < m_{Z^0} |\cos(2\beta)|$ holds although the squared mass of h^0 is subject to important quantum corrections. After including several contributions such as those from top and stop loops, top-squarks mixing and others, a bound is obtained [1]:

$$m_{h^0} \leq 135 \text{ GeV}. \quad (3.34)$$

2. Neutralinos and charginos.

After SUSY breaking, higgsinos and gauginos mix to form mass eigenstates:

- $\tilde{H}_u^0, \tilde{H}_d^0, \tilde{B}^0$ and \tilde{W}^0 mix to form four neutralinos, $\tilde{\chi}_i^0$, by convention defined so that:

$$m_{\tilde{\chi}_1^0} < m_{\tilde{\chi}_2^0} < m_{\tilde{\chi}_3^0} < m_{\tilde{\chi}_4^0};$$

$\tilde{\chi}_1^0$ usually appears to be the Lightest Supersymmetric Particle (LSP), unless there is a lighter gravitino.

- $\tilde{H}_u^+, \tilde{H}_d^-, \tilde{W}^+$ and \tilde{W}^- mix to form four charginos, $\tilde{\chi}_i^\pm$, by convention defined as:

$$m_{\tilde{\chi}_1^\pm} < m_{\tilde{\chi}_2^\pm}.$$

In the gauge-eigenstate basis $(\varphi^0)^T = (\tilde{B}^0, \tilde{W}^0, \tilde{H}_d^0, \tilde{H}_u^0)$ the neutralino mass term can be written as:

$$L_{\tilde{\chi}^0 \text{ mass}} = -\frac{1}{2}(\varphi^0)^T \mathbf{M}_{\tilde{\chi}^0} \varphi^0 + c.c., \quad (3.35)$$

where

$$\mathbf{M}_{\tilde{\chi}^0} = \begin{pmatrix} M_1 & 0 & -g'v_d/\sqrt{2} & g'v_u/\sqrt{2} \\ 0 & M_2 & gv_d/\sqrt{2} & -gv_u/\sqrt{2} \\ -g'v_d/\sqrt{2} & gv_d/\sqrt{2} & 0 & -\mu \\ g'v_u/\sqrt{2} & -gv_u/\sqrt{2} & -\mu & 0 \end{pmatrix}. \quad (3.36)$$

Analogously, the chargino mass term can be written in the gauge-eigenstate basis $\varphi^\pm = (\tilde{W}^+, \tilde{H}_u^+, \tilde{W}^-, \tilde{H}_d^-)$ as:

$$L_{\tilde{\chi}^\pm \text{mass}} = -\frac{1}{2}(\varphi^\pm)^T \mathbf{M}_{\tilde{\chi}^\pm} \varphi^\pm + c.c., \quad (3.37)$$

where

$$\mathbf{M}_{\tilde{\chi}^\pm} = \begin{pmatrix} \mathbf{0} & \mathbf{X}^T \\ \mathbf{X} & \mathbf{0} \end{pmatrix}, \quad (3.38)$$

with

$$\mathbf{X} = \begin{pmatrix} M_2 & gv_u \\ gv_d & \mu \end{pmatrix} = \begin{pmatrix} M_2 & \sqrt{2} \sin \beta m_W \\ \sqrt{2} \cos \beta m_W & \mu \end{pmatrix}. \quad (3.39)$$

Mass eigenstates are related to gauge eigenstates by two unitary 2×2 matrices \mathbf{U} and \mathbf{V} according to:

$$\begin{pmatrix} \tilde{\chi}_1^+ \\ \tilde{\chi}_2^+ \end{pmatrix} = \mathbf{V} \begin{pmatrix} \tilde{W}^+ \\ \tilde{H}_u^+ \end{pmatrix}, \quad \begin{pmatrix} \tilde{\chi}_1^- \\ \tilde{\chi}_2^- \end{pmatrix} = \mathbf{U} \begin{pmatrix} \tilde{W}^- \\ \tilde{H}_d^- \end{pmatrix}. \quad (3.40)$$

Note that the mixing matrix for the positively charged left-handed fermions is different from that for the negatively charged left-handed fermions. They are chosen so that:

$$\mathbf{U}^* \mathbf{X} \mathbf{V}^{-1} = \begin{pmatrix} m_{\tilde{\chi}_1^+} & 0 \\ 0 & m_{\tilde{\chi}_2^+} \end{pmatrix} \quad (3.41)$$

After diagonalising these matrices, masses for neutralino and chargino mass eigenstates are obtained as a function of M_1, M_2, v_u, v_d, g and g' . Important corrections to this LO masses are derived by 1-loop corrections.

3. Squarks and sleptons.

Any scalars with the same quantum numbers can mix. In principle, three 6×6 matrices of squared masses should be diagonalised for $(\tilde{u}_L, \tilde{c}_L, \tilde{t}_L, \tilde{u}_R, \tilde{c}_R, \tilde{t}_R)$, $(\tilde{d}_L, \tilde{s}_L, \tilde{b}_L, \tilde{d}_R, \tilde{s}_R, \tilde{b}_R)$ and $(\tilde{e}_L, \tilde{\mu}_L, \tilde{\tau}_L, \tilde{e}_R, \tilde{\mu}_R, \tilde{\tau}_R)$ and a 3×3 matrix for $(\tilde{\nu}_e, \tilde{\nu}_\mu, \tilde{\nu}_\tau)$.

Nevertheless, a general hypothesis is usually assumed: because of the large Yukawa couplings (y_t, y_b, y_τ) compared to the others, the mixing angles between the first two families are taken to be negligible and their masses are taken to be degenerated in pairs: $(\tilde{u}_L, \tilde{c}_L)$, $(\tilde{u}_R, \tilde{c}_R)$, $(\tilde{d}_L, \tilde{s}_L)$, $(\tilde{d}_R, \tilde{s}_R)$, $(\tilde{e}_L, \tilde{\mu}_L)$, $(\tilde{e}_R, \tilde{\mu}_R)$, $(\tilde{\nu}_e, \tilde{\nu}_\mu)$.

Only mixing in the third family is considered for $(\tilde{t}_L, \tilde{t}_R)$, $(\tilde{b}_L, \tilde{b}_R)$ and $(\tilde{\tau}_L, \tilde{\tau}_R)$ giving rise to mass eigenstates $(\tilde{t}_1, \tilde{t}_2)$, $(\tilde{b}_1, \tilde{b}_2)$ and $(\tilde{\tau}_1, \tilde{\tau}_2)$.

4. Gluinos.

Gluinos are the only color octet fermions in the theory since $SU(3)_C$ is unbroken. As a result, gluinos do not mix with any other field. Their mass term is simply:

$$L_{\tilde{g}^a \text{mass}} = -\frac{1}{2} M_3 \tilde{g}^a \tilde{g}^a + c.c. \quad (3.42)$$

Table 3.3: The undiscovered particles in the Minimal Supersymmetric Model (with sfermions mixings for the first two families assumed to be negligible).

Names	Spin	P _R	Gauge Eigenstate	Mass Eigenstate
Higgs Bosons	0	+1	$H_u^0 H_d^0 H_u^+ H_d^-$	$h^0 H^0 A^0 H^\pm$
squarks	0	-1	$\tilde{u}_L \tilde{u}_R \tilde{d}_L \tilde{d}_R$ $\tilde{s}_L \tilde{s}_R \tilde{c}_L \tilde{c}_R$ $\tilde{t}_L \tilde{t}_R \tilde{b}_L \tilde{b}_R$	(same) (same) $\tilde{t}_1 \tilde{t}_2 \tilde{b}_1 \tilde{b}_2$
sleptons	0	-1	$\tilde{e}_L \tilde{e}_R \tilde{\nu}_e$ $\tilde{\mu}_L \tilde{\mu}_R \tilde{\nu}_\mu$ $\tilde{\tau}_L \tilde{\tau}_R \tilde{\nu}_\tau$	(same) (same) $\tilde{\tau}_1 \tilde{\tau}_2 \tilde{\nu}_\tau$
Neutralinos	1/2	-1	$\tilde{B}^0 \tilde{W}^0 \tilde{H}_u \tilde{H}_d$	$\tilde{\chi}_1^0 \tilde{\chi}_2^0 \tilde{\chi}_3^0 \tilde{\chi}_4^0$
Charginos	1/2	-1	$\tilde{W}^\pm \tilde{H}_u^\pm \tilde{H}_d^\mp$	$\tilde{\chi}_1^\pm \tilde{\chi}_2^\pm$
gluino	1/2	-1	\tilde{g}	(same)
goldstino	1/2	-1	\tilde{G}	(same)
(gravitino)	(3/2)	-1	\tilde{G}	(same)

In Table 3.3, the list of particles predicted by the Minimal Supersymmetric Model which have not been observed so far, is shown.

3.1.4 mSUGRA

The Super Gravity (SUGRA) model [83] adopts a conventional ansatz assuming the transmission of supersymmetry breaking via gravity. In this model, spontaneous SUSY breaking sector connects with the MSSM dominantly through gravitational-strength interactions. This means that the supergravity effective lagrangian contains non-renormalisable terms — like all known theories that include general relativity — that communicate between the two sectors. Fortunately, non-renormalisable interactions can be neglected for most phenomenological purposes because their effects at energies E ordinarily accessible to experiments are typically suppressed by powers of E/M_P .

Still there are some interests for non-renormalisable terms:

1. Several very rare processes can only be described using an effective lagrangian that includes non-renormalisable terms.
2. They are important to study physics at very high energies, for instance the early universe.
3. Non-renormalisable terms can be important in understanding how SUSY breaking is transmitted to the MSSM.

In a “minimal” form of the normalisation of kinetic terms and gauge interactions in the full non-renormalisable supergravity lagrangian, a dramatic simplification occurs: one common coupling appears for the three gauginos, one for all scalars, one for all three-field interactions and one for all two-field interactions, in a way that makes all gauginos to be degenerated and all squark, sleptons and higgsinos to be degenerated at the Planck mass scale:

$$\begin{aligned}
M_1 &= M_2 = M_3 = m_{1/2}, \\
m_Q^2 &= m_{\tilde{u}}^2 = m_{\tilde{d}}^2 = m_L^2 = m_{\tilde{e}}^2 = m_0^2 \cdot 1; & m_{H_u}^2 &= m_{H_d}^2 = m_0^2, \\
a_u &= A_0 y_u; & a_d &= A_0 y_d; & a_e &= A_0 y_e, \\
b &= B_0 \mu.
\end{aligned} \tag{3.43}$$

The strength of the two-field interaction, B_0 and the parameter of the Higgs mass term, μ , can be substituted by $\tan\beta$ and the sign of the μ term, $\text{sgn}(\mu)$. Hence, the minimal Super Gravity (mSUGRA) [84] model can be determined by only five parameters: the fermions mass at the Planck scale, $m_{1/2}$; the scalars mass at the Planck scale, m_0 ; the coupling strength for three-field interactions, A_0 ; the ratio of the vevs of the two neutral Higgses, $\tan\beta$; and the sign of the Higgs mass term, $\text{sgn}(\mu)$.

Following the boundary conditions of mSUGRA, the RGEs for the running masses will give different masses for all different particles at energies E where experiments work. From these RGEs, it turns out that masses of squarks should be larger than those of sleptons. In Figure 3.11 a picture of this situation is represented (see Ref. [1] for details).

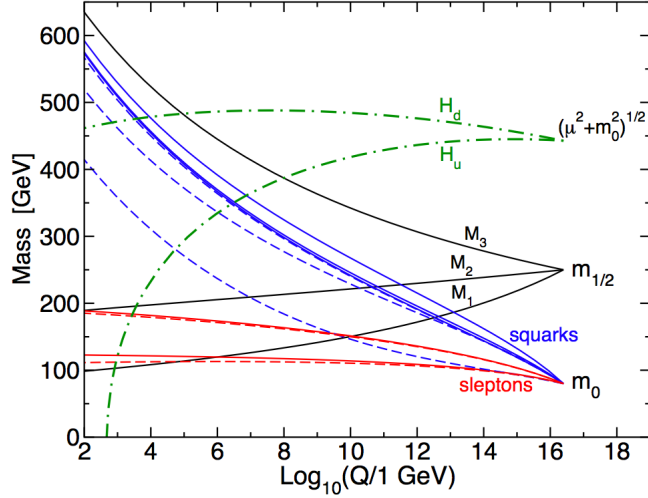


Figure 3.11: RG evolution of scalar and gaugino mass parameters in the MSSM with typical minimal supergravity-inspired boundary conditions imposed at $Q_0 = 2.5 \times 10^{16}$ GeV. The parameter $\mu^2 + m_{H_u}^2$ runs negative, provoking electroweak symmetry breaking.

3.2 R -parity violation (RPV)

In the previous section, the minimal supersymmetric model able to reproduce the known phenomenology was introduced. However, there are many additional terms that one can write which are gauge invariant and analytic in the superfields. Among them, terms violating either baryon (B) or total lepton (L) numbers are in principle allowed to enter in the SUSY superpotential in the form:

$$W_{\Delta L=1}^{\text{inv}} = \frac{1}{2} \lambda^{ijk} \widehat{L}_i \widehat{L}_j \widehat{e}_k + \lambda'^{ijk} \widehat{L}_i \widehat{Q}_j \widehat{d}_k + \epsilon^i \widehat{L}_i \widehat{H}_u, \quad (3.44)$$

$$W_{\Delta B=1}^{\text{inv}} = \frac{1}{2} \lambda''^{ijk} \widehat{u}_i \widehat{d}_j \widehat{d}_k, \quad (3.45)$$

where ϵ and $\lambda, \lambda', \lambda''$ are couplings of the type of M^{ij} and y^{ijk} in Eq. (3.10), respectively.

There does not exist any theoretical reason for these quantum numbers to be conserved. In fact in the SM, although no renormalisable terms exist that violate B or L , they are both violated by non-renormalisable electroweak effects.

For the sake of simplicity, most of the SUSY models choose to deliberately exclude this kind of terms. To do so, one can simply assume B and L conservation, but that would clearly be a step backwards since this assumption is absent in the SM, where only the conservation of $B - L$ is present.

One option is to impose the conservation of $B - L$ through the conservation of Matter Parity, a discrete multiplicative quantum number defined as:

$$P_M = (-1)^{3(B-L)}. \quad (3.46)$$

The main feature of this operator is that it commutes with SUSY, so particles in the same supermultiplet have the same P_M . Quark and lepton supermultiplets have $P_M = -1$; Higgs supermultiplets have $P_M = +1$; gauge bosons and gauginos do not carry any baryon or lepton number, so they are assigned $P_M = +1$.

One advantage of this operator is that it could be an exact symmetry, which B and L themselves could not since they are known to be violated by non-perturbative EW effects. So even if P_M is conserved, B and L could be violated in the same tiny amount. Nevertheless, no renormalisable terms exist that violate B or L in a way such that $B - L$ is preserved. Thus, conserving P_M would imply conserving both B and L , and terms in Eq. (3.44) and (Eq. 3.45) would be excluded.

A more phenomenologically useful way to preserve B and L is through the conservation of R -parity. It is also a discrete multiplicative quantum number defined as:

$$P_R = (-1)^{3(B-L)+2s}, \quad (3.47)$$

where s stands for the spin.

The operator P_R does not commute with SUSY, so particles in the same supermultiplet do not share the same value for P_R . Instead, all of the SM particles have the same $P_R = +1$ and all of their superpartners have $P_R = -1$.

The assumption of R -parity conservation (RPC), as it is taken in the MSSM, leads to four main consequences:

1. The lightest supersymmetric particle (LSP) must be stable and neutral. Otherwise, if they participated in electromagnetic and/or strong interactions, LSPs surviving the Big Bang era would have bound with nuclei, forming objects with unusually large charge to mass ratios [85] [86].
2. Being neutral and stable weakly interacting massive particles, LSPs become viable Dark Matter (DM) candidates in the case of RPC.
3. Each sparticle must decay into an odd number of sparticles.
4. In collider experiments, sparticles are produced in even numbers.

As a result, RPC SUSY events in collider experiments will end up having two massive stable neutral LSPs, that will escape their detection. Hence, these events are characterised by large unbalanced energy signals. At the LHC, where the parton z -direction energy is not well defined and the energy balance is measured in the $x - y$ plane only, this is translated into large missing transverse energy (E_T^{miss}).

There is no fundamental motivation for R -parity to be an exact symmetry. In the case it is not, its breaking should be through feeble interactions since B or L violating processes have never been observed experimentally. The most obvious experimental constraint to R -parity violation comes from the non-observation of the proton decay, which would violate both B and L , through the diagram in Figure 3.12.

$$\Gamma_{p \rightarrow e^+ \pi^0} = m_p^5 \frac{\sum_{i=2,3} |\lambda'^{11i} \lambda''^{11i}|^2}{m_{\tilde{d}_i}^4} \quad (3.48)$$

Figure 3.12: Example of proton decay through both B and L violation.

If $|\lambda'^{11i} \lambda''^{11i}| \sim O(1)$ and $m_{\tilde{d}_i} \sim O(1 \text{ TeV})$, then the proton would decay in a tiny fraction of a second, whilst experimental limits for the proton lifetime are $\tau_p > 10^{31}$ to 10^{33} years, depending on the decay mode ($\tau_{p \rightarrow e^+ \pi^0} > 8.2 \times 10^{33}$ years) [14].

If R -parity is finally broken, the RPC consequences enumerated above are no longer valid. The LSP would not be stable (the LSP loses validity as a DM candidate, still axion-like gravitinos or majoron could occupy this place [22, 23]) and it could be strongly interacting or charged. In this case, mSUGRA parameters leading to $\tilde{\tau}$ -LSP are also viable [38].

3.2.1 Bilinear R -parity violation (bRPV)

Among the different ways to break R -parity, there are several reasons to focus on the bilinear term in Eq. (3.44). As it was already mentioned, the preferred mechanism to break a symmetry is spontaneously. This also applies to P_R , which can be spontaneously broken at high energy scales through the violation of L while B is conserved. Hence, breaking L seems more natural than breaking B . In Eq. (3.44) there are one kind of bilinear and two kinds of trilinear terms which break lepton number. If RPV is induced by any of the trilinear terms, it is unavoidable for the theory to contain bilinear terms, since they arise from the Renormalisation Group Evolution (RGE) of the trilinears. In contrast, it is perfectly consistent to have an R -parity breaking through bilinear terms without the presence of trilinear ones [?]. In addition, after the symmetry breaking through the bilinear terms, neutrinos naturally acquire masses as it will be shown later. At low energy scale, these same effects are explicit through bilinear terms and the corresponding soft SUSY breaking terms.

Hence, bRPV-mSUGRA is the simplest effective model, showing the most important features of spontaneous R -parity symmetry breaking at the weak scale and moreover naturally providing neutrino masses accounting for the current oscillation data [16].

In order to include bRPV, the following terms are added to the superpotential (for details on this model see Ref. [87–89]):

$$W_{\text{bRPV}}^{\text{inv}} = \epsilon_i \tilde{L}_i \tilde{H}_u \quad \text{and} \quad W_{\text{bRPV}}^{\text{soft}} = -B_i \epsilon_i \tilde{L}_i \tilde{H}_u \quad (3.49)$$

In general, there is no basis where both sets of bilinear RPV terms ($\epsilon_i \tilde{L}_i \tilde{H}_u$ and $B_i \epsilon_i \tilde{L}_i \tilde{H}_u$) can be eliminated at the same time.

EW symmetry is broken when the two Higgs doublets and neutral component of the slepton doublets, \tilde{L}_i , acquire vevs. Then:

$$m_W^2 = \frac{1}{4} g^2 v^2; \quad v^2 = v_u^2 + v_d^2 + v_1^2 + v_2^2 + v_3^2 \sim (246 \text{ GeV})^2, \quad (3.50)$$

where v_1, v_2, v_3 are vevs for the three sneutrinos. In the following, the definition of $\tan \beta = v_u/v_d$ is preserved.

In addition to the mSUGRA parameters, bRPV introduces a new set of parameters: ϵ_i, B_i and v_i , with $i = 1, 2, 3$.

- v_i are determined by the tadpole equations, which give the minimum of the potential. Requiring the null derivative of the potential with respect to every field, results in a relation between the vevs v_i and the parameters ϵ_i and B_i .
- B_i and ϵ_i are constrained by the observed neutrino masses and mixing angles.
- universality of $B_i = B$ is usually assumed.

Finally, only three constrained free parameters are left, ϵ_i , in addition to the five mSUGRA parameters. Parameters B_i are usually traded by the alignment parameters, $\Lambda_i = \mu v_i + v_d \epsilon_i$, which are more directly related to the neutrino - neutralino properties.

It has been confirmed that current neutrino oscillation parameters [16] can be well reproduced provided $|\epsilon_i| \ll |\mu|$, where μ denotes the SUSY bilinear mass parameter [90]. A proper value of Δm_{atm}^2 can be easily obtained by an appropriate choice of $|\vec{\Lambda}|$.

The bRPV terms give rise to mixing between SM and SUSY particles. After EWSB, gauginos, higgsinos and neutralinos mix in a 7×7 mass matrix to give mass eigenstates. General Eqs. (3.35) and (3.36) in the MSSM, become:

$$\begin{aligned} L_{\tilde{\chi}^0 \text{mass}} &= -\frac{1}{2}(\varphi^0)^T \mathbf{M}_N \varphi^0 + c.c. , \\ (\varphi^0)^T &= (\tilde{B}^0, \tilde{W}^0, \tilde{H}_d^0, \tilde{H}_u^0, \nu_e, \nu_\mu, \nu_\tau), \end{aligned} \quad (3.51)$$

$$\mathbf{M}_N = \begin{pmatrix} \mathbf{M}_{\tilde{\chi}^0} & \mathbf{m}^T \\ \mathbf{m} & \mathbf{0} \end{pmatrix}, \quad (3.52)$$

where $\mathbf{M}_{\tilde{\chi}^0}$ is the same as in the MSSM, Eq. (3.36), and

$$\mathbf{m} = \begin{pmatrix} -\frac{1}{2}g'v_1 & \frac{1}{2}g v_1 & 0 & \epsilon_1 \\ -\frac{1}{2}g'v_2 & \frac{1}{2}g v_2 & 0 & \epsilon_2 \\ -\frac{1}{2}g'v_3 & \frac{1}{2}g v_3 & 0 & \epsilon_3 \end{pmatrix}. \quad (3.53)$$

By diagonalising \mathbf{M}_N , mass eigenvalues for the mass eigenstates are obtained:

$$\mathbf{N}^* \mathbf{M}_N \mathbf{N} = \text{diag}(m_{\tilde{\chi}_1^0}, m_{\tilde{\chi}_2^0}, m_{\tilde{\chi}_3^0}, m_{\tilde{\chi}_4^0}, m_{\nu_1}, m_{\nu_2}, m_{\nu_3}). \quad (3.54)$$

If RPV parameters are small, then one can find an approximate solution for the mixing matrix \mathbf{N} such that at leading order (LO):

$$m_{\nu_1} = m_{\nu_2} = 0; \quad (3.55)$$

$$m_{\nu_3} = \frac{M_1 g^2 + M_2 g'^2}{4 \det(\mathbf{M}_N)} |\vec{\Lambda}|^2, \quad (3.56)$$

and the following relations between the alignment parameters and the neutrino mixing angles arise:

$$\tan \theta_{13} = \frac{\Lambda_e}{\sqrt{(\Lambda_\mu^2 + \Lambda_\tau^2)}}, \quad (3.57)$$

$$\tan \theta_{23} = \frac{\Lambda_\mu}{\Lambda_\tau}. \quad (3.58)$$

bRPV naturally predicts a hierarchical neutrino mass spectrum where one neutrino acquires mass by mixing with neutralinos at LO while the other two acquire mass only through radiative corrections, which have been calculated to 1-loop in this model. Tree level scale correspond to the atmospheric scale where solar neutrino oscillations do not take place. This only happens when loops are included [88].

The main phenomenological consequence of RPV is the instability of the LSP and its decay to SM particles. In the case of bRPV, the allowed decays are given by the bilinear terms in Eq. (3.44). In scenarios where the lightest neutralino is the LSP, its main decays are:

$$\begin{array}{ll}
 \cdot \text{leptonic decays :} & \cdot \text{semi - leptonic decays :} \\
 \tilde{\chi}_1^0 \rightarrow \nu \ell^+ \ell^-; & \text{with } \ell = e, \mu \quad \tilde{\chi}_1^0 \rightarrow \nu q \bar{q} \\
 \tilde{\chi}_1^0 \rightarrow \nu \tau^+ \tau^- & \tilde{\chi}_1^0 \rightarrow \tau q' \bar{q} \\
 \tilde{\chi}_1^0 \rightarrow \nu \ell \tau & \tilde{\chi}_1^0 \rightarrow \ell q' \bar{q} \\
 \cdot \text{invisible decays :} & \tilde{\chi}_1^0 \rightarrow \nu b \bar{b} \\
 \tilde{\chi}_1^0 \rightarrow \nu \nu \nu &
 \end{array} \tag{3.59}$$

It should be mentioned that many intermediate states contribute to the above decays, like gauge bosons or scalars. Depending on the spectrum, some of these final states can be dominated by 2-body decays. For instance, the decay $\tilde{\chi}_1^0 \rightarrow lq'\bar{q}$ can be dominated by the 2-body decay $\tilde{\chi}_1^0 \rightarrow lW$ followed by $W \rightarrow q'\bar{q}$. In other RPV scenarios, similar decay modes are allowed as for example in the case $\lambda' \neq 0$, where the decay $\tilde{\chi}_1^0 \rightarrow lq'\bar{q}$ is also significant. This fact can be used to interpret various scenarios in an analysis based on the search for final states involving one lepton and two jets, requiring an invariant mass of the pair of jets to be close to the W mass in the case of bRPV and with no constraints on this variable for the trilinear RPV case.

In terms of branching ratios (BR), the relation Eq. (3.58) can be written as:

$$\tan \theta_{23} = \frac{\Lambda_\mu}{\Lambda_\tau} \sim \frac{BR(\tilde{\chi}_1^0 \rightarrow W\mu)}{BR(\tilde{\chi}_1^0 \rightarrow W\tau)} \sim \frac{BR(\tilde{\chi}_1^0 \rightarrow qq\mu)}{BR(\tilde{\chi}_1^0 \rightarrow qq\tau)} \tag{3.60}$$

The smallness of the neutrino masses ensure very small parameters ϵ_i , so that all the predictions of superparticle productions and decays down to the LSP remain essentially the same as in mSUGRA with the only difference being that the LSP is predicted to decay with its lifetime and BRs determined in terms of the abovementioned bRPV parameters and the gaugino mass parameters. It has been shown that, despite the smallness of bRPV indicated by the neutrino data, its effects can be tested and the model falsified at the LHC.

Although bRPV parameters are very much constrained by neutrino experiment data and cosmology observations (solar angle relatively well determined; atmospheric angle and mass squared splittings relatively large uncertainties [16]) there is still some range allowed. For a given mSUGRA parameter space point, there is a variation range in the bRPV parameters ϵ_i and Λ_i . This variation does not have a noticeable effect in the production cross section of supersymmetric states, but it affects the LSP decay length by not more than $\simeq 30\%$ for a fixed value of $m_{1/2}$ over the allowed range of the bRPV parameters (except at small m_0 where light scalars play an important part in the LSP decay) [88]. Within a large range of bRPV-mSUGRA parameters, the LSP can live enough to give rise to displaced vertices (DVs), giving thus an extra possible variable for the searches. The decay length of the neutralino LSP in its rest frame is about 180 mm for $m_{\tilde{\chi}_1^0} \sim 80$ GeV and goes down inversely as its mass thereafter. Figure 3.13 [?] shows the $\tilde{\chi}_1^0$ LSP decay length distribution for a range of m_0 and $m_{1/2}$ values.

Eq. (3.60) is experimentally interesting for several reasons. Both $\tilde{\chi}_1^0 \rightarrow \mu W$ and $\tilde{\chi}_1^0 \rightarrow \tau W$ are observable channels whose measurement could shed some light into neutrino physics. Furthermore, since no neutrino is present in any of these decay modes, they are useful instruments to

try and reconstruct the neutralino mass. Among them two, $\tilde{\chi}_1^0 \rightarrow \mu W$ turns out to be simpler from an experimental point of view since reconstruction of taus is more complicated than that of muons. The Branching Ratio for this decay mode is quite considerable, falling in the range (10% – 40%) depending on the parameter space point. In Figure 3.14 [?] the distribution of this BR is shown for a range of $m_0, m_{1/2}$.

For these reasons, the aim of this thesis will be the analysis of the $\tilde{\chi}_1^0 \rightarrow \mu W$ decay mode with two main goals:

1. Discovery / exclusion of the bRPV model in a certain range of the parameter space, accessible by ATLAS at the LHC.
2. Reconstruction of the $\tilde{\chi}_1^0$ LSP mass.

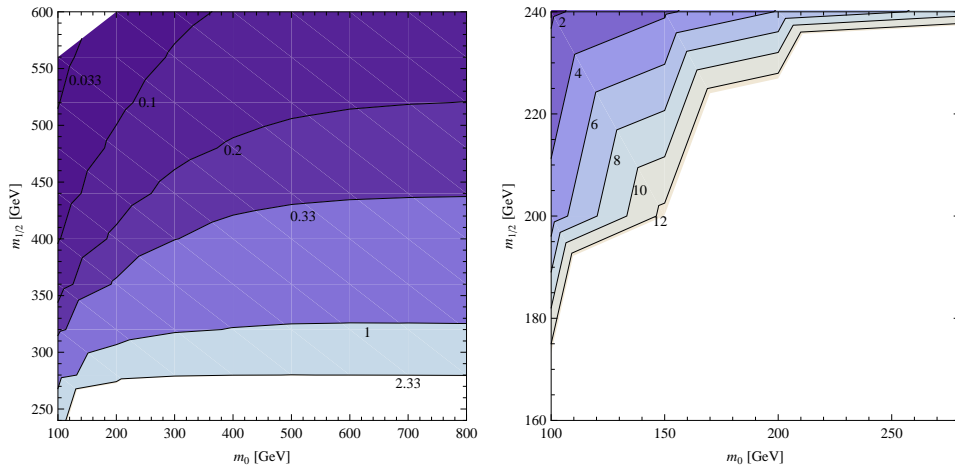


Figure 3.13: Distribution of the $\tilde{\chi}_1^0$ LSP decay length in the $\tilde{\chi}_1^0$ rest frame for bRPV-mSUGRA as a function of m_0 and $m_{1/2}$ for $A_0 = 0$; $\tan\beta = 10$; $\text{sgn}(\mu) = +$. Contour lines in units of mm.

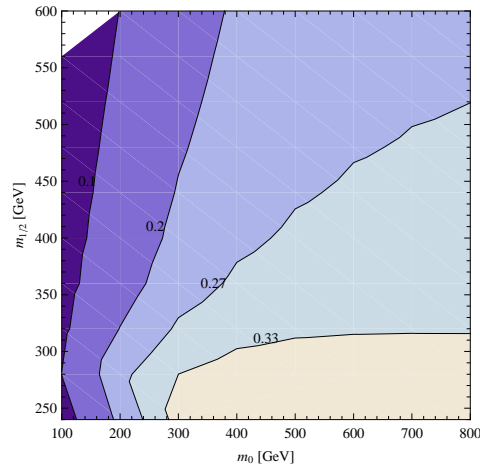


Figure 3.14: Distribution of the branching ratio $BR(\tilde{\chi}_1^0 \rightarrow \mu^\pm W^\mp)$ as a function of m_0 and $m_{1/2}$ for $A_0 = 0$; $\tan\beta = 10$; $\text{sgn}(\mu) = +$.

Chapter 4

Monte Carlo analysis

4.1 Introduction

Supersymmetry (SUSY) (see Chapter 3) is a theoretically favoured candidate for physics beyond the Standard Model. If strongly interacting supersymmetric particles are present at the TeV scale, then such particles should be copiously produced in the pp collisions at the Large Hadron Collider (see Chapter 2).

In this chapter a Monte Carlo (MC) analysis is performed to search for SUSY with bilinear R -parity violation. The aim of the analysis is to test the feasibility of discovering / excluding this model and that of reconstructing the neutralino LSP mass, looking for its decay $\tilde{\chi}_1^0 \rightarrow \mu W$. An example of an event in the bRPV model under study, including a $\tilde{\chi}_1^0$ decay of the type of interest, is shown in Figure 4.1. Since one of the objectives of this work is to reconstruct the $\tilde{\chi}_1^0$ mass, the focus will be on the hadronic decay of the W rather than on the leptonic decay. The latter would only allow an (indirect) mass reconstruction if the observed E_T^{miss} could be attributed to the resulting neutrino. However being the LSP, the $\tilde{\chi}_1^0$ will appear twice in every event. Taking into account that the BR of the neutralino decay channels involving neutrinos is about 95% (see Section 4.3.1), some LSP-induced E_T^{miss} is expected in most of the events. Furthermore, the hadronic channel of the W is the one with the highest branching ratio, which is around 68%. So we are looking for a signal containing two jets coming from a W and a muon. Thus, the basic requirement is for the events to contain at least one muon and at least two jets. In the following, the whole SUSY production sample will be referred to as “SUSY inclusive” and the sample with at least one neutralino-LSP decaying in the targeted decay mode as “signal decay”.

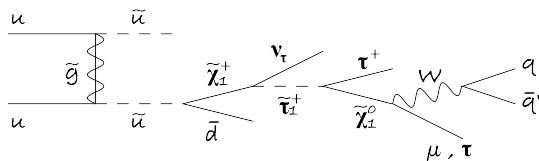


Figure 4.1: Example of a bRPV SUSY signal decay event with $\tilde{\chi}_1^0 \rightarrow \mu W(\rightarrow q\bar{q}')$.

In the context of these requirements, a study is presented for a single bRPV-mSUGRA parameter space point for three different LHC energies: the LHC nominal energy (14 TeV), an intermediate energy (10 TeV) and the energy at which the LHC started to work at the end of 2010, and during 2011 (7 TeV). The LHC working-energy plan has gone through a series of

intermediate steps during its preparation for collision data. At the time of the beginning of this work all the MC analyses were performed at the LHC nominal energy: 14 TeV. The plan, however, was for the LHC to start working at 10 TeV, with 5 TeV per beam. The LHC was switched on for the first time on 10th September 2008. Unfortunately, the 19th September 2008 incident forced the LHC beams to stop for about one year and the energy for the first collisions was planned to be diminished down to 7 TeV. On November 12th 2009 beams were back to the LHC with 450 GeV per beam. After some tests, the energy was raised up to 3.5 TeV per beam, giving the LHC a total energy of 7 TeV. In each of these steps MC samples have been fully simulated and analyses have been performed in order to have deep knowledge of what to expect when data were finally available in any of the LHC scenarios.

One of the main tasks in these analyses with MC samples is to distinguish a sample of bRPV-mSUGRA signal from the SM background containing common features in their final states, namely muons and jets. In the case of the LHC, that set is formed mainly by QCD di-jets, $\bar{t}t$ events, events containing W or Z bosons plus jets, single top events and WW , WZ and ZZ events. The QCD sample also includes $b\bar{b}$ events, which constitute a considerable source of muons.

In the following subsections these analyses are presented. The work explained in this chapter have been documented, in the 10 TeV case, in the ATLAS Internal Note ATL-PHYS-INT-2010-042 [91].

4.2 Analysis strategy

This analysis aims at the discrimination of the SM background from the interesting SUSY events (more specifically, events in which the $\tilde{\chi}_1^0$ -LSP decays in the mode $\tilde{\chi}_1^0 \rightarrow \mu^\pm W^\mp (\rightarrow qq')$) and at the reconstruction of the neutralino-LSP mass through the search for a peak in the invariant mass distribution of one muon and two jets.

Three main steps are carried out:

- Trigger and preselection:

Since the final objective is the reconstruction of the invariant mass of a muon and two jets, the high number of potential data events (mainly QCD) can be very much reduced by requiring every event to contain at least one muon and two jets. This is done by the application of a relatively high- p_T muon trigger and an event preselection in which the muon that fired the trigger is required to be isolated and high- p_T jets are demanded in every event. This preselection helps selecting interesting events with very high efficiency for the signal. Trigger and preselection studies are presented in Section 4.4.

- SM background study:

In this second step the bulk of the SM background is expected to be eliminated. This is done using mainly three event global variables in order to reject the highest number of SM events while keeping most of the interesting SUSY events. This is developed in Section 4.5.

- Combinatorial background study:

The final step of the analysis consists of the attenuation of the combinatorial SUSY background, understood as the combination of jets and muons which do not come from an LSP. These combinations are reduced by applying a set of extra cuts on specific discriminating variables which will be defined in Section 4.6.

After these three steps, the invariant mass of the selected muon and pair of jets is constructed and presented in Section 4.7.

4.3 Simulated samples

In order to develop this analysis, both the bRPV-mSUGRA signal and all of the possible background sources coming from SM processes are taken into account. MC samples have been simulated for the signal and backgrounds in the three-energy configurations using the ATLAS software framework named Athena [92]. For all of the three-energy configurations, a full simulation process has been followed up, involving four main steps:

1. Generation

It refers to the production of particle four vectors from specified physics processes. There are many event generators available, each of them specifically developed for a particular physics process. In the case of the model studied in this work, the generator used is PYTHIA [93]. This generator includes the option of breaking R -parity through trilinear terms, but bilinear RPV is not implemented. To generate events within bRPV, the necessary parameters for the generation (masses, branching ratios, decay lifetimes, etc.) within the model are calculated with SPheno [94]. SPheno uses as input the mSUGRA parameters and the neutrino physics constraints, and delivers as output the bRPV parameters (together with the mass spectra and the decay modes) compatible with these constraints. Once those quantities are calculated for a given set of bRPV parameters within an mSUGRA benchmark point, they are passed to PYTHIA through a SUSY Les Houches Accord file (SLHA2) [95, 96]. The total cross section for the bRPV signal is calculated by PYTHIA at Leading Order (LO) and, for the 7 TeV sample, with Prospino [97, 98] at Next-to-Leading Order (NLO).

2. Simulation

It is the process whereby generated events are passed through a GEANT4 [99] simulation of the ATLAS detector to produce GEANT4 Hits, i.e. a record of where each particle traversed the detector and how much energy was deposited.

3. Digitisation

In this step, the GEANT4 Hits from the simulation are subjected to the response of the detector to produce Digits as produced in the Raw Data from the real detector.

4. Reconstruction

In this last part of the process, the raw data Digits, such as times and voltages, are reconstructed into tracks and energy deposits. After this step, the shape of the MC data is exactly the same as that of the real data got from the detector.

4.3.1 Signal samples

Although the channel of interest is $\tilde{\chi}_1^0 \rightarrow \mu^\pm W^\mp$, all possible $\tilde{\chi}_1^0$ decay modes were enabled during the bRPV-SUSY event generation, since they contribute to the combinatorial background. All possible SUSY production processes in a proton-proton collider were generated, dominated by $\tilde{q}\tilde{g}$ and $\tilde{q}\tilde{q}$ production. For an example on the full list of possible SUSY subprocesses generated for the 7 TeV sample, see in Appendix A, Section A.1. It is worth noting that the bRPV couplings only affect the SUSY phenomenology in allowing the LSP to decay. Other than that, the cascade decay from heavier to lighter sparticles proceeds mainly as in the RPC case. Any observed difference in the branching fraction of the other decays is of the same order as the discrepancy between the predictions by various spectrum calculators.

It is necessary to mention that the comparison of the three-energy configurations is not straight-forward since the bRPV-mSUGRA points studied in each of them are slightly different. The reason for this is based in the continuous improvement of the generation and simulation tools, which result in a better bRPV parameter determination and in a better description of the ATLAS detector effects on the generated particles, and in the ATLAS SUSY Working Group needs and preferences during the time of the development of this thesis.

Despite this fact, the three points share the most important features such as similar branching ratios for the decay channels of interest and the distributions of missing transverse energy (E_T^{miss}), effective mass (M_{eff}), number and p_T of objects, etc. As an example, distribution of E_T^{miss} and number of muons and jets are shown in Figures 4.2 for the three simulated points.

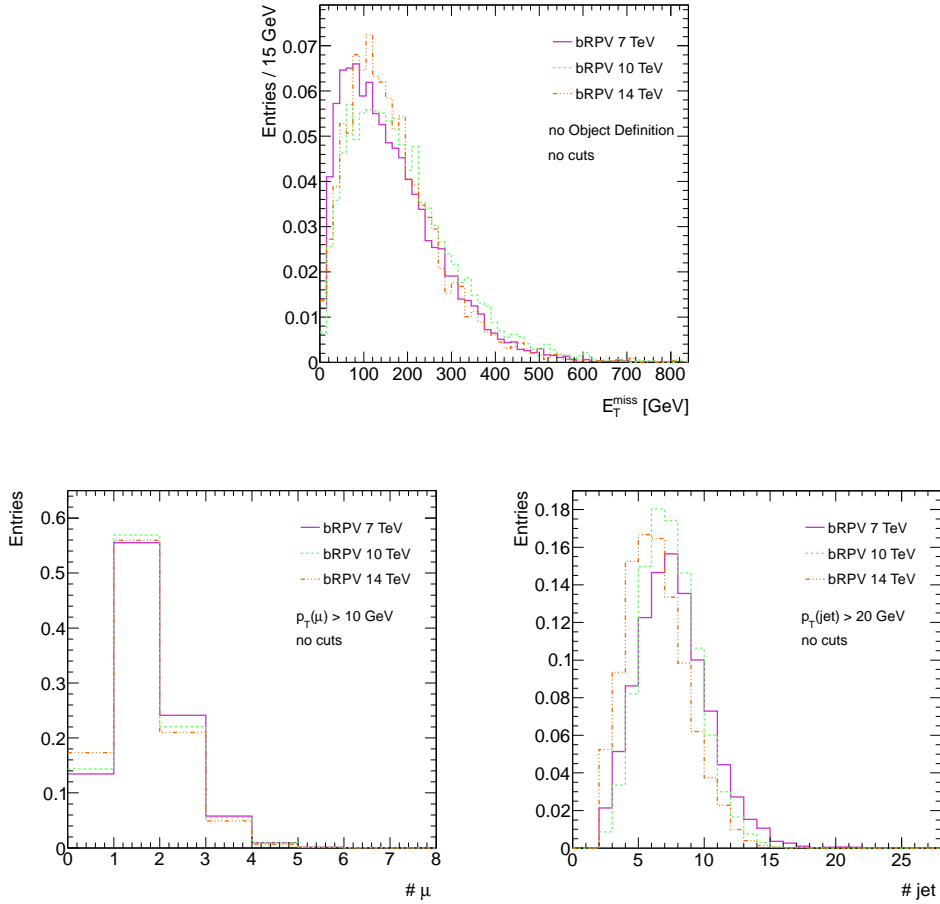


Figure 4.2: Comparison of the E_T^{miss} (top), number of muons with $p_T > 10 \text{ GeV}$ per event (bottom left) and number of jets with $p_T > 20 \text{ GeV}$ per event (bottom right) distributions for the SUSY inclusive signal in the three-energy scenarios studied, normalised to unit area. The purple continuous line corresponds to the 7 TeV sample, the green dashed line to the 10 TeV sample and the orange discontinuous line to the 14 TeV sample.

The mSUGRA model is defined by five parameters: the common boson mass at the Grand Unification (GUT) scale m_0 , the common fermion mass at the GUT scale $m_{1/2}$, the ratio of the Higgs vacuum expectation values $\tan\beta$, the common GUT scale trilinear coupling A_0 and the sign of the Higgs potential parameter μ . Neutrino physics experimental constraints are taken into account for the bRPV parameters (the three sneutrinos vevs, v_1, v_2, v_3 and the three bilinear coupling parameters, $\epsilon_1, \epsilon_2, \epsilon_3$) to be determined. It has been shown that requiring a fit of the bilinear RPV parameters to neutrino oscillation data leads to a set of bRPV parameters consistent with all experimental constraints from rare processes. More specifically, it has been demonstrated that imposing the constraints from neutrino oscillation data, both experimental bounds due to neutrinoless double beta decay and charged lepton flavour violating decays, are generically fulfilled (see Ref. [100] and [101]).

For the 7 TeV study, a point close to the ATLAS benchmark point SU3 in mSUGRA is selected. In the 10 TeV case, the study is performed over the SU3 ATLAS benchmark point in mSUGRA and the 14 TeV sample corresponds to the SPS1a ATLAS benchmark point in mSUGRA. The generation and simulation details for these points can be found in Table A.2. The mSUGRA parameters values in the selected points and the neutralino-LSP ($\tilde{\chi}_1^0$) characteristics are listed in Table 4.1 for the three-energy scenarios. The full list of parameters, including neutrino physics experimental constraints and bRPV parameters can be found in Table A.3.

The cross section for each of the generation processes in each of the three energies has been calculated by PYTHIA at LO (and by Prospino at NLO for the 7 TeV sample. In this case, the total cross section has then been calculated taking into account the different NLO corrections for each of the generation subprocesses). As an example, details on the subprocesses cross sections for the 7 TeV sample are given in Table A.1 in Appendix A.

Table 4.1: Parameters for the mSUGRA point and $\tilde{\chi}_1^0$ LSP characteristics for the signal sample in the three-energy scenarios.

mSUGRA point	LSP mass	LSP lifetime	cross section
7 TeV sample			
$m_0 = 100$ GeV	$m_{\tilde{\chi}_1^0} = 109.8$ GeV	$c\tau(\tilde{\chi}_1^0) = 677$ μm	3.3 pb
$m_{1/2} = 280$ GeV			
$\tan\beta = 10$			
$A_0 = 0$ GeV			
$\text{sgn}\mu = +1$			
10 TeV sample			
$m_0 = 100$ GeV	$m_{\tilde{\chi}_1^0} = 118.0$ GeV	$c\tau(\tilde{\chi}_1^0) = 290$ μm	4.8 pb
$m_{1/2} = 300$ GeV			
$\tan\beta = 6$			
$A_0 = -300$ GeV			
$\text{sgn}\mu = +1$			
14 TeV sample			
$m_0 = 100$ GeV	$m_{\tilde{\chi}_1^0} = 97.1$ GeV	$c\tau(\tilde{\chi}_1^0) = 1.6$ mm	41 pb
$m_{1/2} = 250$ GeV			
$\tan\beta = 10$			
$A_0 = -100$ GeV			
$\text{sgn}\mu = +1$			

As mentioned previously, one important fact about RPV is that it does not contain as much E_T^{miss} as the RPC case, due to the LSP decay. Nevertheless, in the particular scenario studied here, some amount of E_T^{miss} is still expected due to the presence of neutrinos throughout the decay chain and (mainly) in most of the neutralino-LSP decay channels. The $\tilde{\chi}_1^0$ main decay modes are shown below for the 7 TeV sample, for the 10 TeV sample (in parentheses) and for the 14 TeV sample [in square brackets]:

$$\begin{array}{llll}
BR(\tilde{\chi}_1^0 \rightarrow e^\pm W^\mp) = 0.01\% & (0.05\%) & [0.05\%] & BR(\tilde{\chi}_1^0 \rightarrow \nu b\bar{b}) = 6.4\% & (9.2\%) & [14.0\%] \\
BR(\tilde{\chi}_1^0 \rightarrow \mu^\pm W^\mp) = 10.1\% & (10.3\%) & [8.1\%] & BR(\tilde{\chi}_1^0 \rightarrow \nu\tau\tau) = 34.1\% & (30.0\%) & [34.0\%] \\
BR(\tilde{\chi}_1^0 \rightarrow \tau^\pm W^\mp) = 8.9\% & (11.0\%) & [8.9\%] & BR(\tilde{\chi}_1^0 \rightarrow \nu\tau\mu) = 19.9\% & (14.8\%) & [16.6\%] \\
BR(\tilde{\chi}_1^0 \rightarrow \nu Z) = 6.1\% & (8.3\%) & [1.8\%] & BR(\tilde{\chi}_1^0 \rightarrow \nu\tau e) = 14.5\% & (14.8\%) & [16.7\%]
\end{array}$$

Including neutrino oscillation data ($\theta_{13} \sim 0^\circ$, $\theta_{23} \sim 45^\circ$) [15, 16] in Eqs. (3.57, 3.58) and taking into account that the Branching Ratio $BR(\tilde{\chi}_1^0 \rightarrow W^\pm \ell_i^\mp)$ is proportional to the squared alignment parameters $|\Lambda_i|^2$, it turns out that $BR(\tilde{\chi}_1^0 \rightarrow W^\pm \mu^\mp) \sim BR(\tilde{\chi}_1^0 \rightarrow W^\pm \tau^\mp) \gg BR(\tilde{\chi}_1^0 \rightarrow W^\pm e^\mp)$, as seen above.

In Table 4.2 the percentage of events in which there exist zero, one or two neutrinos (muons) coming from a neutralino decay is listed for the three-energy samples. It is noticeable that, in the three samples, about 95% of the events will contain some E_T^{miss} due to a neutralino-LSP decay involving neutrinos, thus making the E_T^{miss} distribution more similar to that of the RPC case. In Figure 4.3 the distributions of E_T^{miss} for events containing zero, one or two neutralinos decaying through a neutrino-containing decay channel are shown. It can be appreciated that for events in which both neutralino decays do not contain neutrinos (orange discontinuous line), the amount of E_T^{miss} is clearly lower than in the rest of cases, showing that an important part of this quantity comes effectively from neutralinos decaying to neutrinos, in accordance with data in Table 4.2.

Table 4.2: Percentage of events containing 0, 1 or 2 muons or neutrinos coming from the two-neutralinos decays for the signal samples in the three-energy scenarios.

object	# objects/ev coming from $\tilde{\chi}_1^0$ decays		
	0	1	2
7 TeV sample			
μ	49.0%	42.0%	9.0%
ν	3.6%	30.8%	65.6%
10 TeV sample			
μ	53.8%	36.8%	6.3%
ν	4.5%	32.8%	59.4%
14 TeV sample			
μ	56.7%	37.2%	6.1%
ν	2.9%	28.2%	68.9%

Another important point for the development of the analysis is the presence of muons coming from neutralino decays. Its percentages are also shown in Table 4.2, showing that about 50% – 40% of the events (depending on the point) will contain at least one muon coming from a neutralino decay. By inspecting the truth (at generation level) information of the SUSY sample and comparing it with the reconstructed objects (after all simulation steps defined previously

in this section), it was found that the muons originating from the lightest neutralino are reconstructed with an efficiency of 94%. This fact leads to the performance of an inclusive analysis, requiring each event to contain at least one muon, in contrast with an exclusive analysis requiring an exact number of muons, as it will be the case in the Chapter 5.

In this area of the parameter space, the decay length of the LSP ranges from 0.1 up to 100 mm [88, 102], so there are some points where the LSP decay takes place inside the inner detector and a study on displaced vertices may be performed at a later stage.

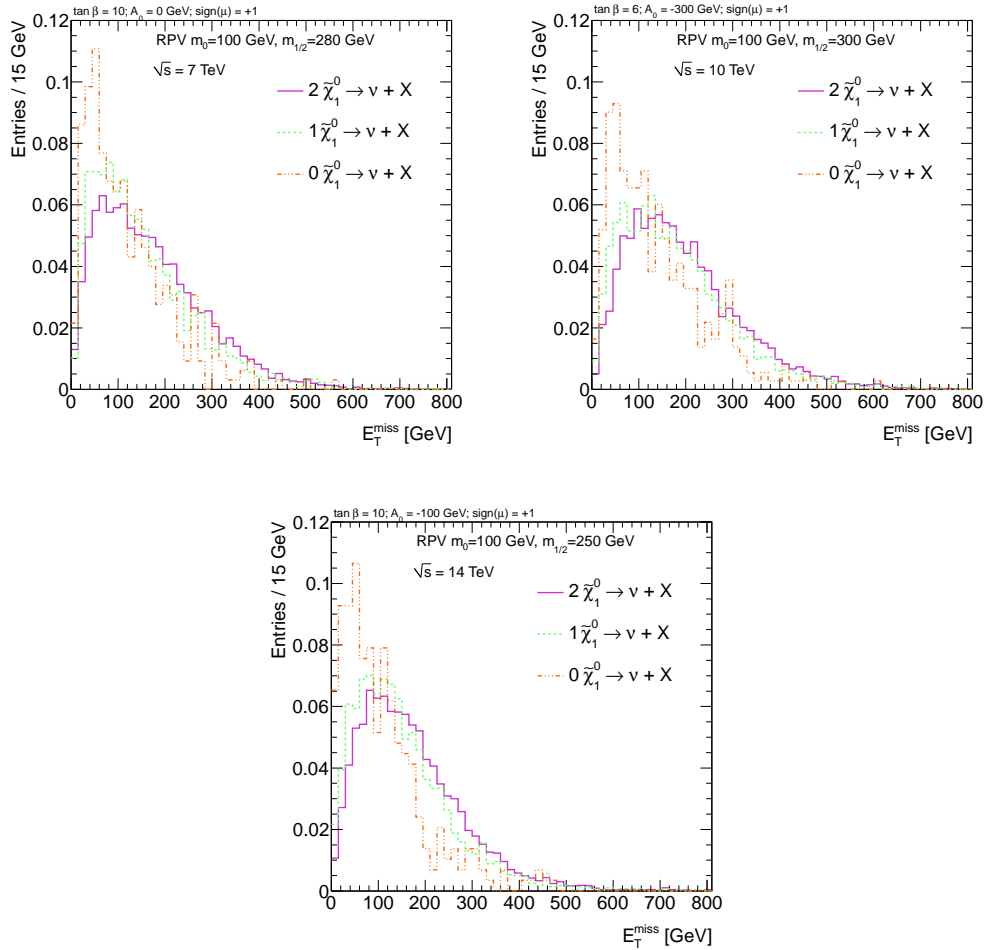


Figure 4.3: E_T^{miss} distributions for the SUSY inclusive signal at 7 TeV (top left), 10 TeV (top right) and 14 TeV (bottom) before any object definitions or cuts applied, for events containing zero, one or two $\tilde{\chi}_1^0$ with neutrinos in their decays, normalised to unit area. The purple continuous line corresponds to events where both neutralino-LSP decays involve neutrinos, the green dashed line to events where one neutralino-LSP decay involve neutrinos and the orange discontinuous line to events where none of the neutralino-LSP decay involve neutrinos.

4.3.2 SM samples

The complete list of SM background sets used in each of the three analyses, is shown in Table 4.3, along with the total cross sections and number of generated events. The samples were produced in release 12 of the ATLAS software for the 14 TeV sample, release 14 for the 10 TeV sample and release 16 for the 7 TeV sample. The MC@NLO [?] generator was used for $t\bar{t}$, single top and di-bosons samples; W +jets, Z +jets were generated with Alpgen [?] and the QCD di-jets samples used PYTHIA [93]. This lastest sample is divided into eight different sub-samples according to the p_T of the generated di-jets, also shown in the table.

Table 4.3: Data sets, cross sections and number of generated events for signal and background samples at $E_{\text{cm}} = 14, 10$ and 7 TeV. Single top sample includes the s -, t - and Wt -channel; $t\bar{t}$ includes semi- and di-leptonic channels; W + jets includes $W(\rightarrow \mu\nu)$ and $W(\rightarrow \tau\nu)$ with (0–5) jets; Z + jets includes $Z(\rightarrow \mu\mu)$ and $Z(\rightarrow \tau\tau)$ with (0–5) jets.

Process	$E_{\text{cm}} = 14$ TeV		$E_{\text{cm}} = 10$ TeV		$E_{\text{cm}} = 7$ TeV	
	σ [pb]	# events	σ [pb]	# events	σ [pb]	# events
SUSY inclusive	41	10 k	4.79	10 k	3.3	10 k
$t\bar{t}$	461	115 k	373.6	500 k	145.0	760 k
single top	–	–	45.7	50 k	37.31	1.4 M
W + (0,1) jets	–	–	–	–	2.4×10^4	10.0 M
W + (2–5) jets	–	–	1727.4	360 k	1539	11.1 M
Z + (0,1) jets	–	–	–	–	2370	15.4 M
Z + (2–5) jets	–	–	176.6	340 k	163.9	1.6 M
WW	–	–	42	1 k	29	2.5 M
WZ	–	–	16	1 k	11	230 k
ZZ	–	–	6.5	1 k	4.6	230 k
QCD dijets						
J0 ($p_T < 17$ GeV)	$1.76 \cdot 10^{10}$	–	1.1×10^{10}	100 k	$9.8 \cdot 10^9$	14 M
J1 ($p_T \in [17, 35]$ GeV)	$1.38 \cdot 10^9$	–	$8 \cdot 10^8$	800 k	$6.8 \cdot 10^8$	7.5 M
J2 ($p_T \in [35, 70]$ GeV)	$9.33 \cdot 10^7$	–	$5.6 \cdot 10^7$	560 k	$4.0 \cdot 10^7$	2.8 M
J3 ($p_T \in [70, 140]$ GeV)	$5.88 \cdot 10^6$	350 k	$3 \cdot 10^6$	300 k	$2.2 \cdot 10^6$	2.8 M
J4 ($p_T \in [140, 280]$ GeV)	$3.08 \cdot 10^5$	400 k	$1.5 \cdot 10^5$	150 k	$8.8 \cdot 10^4$	2.8 M
J5 ($p_T \in [280, 560]$ GeV)	$1.25 \cdot 10^4$	200 k	$5 \cdot 10^3$	70 k	$2.3 \cdot 10^3$	2.8 M
J6 ($p_T \in [560, 1120]$ GeV)	360	90k	112	215 k	33.9	2.8 M
J7 ($p_T \in [1.12, 2.24]$ TeV)	5.71	22k	1.1	1 k	0.14	1.4 M

4.4 Trigger and preselection

As mentioned before, the main objective of the analysis is to distinguish a sample of bRPV-mSUGRA signal from a set of SM backgrounds containing common features in their final states. Given the final state being searched for, the first step in this analysis is to select events involving at least one muon. All the events are required to fire the lowest unprescaled single muon trigger. Within the plans for 14 TeV and 10 TeV this trigger was `EF_mu10`, that requires the event to contain at least one muon with transverse momentum $p_T > 10$ GeV passing the Event Filter trigger (for a definition of the different trigger levels see Section 2.3.5). After the luminosity was increased in the 2011 data taking, the lowest unprescaled muon trigger became `EF_mu18`, requiring the event to contain at least one muon with transverse momentum $p_T > 18$ GeV passing the Event Filter trigger, which is the one used for the 7 TeV analysis.

4.4.1 Analysis at 7 TeV

As shown in Section 4.3.1, about 50% of the SUSY inclusive events contain at least one muon coming from a neutralino decay. Furthermore, other muons can be present during the event decay chain in SUSY. Hence, the application of a muon trigger should have a good efficiency for SUSY events while it is expected to be much lower for certain SM backgrounds. The most important case is QCD, the dominant background in the LHC, with huge cross sections but very few muons per event, especially for low values of jet p_T (see Table 4.3). In Figure 4.4 the number of muons with $p_T > 10$ GeV is shown for the SUSY inclusive signal and for all the SM backgrounds before applying any trigger or cut. It is clear that most QCD events do not contain any such muon. It is also visible how the distribution for SUSY is smoother than the others, with a soft peak in one instead of zero.

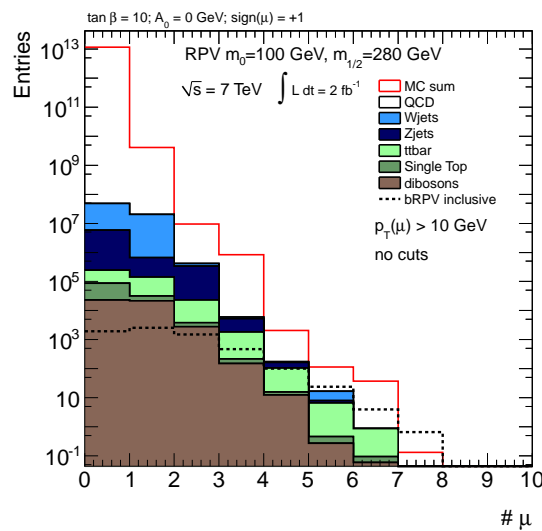


Figure 4.4: Number of muons with $p_T > 10$ GeV per event for the SUSY inclusive signal and for all SM backgrounds at 7 TeV before any trigger or preselection, normalised to 2 fb^{-1} . Notice that *MC sum* refers to the normalised sum of all SM background sources.

The trigger $EF_{\mu 18}$ efficiencies for the SUSY events and the background sources are listed in Table 4.4. Although the selection of the trigger is chosen as the lowest unpre-scaled single muon trigger available, efficiencies for the trigger $EF_{\mu 10}$ and $EF_{\mu 20}$ are also presented to allow for a comparison with the 10 TeV and 14 TeV analyses. The inclusive SUSY events are selected with high efficiency of 60 – 70%, whilst an efficiency of 95 – 85% is given for the signal decay subsample.

In a second stage and after passing the $EF_{\mu 18}$ trigger, a set of preselection requirements is applied to the event: it is demanded to contain at least two jets with $p_T > 20$ GeV (2j20 cut) and the muon firing the trigger to be isolated ($\mu 18i$ cut). The muon is considered to be isolated when the total transverse energy in a cone with a radius $\Delta R = 0.2$ ¹⁾ around the muon is below a certain threshold, X ($E[\Delta R_{\mu} < 0.2] < X \text{ GeV}$). The selected threshold for this requirement

¹⁾ R is a Lorentz invariant variable under longitudinal boosts, defined in terms of the pseudorapidity (η) and the polar angle (ϕ) such that $\Delta R = \sqrt{\Delta\eta^2 + \Delta\phi^2}$

is the one recommended by the ATLAS Muon Combined Performance working group [103]: $E[\Delta R_\mu < 0.2] < 40$ GeV, a soft requirement which will be denoted as “i_loose”. In Table 4.4, the efficiencies of the preselection cut `mu18i_loose_2j20` are also listed for the SUSY events and for each of the backgrounds considered. The ratio between the SUSY inclusive signal and all of the SM backgrounds after passing the `EF_mu18` trigger is improved mainly due to the requirement of an isolated muon although many low- p_T QCD events are rejected after the `2j20` cut. In the analysis at 7 TeV that follows, a first selection of events by the trigger plus cuts `mu18i_loose_2j20` is always assumed, i.e. at least one isolated muon with $p_T > 18$ GeV and at least two jets with $p_T > 20$ GeV in each event.

Table 4.4: SUSY and SM background efficiencies at 7 TeV before event selection for three trigger signatures and for one preselection cut.

Process	Efficiencies (%)			
	EF_mu10	EF_mu18	EF_mu20	mu18i_loose_2j20
SUSY inclusive	70.6	62.6	60.4	59.6
Signal decay	94.8	88.9	86.7	91.3
$t\bar{t}$	45.7	37.4	35.5	36.7
single top	14.8	10.1	9.3	9.5
W + jets	31.4	27.8	26.2	4.3
Z + jets	13.0	9.7	9.1	3.0
WW + WZ + ZZ	51.6	44.2	42.3	32.0
QCD dijets	0.036	6.8×10^{-3}	5.6×10^{-3}	2.2×10^{-3}
Total background	0.036	6.8×10^{-3}	5.6×10^{-3}	2.2×10^{-3}

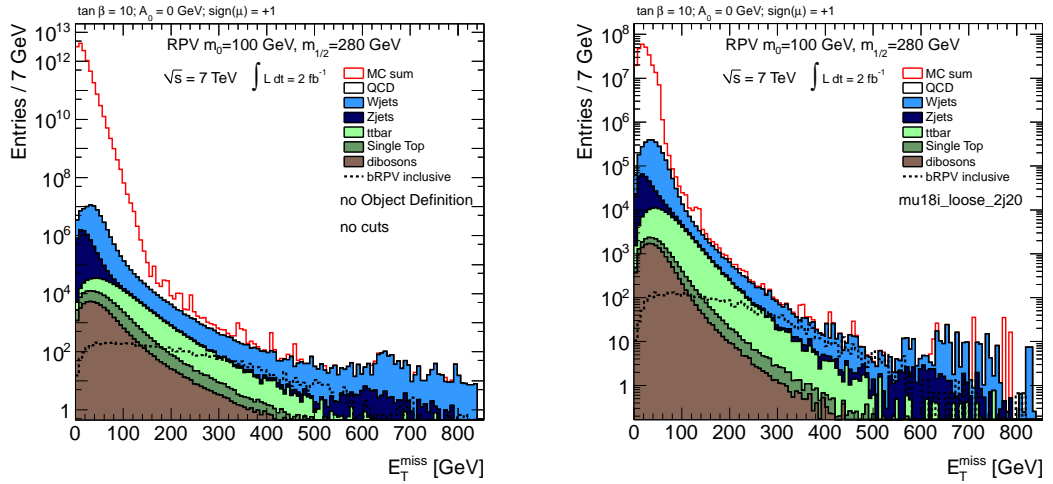


Figure 4.5: E_T^{miss} distributions for the SUSY inclusive signal and for all SM backgrounds at 7 TeV before any trigger or preselection (left) and after preselection `mu18i_loose_2j20` (right), normalised to 2 fb^{-1} . *MC sum* refers to the normalised sum of all SM background sources.

In Figure 4.5, E_T^{miss} distributions for SUSY inclusive signal and for all SM backgrounds are shown before any trigger or preselection (left) and after the mu18i_loose_2j20 preselection (right). Whilst the bRPV-SUSY inclusive signal remains practically undistorted, the total SM background distribution is very much reduced at low values of E_T^{miss} , mainly due to the QCD reduction but also to a lesser extent to a reduction in all the SM contributions.

4.4.2 Analysis at 10 TeV

The lowest unrescaled trigger EF_mu10 efficiencies for the SUSY events and for the background sources are listed in Table 4.5. For comparison with the 7 TeV analysis where EF_mu18 is applied, efficiencies for EF_mu20 are also presented, since the selection EF_mu18 was not available in the 10 TeV trigger menu. Same as in the 7 TeV case, the SUSY events are selected with high efficiency of 60 – 70%, whilst an efficiency of 97 – 90% is given for the signal decay.

As preselection cuts the event is demanded to contain at least two jets with $p_T > 20$ GeV (2j20 cut) and the muon firing the trigger to be isolated (mu10i cut).

Since no recommendation on the isolation requirement was set at this energy, several thresholds were tested being 20 GeV and 40 GeV the ones giving the best (inclusive) signal to background ratio, not removing a significative amount of signal decay events. In Table 4.5, the efficiencies of two preselection cuts are also listed for the SUSY events and for each of the backgrounds considered, with mu10i_loose corresponding to a cut on $E[\Delta R_\mu < 0.2] < 40$ GeV and mu10i_tight to $E[\Delta R_\mu < 0.2] < 20$ GeV. Choosing a looser cut on this variable would accept considerably more high- p_T QCD events, whilst a tighter cut would reject too much signal. As seen in the last column of the table, the mu10i_tight preselection already eliminates a noticeable fraction of SUSY signal decay events whereas the background is barely affected by the tighter isolation requirement. Hence, the loose muon isolation is considered for this analysis. The ratio S_{SUSY}/B after passing the trigger mu10 is improved mainly due to the requirement of an isolated muon although many low- p_T QCD events are rejected after the 2j20 cut. In the 10 TeV analysis that follows, a first selection of events by the trigger plus cuts mu10i_loose_2j20 is always assumed, i.e. at least one loosely isolated muon with $p_T > 10$ GeV and at least two jets with $p_T > 20$ GeV in each event. A similar preselection cut is assumed for the 14 TeV analysis.

Table 4.5: SUSY and SM background efficiencies at 10 TeV before event selection for two trigger signatures and for two different preselection cuts.

Process	Efficiencies (%)			
	mu10	mu20	mu10i_loose_2j20	mu10i_tight_2j20
SUSY inclusive	69.9	58.9	66.7	65.1
Signal decay	97.9	90.7	97.4	90.2
$t\bar{t}$	55.5	34.7	44.5	43.5
single top	50.0	36.9	36.2	36.0
W + jets	42.8	36.4	33.0	32.9
Z + jets	53.6	48.2	42.2	42.1
WW + WZ + ZZ	44.4	43.7	22.7	22.6
QCD dijets	0.119	0.118	0.047	0.046
Total background	0.119	0.118	0.047	0.046

4.4.3 Analysis at 14 TeV

The 14 TeV trigger menu was very similar to the 10 TeV menu. Also in this case the $\text{EF}_{\mu 10}$ was the lowest unpre-scaled trigger and also the $\text{EF}_{\mu 18}$ was absent from the trigger menu. The $\text{EF}_{\mu 10}$ efficiencies for the SUSY events and the background sources are listed in Table 4.6 together with efficiencies for $\text{EF}_{\mu 20}$ for comparison with the 7 TeV analysis. Only $W(\rightarrow \mu\nu) + (2,3)$ jets and $Z(\rightarrow \mu\mu) + (2,3)$ jets are considered and hence this type of background is underestimated. The contribution from WW, ZZ, WZ and single top is expected to be small, as in the 7 and 10 TeV. Similar efficiencies as in the 7 TeV and 10 TeV cases are observed for SUSY inclusive events (55 – 70%) and for the signal decay (80 – 95%).

Considering that the 14 TeV analysis is only meant to be a tentative study on the feasibility of distinguishing a bRPV sample from the SM one, no isolation was applied on the muon for simplification. Therefore, the preselection mu10_2j20 will be applied in the 14 TeV analysis that follows. In Figure 4.6, E_T^{miss} distributions for SUSY inclusive signal and for the SM backgrounds considered are shown before any trigger or preselection (left) and after the preselection (right).

Table 4.6: SUSY and SM background efficiencies at 14 TeV before event selection for two trigger signatures.

Process	Efficiencies (%)	
	mu10	mu20
SUSY inclusive	67.5	54.7
Signal decay	92.3	79.3
$t\bar{t}$	55.8	37.3
W +jets + Z +jets	49.6	41.5
QCD dijets	0.10	0.09
Total background	0.10	0.09

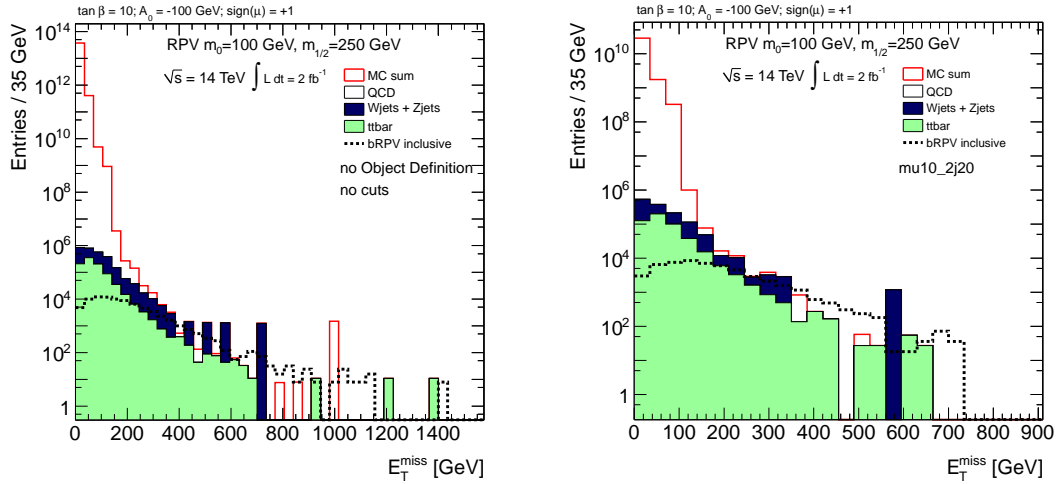


Figure 4.6: E_T^{miss} distributions for the SUSY inclusive signal and for all SM backgrounds at 14 TeV before any trigger or preselection (left) and after preselection mu10_2j20 (right), normalised to 2 fb^{-1} . *MC sum* refers to the normalised sum of the indicated SM background sources.

4.5 SM background suppression

In order to discriminate the SUSY inclusive signal from the SM background, the following variables are considered, also employed in RPC SUSY analyses:

Missing Transverse Energy (E_T^{miss}): It is the vectorial sum of leptons \mathbf{p}_T , jets \mathbf{p}_T and other calorimeter activity.

Among the background processes, $t\bar{t}$ and $W + \text{jets}$ have a relatively high E_T^{miss} due to the neutrino(s) occurring in the leptonic decay of the W . The SUSY inclusive signal is also characterised by high E_T^{miss} , although lower than that of the SU3 RPC sample (which peaks at around 250 GeV; a comparison of RPC vs. bRPV E_T^{miss} distributions can be found in Appendix D for several mSUGRA points). This is due to the presence of at least one neutrino from the LSP decay in $\sim 95\%$ of the events. Since the decay channel we are considering does not involve a neutrino only a conservative cut on E_T^{miss} will be applied to reduce the SM background.

Effective Mass (M_{eff}): It is defined as the scalar sum of all electrons and muons p_T in the event and the four highest- p_T jets (H_T) and the E_T^{miss} :

$$H_T = \sum_{1..4} p_T^{\text{jet}} + \sum p_T^{\text{electrons}} + \sum p_T^{\text{muons}}, \quad (4.1)$$

$$M_{\text{eff}} = E_T^{\text{miss}} + H_T. \quad (4.2)$$

This definition for M_{eff} provides a satisfactory discrimination between signal and background for the three-energy scenarios. As an example, the left panel of Figure 4.7 shows this variable distribution for all the SM backgrounds and the inclusive SUSY sample at 7 TeV, before any cut or trigger applied.

Transverse Sphericity (S_T): The transverse sphericity tensor is defined as:

$$S_T^{\alpha\beta} = \frac{\sum_i p_i^\alpha p_i^\beta}{\sum_i \|\mathbf{p}_i\|^2}, \quad (4.3)$$

where α and β run over the x and y axis and i runs over all the jets, electrons, muons and taus in the event.

By standard diagonalisation of $S_T^{\alpha\beta}$ one may find two eigenvalues $\lambda_1 \geq \lambda_2$, with $\lambda_1 + \lambda_2 = 1$. The transverse sphericity (S_T) of the event is then defined as

$$S_T = \frac{2\lambda_2}{\lambda_1 + \lambda_2}, \quad (4.4)$$

so that $0 \leq S_T \leq 1$. Transverse sphericity is essentially a measure of the summed transverse momenta with respect to the event axis, p_\perp^2 ; a (back-to-back) 2-jet event corresponds to $S_T \approx 0$ and a transversely isotropic event to $S_T \approx 1$.

The event shape as parameterised in the S_T is different between the SM processes and the SUSY inclusive signal. The right panel of Figure 4.7 shows the S_T distribution for all the SM backgrounds and the inclusive SUSY sample at 7 TeV, before any cut or trigger

applied. Zooming into the low S_T region, it is clear how most of the SM background processes have very low values for this variable, while the distributions for $t\bar{t}$, single top and SUSY are smoother. Requiring high event sphericity helps in the suppression of the QCD background, while it does not considerably affect the $t\bar{t}$, W + jets and Z + jets background.

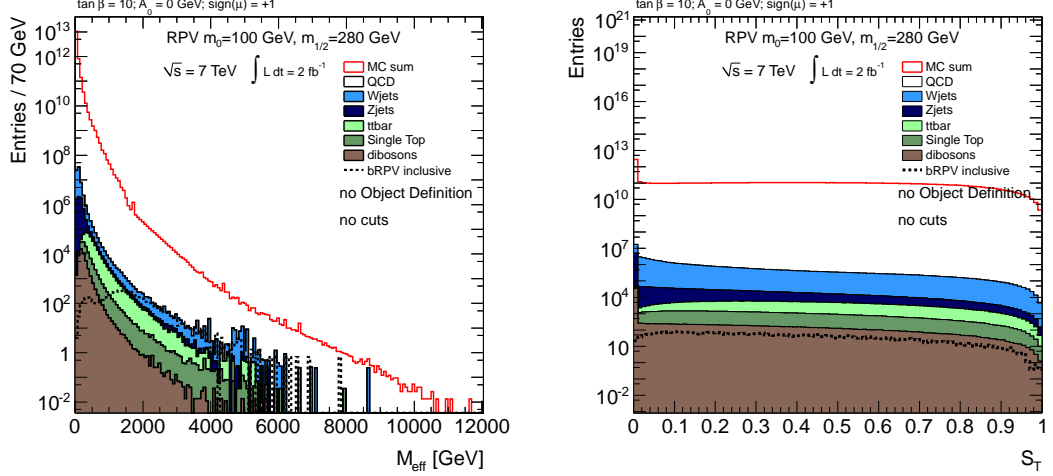


Figure 4.7: M_{eff} and S_T distribution for the SUSY inclusive signal and for all SM backgrounds at 7 TeV before any trigger or preselections, normalised to 2 fb^{-1} . *MC sum* refers to the normalised sum of all SM background sources.

In order to find the optimal S_{SUSY}/B ratio, a systematic study has been performed for each of the three energy scenarios, testing several thresholds in the variables defined above and the relations among them. A significant reduction of the SM background was required, together with a high signal efficiency and a considerable final number of SUSY signal decay events. This relatively high number of surviving SUSY signal decay events is necessary in view of the subsequent *Combinatorial cuts*, which will be defined in Section 4.6, needed to disentangle the SUSY signal decay from the combinatorial SUSY background. A small number of surviving SUSY signal decay events would lead to a low statistics invariant mass plot in which a fit to the neutralino mass would not be feasible.

Slightly different sets of cuts were found optimal for each of those scenarios, although they gave rise to similar optimised S_{SUSY}/B ratios fulfilling the mentioned conditions. Due to this similarity in the results and for a better comparison between different energy configurations, it was decided to apply the same set of cuts to the three cases. This set of cuts, from now on referred to as *SM cuts*, will be defined and justified in the next subsection.

4.5.1 Analysis at 7 TeV

The reconstruction algorithms considered to define objects are AntiKt4TopoNew_EM (defined in Section 2.3.6.5) for jets and Staco (defined in Section 2.3.6.3) for muons. Only jets and leptons (electrons and muons) with $p_T > 20 \text{ GeV}$ are considered for the rest of the analysis. The variable $E_{T,\text{RefFinal}}^{\text{miss}}$ as defined in Section 2.3.6.7 is used for the missing transverse energy throughout the

analysis. The transverse momentum of all leptons and jets with $p_T > 20$ GeV reconstructed in each event are taken into account in the calculation of the S_T .

In Figures 4.8 correlation plots are shown for M_{eff} , E_T^{miss} and S_T for the SUSY inclusive signal and for the normalised sum of all SM backgrounds, after the preselection `mu18i_loose_2j20` is applied. As no significant correlation appears among none of these variables, the cuts on each of them are applied independently.

A systematic study applying various thresholds on these variables has been performed. When combining and optimising them, the following set of cuts is selected:

$$\begin{aligned} M_{\text{eff}} &> 1.2 \text{ TeV}, \\ E_T^{\text{miss}} &> 40 \text{ GeV}, \\ S_T &> 0.2. \end{aligned} \tag{4.5}$$

This selection gives a good S_{SUSY}/B ratio. Eliminating a considerable part of the SM background, it still leaves behind a significant amount of signal so that the requirements to reduce the combinatorial background, to be set in the next section, can provide a meaningful invariant mass distribution.

The efficiencies and cut flow for this combination of cuts (“*SM cuts*”) are shown in Table 4.7. As in previous sections, *SUSY signal decay* events refer to those with at least one $\tilde{\chi}_1^0$ decaying to a muon and a hadronically decaying W . The *SUSY background* subsample consists of all the other events in the SUSY sample in which none of the $\tilde{\chi}_1^0$ decay in the targeted decay mode. The sample *SUSY inclusive* refers to the sum of the previous two.

The M_{eff} distributions for signal and background for $E_T^{\text{miss}} > 40$ GeV and $S_T > 0.2$ are shown in Figure 4.9. The 1.2 TeV cut on the effective mass cannot eliminate all the top-pair and QCD background which largely dominate because of the very conservative cut on the E_T^{miss} . However, as we shall see later, further selection criteria, aiming at discriminating the targeted decay channel from the SUSY combinatorics, also reject a large fraction of SM background.

After applying all *SM cuts*, the E_T^{miss} is distributed as shown in Figure 4.10. A significant excess of SUSY inclusive events over the background can be seen in the high- E_T^{miss} region, due to the presence of neutrinos in the LSP decay products, resembling thus a signal of R -parity conserving SUSY. This became evident in Figure 4.3, where the truth E_T^{miss} distributions were shown for various SUSY “sub-samples”, classified according to the $\tilde{\chi}_1^0$ decay mode. As expected, the signal decay is characterised by much lower E_T^{miss} than the rest of SUSY events. Therefore, a low E_T^{miss} threshold (40 GeV) is retained, although a higher one would be more efficient against the QCD background.

Table 4.7: Efficiencies and cut flow for the *SM cuts* after the preselection `mu18i_loose_2j20` with respect to the initial number of events (before the trigger) for the 7 TeV samples. The numbers of events are normalised to 2 fb^{-1} .

	$M_{\text{eff}} > 1.2 \text{ TeV}$		$M_{\text{eff}} > 1.2 \text{ TeV}$ $S_T > 0.2$		$M_{\text{eff}} > 1.2 \text{ TeV}$ $S_T > 0.2$ $E_T^{\text{miss}} > 40 \text{ GeV}$	
	# events	eff (%)	# events	eff (%)	# events	eff (%)
SUSY signal decay	706.3	62.8	468.8	41.7	437.1	38.6
SUSY background	1880.3	34.3	1222.2	22.3	1178.0	21.5
SUSY inclusive	2586.6	37.0	1691.0	24.2	1615.1	23.1
$t\bar{t}$	1192.5	0.41	431.7	0.15	375.8	0.1295
single top	60.5	0.08	20.9	0.028	17.5	0.0235
W + jets	2109.2	0.0034	363.7	0.00058	305.4	0.000487
Z + jets	380.6	0.0059	77.8	0.0012	37.4	0.000584
WW + WZ + ZZ	14.1	0.030	1.1	0.0024	0.94	0.00196
QCD dijets	32880.4	3.0×10^{-7}	2674.2	7.0×10^{-8}	1463.9	1.3×10^{-8}
Total SM bkg	36637.3	3.0×10^{-7}	3569.4	7.0×10^{-8}	2200.9	1.3×10^{-8}
S_{SUSY}/B	0.071	–	0.47	–	0.74	–
S_{SUSY}/\sqrt{B}	13.5	–	28.3	–	34.4	–

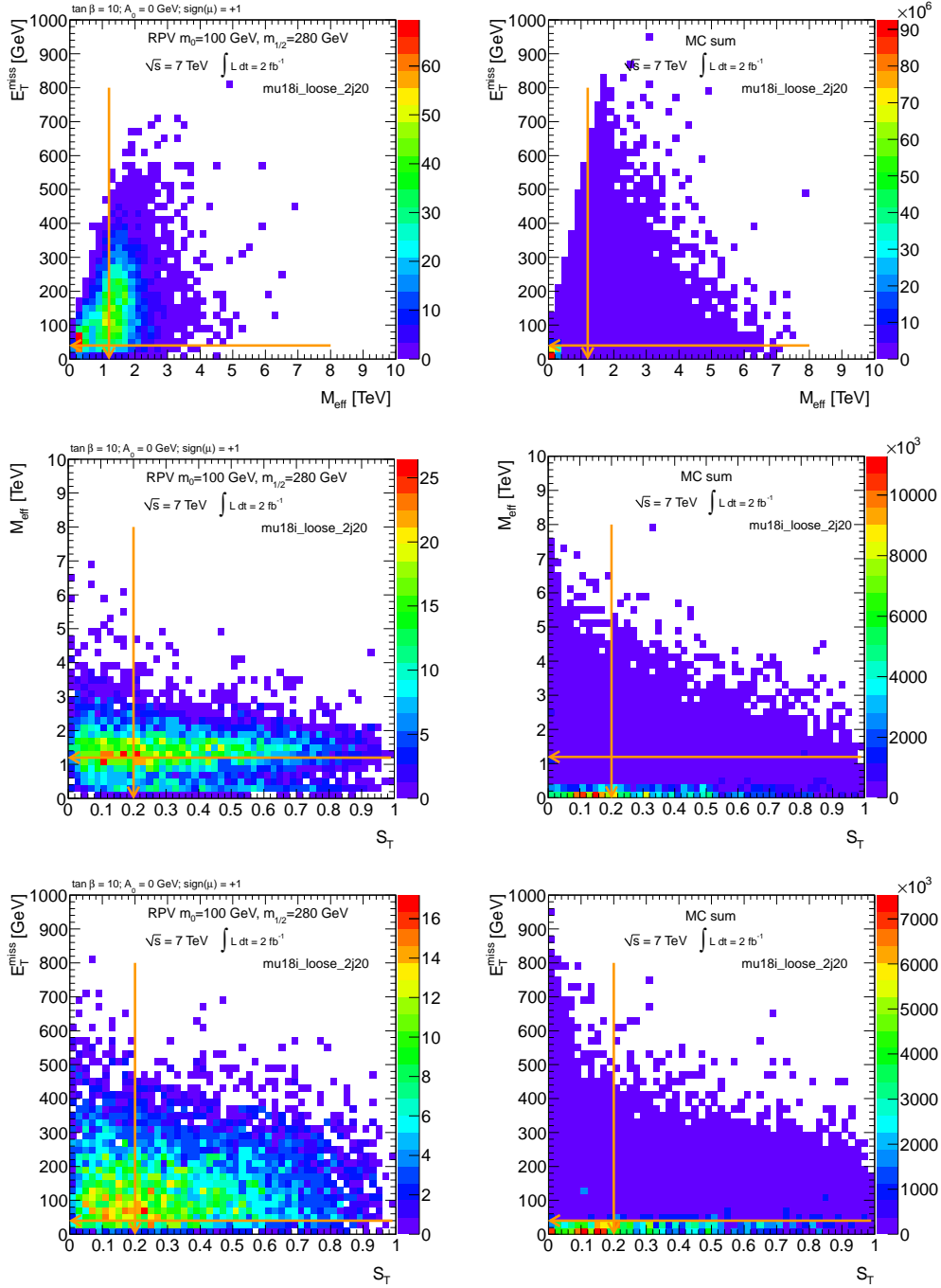


Figure 4.8: M_{eff} vs. E_T^{miss} (top), S_T vs. M_{eff} (centre) and S_T vs. E_T^{miss} (bottom) distributions for the SUSY inclusive signal (left) and for the normalised sum of all SM backgrounds, *MC sum*, (right) at 7 TeV after the $\mu 18i_loose_2j20$ selection, normalised to 2 fb^{-1} . The arrows show the cut values to be applied.

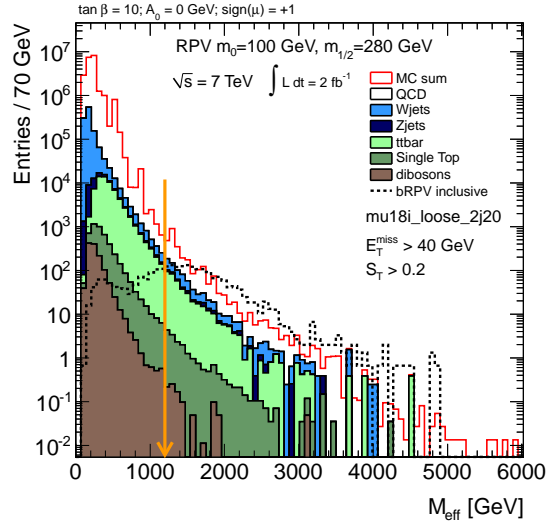


Figure 4.9: M_{eff} distributions for the SUSY inclusive signal and for all SM backgrounds at 7 TeV after the preselection $\mu 18i_loose_2j20$ and after applying the $E_T^{\text{miss}} > 40$ GeV and $S_T > 0.2$ cuts, normalised to 2 fb^{-1} . *MC sum* refers to the normalised sum of all SM background sources. The arrow shows the M_{eff} cut value to be applied.

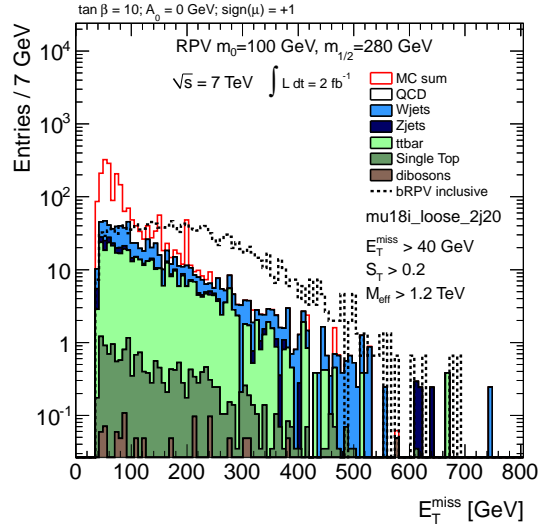


Figure 4.10: E_T^{miss} distributions for the SUSY inclusive signal and for all SM backgrounds at 7 TeV after the preselection $\mu 18i_loose_2j20$ and after applying the final set of *SM cuts* (Eq. 4.5), normalised to 2 fb^{-1} . *MC sum* refers to the normalised sum of all SM background sources.

4.5.2 Analysis at 10 TeV

In this case the reconstruction algorithms considered to define objects are Cone4H1TowerJets (defined in Section 2.3.6.5) for jets and Staco for muons, with no further requirements. The missing transverse energy corresponds to the variable $E_{T, \text{ReffFinal}}^{\text{miss}}$. In Figures 4.11, M_{eff} and E_T^{miss} distributions are shown for all SM backgrounds and for the SUSY inclusive signal after passing the preselection mu10i_loose_2j20.

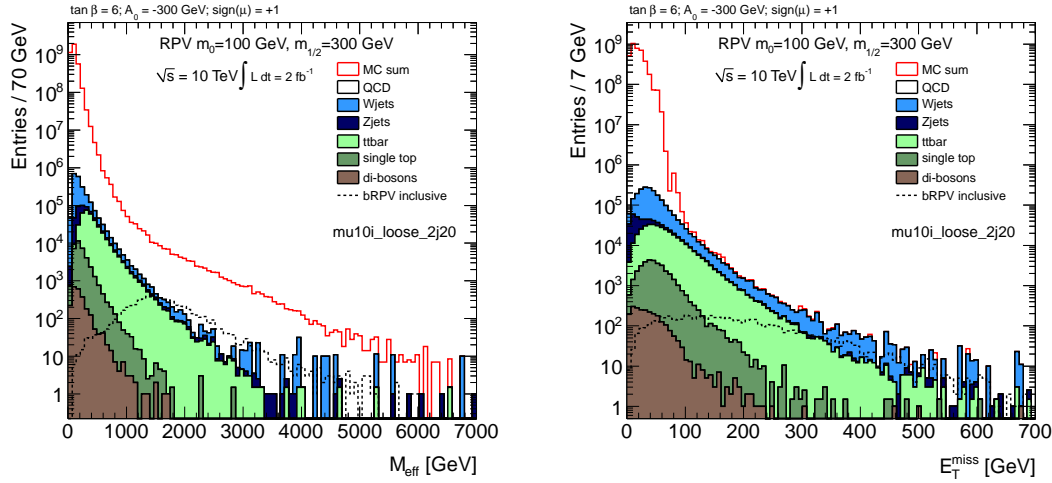


Figure 4.11: M_{eff} and E_T^{miss} distributions for the SUSY inclusive signal and for all SM backgrounds at 10 TeV after the mu10i_loose_2j20 selection, normalised to 2 fb^{-1} . *MC sum* refers to the normalised sum of all SM background sources.

Analogous checks to the 7 TeV analysis have been performed in correlation plots for M_{eff} , E_T^{miss} and S_T . Also in this case no noticeable correlation appears between none of these variables and therefore the cuts on each of them are applied independently. These correlation plots can be found in Section B.1 of Appendix B.

The same systematic study as in the 7 TeV case, applying various thresholds on these variables, has been carried out showing that the same set of cuts applied there, the *SM cuts* defined in Eq. (4.5), is also suitable for this energy. The efficiencies and cut flow for this combination of cuts are shown in Table 4.8.

The M_{eff} distribution for signal and background for $E_T^{\text{miss}} > 40 \text{ GeV}$ and $S_T > 0.2$ is shown in the left panel of Figure 4.12. As in the 7 TeV case, the 1.2 TeV cut on the effective mass cannot eliminate the top-pair and QCD background which dominate largely because of the very conservative cut on the E_T^{miss} . However, after applying all *SM cuts* a significant excess of events over the background can be seen in the high- E_T^{miss} region for the SUSY sample due to the presence of neutrinos in the LSP decay products, as shown in Figure 4.12 right panel.

Table 4.8: Efficiencies and cut flow for the *SM cuts* after the preselection *mu10i_loose_2j20* with respect to the initial number of events (before the trigger) for the 10 TeV samples. The numbers of events are normalised to 2 fb^{-1} .

	$M_{\text{eff}} > 1.2 \text{ TeV}$		$M_{\text{eff}} > 1.2 \text{ TeV}$ $S_T > 0.2$		$M_{\text{eff}} > 1.2 \text{ TeV}$ $S_T > 0.2$ $E_T^{\text{miss}} > 40 \text{ GeV}$	
	# events	eff (%)	# events	eff (%)	# events	eff (%)
SUSY signal decay	760	81.5	534	57.2	486	50.1
SUSY background	4187	44.1	2784	29.3	2705	28.4
SUSY inclusive	4947	52.1	3318	34.9	3191	33.6
$t\bar{t}$	3942	0.53	1324	0.18	1107	0.15
single top	46	0.051	7	0.008	7	0.008
W + jets	2150	0.062	285	0.008	171	0.005
Z + jets	512	0.15	122	0.036	52	0.015
WW + WZ + ZZ	4	0.12	0	0.0	0	0.0
QCD dijets	136904	3.3×10^{-6}	39449	9.6×10^{-7}	5965	1.5×10^{-7}
Total SM bkg	142556	3.5×10^{-6}	41188	1.0×10^{-6}	7302	1.8×10^{-7}
S_{SUSY}/B	0.03	–	0.08	–	0.44	–
S_{SUSY}/\sqrt{B}	13.1	–	16.4	–	37.3	–

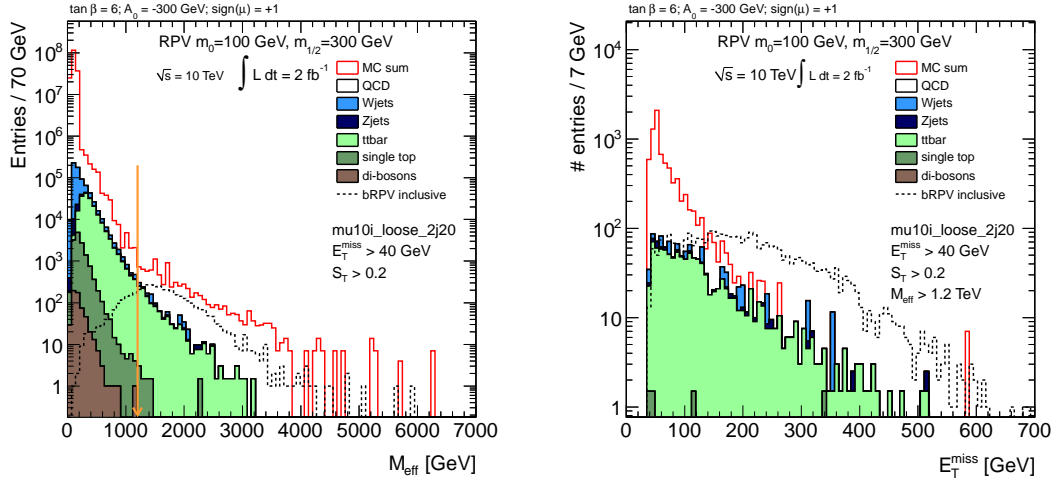


Figure 4.12: *Left*: M_{eff} distributions for the SUSY inclusive signal and for all SM backgrounds at 10 TeV after the preselection *mu10i_loose_2j20* and after applying the $E_T^{\text{miss}} > 40 \text{ GeV}$ and $S_T > 0.2$ cuts, normalised to 2 fb^{-1} . The arrow shows the M_{eff} cut value to be applied. *Right*: E_T^{miss} distributions for the SUSY inclusive signal and for all SM backgrounds at 10 TeV after the preselection *mu10i_loose_2j20* and after applying the final set of *SM cuts* (Eq. 4.5), normalised to 2 fb^{-1} . *MC sum* refers to the normalised sum of all SM background sources.

4.5.3 Analysis at 14 TeV

The reconstruction algorithms considered to define objects are Kt4 (defined in Section 2.3.6.5) for jets and Staco for muons, with no further requirements. The missing transverse energy corresponds to the variable $E_{T, \text{RefFinal}}^{\text{miss}}$.

The same systematic study done for the 7 TeV and 10 TeV analyses, applying various thresholds on these variables, has been performed, showing that the same set of *SM cuts*, defined in Eq. (4.5), applied there is also suitable for this energy. After the application of the *SM cuts*, distributions shown in Figure 4.13 are obtained. The M_{eff} and S_T plots analogous to Figures 4.7 in the 7 TeV analysis can be found in Section B.2 of Appendix B. The efficiencies for the preselection cut and for the *SM cuts* are shown in Table 4.9.

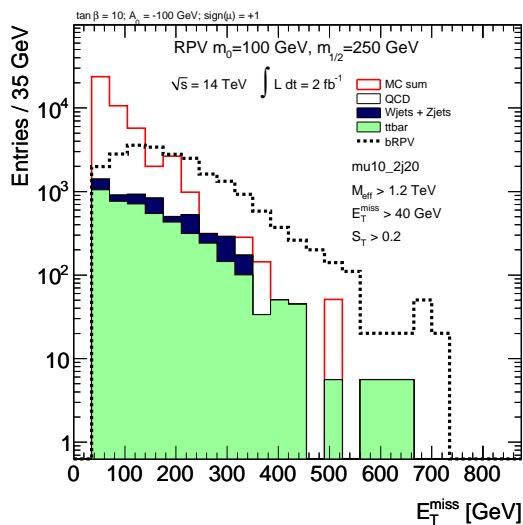


Figure 4.13: E_T^{miss} distribution for the SUSY inclusive signal and for all SM backgrounds at 14 TeV after the mu10_2j20 preselection and the final set of *SM cuts* (Eq. 4.5), normalised to 2 fb^{-1} . *MC sum* refers to the normalised sum of all SM background sources taken into account.

4.5.4 Conclusions on the SM background suppression

As shown in the signal definition Section 4.3, the behaviour of the bRPV samples is not identical in the three energy scenarios. There are some differences mainly due to the mSUGRA selected point but also due to the distinct centre-of-mass energy and to the continuous improvement in the generation and simulation tools used to obtain the samples. Also some differences are found in the SM background distributions when comparing them among the three scenarios.

In Figure 4.2 it was seen how the E_T^{miss} distribution in the 10 and 14 TeV samples is slightly shifted towards higher values with respect to the 7 TeV sample. A similar response is observed in the SM background samples. The M_{eff} distributions acts in a similar way, drifting towards higher values with the energy both in the SUSY samples and in the SM background. This has an effect on the *SM cuts* applied. For example in the M_{eff} cut it is seen how lower efficiencies

Table 4.9: Efficiencies for the preselection mu10_2j20 and for the selected set of cuts after the preselection with respect to the initial number of events (before the trigger) for the 14 TeV samples.

	mu10_2j20	$M_{\text{eff}} > 1.2 \text{ TeV}$ $S_T > 0.2$ $E_T^{\text{miss}} > 40 \text{ GeV}$
	eff (%)	eff (%)
SUSY signal decay	89.9	41.2
SUSY background	60.1	25.7
SUSY inclusive	64.7	28.0
$t\bar{t}$	53.4	0.5
W + jets	41.7	0.08
QCD dijets	0.08	1.3×10^{-7}
Total SM bkg	0.08	1.5×10^{-7}
S_{SUSY}/B	1.7×10^{-6}	0.40
S_{SUSY}/\sqrt{B}	0.3	95.3

are obtained in the 7 TeV sample with 62% ($3 \times 10^{-7}\%$) for signal (SM background) than in the 10 TeV sample, with efficiency of 81.5% (3.3×10^{-6}). Distributions for S_T are similar in the three energy cases.

Combining these effects results in a slightly better S_{SUSY}/B for the lowest energy, decreasing as the energy grows, oppositely to S_{SUSY}/\sqrt{B} . The *SM cuts* give a similar number of surviving SUSY signal decay events (> 400) in the three cases and a signal efficiency better than 40%.

It is worth reminding that no *RPV-model-specific* selection criteria have been applied so far. Henceforth any mention to *SM cuts* will imply the set of cuts in Eq. (4.5) applied on events that already have passed the preselection.

4.6 Combinatorial background study

In this section the attempt is to establish additional selection criteria allowing the extraction of the LSP decay channel under study, $\tilde{\chi}_1^0 \rightarrow \mu W (\rightarrow \bar{q}q')$, from the SUSY combinatorial background in terms of the invariant mass $M_{\mu jj}$. In a hadronically produced SUSY event, several muons and W -bosons can be produced during the cascade decay of supersymmetric particles. Moreover, in every event there are two lightest neutralinos produced at the end of the decay chain. Since the channel we are interested in has a branching ratio of approximately 10%, most of the times the LSP decays through different channels, in some cases also involving a muon or a W . In Figure 4.14 (left) the number of muons per event is represented as a function of the number of signal decays in that event. In a considerable fraction of events there is a number of muons besides those coming from a $\tilde{\chi}_1^0 \rightarrow \mu W$ decay, being this number of extra muons up to four or five even in events not containing any signal decay.

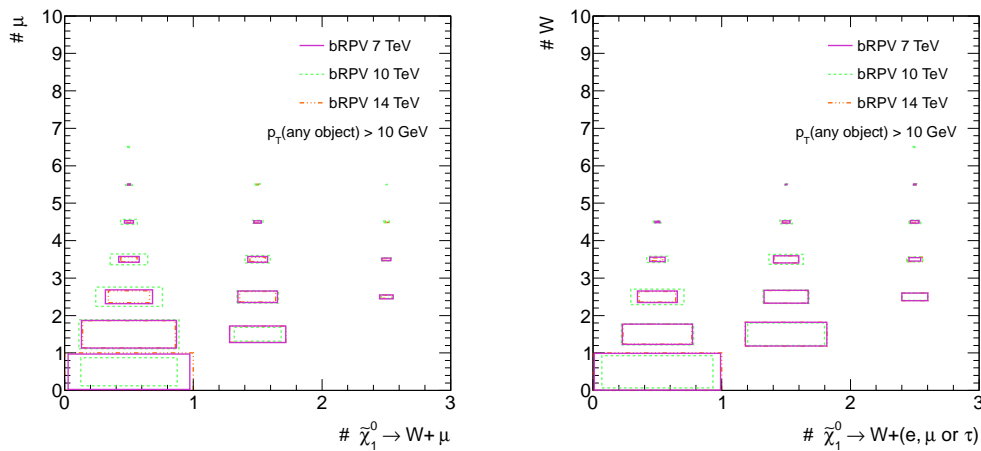


Figure 4.14: *Left*: Number of muons per event as a function of the number of signal decays in that event for the three-energy scenarios. *Right*: Number of W bosons per event with respect to the number of $\tilde{\chi}_1^0$ decays containing a W in that event for the three-energy scenarios. The size of the boxes is proportional to the number of entries in each bin. Size unity corresponds to the greatest number of entries (among the three samples).

The same comparison is done for the number of W -bosons with respect to the number of $\tilde{\chi}_1^0$ decays containing a W in Figure 4.14 (right). In this case up to three or four extra W may be present, besides those coming from a $\tilde{\chi}_1^0$ decay. This situation is equally important in the three-energy configurations, so the need of a second stage in the analysis in order to reconstruct the invariant mass of the neutralino is the same in the three cases. The aim is thereby to select the actual muon and jets originating from the LSP decay for the invariant mass calculation, which should provide the $\tilde{\chi}_1^0$ mass. The rest of combinations of jet pairs to form a W -candidate and pairs of a muon and a W -candidate to form a $\tilde{\chi}_1^0$ -candidate are referred to as *Combinatorial background*. To accomplish this selection, the separation angle between two reconstructed objects, defined as $\Delta R = \sqrt{\Delta\phi^2 + \Delta\eta^2}$, is used as discriminating variable. Considering that the lightest neutralino is sufficiently boosted, the separation angle between the muon and the W , $\Delta R_{\mu W}$, is expected to be rather small. The same is expected for the separation angle between the two quarks originating from the W -boson, ΔR_{jj} although to a lesser extent due to the lower p_T expected for the W compared to that of the $\tilde{\chi}_1^0$.

4.6.1 Analysis at 7 TeV

In Figure 4.15, truth (left) and reconstructed (right) muon momenta are presented for inclusive SUSY events passing the *SM cuts*. p_T distribution for all muons in the event and for muons originating from a neutralino decay are compared for both cases. In the reconstructed p_T distribution (right) the determination of muons from $\tilde{\chi}_1^0$ has been carried out by matching them in (η, ϕ) with true muons coming from a $\tilde{\chi}_1^0$. Although the muon- p_T is not a decisive discriminant for $\tilde{\chi}_1^0$ -candidates, it is seen that muons coming from LSPs have slightly higher- p_T than the rest of muons. A study in this direction has been done and a final cut on the muon- $p_T > 25$ GeV has been applied. A short discussion on this study can be found in Appendix C.

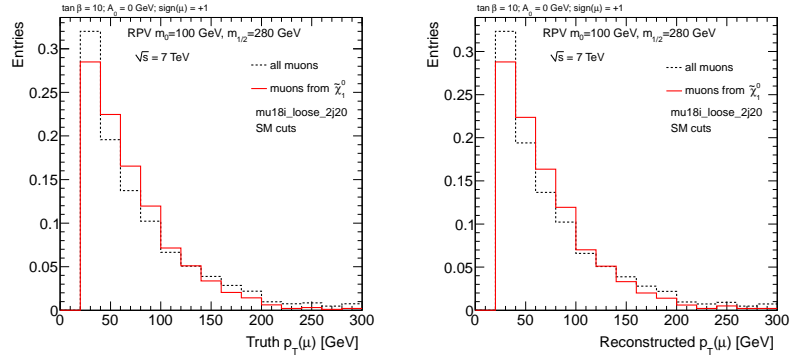


Figure 4.15: Distributions of muons in the SUSY inclusive sample at 7 TeV after applying the *SM cuts*. *Left*: Truth p_T of all muons (black dashed line) and muons coming from a $\tilde{\chi}_1^0$ (red continuous line). *Right*: Reconstructed p_T of all muons (black dashed line) and muons coming from a $\tilde{\chi}_1^0$ (red continuous line). All distributions have been normalised to unit area.

SUSY events are in general characterized by high jet multiplicity. This is also the case in the bRPV model, as it can be seen in Figure 4.16, where the number of truth and reconstructed jets (recall that only jets with $p_T > 20$ GeV are considered for this analysis) is plotted.

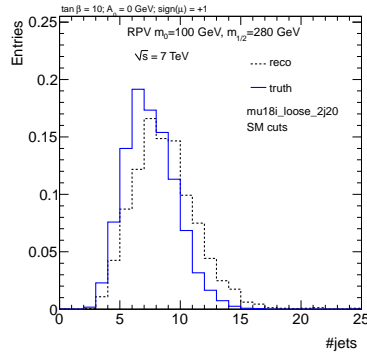


Figure 4.16: Distributions of number of truth (blue continuous line) and reconstructed (black dashed line) jets in the SUSY inclusive sample at 7 TeV after applying the *SM cuts*. All distributions have been normalised to unit area.

This fact, together with the high W bosons multiplicity already shown, makes it necessary to impose several conditions for the selection of jet pairs to form W -candidates. As a first approximation, a W -candidate is defined as a pair of jets with an invariant mass close the M_W within a certain threshold. In the left plot of Figure 4.17 the number of W -candidates with $m_{jj} \in \{M_W \pm 10 \text{ GeV}\}$ are shown. This definition yields a high number of fake reconstructed W and the tighter definition of $m_{jj} \in \{M_W \pm 5 \text{ GeV}\}$ is finally applied. As seen in the right hand side plot, this definition still leads to a high number of fake W , where the excess of W -candidates over the truth distribution can not be attributed only to the higher number of reconstructed jets with respect to truth jets. Therefore, stronger requirements on the W -candidates definition are needed.

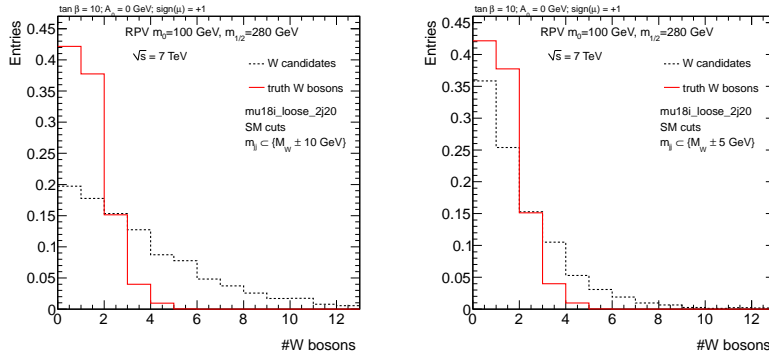


Figure 4.17: Distributions of number of W bosons in the SUSY inclusive sample at 7 TeV after applying the *SM cuts*. *Left*: Number of truth W bosons (red continuous line) and W candidates (black dashed line), defined as the jet pairs whose reconstructed invariant mass is within $M_W \pm 10 \text{ GeV}$. *Right*: Number of truth W bosons (red continuous line) and W candidates (black dashed line), defined as the jet pairs whose reconstructed invariant mass is within $M_W \pm 5 \text{ GeV}$. All distributions have been normalised to unit area.

Finally, even if the pair of jets selected are indeed generated from the same W , further selection criteria have to be employed to choose the correct one, due to the high W multiplicity. As stated before, the separation angles between the two quarks originating from the W -boson, ΔR_{jj} and between the muon and the W , $\Delta R_{\mu W}$, are expected to be rather small. This is supported by the top panels of Figure 4.18, where the correlation for the W (left) and $\tilde{\chi}_1^0$ (right) momentum and the separation angle between their decay products is plotted for truth particles in the signal decay. As expected, higher momenta of the decaying particle imply smaller separation angles for the decay products. The same quantities are represented for the SUSY inclusive sample on the bottom plots, where all possible combinations of jets with $m_{jj} \in \{M_W \pm 5 \text{ GeV}\}$ (left) and of W -candidates and muons (right) are included.

In the bottom panels of Figure 4.18, the clear correlation between the $p_T(W)$ and the angular distance of its decay products, seen both in the truth particle plot (top) and in the reconstructed particles plot (bottom), lead to a study on a combined cut on $p_T(W) - \Delta R_{jj}$. Nevertheless, since the shape of the correlation is exactly the same in both plots, an individual cut on ΔR_{jj} was found to be more effective. A similar test was done for the $p_T(\tilde{\chi}_1^0) - \Delta R_{\mu W}$ correlation, with a more different behaviour in the truth and reconstructed versions. Several triangular cuts, for example in the line $p_T(\tilde{\chi}_1^0) < -300 \Delta R_{\mu W} + 600$ were tested, always leaving a higher efficiency for the reconstructed events than the individual cut on $\Delta R_{\mu W}$, keeping the same number of truth events. Therefore, no combined cut on any of these variables is finally applied.

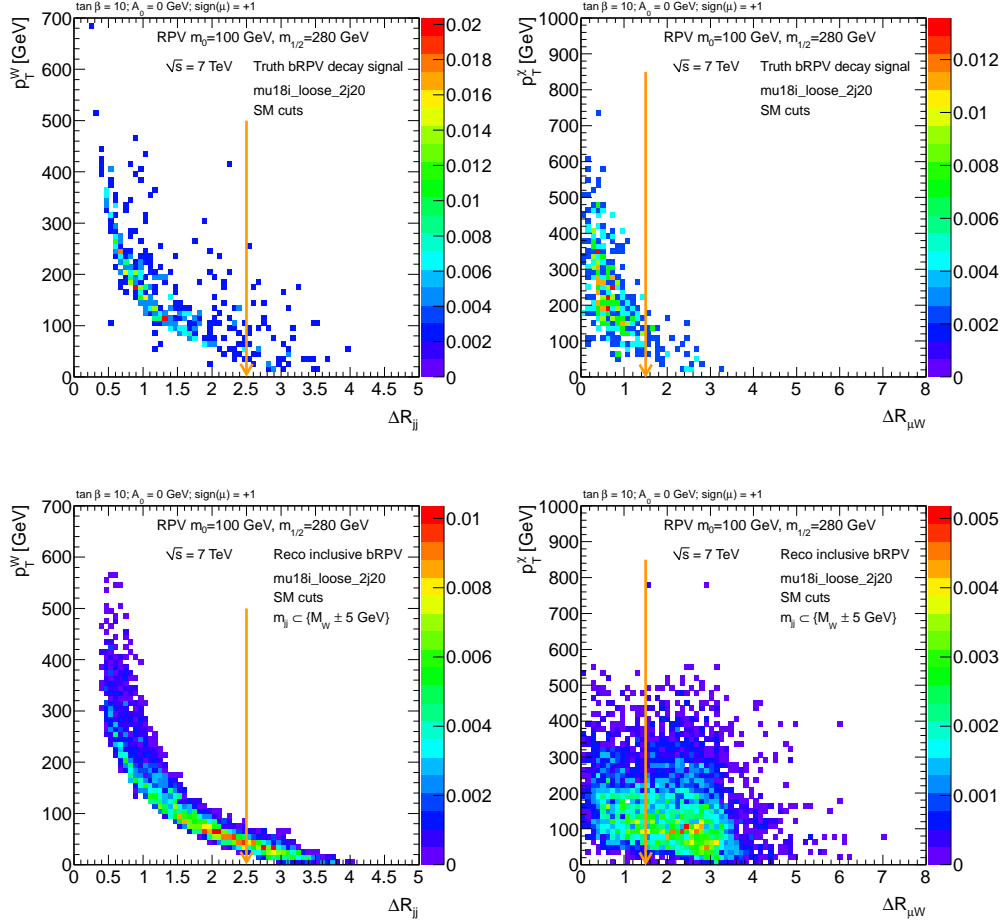


Figure 4.18: $p_T - \Delta R$ correlations for the SUSY sample at 7 TeV. *Top left*: p_T of truth W bosons coming from LSPs vs. the angle between their decay products: two jets. *Top right*: p_T of truth $\tilde{\chi}_1^0$ vs. the angle between its decay products: a muon and a W . *Bottom left*: p_T of all W candidates (with $m_{ij} \subset \{M_W \pm 5 \text{ GeV}\}$) vs. the angle between the pair of reconstructed jets used to form it. *Bottom right*: $\tilde{\chi}_1^0$ -candidate p_T vs. the angle between the reconstructed muon and the W -candidate (with $m_{ij} \subset \{M_W \pm 5 \text{ GeV}\}$) used to identify it. All distributions have been normalised to unit area. The arrows show the cut values.

In Figure 4.19, two separation angle distributions are compared between the signal decay only and all other possible combinations. In the former case, ΔR_{jj} ($\Delta R_{\mu W}$) peaks around 1.0 (0.5, a lower value as expected, due to the higher boost in the $\tilde{\chi}_1^0$), while in the latter they are evenly distributed towards higher values.

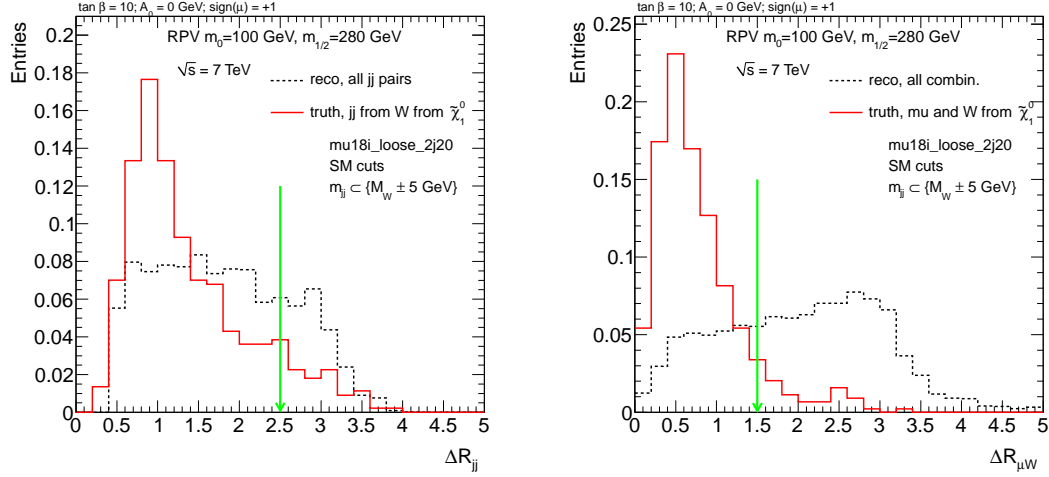


Figure 4.19: Distributions of separation angles in the SUSY sample at 7 TeV after applying the *SM cuts*. *Left*: Angle between truth jets coming from a W that comes from an LSP (red continuous line) and for all reconstructed jets with an invariant mass $m_{ij} \in \{M_W \pm 5 \text{ GeV}\}$ (black dashed line). *Right*: Angle between a truth muon and a truth W both coming from an LSP (red continuous line) and between all reconstructed muons and all W -candidates (with $m_{ij} \in \{M_W \pm 5 \text{ GeV}\}$) (black dashed line). The distributions have been normalised to unit area. The arrows show the cut values.

As seen in Figure 4.20, no correlation between these two variables is observed neither among the signal decay events (left) nor in the sample of all possible combinations (right). In order to select the pertinent cuts on this variables, a systematic study similar to that performed for the SM background study was carried out, with the final cuts set at $\Delta R_{\mu W} < 1.5$ and $\Delta R_{jj} < 2.5$.

In Figure 4.21, the relation between the muon and the W momenta coming from a $\tilde{\chi}_1^0$ is presented for truth particles on the left and for reconstructed $\tilde{\chi}_1^0$ -candidates on the right. In the left panel a correlation between these two variables is observed for the truth SUSY decay signal, so the cut $p_T^\mu < 5/7 p_T^W + 50 \text{ GeV}$ may be applied. Nevertheless it has been confirmed that the effect of this cut is negligible after the application of the abovementioned cuts, so it will not be taken into account in the final list of cuts applied for the determination of the invariant mass $M_{\mu jj}^{inv}$. A cut on the W -candidate p_T was also tried with a similar result, so it is not included in the final list of cuts.

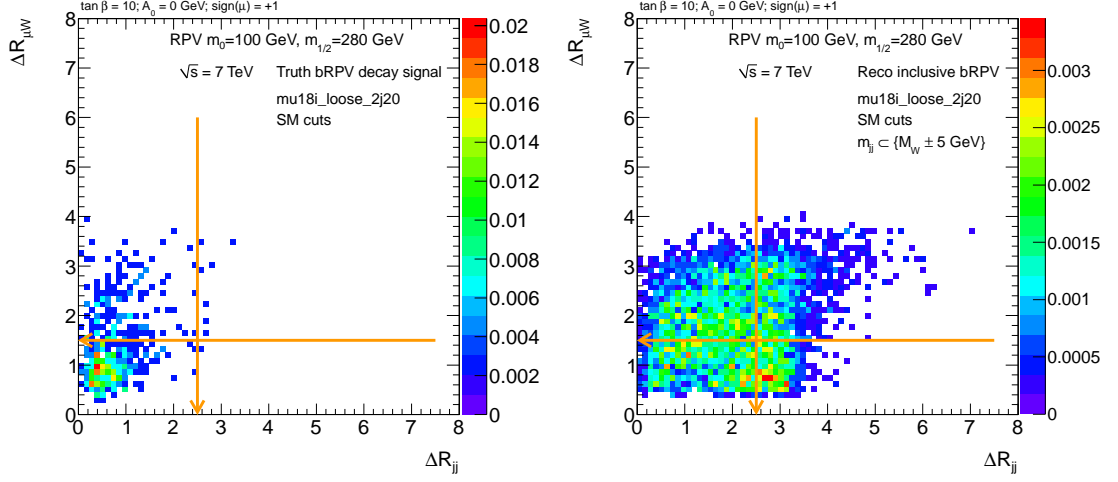


Figure 4.20: Correlation of angular distances for the SUSY sample at 7 TeV. *Left*: Angle between true jets coming from an LSP-originating W vs. angle between a true muon and a true W both coming from an LSP. *Right*: Angle between all reconstructed jets to form a W candidate (with $m_{ij} \in \{M_W \pm 5 \text{ GeV}\}$) as a function of the angle of all reconstructed muons and all W -candidates. The distribution for all combinations have been normalised to unit area. The arrows show the cut values.

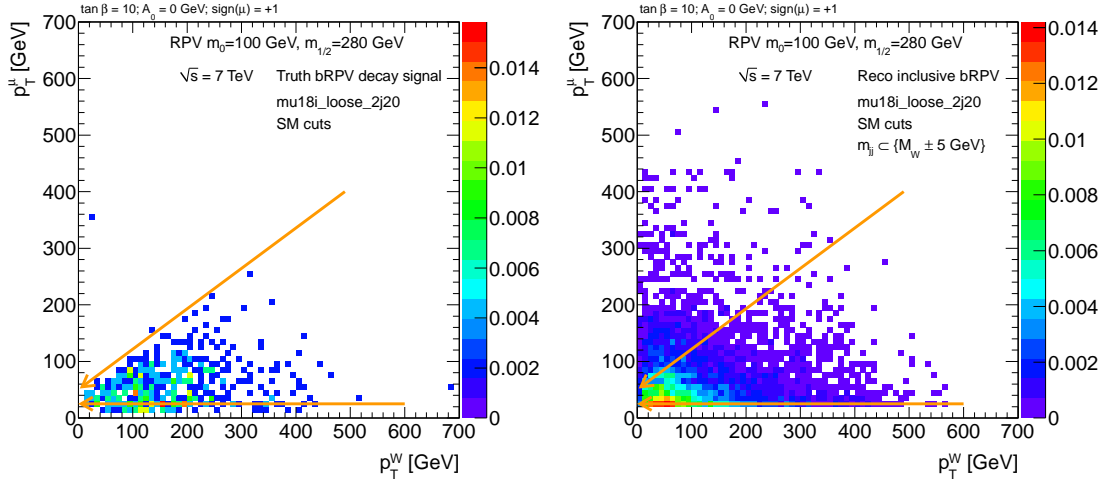


Figure 4.21: Transverse momenta correlations for the SUSY sample at 7 TeV. *Left*: True- $W p_T$ coming from an LSP vs. true-muon p_T coming from the same LSP. *Right*: W -candidate (with $m_{ij} \in \{M_W \pm 5 \text{ GeV}\}$) p_T vs. reconstructed-muon p_T to be combined with it to form a $\tilde{\chi}_1^0$ -candidate. The distribution for all combinations have been normalised to unit area. The arrows show the studied cut values.

The final set of cuts applied in order to discriminate the combinatorial background from the muon and pair of jets originating from a $\tilde{\chi}_1^0$, in the following called *Combinatorial cuts*, are:

$$\begin{aligned} p_T(\mu) &> 25 \text{ GeV}, \\ \Delta R_{\mu W} &< 1.5, \\ \Delta R_{jj} &< 2.5. \end{aligned} \tag{4.6}$$

The cut flow for the *Combinatorial cuts* is shown in Table 4.10. In this table, the number of $\tilde{\chi}_1^0$ -candidates ($\tilde{\chi}_1^0$ -cands), within the definition given by each of the *Combinatorial cuts*, in events passing the *SM cuts*, is shown for every SM background process and for SUSY events. The effect of the cuts on suppressing the background due to the SUSY combinatorics is observed in the first two rows of the table. The efficiencies are calculated with respect to the number of $\tilde{\chi}_1^0$ -candidates in the first column, before applying any Combinatorial cut.

Table 4.10: Cut flow for the number of $\tilde{\chi}_1^0$ -candidates ($\tilde{\chi}_1^0$ -cands) fulfilling the requirements in each step, for the SUSY sample and all SM backgrounds at 7 TeV for the *Combinatorial cuts* after the *SM cuts*. The efficiencies are calculated with respect to the number of $\tilde{\chi}_1^0$ -candidates before applying any Combinatorial cut (first column). The numbers of events are normalised to 2 fb^{-1} .

	SM cuts	SM cuts $\Delta R_{jj} < 2.5$	SM cuts $\Delta R_{jj} < 2.5$ $p_T^\mu > 25 \text{ GeV}$	SM cuts $\Delta R_{jj} < 2.5$ $p_T^\mu > 25 \text{ GeV}$ $\Delta R_{\mu W} < 1.5$			
	$\# \tilde{\chi}_1^0$ - cands	$\# \tilde{\chi}_1^0$ - cands	eff (%)	$\# \tilde{\chi}_1^0$ - cands	eff (%)	$\# \tilde{\chi}_1^0$ - cands	eff (%)
SUSY signal decay	998.1	781.1	78.3	709.7	71.1	289.6	29.0
SUSY background	2036.3	1569.4	77.1	1392.9	68.4	465.0	22.8
SUSY inclusive	3034.5	2350.5	77.5	2102.6	69.3	754.6	24.7
$S_{\text{decay}}/B_{\text{SUSY}}$	0.49	0.50	–	0.51	–	0.62	–
$t\bar{t}$	650.0	424.8	65.4	388.1	59.7	97.5	15.0
single top	23.0	15.7	68.1	14.2	61.8	2.8	12.1
W + jets	1007.5	301.8	30.0	283.6	28.1	57.5	5.7
Z + jets	207.7	74.0	35.6	68.2	32.8	14.2	6.8
WW + WZ + ZZ	0.37	0.28	75.0	0.28	75.0	0.02	6.0
QCD dijets	219.8	168.3	76.6	114.4	52.1	46.4	21.1
Total SM bkg	2108.4	984.7	46.7	868.7	41.2	218.3	10.4
$S_{\text{SUSY inclusive}}/B_{\text{SM}}$	1.44	2.39	–	2.42	–	3.46	–
$S_{\text{SUSY inclusive}}/\sqrt{B_{\text{SM}}}$	66.1	74.9	–	71.3	–	51.1	–

In Table 4.11 the number of events passing the *SM cuts* and containing at least one $\tilde{\chi}_1^0$ -candidate ($\tilde{\chi}_1^0$ -cands), within the definition given by the *Combinatorial cuts*, is shown. Hence, the first column corresponds to the number of events in the last column of Table 4.7 that contain at least one neutralino candidate with $m_{jj} \in \{M_W \pm 5 \text{ GeV}\}$ and no further requirements. The second column corresponds to the number of events which contain at least one neutralino candidate whose $\Delta R_{jj} < 2.5$ and so on. The efficiencies are calculated with respect to the initial number of events. The overall SM background is reduced by an order of magnitude requiring at least one neutralino-LSP candidate.

Table 4.11: Cut flow for the SUSY sample and all SM backgrounds at 7 TeV for the *Combinatorial cuts* after the *SM cuts*. The cut flow is shown for events passing these cuts and containing at least one $\tilde{\chi}_1^0$ -candidate ($\tilde{\chi}_1^0$ -cand) fulfilling the requirements given by the *Combinatorial cuts* applied in each step. The efficiencies are calculated with respect to the initial number of events (before the trigger). The numbers of events are normalised to 2 fb^{-1} .

	SM cuts $\# \tilde{\chi}_1^0 - \text{cand} \geq 1$		SM cuts $\# \tilde{\chi}_1^0 - \text{cand} \geq 1$ $\Delta R_{jj} < 2.5$		SM cuts $\# \tilde{\chi}_1^0 - \text{cand} \geq 1$ $\Delta R_{jj} < 2.5$ $p_T^\mu > 25 \text{ GeV}$		SM cuts $\# \tilde{\chi}_1^0 - \text{cand} \geq 1$ $\Delta R_{jj} < 2.5$ $p_T^\mu > 25 \text{ GeV}$ $\Delta R_{\mu W} < 1.5$	
	# events	eff (%)	# events	eff (%)	# events	eff (%)	# events	eff (%)
SUSY signal decay	263.9	23.3	245.8	21.8	229.5	20.4	158.2	14.2
SUSY background	626.3	11.4	566.5	10.3	523.2	9.5	291.7	5.3
SUSY inclusive	888.3	12.1	811.5	11.6	752.7	10.8	449.7	6.4
$S_{\text{decay}}/B_{\text{SUSY}}$	0.42	–	0.43	–	0.44	–	0.54	–
$t\bar{t}$	204.9	0.07	188.1	0.07	167.9	0.06	66.1	0.02
single top	8.0	0.01	7.4	0.01	6.90	0.009	2.3	0.003
W + jets	119.0	1.9×10^{-4}	103.1	1.7×10^{-4}	95.5	1.5×10^{-4}	34.2	6×10^{-5}
Z + jets	10.8	1.7×10^{-4}	8.5	1.3×10^{-4}	7.8	1.1×10^{-4}	4.4	6.8×10^{-5}
WW + WZ + ZZ	0.18	3.4×10^{-4}	0.13	2.8×10^{-4}	0.13	2.8×10^{-4}	0.01	2.4×10^{-4}
QCD dijets	102.3	9.3×10^{-10}	92.1	8.4×10^{-10}	62.8	5.7×10^{-10}	33.4	3.4×10^{-10}
Total SM bkg	445.2	3.7×10^{-9}	399.4	3.3×10^{-9}	340.9	2.8×10^{-9}	140.4	1.2×10^{-9}
$S_{\text{SUSY inclusive}}/B_{\text{SM}}$	2.0	–	2.0	–	2.2	–	3.2	–
$S_{\text{SUSY inclusive}}/\sqrt{B_{\text{SM}}}$	42.1	–	40.6	–	40.8	–	38.0	–

4.6.2 Analysis at 10 TeV

Analogously to the 7 TeV case, muon multiplicity and momenta are presented in Figure 4.22 for events passing the *SM cuts*.

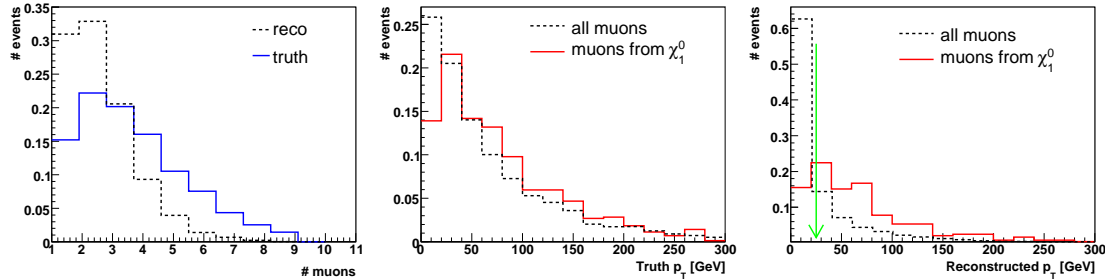


Figure 4.22: Distributions of muons in the SUSY inclusive sample at 10 TeV after applying the *SM cuts*. *Left*: Total number of truth (blue continuous line) and reconstructed (black dashed line) muons. *Centre*: Truth p_T of all muons (black dashed line) and muons coming from a $\tilde{\chi}_1^0$ (red continuous line). *Right*: Reconstructed p_T of all muons (black dashed line) and muons coming from a $\tilde{\chi}_1^0$ (red continuous line). All distributions have been normalised to unit area.

The high multiplicity of jets and W bosons is shown in Figure 4.23, where a W -candidate is defined as a pair of jets with an invariant mass $m_{jj} \in \{M_W \pm 5 \text{ GeV}\}$.

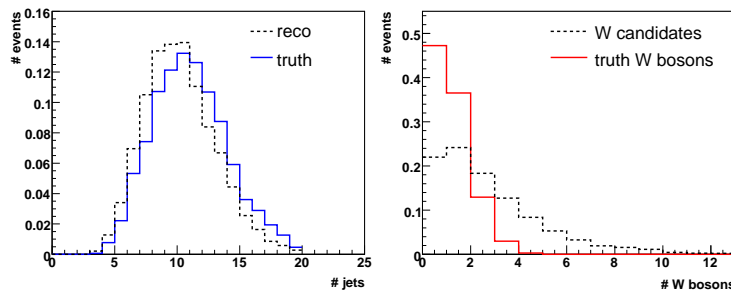


Figure 4.23: Distributions of number of jets and W bosons in the SUSY sample at 10 TeV after applying the *SM cuts*. *Left*: Number of truth (blue continuous line) and reconstructed (black dashed line) jets. *Right*: Number of truth W bosons (red continuous line) and W candidates (black dashed line), defined as the jet pairs whose reconstructed invariant mass is within $M_W \pm 5 \text{ GeV}$. All distributions have been normalised to unit area.

An analogous analysis to that of 7 TeV samples has been performed for this energy. All of the plots shown for the 7 TeV case have exactly the same shapes and correlations for the 10 TeV sample. Hence, the *Combinatorial cuts* applied in order to discriminate the SUSY decay signal from the SUSY background in the 7 TeV sample are also adequate for the 10 TeV sample. In Figure 4.24 the separation angle distributions are shown for ΔR_{jj} and $\Delta R_{\mu jj}$ compared between the signal decay only and all other possible combinations, showing the values where the cuts are applied. All the 10 TeV sample correlation plots analogue to those of the 7 TeV sample can be found in Appendix B, Section B.3.

The cut flow of the *Combinatorial cuts* is shown in Table 4.12. In this table, the number of events passing the *SM cuts* and containing at least one $\tilde{\chi}_1^0$ -candidate, within the definition given by the *Combinatorial cuts*, is presented. The efficiencies are calculated with respect to the initial number of events. The overall SM background is further reduced by an order of magnitude.

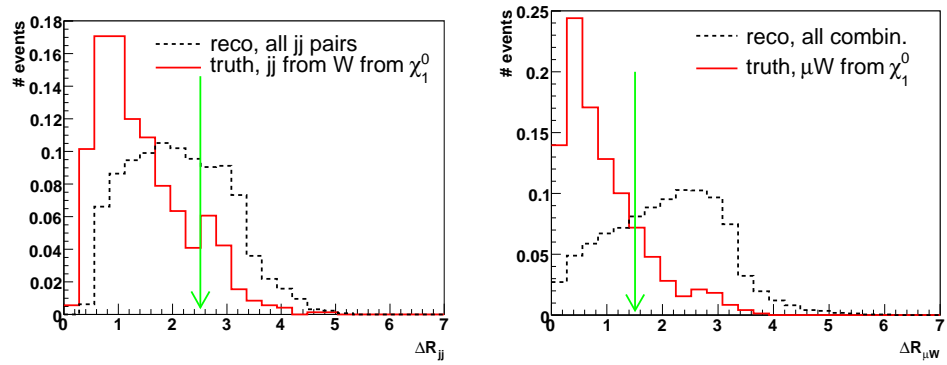


Figure 4.24: Distributions of separation angles in the SUSY sample at 10 TeV after applying the *SM cuts*. *Left*: Angle between truth jets coming from a W that comes from an LSP (red continuous line) and for all reconstructed jets (black dashed line). *Right*: Angle between a truth muon and a truth W both coming from an LSP (red continuous line) and between all reconstructed muons and all W -candidates (black dashed line). The distribution have been normalised to unit area. The arrows show the cut values.

Table 4.12: Cut flow for the SUSY sample and all SM backgrounds at 10 TeV for the *Combinatorial cuts* after the *SM cuts*. The events passing these cuts contain at least one $\tilde{\chi}_1^0$ -candidate ($\tilde{\chi}_1^0$ -cand) fulfilling the requirements given by the combinatorial cuts applied. The efficiencies are calculated with respect to the initial number of events (before the trigger). The numbers of events are normalised to 2 fb^{-1} .

	SM cuts # $\tilde{\chi}_1^0$ -cand ≥ 1		SM cuts # $\tilde{\chi}_1^0$ -cand ≥ 1 $\Delta R_{jj} < 2.5$		SM cuts # $\tilde{\chi}_1^0$ -cand ≥ 1 $\Delta R_{jj} < 2.5$ $p_T^\mu > 25 \text{ GeV}$		SM cuts # $\tilde{\chi}_1^0$ -cand ≥ 1 $\Delta R_{jj} < 2.5$ $p_T^\mu > 25 \text{ GeV}$ $\Delta R_{\mu W} < 1.5$	
	# events	eff (%)	# events	eff (%)	# events	eff (%)	# events	eff (%)
SUSY signal decay			430	46.1	380	40.7	314	33.6
SUSY background			1774	18.7	1361	14.3	616	6.5
SUSY inclusive			2204	23.2	1741	18.3	930	9.8
$S_{\text{decay}}/B_{\text{SUSY}}$			0.24	–	0.28	–	0.51	–
$t\bar{t}$			613	0.082	453	0.06	137	0.018
single top			4	0.004	4	0.004	0	0.0
W + jets			57	0.002	38	0.001	0	0.0
Z + jets			15	0.004	11	0.003	4	0.001
WW + WZ + ZZ			0	0.0	0	0.0	0	0.0
QCD dijets			3541	8.6×10^{-8}	808	2.0×10^{-8}	183	4.4×10^{-9}
Total SM bkg			4229	1.0×10^{-7}	1313	3.2×10^{-8}	324	7.9×10^{-9}
$S_{\text{SUSY inclusive}}/B_{\text{SM}}$			0.52	–	1.33	–	2.89	–
S_{SUSY}/\sqrt{B}			33.9	–	48.1	–	51.7	–

4.7 Invariant mass of muon+jets

Finally, the distribution of the invariant mass $M_{\mu jj}$ is plotted, where all possible combinations of muons and jets forming a W -candidate after applying all the selection criteria are included.

Summary of selection criteria:

- **Preselection:**
 - at least one isolated muon with $p_T^\mu > 18$ GeV ($p_T^\mu > 10$ GeV) and at least two jets with $p_T^{\text{jet}} > 20$ GeV, for the 7 TeV (10 TeV) analysis;
- **SM cuts:**
 - effective mass $M_{\text{eff}} > 1200$ GeV;
 - missing transverse energy $E_T^{\text{miss}} > 40$ GeV;
 - transverse sphericity $S_T > 0.2$;
- **Combinatorial cuts:**
 - $m_{jj} \subset \{M_W \pm 5 \text{ GeV}\}$;
 - all muons with $p_T > 25$ GeV are selected;
 - separation angle between the muon and the W -candidate $\Delta R_{\mu W} < 1.5$;
 - separation angle between jets forming a W -candidate $\Delta R_{jj} < 2.5$;

The $M_{\mu jj}$ for every SM background process and for the SUSY signal is shown in Figure 4.25 (left for the 7 TeV case, right for the 10 TeV sample). Most of the SM background has been eliminated after the application of cuts, only QCD and to a lesser extent $t\bar{t}$ and W +jets remain visible. The red line represents their normalised sum. The dashed line, *bRPV inclusive*, corresponds to all possible combinations of muons and W -candidates in the SUSY sample, fulfilling all the requirements; the grey area, *bRPV background*, corresponds to the bulk of the SUSY combinatorial background: they are $\tilde{\chi}_1^0$ -candidates belonging to events where none of the truth $\tilde{\chi}_1^0$ decay in the signal decay mode.

The LSP mass peak standing out over the SM background is clearly seen in both figures and the fit of the peak to a gaussian in the mass window 90 to 140 GeV gives a value for the $\tilde{\chi}_1^0$ mass of (114.8 ± 1.1) GeV for the 7 TeV case and (115.9 ± 0.8) GeV for the 10 TeV case. Only the statistical error has been considered on this fit and the small discrepancy between this value and the neutralino mass (109 GeV in the 7 TeV sample; 118 GeV in the 10 TeV sample) could be due to systematic errors that will be commented in the next subsection. Looking at the signal decay peak, i.e. the difference between *bRPV inclusive* and *bRPV background*, the value of the fit in the same range would be (112.9 ± 0.9) GeV for the 7 TeV case and (118.3 ± 1.3) GeV for the 10 TeV case, much closer to their truth value.

The SM model background may be estimated and subtracted from the measured distribution by a combination of dedicated measurements and MC techniques. Since the SM background is lepton flavour-symmetric, another possibility is to subtract the measured invariant mass distribution of an electron and two jets, after correcting for the differences in efficiency, acceptance, etc. between muons and electrons. In general, for the first ATLAS runs, data-driven background estimation methods will be necessarily developed and applied. Although many techniques have been developed for *RPC SUSY* —mainly for QCD and top-pairs—, the *RPV* topologies are distinct from the *RPC* ones and dedicated studies have to be performed. In particular, the signal and control regions have to be redefined and the SUSY contamination in the

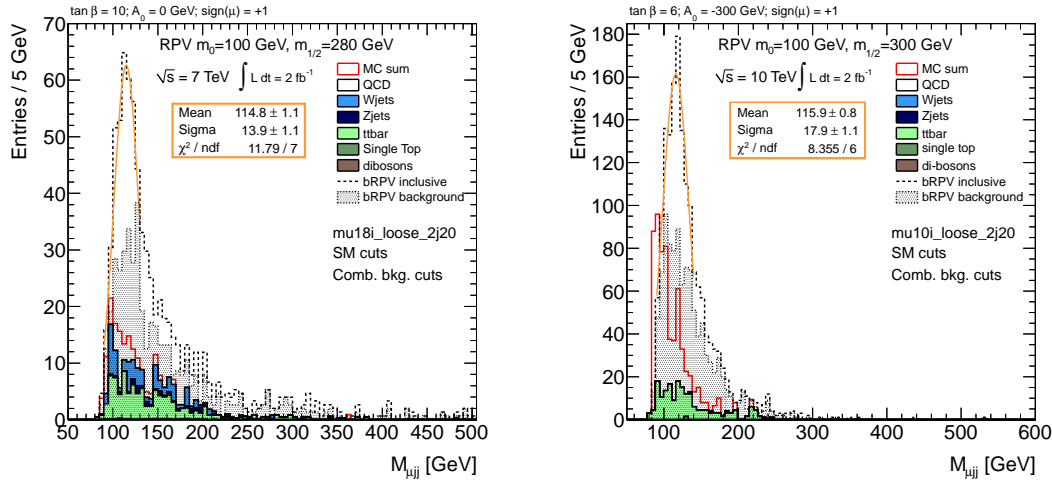


Figure 4.25: Invariant mass distributions $M_{\mu_{ij}}$ for the SUSY sample and all SM backgrounds at 7 TeV (left) and at 10 TeV (right) after applying *SM cuts* and the final set of *Combinatorial cuts*, normalised to an integrated luminosity of 2 fb^{-1} . *MC sum* refers to the normalised sum of all SM background sources.

control sample has to be studied. Some of these methods are based on the independence of E_T^{miss} to a specific variable; in RPV another variable should be used instead. The trigger efficiency can be measured, on the other hand, by applying the tag&probe method for $Z \rightarrow \mu\mu$, comparing with Monte Carlo data and derive differential trigger efficiency dependencies.

When inspecting the number of SUSY inclusive signal and SM background events surviving the *SM cuts* applied, a significance of $Z_n = 1.28$ ($Z_n = 0.60$) is obtained for the 7 TeV sample (10 TeV sample) a luminosity of 2 fb^{-1} , with Z_n defined as in Ref. [9]. In this definition of Z_n an uncertainty of 50% is assumed for the background from QCD multijet events and 20% for the background from $t\bar{t}$, $W + \text{jets}$, $Z + \text{jets}$ and W/Z pairs. Nevertheless, looking at the number of neutralino-candidates after the *Combinatorial cuts* are applied (Figure 4.25), we obtain a significance of $Z_n = 7.22$ ($Z_n = 3.55$) and even better significance of $Z_n = 7.74$ ($Z_n = 5.37$) in the mass window 90 to 140 GeV for a luminosity of 2 fb^{-1} .

Taking into account the systematic uncertainties described in the next section, the determination of the LSP mass is expected to be less precise than quoted above. An integrated luminosity of around 200 pb^{-1} would be enough to obtain a significance of $Z_n = 5$ in the invariant mass distribution.

4.8 Systematic uncertainties

Major sources of systematic errors for this analysis can become the following uncertainties:

Jet absolute energy scale. This should be the most important uncertainty affecting various aspects of the analysis: from the jet selection, the M_{eff} and E_T^{miss} values to the measured value of the neutralino mass. The error on the momentum of the reconstructed jets is expected to be of the order of 10%.

SUSY combinatorics. The objective of this study is to probe the LSP decay channel $\tilde{\chi}_1^0 \rightarrow \mu W \rightarrow$

$\mu q' \bar{q}$ through the possible observation of an excess of events in the μjj invariant mass. Nonetheless, the underlying SUSY model and parameters affect the shape of the distribution, introducing an uncertainty difficult to quantify in terms of error in the measured $m_{\tilde{\chi}_1^0}$. This could be tackled by studying the shape of the $M_{\mu jj}$ distribution on events generated in a grid of (a large number of) SUSY-model points. Alternatively, template morphing [104] could be applied on a limited number of SUSY points, with some of the SUSY-model parameters, e.g. m_0 and $m_{1/2}$ for mSUGRA, as morph parameters.

SM background. The background due to SM processes introduces another uncertainty whatever is its estimation based on: Monte Carlo, real data or a combination of both. The influence of this uncertainty on the measured excess of events has already been incorporated in the significance calculation, as inferred from data-driven background estimation methods [9]. Moreover, this uncertainty affects the shape of the $M_{\mu jj}$ distribution, thus having an impact on the neutralino mass measurement.

Fit range. The choice of the fit interval is expected to affect the measured value of the LSP mass.

4.9 Conclusion

A study has been performed, analysing the possibility to observe bilinear R -parity violation in supersymmetry in ATLAS for three different energy configurations of the LHC, in events containing at least one muon and two jets. All possible sources of SM background have been properly taken into account, together with the combinatorial background arising from the high lepton and jet multiplicity environment characterising SUSY events.

After the event selection, when inspecting the number of SUSY inclusive signal and SM background events surviving the SM cuts applied, a signal of $S_{\text{SUSY}}/\sqrt{B} > 30$ can be seen for both the 7 TeV and 10 TeV samples, giving rise to a significance of $Z_n = 1.28$ ($Z_n = 0.60$) for the 7 TeV sample (10 TeV sample) with a luminosity of 2 fb^{-1} (Z_n defined as in Ref. [9]). In this definition of Z_n an uncertainty of 50% is assumed for the background from QCD multijet events and 20% for the background from $t\bar{t}$, W + jets, Z + jets and W/Z pairs. In the 14 TeV sample and for the same selection $S_{\text{SUSY}}/\sqrt{B} > 95$ is seen, although not all sources of background were included in this case, so it should be understood only as an approximation.

Looking at the invariant mass distribution of one muon and two jets and after applying an extra selection in the object combination resembling that expected for the neutralino decay to a muon and a hadronic W , a signal of $S_{\text{SUSY}}/\sqrt{B} > 30$ ($S_{\text{SUSY}}/\sqrt{B} > 50$) is observed for the 7 TeV sample (10 TeV sample). From this distribution it is possible to reconstruct the neutralino mass, obtaining a mass peak on $114.8 \pm 1.1 \text{ GeV}$ ($115.9 \pm 0.8 \text{ GeV}$), where the theoretical value for the $\tilde{\chi}_1^0$ mass is 109.8 GeV (118 GeV), only statistical errors taken into account. This distribution leads to a significance of $Z_n = 7.22$ ($Z_n = 3.55$) and even better significance of $Z_n = 7.74$ ($Z_n = 5.37$) in the mass window 90 to 140 GeV for a luminosity of 2 fb^{-1} .

This feasibility study was performed assuming a bRPV-mSUGRA point (SU3) with rather low m_0 and $m_{1/2}$ parameter values (100 GeV and 300 GeV, respectively) characterised by a high SUSY cross section ($\sigma \simeq 5 \text{ pb}$) and a low neutralino mass ($M_{\tilde{\chi}_1^0} \simeq 120 \text{ GeV}$). In higher values of $m_{1/2}$, although the production cross section is lower, the LSP mass peak should be more prominent over the background, migrating to higher values of $M_{\mu jj}$. The branching ratio $BR(\tilde{\chi}_1^0 \rightarrow \mu W)$, on the other hand, as evident from Figure 2 of Ref. [88], is expected to increase with m_0 from $\sim 10\%$ in SU3 up to $\gtrsim 25\%$ for $m_0 \gtrsim 500 \text{ GeV}$, depending also on the other mSUGRA parameters, in particular $m_{1/2}$, and the atmospheric neutrino mixing angle. In order to generalise

the results, a systematic study involving the production of fast simulation (ATLFAST II) samples in a grid of mSUGRA parameters may be performed in the future to determine the exclusion and discovery reach for this model. Moreover, the assumed R -parity violating couplings may be embedded in other supersymmetric frameworks, distinct from mSUGRA, such as the phenomenological MSSM (pMSSM [105]) or the minimal Anomaly Mediated Supersymmetry Breaking (mAMSB) [106].

Even though this analysis is performed and the selection criteria are chosen and optimised for a specific RPV model where the breaking occurs through bilinear terms, it may be generalised to investigate trilinear RPV , such as when $\lambda'_{2jk} \neq 0$. By relaxing, for instance, the W -mass constraint on the two jets, the decay $\tilde{\chi}_1^0 \rightarrow \mu\bar{q}q'$ may be probed.

RPV SUSY signals may be characterised, in certain models, by a fairly high missing energy though lower than the corresponding RPC case. This means that if evidence of SUSY should be observed in a similar conventional E_T^{miss} -based inclusive search at the LHC, the case of R -parity violation should not be excluded.

The significance can be increased if the delayed decay of the neutralino, having a decay length of $\sim 300 \mu\text{m}$, is exploited. This is a generic feature not only of the specific scenario (b RPV) we studied, where the LSP decay length ranges from 0.1 to 100 mm [88, 102], but of other trilinear RPV scenarios with $\lambda' \sim 10^{-3}$ [107]. Such an analysis, however, addresses the issue of distinguishing the LSP from B -mesons —since they have comparable lifetimes— which requires dedicated studies.

Chapter 5

Searches for bRPV SUSY with 2011 ATLAS data

The ATLAS experiment has a complete program for the search of Supersymmetry in a wide model spectrum, already cited in Section 1.3. To be able to cope with such amount of possible scenarios, searches on different final states common to several models are developed. In R -parity conserving models, strongly interacting supersymmetric particles decay directly or in cascades into jets, leptons, and the neutral lightest supersymmetric particle (LSP), which escapes detection and leads to missing transverse energy, E_T^{miss} . If R -parity is violated a very similar decay process takes place, at the end of which the LSP decays through several modes involving muons, neutrinos and other SM particles. Thus, the final state in both cases is characterised by jets, E_T^{miss} and the eventual presence of leptons.

After considering all the analyses being carried out by the ATLAS SUSY Working Group, it was decided that a bRPV search could very much fit into an analysis requiring the final state to contain exactly one isolated muon, at least three or four high- p_T jets and certain amount of E_T^{miss} , the so-called “one-lepton analysis in the muon channel”, from now on, “one-muon analysis”. The existence of muons in the bRPV events is enhanced by the fact that an appreciable percentage of LSP decays involve muons (see Section 4.3.1). This point makes bRPV to be efficient for the selection of events containing muons.

There are many features bRPV-mSUGRA model shares with RPC-mSUGRA models that makes the one-muon analysis suitable also for bRPV:

- They both are developed assuming the mSUGRA scenario.
- The analysis is based on single muon triggers and events are required to contain certain number of high p_T jets.
- The same object definitions, good-run lists (GRLs, to be defined in Section 5.2.1) and pile-up treatment can be applied to them both.
- Events are characterised by long cascade decays. Actually, the bulk of bRPV events develop a cascade which is the same as in RPC with the only difference of the LSPs decay at the end of it.
- Both models contain a considerable distribution of E_T^{miss} . In the RPC case it is due to the (two) neutral, weak interacting LSP at the end of the cascade. In the bRPV case, due to the high percentage of LSP decays containing neutrinos.

Although the optimal analysis to search for bRPV would be the one presented in the previous chapter, it has been proven that the acceptance of bRPV within the one-muon analysis (about 10 times lower than that of RPC) can lead to an exclusion limit setting, as it will be shown in the following.

This chapter presents the first search for signals involving jets and missing transverse momentum and exactly one isolated muon in the bilinear R -parity violating (bRPV) scenario, using 1.04 fb^{-1} of ATLAS 2011 data at 7 TeV. It should be noted that the selection is sensitive not only to R -parity conserving and bRPV-SUSY particle production, but also to any model in which one or more strongly-interacting particles decay semi-invisibly producing leptons and jets.

It is also worth to mention that this analysis is carried out for the very first time in the bRPV case and for the first time at hadron colliders for the RPC case (Tevatron experiments investigated only zero lepton and three leptons final states [108–110]). In the RPC case, two previous very similar analyses were performed with luminosities of 35 pb^{-1} [111] and 165 pb^{-1} [112].

The results of this work have been published in Physical Review D [113] and documented in detail in an ATLAS Internal note [114]. The interpretation in terms of RPC can be also found in these papers, as an update of the ones for 35 pb^{-1} and 165 pb^{-1} mentioned above. Searches with zero, two and more leptons in the final state are described elsewhere for the RPC case [115, 116], as well as similar one lepton analysis with b -jets also for the RPC case [117] and other analyses involving alternative RPV models [36–38].

5.1 Analysis overview

This section briefly introduces the main concepts of the one-lepton SUSY analysis involving two channels:

- Exactly 1 isolated muon + ≥ 3 jets + missing transverse energy + 0 electrons
- Exactly 1 isolated muon + ≥ 4 jets + missing transverse energy + 0 electrons

For every channel, a so-called “loose” and “tight” selection is applied. As the names suggest, the “loose” selection only applies moderate requirements on discriminating kinematic variables, resulting in larger signal efficiencies but also higher background rates, while the “tight” selection reduces the backgrounds to a few events in every channel.

This analysis is a counting experiment where the signal-over-background ratio is enhanced by using a combination of three discriminating variables in the beam transverse plane (after lepton and jet kinematic selection, defined in Section 5.3):

- the missing transverse energy (E_T^{miss}), vectorial sum in the transverse plane of lepton and jets energy and other calorimeter activity,
- the transverse mass, $m_T = \sqrt{2 \cdot p_T^\ell \cdot E_T^{\text{miss}} \cdot (1 - \cos(\Delta\phi[\ell, E_T^{\text{miss}}]))}$, where p_T^ℓ is the p_T of the selected lepton,
- the transverse scalar sum, $H_T = p_T^\ell + \sum_{i=1}^{3(4)} p_T^{\text{jet}_i}$, where $p_T^{\text{jet}_i}$ are the p_T of the 3 (4) leading jets.

The sum of the transverse scalar sum H_T and the missing transverse energy E_T^{miss} is called “effective mass”, M_{eff} :

$$M_{\text{eff}} = H_T + E_T^{\text{miss}} = p_T^\ell + \sum_{i=1}^{3(4)} p_T^{\text{jet}_i} + E_T^{\text{miss}} \quad (5.1)$$

The analysis strategy consists of defining, in terms of the simple discriminating kinematic variables presented above, a number of Signal Regions (SRs, Section 5.5.1), where the SUSY signal clearly dominates over the SM background and determining the probability of the real data lying in those SRs to be generated from SUSY events. To reduce systematic uncertainties on background estimation in this regions, enriched background control regions are also defined (CRs, Section 5.1.2). Extrapolation factors from the control regions to the signal regions are furthermore checked using validation regions in between the control and signal regions.

5.1.1 Signal regions

This analysis is designed to be applied not only over a bRPV model signal grid, but also over an RPC model grid and over simplified models grids. To cover such a broad range of signals, the analysis includes searches in four different signal regions, two of them involving 3-jet inclusive selections and the other two involving 4-jet inclusive selections. For every kind of background, dedicated control regions have been defined related to these signal regions.

The definition of the signal regions can be found in Section 5.5.1.

5.1.2 Control regions

The main background processes in the SRs are top quark production (mostly semi- and fully-leptonic $t\bar{t}$ pairs, but also single top to a lesser extent) and the production of W -bosons in association with jets (where the W -boson decays leptonically, $W \rightarrow \ell\nu$). In addition, an estimate on the QCD jet production is required in the SR, since large uncertainties affect both the theory and the lepton fake rates.

To perform this background determination, different control regions (CRs) orthogonal to the SRs and with their same object requirements are defined. The CRs are defined as follows:

- **W +jets control region (WR)** probes a part of the (E_T^{miss}, m_T) plane enriched in W +jets in an intermediate missing transverse energy range ($30 < E_T^{\text{miss}} < 80$ GeV), an intermediate transverse mass range ($40 < m_T < 80$ GeV) and the requirement that no jet among the three (four) hardest jets is tagged as a b -jet.
- **Top control region (TR)** uses the same box (E_T^{miss}, m_T) as the WR, but requires at least one b -tagged jet among the three (four) hardest jets in order to separate the top production from W region.
- **QCD control region (QR)** is defined by low missing transverse energy ($E_T^{\text{miss}} < 30$ GeV) and is used to measure lepton fake rates that are later used to get a QCD estimation using the matrix method, outlined in Section 5.5.2.

A visual representation of the CRs definition in the (E_T^{miss}, m_T) plane is shown in Figure 5.1. This definitions permit a large number of events in the CRs. Thus, it is possible to apply a cut on the effective mass similar to the ones that will be applied in the signal regions. This brings the selection in the control regions even closer to the signal regions, so that the uncertainties on the extrapolation factors can be reduced. Although different M_{eff} cuts are applied in the loose and tight SRs definitions (see Table 5.5), only one cut on M_{eff} is applied for each the 3-jet and the 4-jet control regions to minimise the number of CRs. This is always the lowest value of the two M_{eff} requirements, say $M_{\text{eff}} > 500$ GeV for the 3-jet selection and $M_{\text{eff}} > 300$ GeV for the 4-jet control region. A possible enrichment of the signal in the control regions caused by this additional M_{eff} selection is studied in Ref. [114]. It is found that the signal contamination is well below 1% and thus negligible.

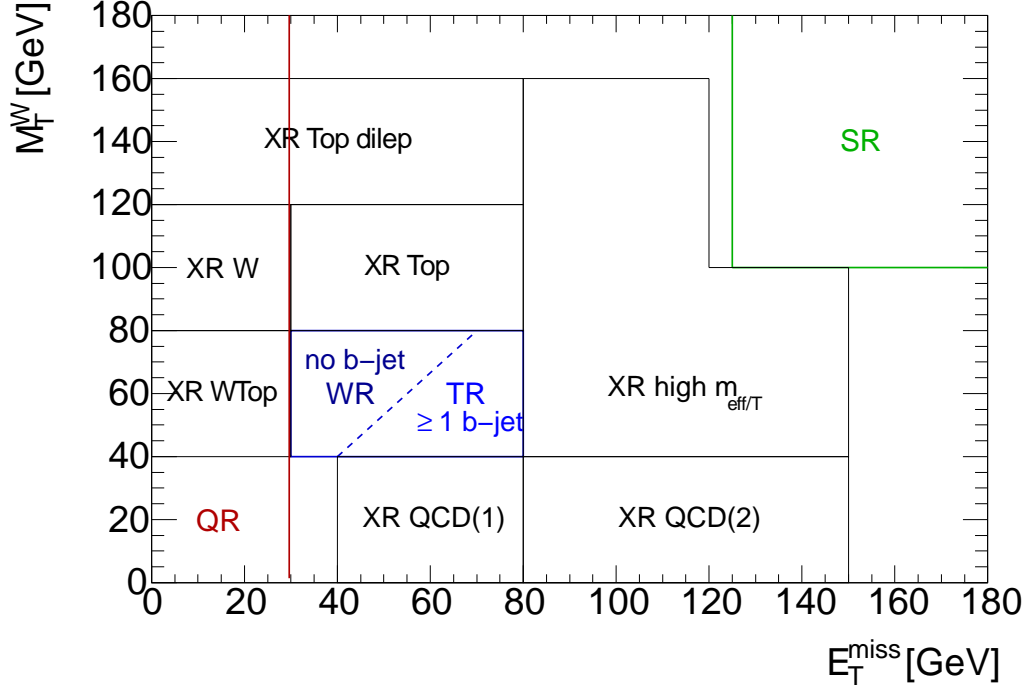


Figure 5.1: Position of the signal region SR3JL (3-jet loose, defined in Section 5.5.1) and the main control regions (CR) in the (E_T^{miss}, m_T) plane. The top enriched control region TR and the W +jets enriched control region WR are separated by the existence of a b -tagged jet candidate among the three (four) leading jets. The XR regions correspond to extra validation regions. It should be noted that the QCD region (QR) is only used to determine the lepton fake rate.

5.1.3 Background determination in the signal regions

A normalisation of the backgrounds to the data can be performed in the control regions. Assuming that the shape of the distributions for the background samples is described correctly by the Monte Carlo simulation, one can define transfer factors from control region iR ($i = W, T$) to the signal region $C_{iR \rightarrow SR}^j$ for the background type j ($j = W$ +jets, top):

$$C_{iR \rightarrow SR}^j = \frac{N(\text{MC}_j, \text{SR})}{N(\text{MC}_j, iR)}, \quad (5.2)$$

where $N(\text{MC}_j, \text{SR})$ is the estimated number of events in the signal region for process j from the Monte Carlo. Thus the predicted background contribution in the signal region is given by

$$N_{\text{MC pred. } j}^{\text{SR}} = N_{\text{data}}^{iR} \times \frac{N(\text{MC}_j, \text{SR})}{N(\text{MC}_j, iR)} = N_{\text{data}}^{iR} \times C_{iR \rightarrow SR}^j. \quad (5.3)$$

However, the cross contamination of the various background processes in the CRs is non negligible. As a consequence, the determination of the backgrounds needs to be performed simultaneously, performing a likelihood fit of the different CRs. The QCD background is extracted using a loose and tight selection and applying the matrix method (see Section 5.5.2). It should be noted that no absolute normalisation from simulation is used in this approach.

The total uncertainty on the number of background events in the SR is a combination of the statistical uncertainties in the CRs and the systematic uncertainties of the extrapolation (both theoretical and experimental errors are considered). As the SR and all CRs are mutually exclusive, the events are statistically independent and Poisson statistics is used. On the other hand, the systematic uncertainties are modelled using nuisance parameters where the constraints are taken to be Gaussian. Correlation within several uncertainties is properly taken into account [118].

As already mentioned, in the extrapolation from CRs to SR, the background variable shapes are assumed to be correctly predicted. To validate this assumption, extra validation regions (XR) are defined in the (E_T^{miss}, m_T) plane (Figure 5.1). They are used in two ways:

1. The combined background is obtained without signal contamination and without taking into account the SRs. It is then extrapolated to the XRs and compared to the corresponding observed number of events.
2. The background is determined using all three CRs and the additional XRs (again without signal contamination and without taking into account the SR). This is an over-constrained system which is used to extract a goodness-of-fit probability (using toys to gauge the probability).

5.1.4 Results interpretation

The total number of background events in the SR, as obtained from the simultaneous determination in the CRs and properly extrapolated to the SR, can be compared to the observed number of events. This is the so-called background-only hypothesis test, which would be used to claim a discovery in case of a significant excess. In order to exclude a given SUSY model, the observed number of events in the SR is tested against the combined background and signal expectation. Uncertainties on the number of signal events are theoretical and experimental (e.g. luminosity, trigger, jet energy scale, etc.). An exclusion is claimed if the number of observed events is significantly lower than the signal + background expected number of events. Note that global uncertainties as for instance on the luminosity enter only for the signal, because the background is normalised using the CRs. Some signal models can contaminate the CRs at the few percent level. In order to be conservative, this contamination is taken into account when setting exclusion limits. Both the discovery and exclusion significances are calculated using pseudo-experiments (toys). A full description of this approach together with a validation against toys and other statistical methods can be found in Ref. [118].

5.1.5 Motivation of analysis setup

The motivation for the described analysis setup, i.e. a simultaneous determination of backgrounds and signal using CRs and SRs, is as follows:

- The background estimation largely relies on data. Simulation is used only in terms of shapes (in the relevant variables) which are used for the extrapolation from the CRs into the SRs.
- Large systematic uncertainties related to global background-level scales such as the jet energy scale as well as the cross sections completely or partially cancel in the final result.
- Statistical uncertainties in the CRs and SRs are correctly accounted for using Poisson statistics.

- Most backgrounds enter all CRs. This contamination as well as possible signal in the CRs is taken into account.
- Correlated systematic uncertainties (between the SRs and CRs, or various background processes), are properly and coherently treated through the use of common nuisance parameters.

As already mentioned, the extrapolation from the CRs into the SRs relies on the shapes as predicted by simulation. It is thus subject to theoretical uncertainties. The use of the simulated shapes is motivated by:

- The main processes $t\bar{t}$ and W +jets benefit from several years of theory developments to predict both higher order QCD corrections [119–121] and high multiplicity final states [122, 123].
- The MC generators used in the present study have been heavily used and constrained in past experiments. Using the full ATLAS 2010 data set, data distributions are in excellent agreement with simulation in all relevant variables. This very good agreement has also been found in the first ATLAS W +jets [124] and top results [125] based on few pb^{-1} of ATLAS 2010 data.

5.2 Samples: data, bRPV and backgrounds

This section briefly describes the data sets and Monte Carlo samples used in this analysis.

5.2.1 Data

All data used in this analysis were collected with the ATLAS detector in pp collisions at a centre-of-mass energy of 7 TeV. Data taken between March 22, 2011 and June 28, 2011 (the so-called periods B2 - H4), are used for analysis, yielding a total integrated luminosity of $\int Ldt = (1238 \pm 46) \text{pb}^{-1}$, corresponding to the requirement of ATLAS being ready for data taking.

Since electrons, muons, jets and E_T^{miss} are required in the analysis, it is mandatory that basically all subsystem of the ATLAS detector are in good condition so that object identification as well as energy and momentum computations do not deviate significantly from their expected behaviour. This is reflected in the SUSY specific good-run list (GRL), which ensures good data quality in all relevant sub-systems. This GRL is taken from the official Data Preparation Group [126]. Applying the good run list results in a loss of approximately 16% of data, leaving an integrated luminosity of $\int Ldt = (1035 \pm 38) \text{pb}^{-1}$ for analysis. The uncertainty on the luminosity is 3.7% [127].

5.2.2 MC background

All Monte Carlo samples used in this analysis have been produced using the standard full Geant-4 ATLAS simulation tool [128]. The average number of interactions per bunch crossing corresponds to $\langle \mu \rangle = 8$, defined in Section 5.3.5 and MC samples are reweighted to the pile-up in data. The cross sections for W +jets and $t\bar{t}$ production at $\sqrt{s} = 7$ TeV are now known at (approximate) NNLO and read $31.4 \pm 1.5 \text{nb}$ [?, ?] for $W \rightarrow \ell\nu$ and $165_{-16}^{+11} \text{pb}$ [125] for $t\bar{t}$. Other backgrounds are also considered: $Z \rightarrow \ell\ell$ with a NNLO cross section of $1.07 \pm 0.05 \text{nb}$ [?] and WW , WZ and ZZ with a NLO cross section of $44.9 \pm 2.2 \text{pb}$, $18.0 \pm 1.3 \text{pb}$ and $6.0 \pm 0.3 \text{pb}$ [?]. All these numbers are used for Monte Carlo normalisation. The Alpgen [122] generator is used for

W, Z +jets and top simulation. Diboson samples are generated using Herwig [?]. Cross sections for every background subsample considered in this analysis are contained in Tables A.4–A.6 of Appendix A. The QCD background is determined completely from data.

A CMSSM benchmark point ($m_0 = 500$ GeV, $m_{1/2} = 330$ GeV, $A_0 = 0$ GeV, $\tan\beta = 10$, $\mu > 0$), at the edge of the exclusion reachable with this analysis, is used throughout this note to illustrate a typical *RPV* SUSY signal.

5.2.3 bRPV grid

In order to extend the search for prompt *RPV* in the bilinear model, a set of mSUGRA input parameters is defined. The mSUGRA model is defined by five parameters: the common boson mass at the Grand Unification (GUT) scale m_0 , the common fermion mass at the GUT scale $m_{1/2}$, the ratio of the Higgs vacuum expectation values $\tan\beta$, the common GUT scale trilinear coupling A_0 and the sign of the Higgs potential parameter μ . For this signal grid, 88 points were generated, spanning a range in $m_0 \in (100, 800)$ GeV and in $m_{1/2} \in (200, 600)$ GeV with equally spaced signal points, while keeping the other parameters fixed at $\tan\beta = 10$, $A_0 = 0$ GeV and $\text{sgn}(\mu) = +1$, as seen in Figure 5.2.

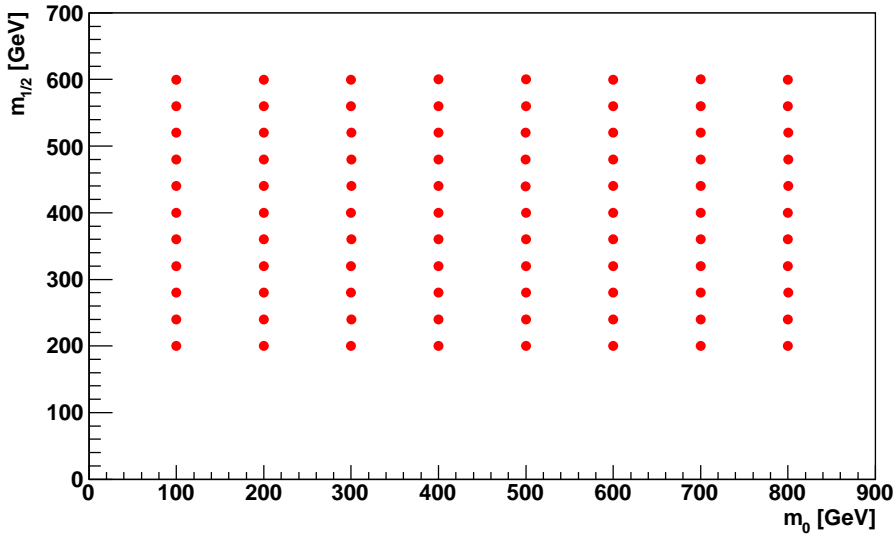


Figure 5.2: Position of the 88 simulated bRPV points in the $(m_0, m_{1/2})$ plane. Fixed values $A_0 = 0$ GeV, $\text{sgn}(\mu) = +1$ and $\tan\beta = 10$ are selected.

The definition of these bRPV-mSUGRA grid points has been motivated by the analysis in Ref. [129]. Using the SPheno version 3.1.0 [94], masses, branching ratios and decay widths for the signal particle spectrum were calculated and given in the SLHA format [95,96]. This format is used as input for the PYTHIA event generator [93] which in turn is used as input for the full detector simulation. For each point, 10000 supersymmetric events have been generated, allowing for all possible production subprocesses and decays.

As already mentioned in Section 4.3.1, a fit of the bilinear *RPV* parameters to neutrino oscillation data leads to a set of bRPV parameters consistent with all experimental constraints from rare processes.

In the bRPV model, the lightest neutralino-LSP is not stable anymore and its decay length varies as a function of the different mSUGRA parameters. An overview of the decay lengths in the $\tilde{\chi}_1^0$ rest frame can be seen in Figure 3.13 for the signal grid region. The branching ratios for the different LSP decay modes are also dependent on the mSUGRA parameters. Branching ratios for the signal decay mode $\tilde{\chi}_1^0 \rightarrow \mu^\pm W^\mp$ are displayed in Figure 3.14 thus providing a phenomenological overview of the signal parameter space under study.

Note that the $\tilde{\chi}_1^0$ decay length (without boost) covers a range from tens of micrometers to several centimetres at low $m_{1/2}$ values around $m_{1/2} \simeq 200$ GeV. See also Ref. [88] for a more general discussion of possible LSP decay length ranges in the bilinear RPV model.

A specific muon selection is performed during the analysis in order to eliminate the cosmic muon background. This selection (specified in Section 5.5.5) eliminates a large fraction of the muons coming from long decaying $\tilde{\chi}_1^0$, thus decreasing sensitivity in the low $m_{1/2}$ region. Hence, this analysis is not focusing on points leading to significant decay lengths. Implications from searches for displaced vertices (see e.g. Ref. [37]) and search results based on pure leptonic decay modes of the LSP with higher sensitivity in this region are studied elsewhere [36].

It should be noted that assuming only trilinear RPV coupling of the type λ'_{2ij} with $i, j = 1, \dots, 3$ would also allow LSP decays of the type $\tilde{\chi}_1^0 \rightarrow \mu qq'$. These decays would however not involve an intermediate on-shell W which can serve as a measure of discriminating the different RPV models in the future. Moreover, trilinear RPV based LSP decays would not obey the characteristic ratios of branching fractions as for example the ones displayed in Section 4.3.1. Here we do not focus on one specific LSP decay channel.

5.3 Definition of objects

In this section, all objects used in the analysis are introduced: jets, electrons and muons as well as the transverse missing energy. In the three first cases, preselection cuts are applied before performing the overlap removal between objects. These objects are tagged as baseline objects and, in the case of electrons and muons, will be used during the event selection. After overlap removal, the object definitions are tightened to form signal objects, used in the event selection as well (see Section 5.5).

5.3.1 Jets and b -jets

Jets are reconstructed using the anti-kt jet clustering algorithm (defined in Section 2.3.6.5) with distance parameter $R = 0.4$. The energy is measured at electromagnetic scale (EM-scale) on which Monte-Carlo based jet energy scale corrections (JES) are applied as a function of p_T and η . Only jets with $p_T > 25$ GeV and within $|\eta| < 2.8$ are considered in this analysis. If a jet candidate overlaps with an electron, i.e. if $\Delta R(\text{jet}, e) < 0.2$, the object is classified as an electron.

Events can occasionally contain very localised high-energy calorimeter deposits not originating from proton-proton collisions but from the calorimeter malfunction. This subsequently gives rise to the reconstruction of a jet which actually is not. Dedicated cuts have been optimised to tag these “bad” jets [130]. Given the very low frequency of bad jets appearance, every event containing at least one bad jet with $p_T > 20$ GeV is removed from the analysis, eliminating all the fake jets but less than one per mill signal jets in a typical SUSY signal as well as in data. The jet selection criteria are summarised in Table 5.1.

To define the $t\bar{t}$ control region, at least one jet must be identified as a b -jet (b -tagged). On the contrary, in the W +jets control region, none of the selected jets must be tagged as a b -jet.

Table 5.1: Summary of the jet and b -jet selection criteria. The signal selection requirements are applied on top of the preselection. The b -tagger definition is given in the text.

Cut Jet Type	Value/description	
	no b -jet	b -jet
	Baseline jet	
Algorithm	AntiKt4Topo	
Acceptance	$p_T > 20 \text{ GeV}, \eta < 2.8$	
Overlap	$\Delta R(\text{jet}, e) > 0.2$	
Quality	reject events with loose bad jets	
Other	–	$\Delta R(\text{jet}, \text{track}) < 0.4$
	Signal jet	
Acceptance	$p_T > 25 \text{ GeV}, \eta < 2.8$	$p_T > 25 \text{ GeV}, \eta < 2.5$
Other	–	JetFitterCombNN > 2.0

The b -tagging is performed using the JetFitterCombNN tagger, described in Section 2.3.6.6, as suggested by the Heavy Flavour Tagging group. The operating point for 60% efficiency is used, corresponding to a cut on the b tag weight of $w > 2.0$. The cut provides a rejection factor of ≈ 370 for light jets and ≈ 8 for charm jets. τ -leptons are suppressed by a factor of 30 [130].

The b -tagging efficiencies and mistag fractions for the JetFitterCombNN algorithms have been measured in data. Since the performance in the simulation is slightly different, scale factors (SF) dependent on the p_T of the jets, are provided by the Heavy Flavour Working Group. The b -jet selection criteria are also summarised in Table 5.1.

5.3.2 Electrons

The electron candidate must fulfil the standard electron reconstruction and identification algorithm (AuthorElectron) [131, 132] as described in Section 2.3.6.2, with medium quality. Its transverse momentum must exceed 20 GeV and the electron must be in the region $|\eta_{\text{clust}}| < 2.47$ (for the η -position, unlike for the p_T value, the information of the calorimeter cluster is used). Electron candidates are removed if they overlap with a jet, i.e. if $0.2 < \Delta R(e, \text{jet}) < 0.4$.

Only baseline electrons are used in this analysis for the event selection. However, signal electrons are also used in the matrix method defined for the QCD background estimation (see Section 5.5.2). All electron selection criteria are summarised in Table 5.2.

On account of the electron identification efficiencies measurement on data using W and Z “Tag & Probe” method [133], scale factors considering the ratio measured between data and Monte Carlo are further applied to the Monte Carlo:

$$f_{\text{scale}} = \frac{\mathcal{E}_{\text{data}}}{\mathcal{E}_{\text{MC}}}. \quad (5.4)$$

These factors depend on the electron η and p_T and are provided by the egamma combined performance group [133]. Averaged over p_T the scale factors are close to 1 with variations of $\pm 5\%$.

Table 5.2: Summary of the electron selection criteria. The baseline selection requirements are applied on top of the preselection.

Cut	Value/description
Algorithm	Baseline Electron AuthorElectron
Acceptance	$p_T > 20 \text{ GeV}, \eta_{\text{clust}} < 2.47$
Quality	Medium
Overlap	$\Delta R(e, \text{jet}) < 0.2$ or $\Delta R(e, \text{jet}) > 0.4$
Quality	Signal Electron Tight
Track	with match
Acceptance	$p_T > 25 \text{ GeV}$
Isolation	$\text{ptcone20}/p_T < 0.10$

5.3.3 Muons

Two types of muons are used: “combined muons” and “segment tagged muons”, as defined in Section 2.3.6.3. The latter are necessary to recover efficiency losses in particular detector regions with poorer MS coverage. The track quality cuts are designed to reject both cosmic muons and decays in flight of π and K mesons, while the isolation requirement reduces these and the contribution from heavy flavour (b, c) decays. Muon candidates are also removed if they overlap with a jet: $\Delta R(\mu, \text{jet}) < 0.4$. All muon selection criteria are summarised in Table 5.3.

Table 5.3: Cuts defining a good-quality reconstructed muon. In this table, n_{TRT} is the total number of TRT hits, including outliers (hits not associated with any track).

Cut	Value/description
Algorithm	Baseline muon STACO, combined or segment-tagged muon
Acceptance	$p_T > 10 \text{ GeV}, \eta < 2.4$
Quality	Loose
Inner detector	≥ 1 pixel hit, ≥ 6 SCT hits, pixel holes + SCT holes < 2 ≥ 1 b-layer hit when it can be expected
Track quality	If $ \eta < 1.9$: $n_{\text{TRT}} \geq 6$ and $n_{\text{TRT}}^{\text{outliers}} < 0.9n_{\text{TRT}}$ If $ \eta \geq 1.9$ and $n_{\text{TRT}} \geq 6$: $n_{\text{TRT}}^{\text{outliers}} < 0.9n_{\text{TRT}}$
Overlap	$\Delta R(\mu, \text{jet}) > 0.4$
Acceptance	Signal muon $p_T > 20 \text{ GeV}$
Track isolation (excluding muon track)	$\sum p_T \Delta R$ cone of $0.2 < 1.8 \text{ GeV}$

Efficiency correction factors are applied to the muons as well, similar to the electron case. These scale factors are provided by the muon combined performance group [103]. In general the Monte Carlo simulation describes the data very well and the scale factors only differ from 1 by ± 1 to 2%.

5.3.4 Missing transverse energy (E_T^{miss})

The missing transverse energy used in this analysis ($E_{T,\text{RefFinal}}^{\text{miss}}$ as described in Section 2.3.6.7) is the vectorial sum of reconstructed objects in the event, namely

1. the jets calibrated at the EM+JES scale (Section 5.3.1) with $p_T > 20$ GeV
2. the signal muon*
3. the topological calorimeter clusters not belonging to any defined objects ($E_{T,\text{RefOut}}$ term in Section 2.3.6.7) calibrated at the EM scale

* no further lepton- p_T are added since the main requirement is the existence of exactly one baseline muon, which in addition needs to be signal muon, and no baseline electrons in the event.

5.3.5 Pile-up treatment

Multiple interactions per LHC bunch crossing (*pile-up*) are given in data. The pile-up conditions change as a function of the instantaneous luminosity of the LHC machine. These differing conditions cannot be modelled in Monte Carlo events. To deal with this, Monte Carlo events are produced with a nominal pile-up contribution in bins of the average number of interactions, which are smeared to generate the number of minimum bias interactions in a given event. This nominal distribution is brought in line with the real pile-up conditions in the data by reweighting this to the average number of interactions per bunch crossing ($\langle\mu\rangle$) in data. The procedure for applying this weights is summarised in Ref. [112] and [114]. The pile-up uncertainty is 1 – 10%.

5.3.6 Liquid Argon (LAr) hole veto

During a part of the data-taking period, an electronics failure in the LAr barrel electromagnetic calorimeter created a dead region in the second and third layers (see a description of the LAr calorimeter in Section 2.3.2), corresponding to approximately 1.4×0.2 in $\Delta\eta \times \Delta\phi$. Events with an electron in this region are vetoed, leading to loss of signal efficiency of about 1%. Furthermore, the energy measurement for jets in data in the problematic region is underestimated. A correction to the jet energy is made using the energy depositions in the cells neighbouring the dead region, and this is also propagated to E_T^{miss} . The correction to the jet energy amounts to a few percent for jets just touching the dead region and reaches 40 percent for jets in the centre of the dead region. The contribution of jets in the dead region to E_T^{miss} can be estimated and is denoted as $E_T^{\text{miss}}(\text{hole})$. Projecting this quantity on the direction of E_T^{miss} gives the quantity $\Delta E_T^{\text{miss}}(\text{hole}) = E_T^{\text{miss}}(\text{hole}) \cdot \cos \Delta\phi(\text{jet}, \vec{E}_T^{\text{miss}})$. Events with $\Delta E_T^{\text{miss}}(\text{hole}) > 10$ GeV and $\Delta E_T^{\text{miss}}(\text{hole})/E_T^{\text{miss}} > 0.1$ are rejected. This requirement rejects less than 0.5% of the events in the signal regions, and up to 2% of the events in the control regions. For the complete study on this veto, see Ref. [114].

5.4 Trigger and preselection

This section presents the different stages of the selection from the trigger and event preselection. In each step, a comparison between data and Monte Carlo for the most relevant kinematic variables is performed and discussed.

5.4.1 Triggers

A single muon trigger is used to select all the events in this analysis. The events are required to fire the lowest unscaled single muon trigger, EF_mu18. The same trigger is selected in both data and Monte Carlo simulation.

In order to properly take into account the discrepancies in muon trigger efficiencies between real data and Monte Carlo simulations, a set of scale factors for the muon signature EF_mu18 have been measured by means of a suitable selected sample of $Z \rightarrow \mu\mu$ decays, according to the ‘‘Tag & Probe’’ method described in Ref. [112].

Efficiencies have been studied in both muon detector barrel ($|\eta| < 1.05$) and end cap ($|\eta| > 1.05$) regions as a function of p_T , η and ϕ with suitable binning choice, using two independent analyses based on different data formats and on slightly different selections and dimuon mass windows around Z peak (10 and 15 GeV) in order to provide systematic uncertainties.

In the barrel, the scale factors are almost flat in p_T while a strong dependence on the spatial position can be observed. Therefore, a scale factor $\eta - \phi$ map has been provided as shown in Figure 5.3 (left). On the other hand, scale factors in the end cap regions show some dependence on p_T while they do not vary significantly in the $\eta - \phi$ plane. Hence, they have been parameterised in p_T only as shown in the right panel of the figure.

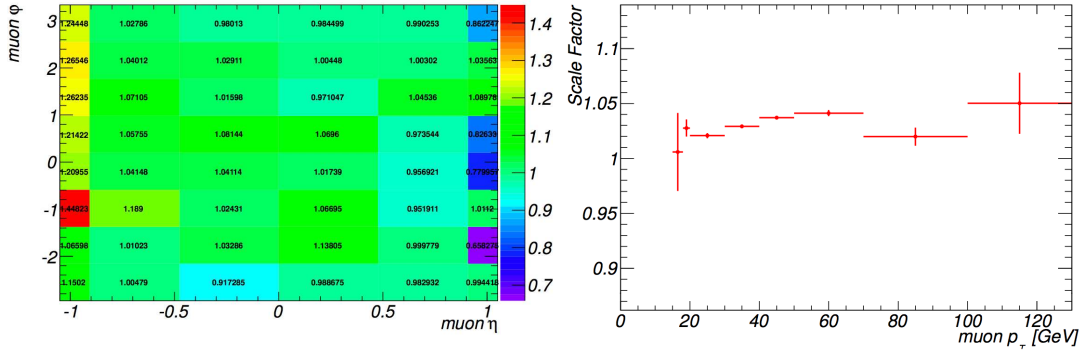


Figure 5.3: Muon scale factors as a function of η and ϕ in the barrel (left) and as a function of p_T in the end caps (right).

While the numbers obtained so far properly work for the signature of interest (EF_mu18) in the endcaps, to derive the final scale factors for EF_mu18 in the barrel another correction is needed to take into account some relevant discrepancies observed between real and simulated data in the high p_T range ($p_T > 50$ GeV). These correction factors, to act as divisors to the numbers shown in the left plot of Figure 5.3, are observed to be uniform in the whole $\eta - \phi$ plane, so they are averaged in p_T bins, as reported in Table 5.4 with systematic errors only (statistical uncertainties are already included in the estimates of scale factors vs. η and ϕ). Details on this study can be found in Ref. [114].

5.4.2 Event preselection

Collision candidates are selected by requiring a primary vertex as defined in Section 2.3.6.1, with at least five tracks, consistent with the beam spot position.

The kinematic selection starts by requiring the presence of exactly one signal muon, as defined in Table 5.3, with $p_T > 20$ GeV. If another baseline lepton (electron or muon), as defined

Table 5.4: Correction factors to obtain EF_mu18 scale factors in the barrel.

p_T range	Corrective factor	Systematic error
20 – 30 GeV	0.999916	0.004128
30 – 40 GeV	0.998411	0.005629
40 – 50 GeV	1.000220	0.00359
50 – 70 GeV	0.979001	0.006605
70 – 100 GeV	0.943875	0.040586
100 GeV - inf	0.906951	0.042084

in Tables 5.2 and 5.3 is reconstructed, the event is rejected as there are dedicated analyses in the RPC case for higher lepton multiplicities. Three/four or more good jets passing the selection criteria defined in Table 5.1 are required depending on the signal or control region studied. The leading jet must satisfy $p_T > 60$ (80) GeV, while the subleading jets transverse momentum must be $p_T > 25$ (40) GeV, again depending on the region. Details on the preselection are given below in Table 5.5. Finally, large mismeasurement of the jet transverse momenta are avoided by requiring the E_T^{miss} not to be aligned with any of the three/four selected jets ($\Delta\phi(j\vec{e}_i, E_T^{\text{miss}}) > 0.2$). This is done consistently among all regions.

In the following, the W and top background is separated by requiring a b -jet in the control region. In this respect, it is important to check that a good agreement between data and Monte Carlo exists for the b -tagged jets. Figure 5.4 shows the distribution of the number of b -tagged jets with $p_T > 25$ GeV in the combined W -plus-top control region for the three jet selection. The yellow band in the following plots shows the Monte Carlo uncertainty due to the jet energy scale, limited statistics, lepton scale-factor uncertainties, and b -tagging uncertainty where appropriate.

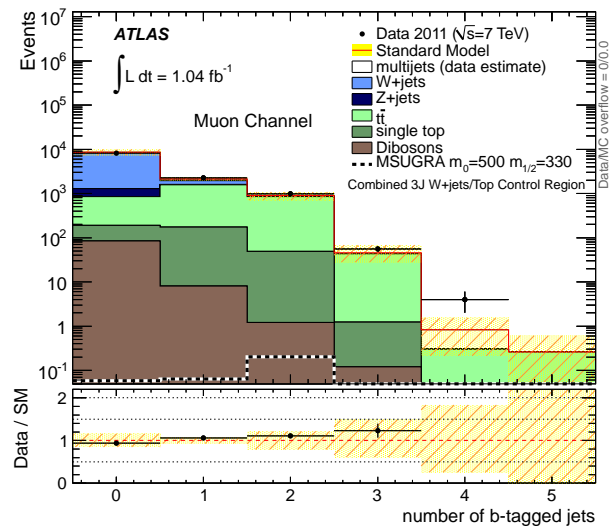


Figure 5.4: Distribution of the number of b -tagged jets with $p_T > 25$ GeV in the combined W -plus-top control region.

Figures 5.5 show E_T^{miss} , m_T and M_{eff} distributions for data and Monte Carlo simulation after kinematic lepton and (three or four) jet selection, as well as $\Delta\phi(\vec{jet}_i, \vec{E}_T^{\text{miss}}) > 0.2$, are applied.

Figures 5.6 show the M_{eff} distributions in the W and top control regions, for the three and four jet inclusive selection. The W and top background simulation is normalised to the cross section as predicted by MC generators. The QCD background estimates are obtained directly from data using the QCD matrix method defined in Section 5.5.2.1.

The kinematic distributions show good agreement between data and simulation over the full tested range. This very good agreement justifies the use of simulation shapes in order to extrapolate the backgrounds from their CRs into the SR.

To ensure additional good data quality, it is required that the LAr error bit (called `larError`) is not set (see Section 5.3.6 for details on the LAr error).

5.5 Event selection

5.5.1 Definition of signal regions

To remove most of the dominant $t\bar{t}$ and W +jets backgrounds, several further cuts are applied on the quantities discussed already in Section 5.1 and four signal regions are defined. The optimisation of these signal regions was performed on 16 benchmark points for simplified models [?] and three RPC-mSUGRA points. The cuts under examination for the optimisation were:

- number of jets
- transverse momentum of leading jet (scanned in steps of 20 GeV)
- missing transverse energy (in steps of 20 GeV)
- effective mass (in steps of 100 GeV)
- $E_T^{\text{miss}} / M_{\text{eff}}$ (in steps of 0.05)

The figure of merit for the optimisation was the signal cross section needed for a three-sigma observation of a given signal point assuming an integrated luminosity of 500 pb^{-1} . By doing this, one obtains an optimised selection for every signal point. It turned out that the best selections clustered in two regions of phase space. Then the cut values were adjusted to reflect the two regions in the best way to define a common selection for every class of clusters. At the end the selections were split in the number of jets (3 or 4) and a loose and a tight selection, resulting in four final signal regions: 3JL (three jets loose), 3JT (three jets tight), 4JL (four jets loose) and 4JT (four jets tight). A summary of all the selection criteria for the four signal regions are given in Table 5.5, together with the W + jets and top control regions criteria.

Table 5.5: Summary of all selection requirements used to isolate the SUSY signal from the standard model background in the four signal regions 3JL, 3JT, 4JL and 4JT. M_{eff} is the scalar sum of p_T of selected objects and E_T^{miss} . The definition of the control regions for W and top background is also given.

Selection	Signal Regions				Control Regions	
	3JL	3JT	4JL	4JT	3J	4J
Number of muons	= 1					
Muon p_T (GeV)	> 20					
Veto further leptons p_T (GeV)	> 20(10) for electrons (muons)					
Number of jets	≥ 3		≥ 4		≥ 3	≥ 4
Leading jet p_T (GeV)	60	80	60	60	60	60
Subsequent jets p_T (GeV)	25	25	25	40	25	25
$\Delta\phi(\vec{\text{jet}}_i, E_T^{\text{miss}})$	[> 0.2 (mod. π)] for all 3 (4) jets					
m_T (GeV)	> 100				40 < m_T < 80	
E_T^{miss} (GeV)	> 125	> 240	> 140	> 200	30 < E_T^{miss} < 80	
$E_T^{\text{miss}} / M_{\text{eff}}$	> 0.25	> 0.15	> 0.30	> 0.15	–	–
M_{eff} (GeV)	> 500	> 600	> 300	> 500	> 500	> 300

In the following, full definition of the four Signal Regions is provided:

- **3-jet Loose selection (3JL)**

At least three jets are required, with p_T higher than 60 GeV on the leading jet and p_T higher than 25 GeV for the second and third jets. To remove most of the W +jets background and semileptonic $t\bar{t}$ decays, a cut on the transverse mass, $m_T > 100$ GeV, is applied. This m_T requirement is applied in all three other signal regions as well. At this point of the selection, $t\bar{t}$ production is already the dominant background component and more specifically dileptonic decays, where one of the leptons is missed or is a τ lepton. To account for the presence of the two LSPs in RPC and for the neutrinos product of the LSP decays in bRPV, which cannot be detected directly in the detector, a large missing transverse energy above 125 GeV is required. This cut rejects a large portion of multijet events, for which no E_T^{miss} is expected, as well as W and top events, since only moderate E_T^{miss} is expected from the $W \rightarrow \ell\nu$ decays. Further background suppression is obtained with two last cuts: $E_T^{\text{miss}}/M_{\text{eff}} > 0.25$ and $M_{\text{eff}} > 500$ GeV.

- **3-jet Tight selection (3JT)**

The requirement on the leading jet transverse momentum is raised to 80 GeV, while the selection on the two subleading jets transverse momenta is kept at $p_T > 25$ GeV, to be sensitive to signals with smaller mass splittings $\Delta M(m_0, m_{1/2})$. As mentioned above, a $m_T > 100$ GeV selection is used to reject $t\bar{t}$ and W +jets decays. Tighter requirements on $E_T^{\text{miss}} > 240$ GeV and $M_{\text{eff}} > 600$ GeV are applied whilst the ratio $E_T^{\text{miss}}/M_{\text{eff}}$ cut is loosened to $E_T^{\text{miss}}/M_{\text{eff}} > 0.15$.

- **4-jet Loose selection (4JL)**

Signals with longer decay chains, in particular signals with gluino dominated production, show an increase in the number of jets accompanied by smaller values of missing transverse energy. Thus, four jets selection with the leading p_T higher than 60 GeV and three subsequent jets $p_T > 25$ GeV are required. A moderate cut of 140 GeV on the missing

transverse energy is applied. The final cuts to define the 4JL signal region are $E_T^{\text{miss}}/M_{\text{eff}} > 0.30$ and $M_{\text{eff}} > 300$ GeV.

• **4-jet Tight selection (4JT)**

Similarly to the three jet case, an additional tight selection with at least four jets is defined. The leading jet requirement is maintained at 60 GeV, while for the subleading jets the requirements is increased to 40 GeV to get better sensitivity in regions where $\Delta M(m_0, m_{1/2})$ is smaller. A tighter cut on E_T^{miss} of 200 GeV is applied as well as $M_{\text{eff}} > 500$ GeV while the ratio cut $E_T^{\text{miss}}/M_{\text{eff}} > 0.30$ is taken as in the 3-jet Tight selection.

Kinematic distributions in the signal regions

Figures 5.7 and 5.8 show the M_{eff} distributions for the 3-jet and 4-jet signal regions after all cuts but M_{eff} applied. The number of expected and observed events are summarised in Table 5.6 in the four signal regions after all selection criteria are applied. Again, a good agreement between data and simulation over the full tested range is observed. No significant excess is observed in any of the signal regions.

Table 5.6: Expected and observed events in the four signal regions and the two W +top control regions.

	3JL	3JT	4JL	4JT	3J WT CR	4J WT CR
Data	58	11	50	7	579	3071
MC	58.3	13.4	50.5	5.7	604	3119

Even though the names “loose” and “tight” are very clear from the cuts point of view, they can be misleading if one looks at the acceptances. These names might give the impression that tighter cuts should imply lower acceptances. However, this is not the case in bRPV as shown in Figures 5.9, where the number of events in the four signal regions selections are plotted for RPC (left) and bRPV (right). By comparing RPC and RPV distributions, it is observed that the regions selected by the cuts are optimal for RPC but not for RPV, as expected, due to the softer E_T^{miss} distribution in the latter case. Moreover, in the loose selection the dominant cut is the one relative to M_{eff} ($E_T^{\text{miss}}/M_{\text{eff}} > 0.25$ (0.30) for the 3J (4J) selection) while in the tight selection is the absolute E_T^{miss} cut. The result is that almost the same fraction of events is rejected in bRPV in both cases “loose” and “tight” for the 3J selection and thus acceptances in both regions are comparable, while in the 4J selection there is a big difference in the final number of bRPV events between the “loose” region, where the number of events is very reduced due to the tighter cut on $E_T^{\text{miss}}/M_{\text{eff}}$ and the “tight” selection with a less restrictive E_T^{miss} cut compared to the 3J region. As a result, the bRPV acceptance is very reduced in the 4JL region but quite high in the 4JT region, as will be seen in the results chapter.

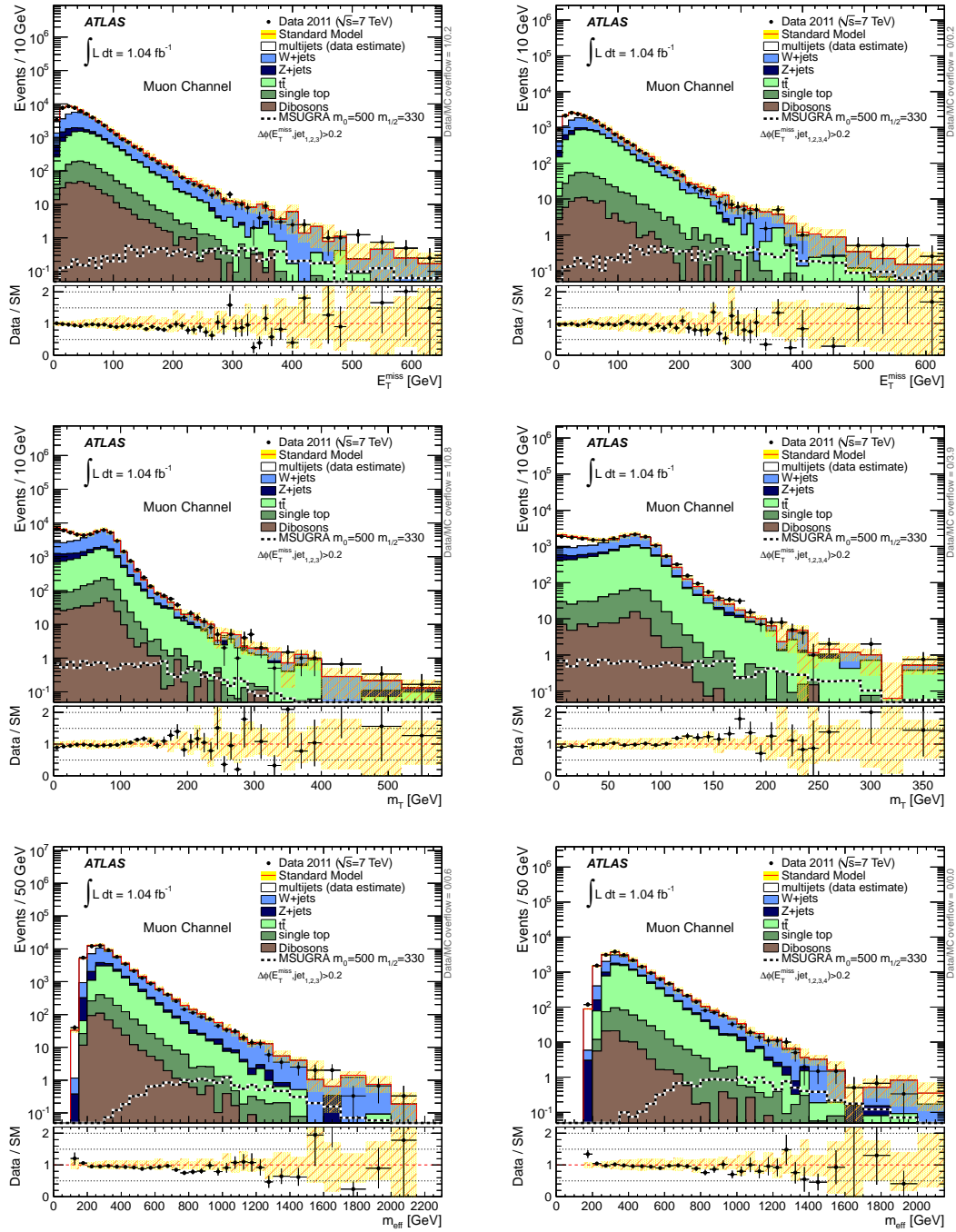


Figure 5.5: E_T^{miss} , m_T and M_{eff} distributions in data and Monte Carlo after the lepton + jets kinematic selection and $\Delta\phi((j\vec{e}_i), E_T^{\text{miss}}) > 0.2$ for three inclusive jets (left), and the same but for four inclusive jets (right). The yellow band definition is given in the text. For each distribution data over Monte Carlo ratio plots are also shown.

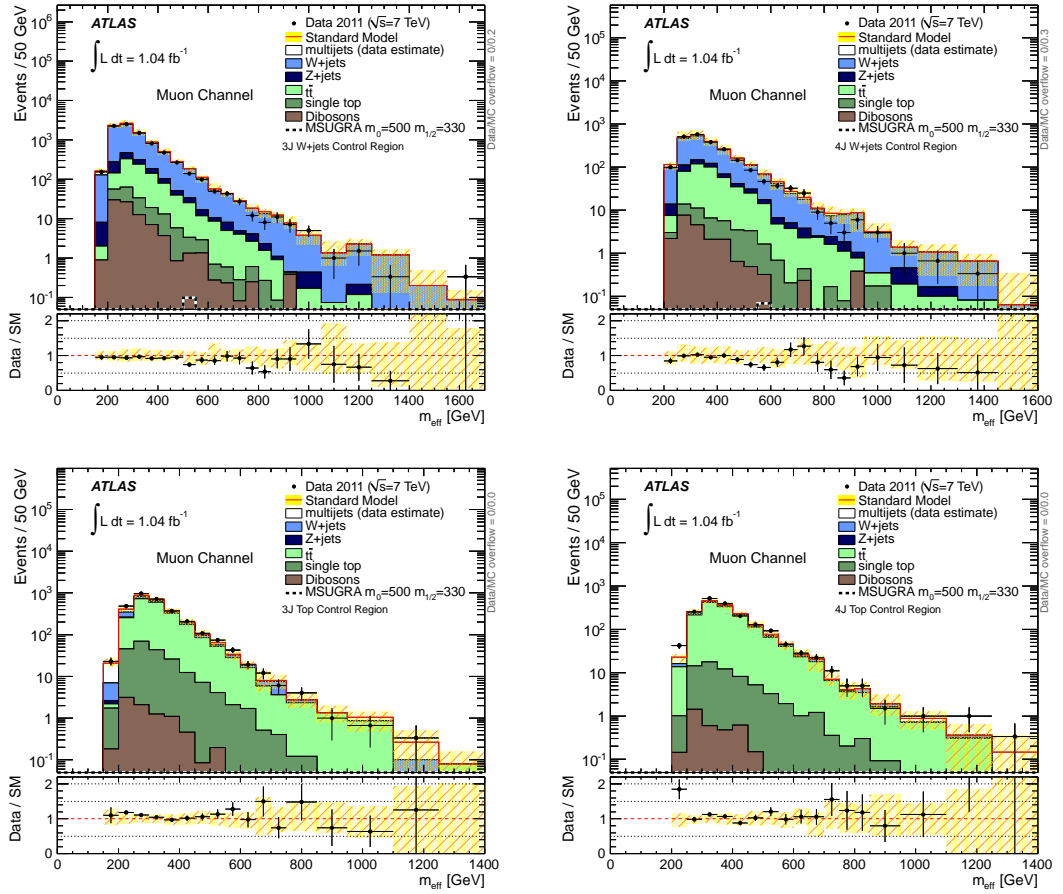


Figure 5.6: M_{eff} distribution in data and Monte Carlo after the lepton + jets kinematic selection and $\Delta\phi((jet_i, E_T^{\text{miss}}) > 0.2$ for three inclusive jets (left) and four inclusive jets (right), shown for the W control region (top) and the top control region (bottom). The yellow band definition is given in the text. For each distribution data over Monte Carlo ratio plots are also shown.

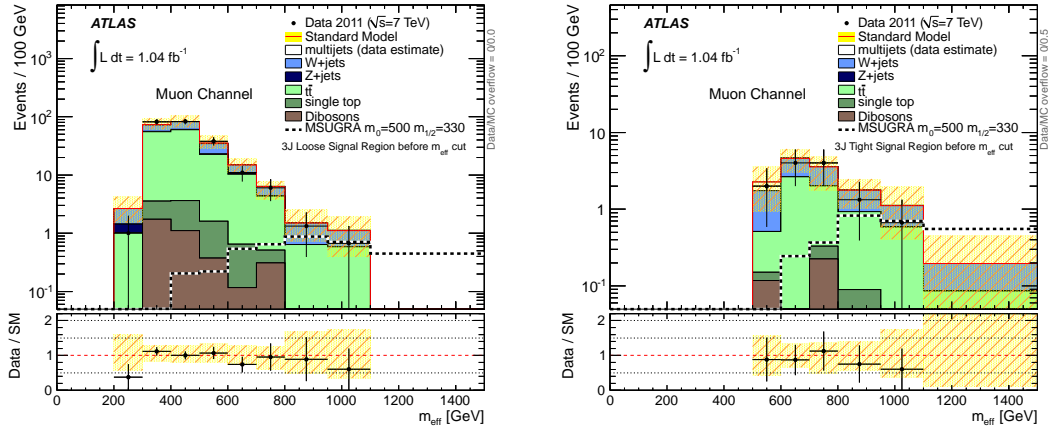


Figure 5.7: M_{eff} distribution in data and Monte Carlo for the 3JL (left) and 3JT (right) signal regions, shown after all selection cuts but M_{eff} . The yellow band definition is given in the text. For each distribution data over Monte Carlo ratio plots are also shown.

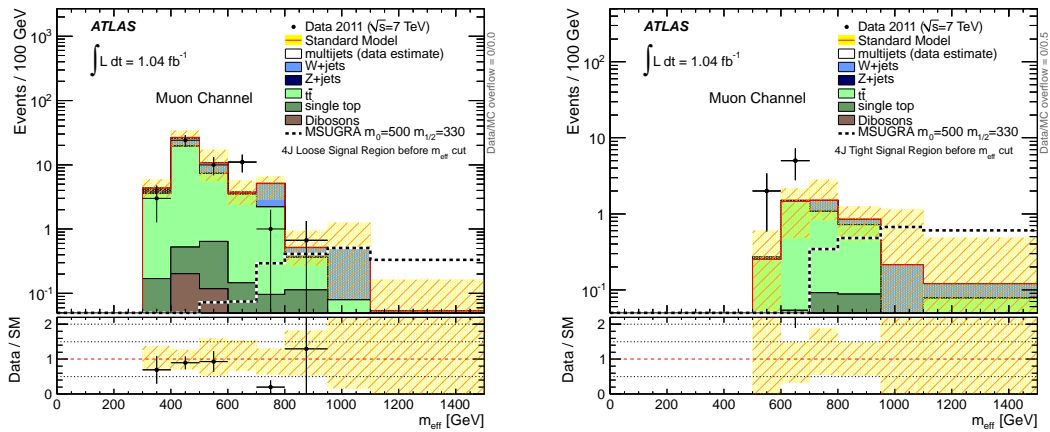


Figure 5.8: M_{eff} distribution in data and Monte Carlo for the 4JL (left) and 4JT (right) signal regions, shown after all selection cuts but M_{eff} . The yellow band definition is given in the text. For each distribution data over Monte Carlo ratio plots are also shown.

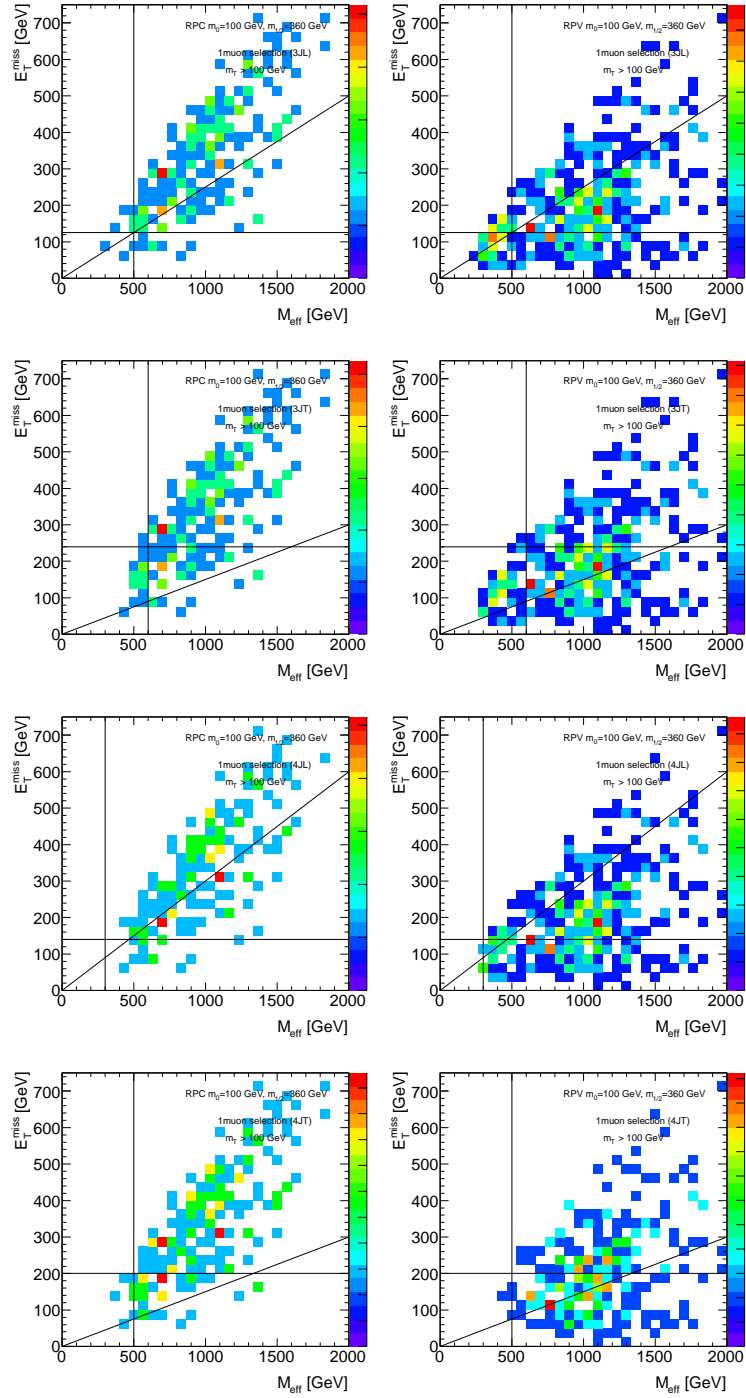


Figure 5.9: E_T^{miss} versus M_{eff} distributions for mSUGRA SUSY point (100, 360) in the R -parity conserving case (left) and in the bRPV case (right) after 3JL (first row), 3JT (second row), 4JL (third row) and 4JT (bottom row) selections. The distributions are normalised to unity.

5.5.2 QCD background estimation

In order to estimate the fake-lepton¹⁾ background, mainly from QCD physics processes, a matrix method is used given the limitations of simulation both in terms of statistics and understanding of the amount of fake-lepton events.

5.5.2.1 The Matrix Method

The method chosen to estimate the fake-lepton background in one-lepton channels has been successfully applied to previous Supersymmetry analyses [111, 112] and has been further developed for this analysis. It relies on the assumption that the fake-lepton background can be estimated from the number of events obtained when relaxing some of the lepton selection criteria via a system of two equations with two unknowns:

$$\begin{aligned} N_{\text{pass}} &= \epsilon^{\text{fake}}(\Omega) \cdot N^{\text{fake}} + \epsilon^{\text{real}}(\Omega) \cdot N^{\text{real}}, \\ N_{\text{fail}} &= (1 - \epsilon^{\text{fake}}(\Omega)) \cdot N^{\text{fake}} + (1 - \epsilon^{\text{real}}(\Omega)) \cdot N^{\text{real}}, \end{aligned} \quad (5.5)$$

where $N_{\text{pass}}, N_{\text{fail}}$ are the number of events satisfying or not extra lepton selection criteria. N^{fake} is the total number of fake-lepton events whereas N^{real} is the total number of prompt-lepton events. ϵ^{fake} and ϵ^{real} are the probabilities for a fake or prompt lepton respectively to pass extra lepton selection criteria. These probabilities can be parameterised as a function of phase space variables Ω .

Solving Eq. (5.5) for a bin in Ω leads to:

$$N_{\text{pass}}^{\text{fake}}(\Omega) = \epsilon^{\text{fake}}(\Omega) \cdot N^{\text{fake}} = \frac{N_{\text{fail}} - (1/\epsilon^{\text{real}}(\Omega) - 1) \cdot N_{\text{pass}}}{1/\epsilon^{\text{fake}}(\Omega) - 1/\epsilon^{\text{real}}(\Omega)}. \quad (5.6)$$

The estimation of the fake-lepton background in practise can be summarised by three steps:

1. Define a fake-lepton enhanced control region CR^{fake} and measure the loose²⁾ to tight³⁾ efficiency for fake-leptons as:

$$\epsilon^{\text{fake}} = \frac{N_{\text{pass}} - b_{\text{pass}}}{N_{\text{pass}} + N_{\text{fail}} - b_{\text{pass}} - b_{\text{fail}}}, \quad (5.7)$$

where $N_{\text{pass}, \text{fail}}$ are the observed number of events passing or failing the extra lepton selection criteria in CR^{fake} and $b_{\text{pass}, \text{fail}}$ are the Monte Carlo estimated non QCD background numbers mainly from $Z \rightarrow \ell\ell$ and $W \rightarrow \ell\nu$ processes. The uncertainty on ϵ^{fake} is derived from the error propagation formula and involves statistical uncertainties and the uncertainty on the background subtraction from Monte Carlo assuming a fully correlated uncertainty between b_{fail} and b_{pass} .

2. Define a prompt-lepton enhanced control region CR^{real} . It can be done either with data using $Z \rightarrow \ell\ell$ events and a ‘‘Tag & Probe’’ method or directly from Monte Carlo. This is useful for obtaining ϵ^{real} .

3. Run over all events with exactly one lepton satisfying the baseline lepton cuts. Eq. (5.6) can be used to derive for each individual event a weight with two possible values

¹⁾ In this section, a fake-lepton refers to a non-prompt lepton. Possible sources of fake leptons are heavy flavour decays, conversions or misidentified hadrons

²⁾ Here the loose definition refers to the baseline lepton definition in Tables 5.2 and 5.3

³⁾ The tight selection corresponds to the signal lepton selection in Tables 5.2 and 5.3

$$\begin{aligned}
w_{\text{fail}}(\Omega) &= 1/(1/\epsilon^{\text{fake}}(\Omega) - 1/\epsilon^{\text{real}}(\Omega)), \\
w_{\text{pass}}(\Omega) &= -(1/\epsilon^{\text{real}}(\Omega) - 1)/(1/\epsilon^{\text{fake}}(\Omega) - 1/\epsilon^{\text{real}}(\Omega)),
\end{aligned}
\tag{5.8}$$

depending on whether the lepton satisfies or not the extra lepton selection criteria. The event weights are then used to reconstruct the fake-lepton contribution in terms of shape and normalisation for any distribution. It should be noted that w_{pass} is negative and thus the fake-lepton estimate can be negative in regions of phase space where this background is small.

QCD events with heavy flavour decays can show a similar signature as signal events. A preselected control sample enriched in such QCD events is defined by relaxing the common muon object definitions by not applying the isolation cut for the selected muon. As explained above, the efficiency ϵ^{fake} for such a preselected muon to pass also the tight signal muon definitions, must be determined from a control region enriched with QCD events. This control region should show a similar topology as the signal region concerning the QCD events, but it should also show sufficient statistics in order to minimise the errors on ϵ^{fake} . Therefore, the control region for ϵ^{fake} is defined as follows:

- exactly 1 muon with $p_T > 20$ GeV;
- ≥ 1 jet with $p_T > 60$ GeV;
- $E_T^{\text{miss}} < 30$ GeV.

Events with mostly isolated muons as $t\bar{t}$, W +jets events, have a large efficiency close to one for the muon to pass the preselection as well as the signal object definitions. Therefore, such events in the control region would increase the value of ϵ^{fake} estimated. For this reason, these events need to be subtracted from the observed events in the control region so that the control region is pure in QCD events. The contamination of other Standard Model backgrounds (mainly $t\bar{t}$, Z +jets and W +jets events) in the control region is less than 9%. As ϵ^{fake} depends on the pseudo-rapidity, ϵ^{fake} is obtained per each bin in η in 10 bins from -2.5 to 2.5. There is some dependence of ϵ^{fake} on the number of jets in the event and on p_T^μ , both taken into account as systematic uncertainty on ϵ^{fake} .

The efficiency for a non-QCD event to pass the preselection as well as the tight object definitions, ϵ^{real} , is obtained from MC. A control region enriched in $t\bar{t}$ and W +jets events is used as follows:

- exactly 1 muon with $p_T > 20$ GeV;
- ≥ 3 jet with $p_T^{\text{first jet}} > 60$ GeV and $p_T^{\text{third jet}} > 25$ GeV;
- $30 < E_T^{\text{miss}} < 80$ GeV and $40 < m_T < 80$ GeV.

ϵ^{real} is obtained in this control region as function of η with its mean value being 0.98 ± 0.02 .

5.5.3 W and top background estimation

W +jets and top pair production are the main backgrounds in the signal regions. Hence, a robust estimate of these processes is a crucial part of the analysis. To this end, semi-data-driven approaches are used where the W and top estimates are rescaled to data in control regions. The constrained results from these approaches are then extrapolated to the signal regions via Monte Carlo simulation. To keep the extrapolation error small, the control regions are defined using very close cuts to the SR, orthogonal to them:

1. Single muon trigger
2. One signal muon with $p_T > 20$ GeV.
3. No additional baseline muons with $p_T > 10$ GeV nor electrons with $p_T > 20$ GeV.
4. Three (four) jets with $p_T > 25$ GeV
5. Leading jet with $p_T > 60$ GeV
6. $\Delta\phi(\vec{jet}_i, E_T^{\text{miss}}) > 0.2$
7. Box cuts in (E_T^{miss}, m_T) plane:
 - 40 GeV $< E_T^{\text{miss}} < 80$ GeV
 - 30 GeV $< m_T < 80$ GeV
8. *b*-tagging requirements:
 - WR: No *b*-tagged jet with JetFitterCombNN > 2.0 among the three (four) selected jets
 - TR: At least one *b*-tagged jet with JetFitterCombNN > 2.0 among the three (four) selected jets

The first cuts 1-6 are similar to the signal regions. In the 3JL and 3JT control regions, identical cuts are used to reduce the number of control regions. The same is valid for the 4JL and 4JT control regions. The cuts listed under 7 ensure that the CRs are orthogonal to the SRs, while requirement 8 is used to separate the top control region from the W control region.

5.5.3.1 *W*+jets background

The *W*+jets background is estimated in the WR region, defined in Section 5.1.2, where the *W*+jets contribution is normalised to data, resulting in k-factors for this background contribution. The normalisation is performed in the profile likelihood fit which is explained in more detail in Section 5.6. Individual k-factors are fitted using the different light parton samples of the Alpgen *W*+jets production (see Table A.5, where the final k-factors are also shown for every light parton sample). The extrapolation factors from the control region to the signal regions are extracted from the Monte Carlo simulation.

Different systematic uncertainties are taken into account: jet energy scale and resolution, lepton resolution, *b*-tagging, luminosity and theory uncertainties such as variations of the renormalisation and factorisation scale or the cut off for the transition from matrix element to parton shower as well as the hadronisation. The theory error is 50%.

5.5.3.2 *t* \bar{t} background

Similar to the *W*+jets contribution, the *t* \bar{t} contribution is extracted from TR region. Again, the normalisation is performed in the profile likelihood fit and the transfer factors from control to signal region are taken from the simulation. The same systematic uncertainties as for the *W*+jets background are considered for the transfer factors. The total theory uncertainty is estimated to 25%. Further details both in *W*+jets and *t* \bar{t} backgrounds can be found in Ref. [112].

In the following, everything labelled top is always the combination of top pair production and single top events.

5.5.4 Initial and final state radiation

The expected contribution for a given background can be altered by the modelling of initial state radiation (ISR) and final state radiation (FSR). ISR is expected to have a larger impact, since a hard jet in the initial state can lead to a large boost of the objects in the final state, thus increasing for example the missing transverse energy of the event. To estimate the impact of ISR, different $t\bar{t}$ samples generated using different PYTHIA tunes dealing with soft and hard radiation are compared. Relative differences in the transfer factors are found to be at the level of 10% for 3JL, 4JL and 4JT signal regions and a bit larger for the 3JT region, which has the harshest cuts on jets, E_T^{miss} and M_{eff} , leading to poorer statistics and thus greater errors. Details on this study can be found in Ref. [114].

5.5.5 Contamination from cosmic events

Muons from cosmic radiation are a potential source of background. They are distributed along the beam line in any direction so there is a chance for them to be reconstructed as a muon from the proton-proton collision if they cross the primary vertex.

Studies performed with previous data [112] show that muons from hard scattering processes are concentrated at very low values of the transverse and longitudinal impact parameters with respect to the primary vertex (PV), $|z_0^{\text{PV}}|$ and $|d_0^{\text{PV}}|$, but muons corresponding to cosmic rays are distributed towards higher $|z_0^{\text{PV}}|$ and $|d_0^{\text{PV}}|$ values. Thus a cut on these variables would help reducing the cosmic muon background. A veto is applied such that if one muon is found above the cuts, the whole event is discarded.

Two sets of cuts have been considered in this analysis. In the tight cosmic-muon selection a muon is tagged as cosmic if any of the following requirements is fulfilled :

$$\begin{aligned} |z_0^{\text{PV}}| &> 1 \text{ mm} \quad \text{AND/OR} \\ |d_0^{\text{PV}}| &> 0.2 \text{ mm} . \end{aligned} \tag{5.9}$$

In the soft cosmic muon selection a muon is tagged as cosmic if:

$$\begin{aligned} |z_0^{\text{PV}}| &> 5 \text{ mm} \quad \text{AND/OR} \\ |d_0^{\text{PV}}| &> 1 \text{ mm} . \end{aligned} \tag{5.10}$$

In RPC SUSY all muons are generated practically at the primary vertex, so any of these selections lead to efficiencies close to 100% with respect to the previous requirement. In the bRPV case, where relatively long-lived neutralinos can decay to muons, any of the cosmic muon selections affect the efficiency at some level.

The impact of the cut depends on two factors: the neutralino decay length, whose distribution for the signal grid can be seen in Figures 3.13, and the branching ratio of all possible decay modes giving rise to muons. As already mentioned in Section 4.3.1, there are mainly two such decay modes: $\tilde{\chi}_1^0 \rightarrow \mu^\pm W^\mp$ (whose branching ratios can be seen in Figure 3.14 as a function of m_0 and $m_{1/2}$) and $\tilde{\chi}_1^0 \rightarrow \nu\tau\mu$ with a significative lower BR throughout the grid (from 0.12 at low m_0 to 0.005 at high m_0 and small dependency on $m_{1/2}$).

In Figure 5.10, bRPV efficiencies with respect to the primary vertex selection are shown for the tight cosmic muon selection (left) and for the soft cosmic muon selection (right). In both figures, the shape of the efficiencies very well match the neutralino decay length distribution, making it evident that the tight selection is too restrictive and eliminates a big amount of bRPV events.

Hence, the soft selection is chosen. It should be noted that even in the soft selection, a reduction in the efficiency is appreciated at low $m_{1/2}$ values. This fact has to be kept in mind in the exclusion result (see Section 5.6.5.1), where a decrease in the sensitivity in this region will appear.

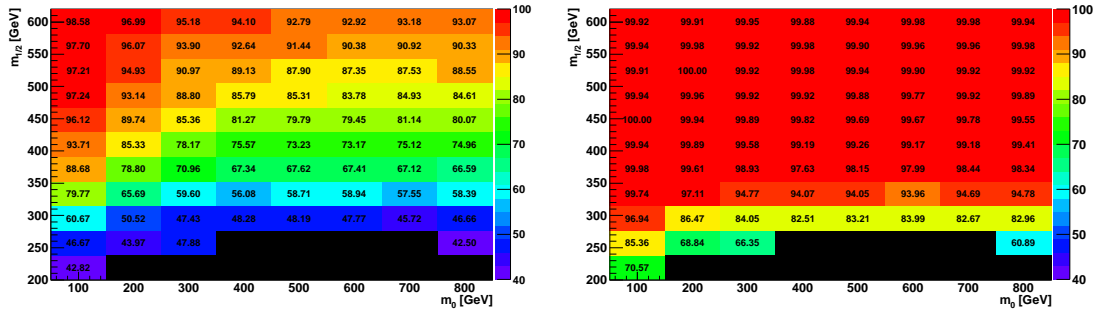


Figure 5.10: Cosmic veto efficiency with respect to the previous cut (good primary vertex requirement) for the tight cut selection (left) and soft cut selection (right). The black areas at low $m_{1/2}$ values are signal points with non-prompt LSP decay.

The effect of the $BR(\tilde{\chi}_1^0 \rightarrow \mu + X)$ distribution in combination with the soft cosmic muon veto can be appreciated in Figure 5.11, where the percentage of muons selected in SR3JL, coming from a neutralino decay is shown. According to the dominant $BR(\tilde{\chi}_1^0 \rightarrow \mu^\pm W^\pm)$ distribution shown in Figure 3.14, there should be a suppression of events in the very low- m_0 region which is appreciable in the plot, but a higher number of $\tilde{\chi}_1^0$ -decaying muons should be selected in the low $m_{1/2}$ region, where the three-body decays become more important. On the contrary, the percentage of events in which the selected muon comes from a neutralino is decreased in this region due to the application of the soft cosmic veto.

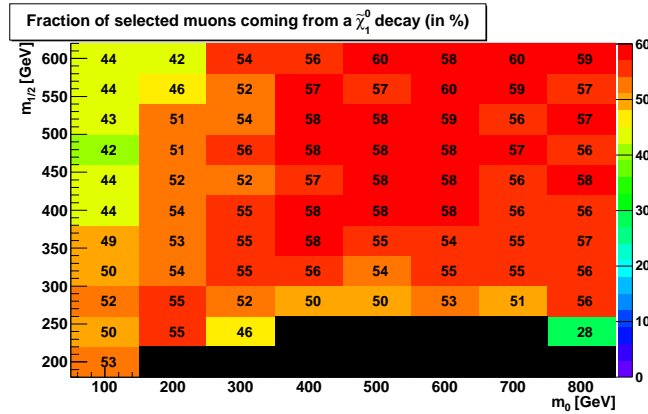


Figure 5.11: Fraction (in %) of the selected muons coming from a lightest neutralino in the bRPV samples, in the SR3JL. The black areas at low $m_{1/2}$ values are signal points with non-prompt LSP decay.

In order to study the contribution of cosmic muons background in the signal regions, a cosmic-enhanced control sample can be obtained by reversing the $|z_0^{\text{PV}}| < 5$ mm cut used in the selection of the signal muons. The contribution of cosmic muons to the signal-like muons can

be estimated using the $|z_0^{\text{PV}}|$ distribution for the cosmics-enhanced sample, which can be fitted as a Gaussian. Using the fit parameters, the contribution from cosmic muons can be computed at $|z_0^{\text{PV}}| < 5$ mm.

Since the analysis signal regions used in this note rely on additional cuts on top of the one-lepton requirement, the effect of those cuts have to be addressed also in the cosmics-enhanced sample. Very few cosmic events have high $E_{\text{T}}^{\text{miss}}$ or m_{T} and only one event out of an estimation of $821 \pm 11(\text{stat}) \pm 9(\text{syst})$ cosmics in the control sample can pass the $m_{\text{T}} > 100$ GeV cut used to define the signal region. With the scale factor used above to estimate the contribution of cosmic muons at $|z_0^{\text{PV}}| < 5$ mm, one can estimate the number of these muons after jets and m_{T} cuts to be $N_{\text{cosmics}}^{\text{SR}} = 0.05 \pm 0.05$ events. Of course this number will be further reduced once the cuts on $E_{\text{T}}^{\text{miss}}$, $\Delta\phi$, $E_{\text{T}}^{\text{miss}}/M_{\text{eff}}$ and M_{eff} are applied. From this control region, the contribution can be estimated by extrapolating in the signal region $|z_0^{\text{PV}}| < 5$ mm. This contribution is found to be negligible. More details are given in Ref. [112].

5.5.6 SUSY signal

In this section, bRPV is studied in the four signal regions previously defined. The bRPV-mSUGRA signal point ($m_0 = 100$ GeV, $m_{1/2} = 280$ GeV) is shown as a representative example through all the steps of the analysis.

The final list of cuts to be applied over both the SM background and over the SUSY signal is as follows (numbers in parentheses indicate requirements on different SRs):

1. Good Run List (GRL)
2. Muon trigger EF_mu18
3. Event cleaning: Jet/MET cleaning, LAr hole veto, PV selection, cosmic muon veto
4. Lepton cut: exactly one signal muon, exactly one baseline muon, no baseline electrons
5. Leading jet $p_{\text{T}} > 60$ (80) GeV
6. Subleading jets $p_{\text{T}} > 25$ (40) GeV
7. $\Delta\phi(\text{jet}, E_{\text{T}}^{\text{miss}}) > 0.2$
8. $E_{\text{T}}^{\text{miss}} > 125$ (240, 140, 200) GeV
9. $m_{\text{T}} > 100$ GeV
10. $E_{\text{T}}^{\text{miss}}/M_{\text{eff}} > 0.25$ (0.15, 0.30)
11. $M_{\text{eff}} > 500$ (600, 300) GeV

The efficiencies and cut flow for this combination of cuts for the bRPV SUSY inclusive signal point ($m_0 = 100$ GeV, $m_{1/2} = 280$ GeV) are shown in Table 5.7 for the 3JL and 3JT signal regions. The efficiencies have been estimated likewise for all bRPV grid signal points. In this table, all numbers of selected events are reweighted for the trigger efficiency, as explained in Section 5.4.1 and for the pile-up effect. The first column shows the number of events passing each of the listed cuts. Up to the lepton cut, requirements are identical in both regions, 3JL and 3JT. The second column shows the isolated effect of each of the cuts, showing their efficiency with respect to the previous one. As it was already mentioned, the effect of the trigger selection has a good efficiency in bRPV. In this point it is around 50% and it is in general above the RPC efficiency for this trigger (see Ref. [114] for trigger efficiencies in the RPC case). This behaviour is similar throughout the bRPV grid.

All the “event cleaning” requirements such as jet/MET cleaning, LAr hole veto, good primary vertex requirement or cosmic muon veto, have very high efficiencies as desired. The

lepton cut introduces a drastic reduction of the efficiency depending on the specific signal point under consideration. It is mainly due to the veto of a second muon in the event (as it was shown in Section 4.3.1, a large fraction of the bRPV events contains a number of muons higher than one) and to a lesser extent, vetoing on additional electrons leads to a signal loss of 20 – 30%. This drop in the efficiency could be recovered by a dilepton selection, which is outside the scope of this work. The E_T^{miss} cut has a considerable effect in the 3JL region and a drastic effect on the 3JT selection, in agreement with what was outlined in Figures 5.9. The m_T cut removes around half of the signal and the M_{eff} cut is of little importance.

Table 5.7: Efficiencies and cut flows for the bRPV SUSY inclusive signal point ($m_0 = 100$ GeV, $m_{1/2} = 280$ GeV) after the 3JL and 3JT selections. The 3JT thresholds are given in parentheses. The number of events have been reweighted for the trigger efficiency and for the pile-up effect.

bRPV 100_280 trigger + PU reweighting	Events		Eff. (%) wrt previous cut		Eff. (%) wrt initial	
	3JL	3JT	3JL	3JT	3JL	3JT
No cut	9953.21					
GRL	9953.21			100.00		100.00
Trigger (EF mu18)	5055.07			50.79		50.79
Jet/MET cleaning	5055.07			100.00		50.79
LAr hole veto	4909.21			97.11		49.32
Primary vertex cut	4828.76			98.36		48.51
Cosmic muon veto	4670.86			96.73		46.93
Lepton cut	1263.08			27.04		12.69
≥ 1 jet $p_T \geq 60$ GeV (80 GeV)	1215.75	1144.65	96.25	90.62	12.21	11.50
≥ 3 jets $p_T \geq 25$ GeV	1164.41	1113.70	95.78	97.30	11.70	11.19
$\Delta\phi(\text{jet}, E_T^{\text{miss}}) > 0.2$	920.18	885.39	79.03	79.50	9.25	8.90
$E_T^{\text{miss}} > 125$ GeV (240 GeV)	574.60	242.15	62.44	27.35	5.77	2.43
$m_T > 100$ GeV	250.99	116.12	43.68	47.95	2.52	1.17
$E_T^{\text{miss}} / M_{\text{eff}} > 0.25$ (0.15)	122.31	115.99	48.73	99.89	1.23	1.17
$M_{\text{eff}} > 500$ GeV (600 GeV)	115.98	115.99	94.82	100.00	1.17	1.17

In Figure 5.12, E_T^{miss} , m_T and M_{eff} distributions are shown for the three most significant stages of the analysis for this point and for an integrated luminosity of $\int L_{\text{int}} = 1.04 \text{ fb}^{-1}$. On the top plots, distributions before any cuts applied are shown. Distributions after the 1-muon selection (trigger EF_mu18, 1 PV, jet/ E_T^{miss} cleaning, cosmic muon veto, 1 signal muon, 1 baseline muon, 0 baseline electrons, 3 jets (60, 25, 25), $\Delta\phi(\text{jet}, E_T^{\text{miss}}) > 0.2$) can be seen in the middle row. The E_T^{miss} distribution extends from 0 to several hundreds of GeV due to the presence of neutrinos, as explained earlier. The m_T distribution peaks around the cut value ($m_T > 100$ GeV) and has an important effect on the cut flow leading to a reduction of signal of around 50%. The M_{eff} distribution is shifted towards higher values compared to the RPC case (see Section 5.5.7 for a comparison RPC vs. bRPV) and thus the effect of the cut $M_{\text{eff}} > 500$ GeV is of minor importance as it can be seen in Figure 5.13 where all cuts in the 3JL region are applied except for the M_{eff} cut itself. The effect of all cuts in the 3JL signal region, i.e. 1-muon selection and $m_T > 100$ GeV, $E_T^{\text{miss}} > 125$ GeV, $E_T^{\text{miss}} > 0.25 M_{\text{eff}}$ and $M_{\text{eff}} > 500$ GeV (SR3JL), over this bRPV point is seen in the bottom plots. Further E_T^{miss} distributions, comparison with R -parity conserving SUSY and an explanation of the origin of high E_T^{miss} can be found in Section 5.5.7.

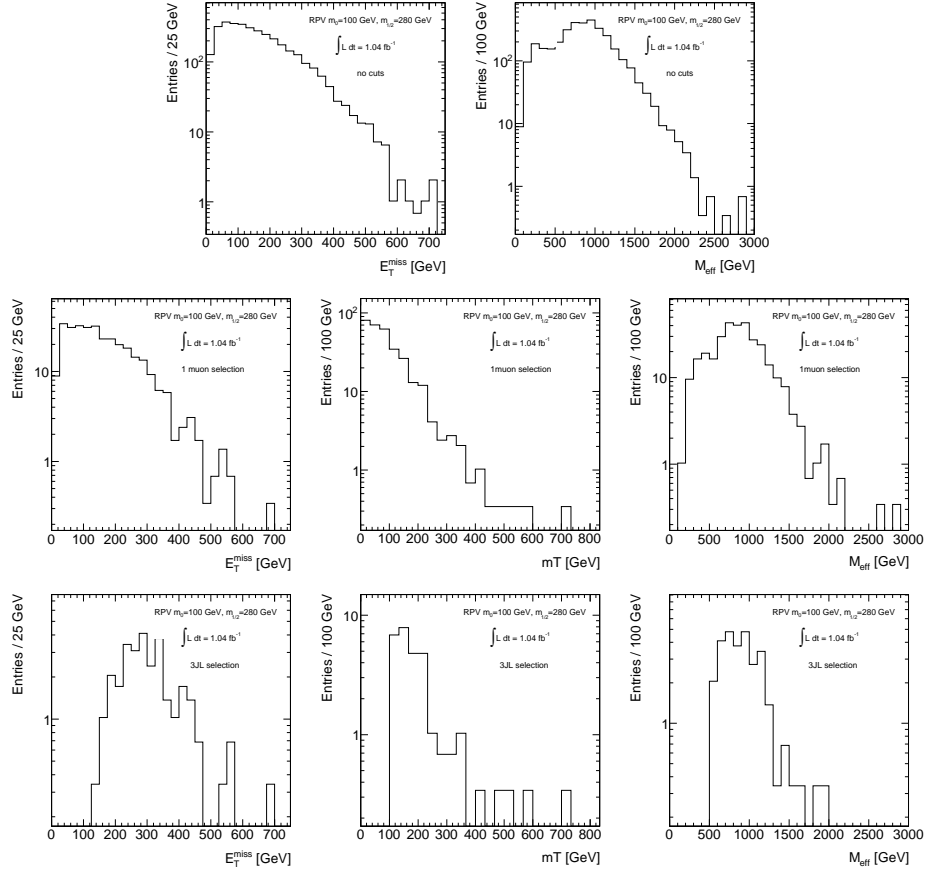


Figure 5.12: E_T^{miss} (left), m_T (middle) and M_{eff} (right) distributions for the SUSY bRPV signal point ($m_0 = 100$ GeV, $m_{1/2} = 280$ GeV) for an integrated luminosity of $\int L_{\text{int}} = 1.04 \text{ fb}^{-1}$ in three stages of the analysis. *Top row*: before any cut or selection is applied. m_T is not included in this case since the selection of one lepton is necessary for its calculation. *Middle row*: after 1-muon selection (trigger EF.mu18, 1 PV, jet/ E_T^{miss} cleaning, cosmic muon veto, 1 signal muon, 1 baseline muon, 0 baseline electrons, 3 jets (60, 25, 25), $\Delta\phi(\text{jet}, E_T^{\text{miss}}) > 0.2$). *Bottom row*: after the 3JL selection (1-muon selection plus $m_T > 100$ GeV, $E_T^{\text{miss}} > 125$ GeV, $E_T^{\text{miss}} > 0.25 M_{\text{eff}}$ and $M_{\text{eff}} > 500$ GeV)

In order to obtain the expected number of bRPV events in the four signal regions under consideration, some quantities need to be defined.

- The **acceptance** gives the number of events passing all the selections at truth level, normalised to the initial number of events. Since various production mechanisms contribute to the total production rate with different K -factors and since the acceptance for distinct processes can be different, the various production processes are treated independently. For low- m_0 , low- $m_{1/2}$, squark-gluino and squark-(anti)squark productions are dominant, while gaugino-gaugino production is the dominant process for the rest of the plane. For every bRPV grid point, the acceptance is first calculated for each of the 67 production subprocesses independently (a complete list of subprocesses can be found in Table A.1), as the effects of the cuts strongly depend on the sparticles initially produced in the event. Every event is then weighted using the corresponding NLO cross section of the subprocess i it

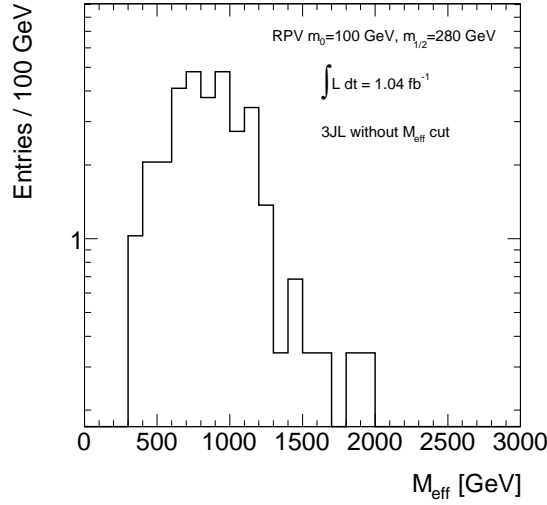


Figure 5.13: M_{eff} distribution for the SUSY bRPV signal point ($m_0 = 100$ GeV, $m_{1/2} = 280$ GeV) after the 3JL selection except for the M_{eff} cut ($m_T > 100$ GeV, $E_T^{\text{miss}} > 125$ GeV and $E_T^{\text{miss}} > 0.25M_{\text{eff}}$) for an integrated luminosity of $\int L_{\text{int}} = 1.04 \text{ fb}^{-1}$.

was originated from. For a given mSUGRA point, the acceptance in the signal region SR is defined as follows:

$$\text{Acc}(\text{SR}) = \frac{1}{\sigma} \sum_i \sigma_i \cdot \frac{n_i^{\text{truth}}(\text{SR})}{n_i^{\text{initial}}} \quad (5.11)$$

where,

σ_i is the NLO cross section for the production subprocess i .

σ is the total NLO cross section for the given bRPV-mSUGRA point: $\sigma = \sum_i \sigma_i$

$n_i^{\text{truth}}(\text{SR})$ is the number of events generated for the production subprocess i , passing all the selections in the signal region SR, at truth level.

n_i^{initial} is the initial number of events generated for the production subprocess i .

- The **efficiency** is a measure of how well the reconstructed objects are identified. It gives the number of events passing all the selections at reconstruction level, normalised to the number of events passing all the selections at truth level. Same as in the acceptance calculation, for every bRPV grid point, the efficiency is first calculated for each of the 67 production subprocesses independently. Every event is then weighted using the corresponding NLO cross section of the subprocess i it was originated from. For a given mSUGRA point, the efficiency in the signal region SR is defined as follows:

$$\text{Eff}(\text{SR}) = \frac{1}{\sigma} \sum_i \sigma_i \cdot \frac{n_i^{\text{reco}}(\text{SR})}{n_i^{\text{truth}}(\text{SR})} \quad (5.12)$$

where $n_i^{\text{reco}}(\text{SR})$ is the number of events generated for the production subprocess i , passing all the selections in the signal region SR, at reconstruction level.

When combining all the processes and applying all the cuts, one gets a final acceptance and efficiency which can be used to predict an expected number of events as a function of m_0 and $m_{1/2}$. Figures 5.14 show the acceptance (right) and the product acceptance \times efficiency (left) (number of reconstructed events normalised to the initial number of events) for every bRPV signal grid point and for the four signal regions being analysed. The acceptance drops at low $m_{1/2}$, both at truth and reconstruction level, mainly due to the cosmic veto and the enlargement of the neutralino decay length in that area mentioned in Section 5.5.5.

The acceptance is in the range 0.1% – 3% and mainly depends on $m_{1/2}$. In the RPC case, for which this analysis is optimised, the acceptance ranges between 0.1% – 11% with a similar dependence on $m_{1/2}$. The corresponding efficiencies can be found in Figure 5.15.

- The **expected number of events** and its error in a given signal region are then defined in terms of these two variables:

$$N_{\text{exp}}(\text{SR}) = \sigma \cdot L \cdot \text{Acc}(\text{SR}) \times \text{Eff}(\text{SR}) = L \cdot \sum_i \sigma_i \cdot \frac{n_i^{\text{reco}}(\text{SR})}{n_i^{\text{initial}}} \quad (5.13)$$

$$\varepsilon(N_{\text{exp}}(\text{SR})) = \frac{1}{N_{\text{exp}}(\text{SR})} \cdot L \cdot \sqrt{\sum_i \frac{\sigma_i^2 \cdot n_i^{\text{reco}}(\text{SR})}{(n_i^{\text{initial}})^2} \cdot \left(1 - \frac{n_i^{\text{reco}}(\text{SR})}{n_i^{\text{initial}}}\right)} \quad (5.14)$$

The number of expected events for an integrated luminosity of $\int L_{\text{int}} = 1035 \text{ pb}^{-1}$ is presented in Figure 5.16 (left) for every bRPV signal grid point and for the four signal regions under consideration together with the corresponding uncertainty in the number of events (right).

- The **uncertainty on the cross section** has been calculated taking into account several factors such as uncertainties on the value of α_S and on the factorisation/renormalisation scale Q . Also the acceptance and efficiency enter in the cross section error and consequently, the uncertainty on the cross section depends on the SR under consideration:

$$\varepsilon(\sigma)(\text{SR}) = \frac{1}{\sigma \cdot \text{Acc}(\text{SR})} \sqrt{\sum_i \sigma_i^2 \cdot \left(\frac{n_i^{\text{reco}}(\text{SR})}{n_i^{\text{initial}}}\right) \cdot (\varepsilon(\alpha_S)^2 + \varepsilon(Q)^2)} \quad (5.15)$$

The total NLO cross section, calculated with Prospino 2.1 [97, 98] is shown in Figures 5.17 as a function of m_0 and $m_{1/2}$. Cross sections span over several orders of magnitude for a fixed value of m_0 and $m_{1/2} \in (200, 600) \text{ GeV}$. All cross sections are in the range $\approx 0.01 - 20 \text{ pb}$. The total cross section relative total uncertainty in the four signal regions under consideration can be found in Figure 5.18.

The contributions from the dominant subprocesses are shown in Figure 5.19. It should be noted that, unlike in the RPC interpretation, the production processes related to gaugino-gaugino and slepton-slepton (both charged and neutral) have been simulated with PYTHIA and taken into account in the final results.

The uncertainties due to the variation of α_S and the PDFs are summarised in Figure 5.20.

Also the effect of the variation of the QCD factorisation scale has been studied for all bRPV signal points and the results for reducing or increasing it by a factor of two can be seen in Figures 5.21 and 5.22, respectively.

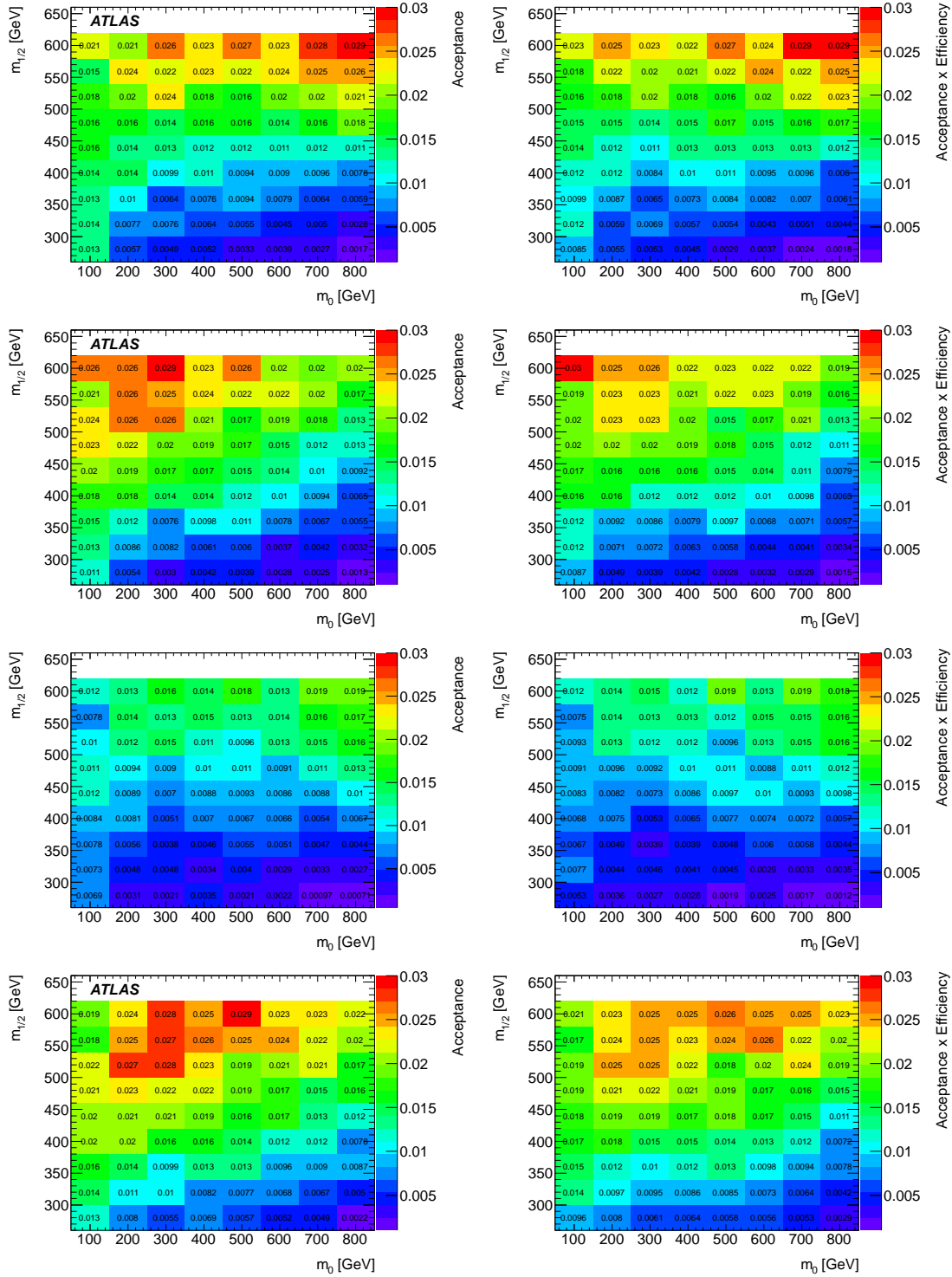


Figure 5.14: Acceptance (left) and reconstruction efficiency times acceptance (right) of the SUSY bRPV signal points for the 3JL (first row), 3JT (second row), 4JL (third row) and 4JT (bottom row) signal regions as a function of m_0 and $m_{1/2}$.

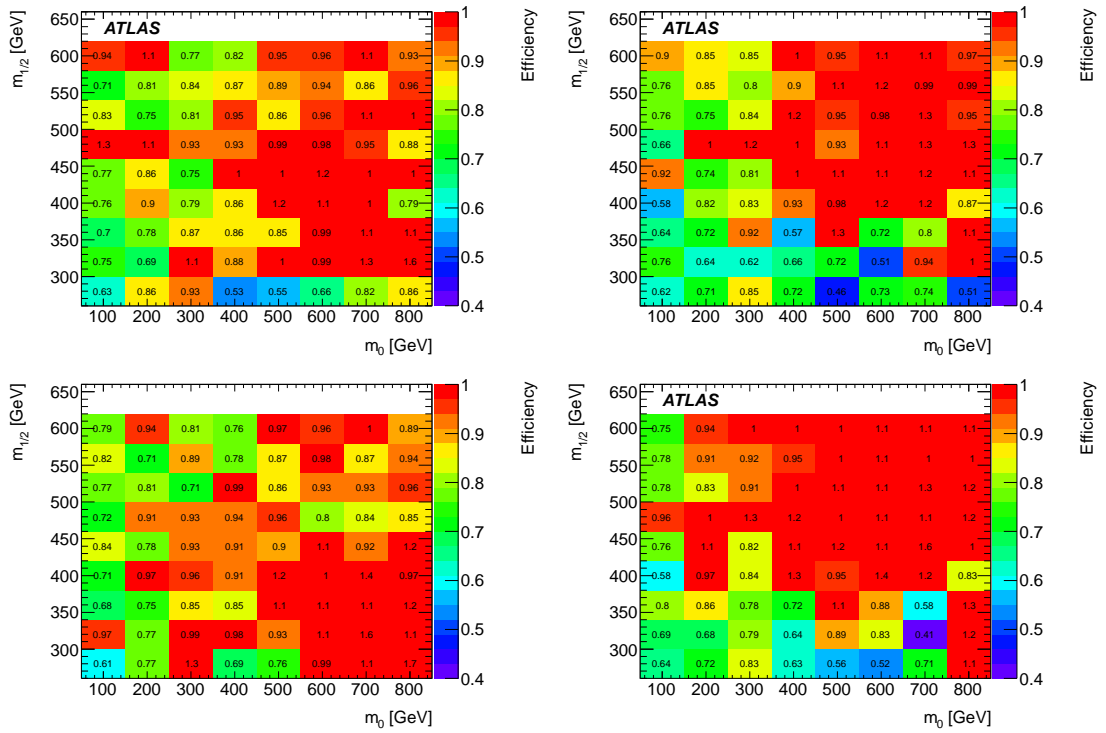


Figure 5.15: Reconstruction efficiency of the SUSY bRPV signal points for the 3JL (top left), 3JT (top right), 4JL (bottom left) and 4JT (bottom right) signal regions as a function of m_0 and $m_{1/2}$.

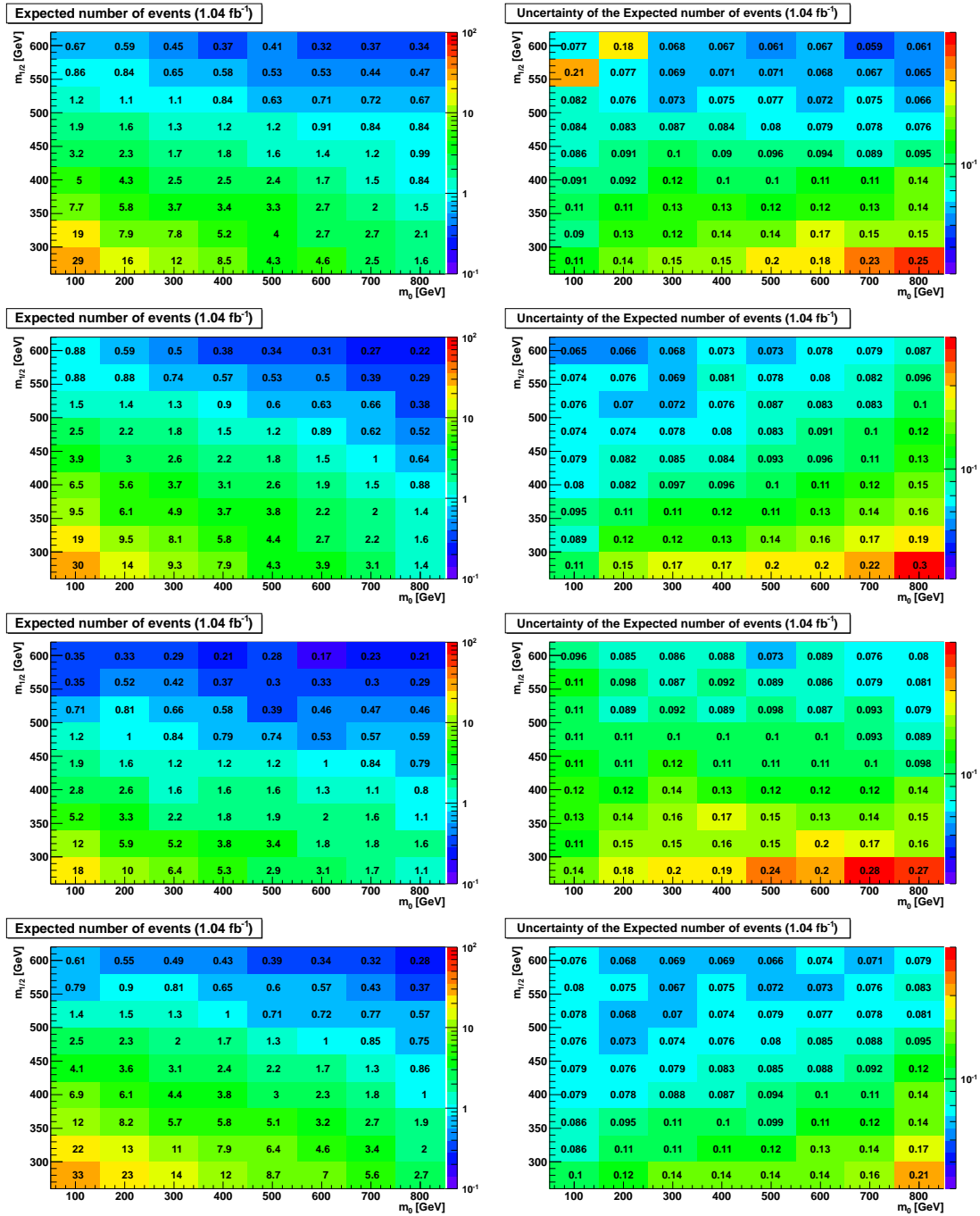


Figure 5.16: Expected number of events at reconstruction level (left) and corresponding uncertainties (right) of the SUSY bRPV signal points for the 3JL (first row), 3JT (second row), 4JL (third row) and 4JT (bottom row) signal regions as a function of m_0 and $m_{1/2}$.

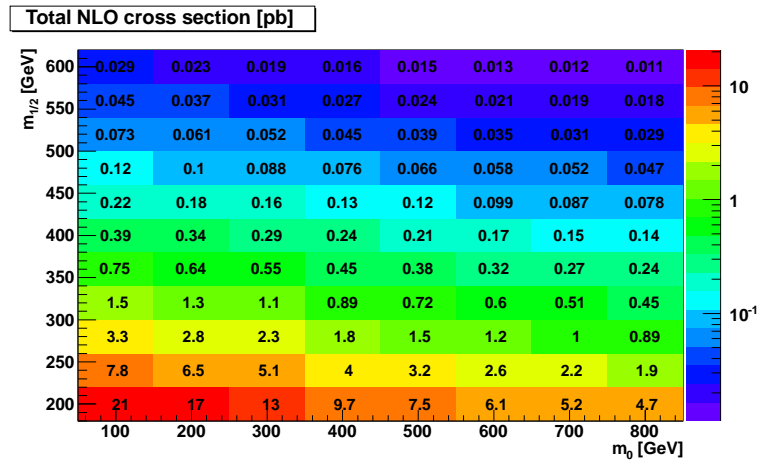


Figure 5.17: Total NLO cross sections in pb for bRPV signal points.

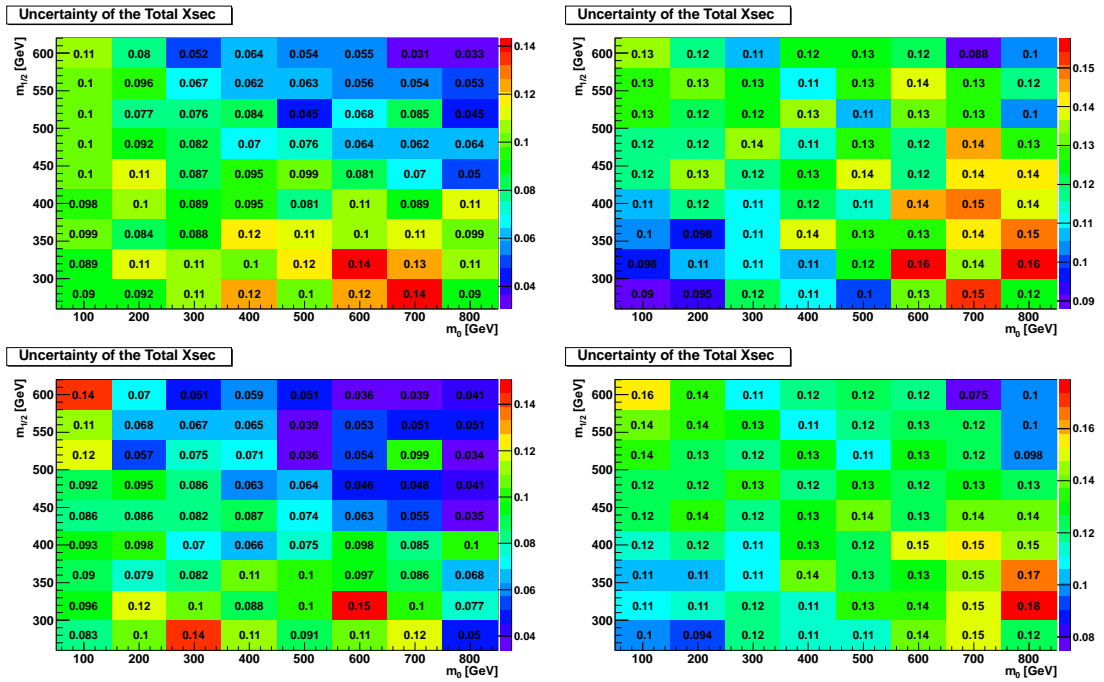


Figure 5.18: Total NLO cross sections relative uncertainties for the bRPV signal points in the 3JL (top left), 3JT (top right), 4JL (bottom left) and 4JT (bottom right) signal regions.

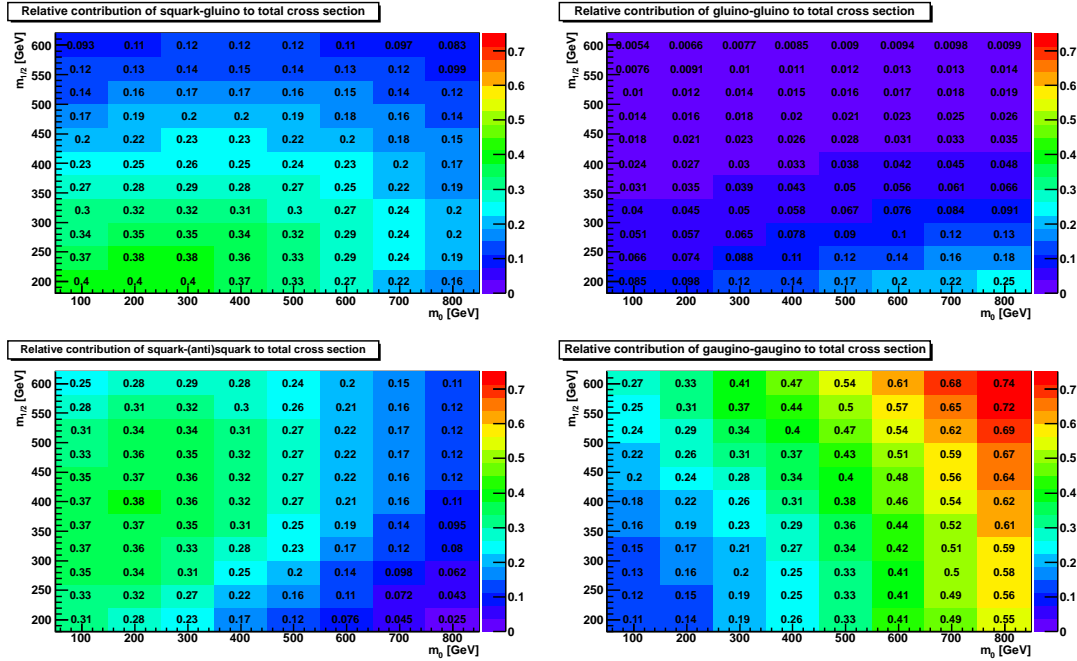


Figure 5.19: Dominant contributions to NLO cross sections for all bRPV signal points.

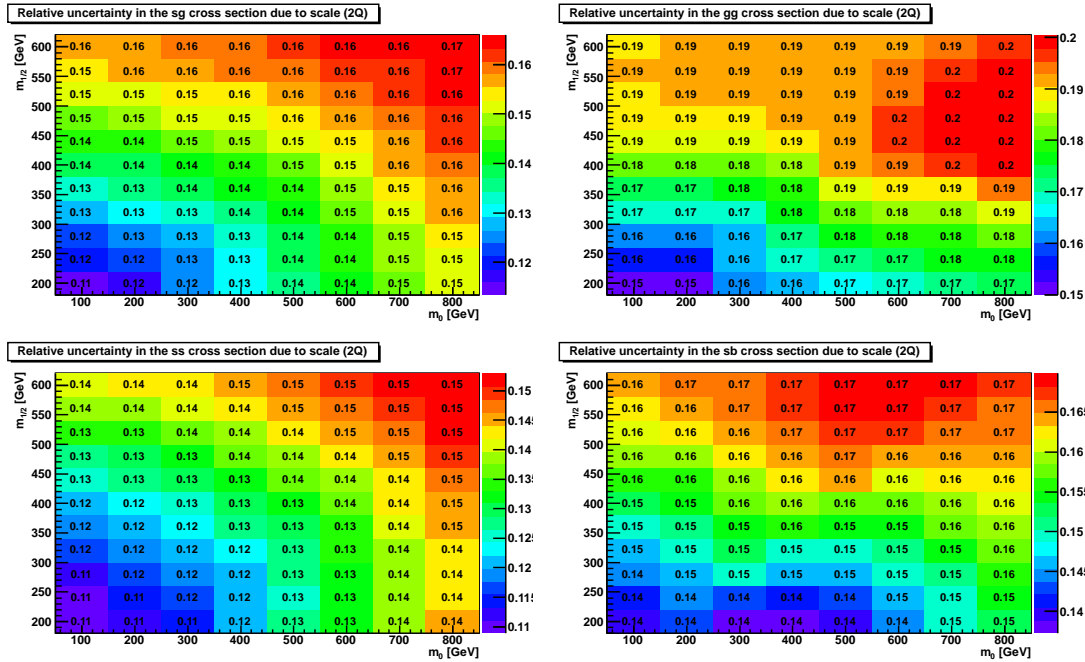


Figure 5.20: Uncertainties due to the increase of QCD factorisation scale by a factor of two for the dominant processes in all bRPV signal points for squark-gluino (top left), gluino-gluino (top right), squark-squark (bottom left) and squark-antisquark (bottom right) production.

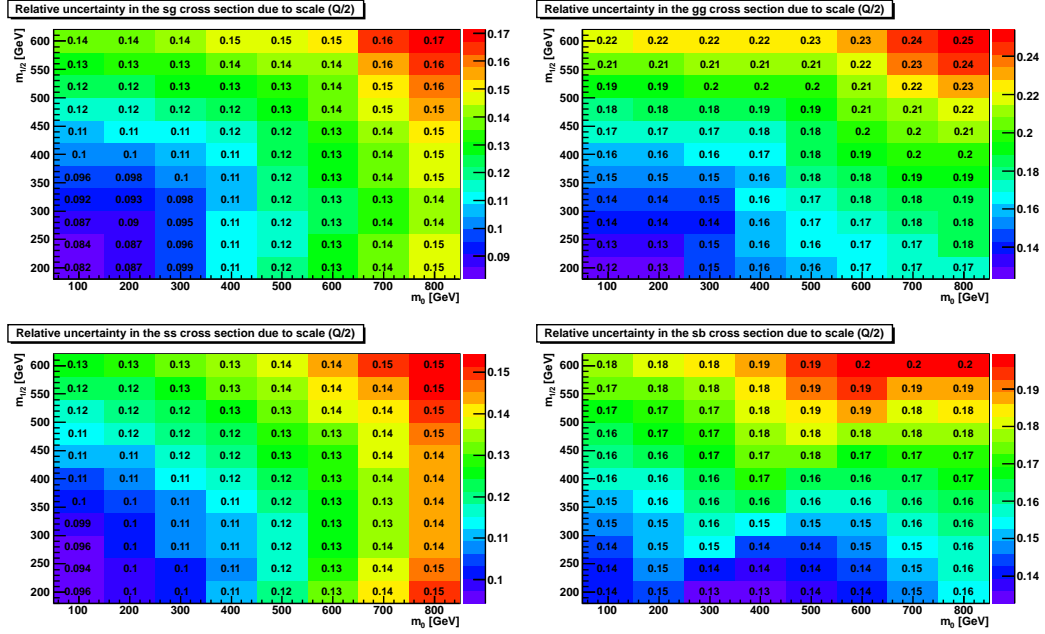


Figure 5.21: Uncertainties due to the reduction of QCD factorisation scale by a factor of two for the dominant processes in all bRPV signal points for squark-gluino (top left), gluino-gluino (top right), squark-squark (bottom left) and squark-antisquark (bottom right) production.

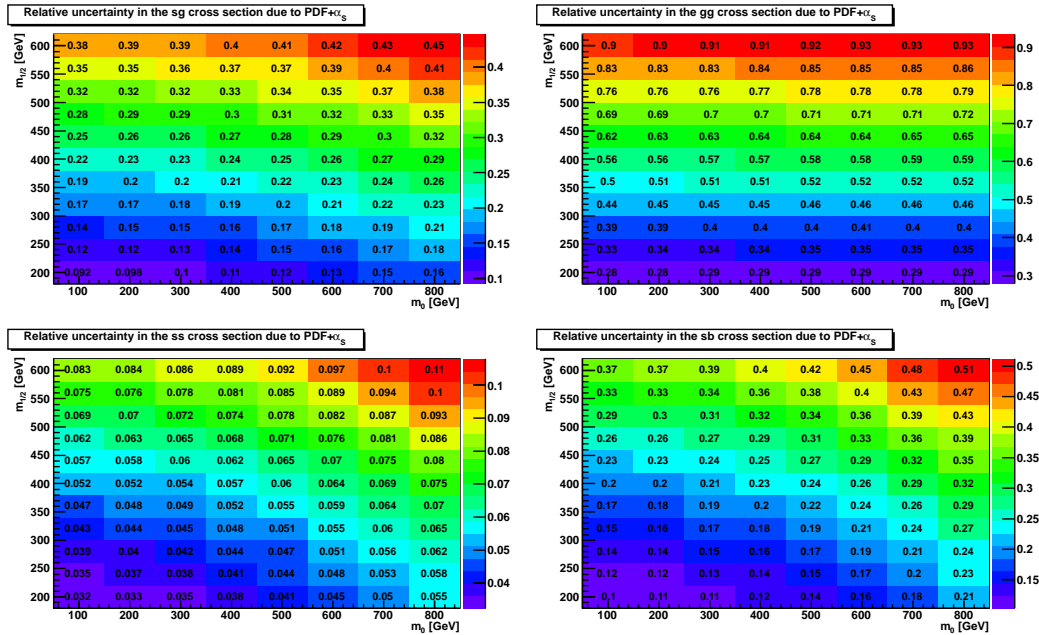


Figure 5.22: Uncertainties due to the variation of α_s and PDFs for the dominant processes in all bRPV signal points for squark-gluino (top left), gluino-gluino (top right), squark-squark (bottom left) and squark-antisquark (bottom right) production.

5.5.7 Comparison between bilinear RPV and RPC SUSY

In this section some comparisons between *RPC*-mSUGRA and *bRPV*-mSUGRA in the relevant quantities for the analysis are presented. Four nearby grid points are compared.

In Figure 5.23 the E_T^{miss} distribution is compared for *RPC* and *bRPV* after the 4-jet tight 1-muon selection and after the m_T cut (but before applying the E_T^{miss} and M_{eff} cuts). It is evident that the E_T^{miss} spectrum for *bRPV* is softer than the *RPC* one, in particular at high $m_0, m_{1/2}$, yet remaining significantly higher than the expected from SM processes.

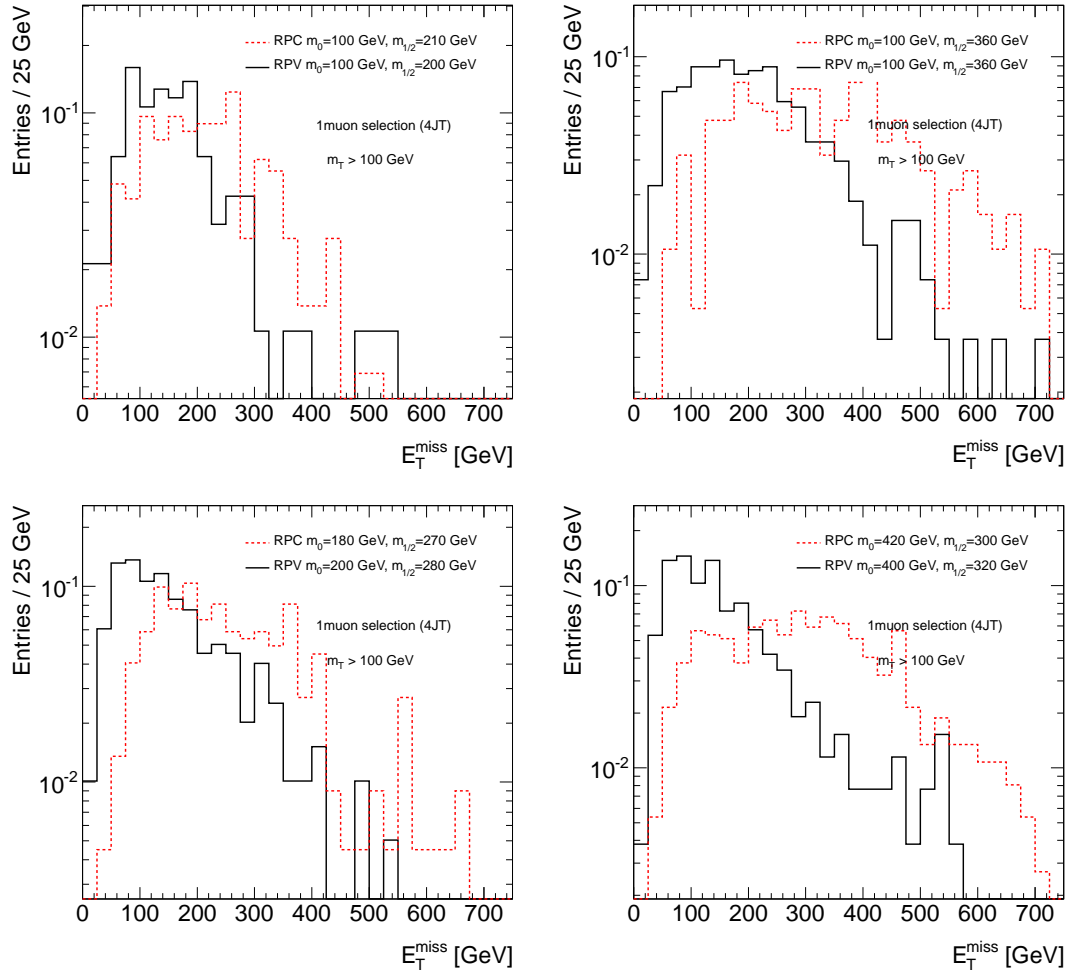


Figure 5.23: E_T^{miss} distributions for various mSUGRA signal points for *bRPV* SUSY (black continuous line) and nearby *RPC* SUSY (red dashed line) after 1-muon 4JT selection and m_T cut. The distributions are normalised to unity.

The origin of the high E_T^{miss} in the *bRPV* SUSY model, where the neutralino LSP decays in the detector, can be attributed to the neutrino-producing LSP decay modes. As shown in Section 4.3.1, these channels account for $\sim 90\%$ of all possible decays. To a smaller extent, E_T^{miss} can be originated from neutrinos produced in the cascade decay of particles and in LSP invisible decays such as $\tilde{\chi}_1^0 \rightarrow \nu\nu$.

In Figure 5.24 the M_{eff} distribution is compared for *RPC* and *bRPV* after the 3-jet tight 1-muon selection. The distribution of this variable is more similar in the *RPC* and *bRPV* cases than that of E_T^{miss} , making the effect on the M_{eff} cut itself to be of similar importance in both cases.

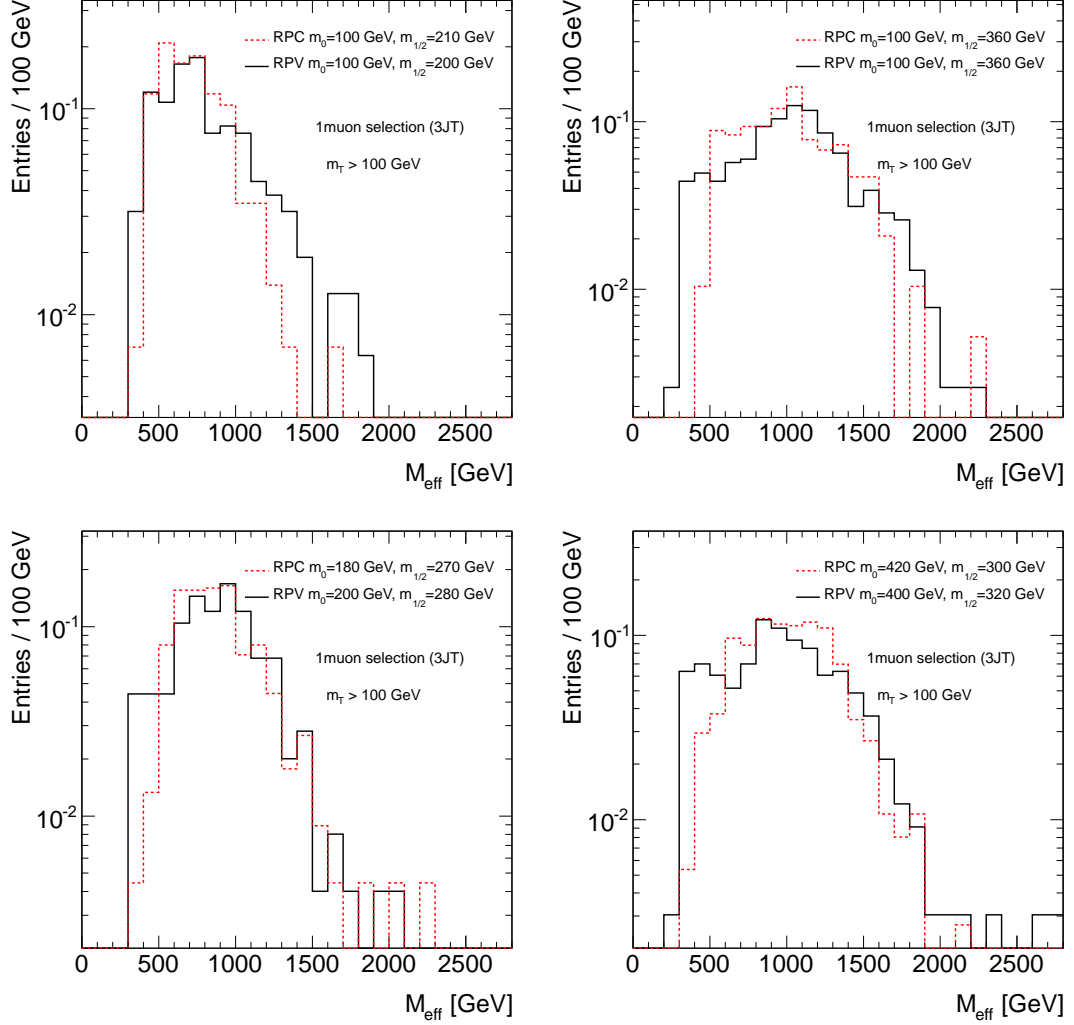


Figure 5.24: M_{eff} distributions for various mSUGRA signal points for *bRPV* SUSY (black continuous line) and nearby *RPC* SUSY (red dashed line) after 1-muon 3JT selection and m_T cut. The distributions are normalised to unity.

The m_T distributions in *RPC* and *bRPV* are very similar throughout the grid, as can be seen in Appendix D, where more details on the comparison between *RPC* and *bRPV* can be found for five mSUGRA points.

5.6 Results

This section presents the main results of the one-muon analysis, obtained by a profile log likelihood ratio (LLR) test. The profile LLR is obtained from a fit to measurements in a signal region and a set of background control regions. The results are obtained in three steps, called “background fit”, “discovery fit” and “exclusion fit” described below.

The profile LLR approach described here allows the simultaneous fit for the background and (if desired) the signal. Cross-contamination of backgrounds across control region boundaries and the propagation of statistical and systematic uncertainties is taken into account [118]. The method allows for a simultaneous fit to several channels.

5.6.1 Fit setup

Three different tests are used in practice, each with a different fit configuration.

- In the **background fit** configuration the signal region is excluded from the fitted data samples, and no signal contamination is assumed to be present in the background control samples. The nuisance parameters related to the signal strength, namely the signal cross section uncertainty, luminosity uncertainty, and signal Monte Carlo statistics uncertainty, are all fixed to zero. All nuisance parameters describing theoretical uncertainties applied when extrapolating the fitted background processes to the signal region, e.g. cross section uncertainties on e.g. the background processes in the SR, and the Monte Carlo statistics uncertainties on these background processes in the SR, are also turned off in the fit.
- The **discovery fit** tests for a (positive) excess of events above the total background-only expectation in the signal region. In different words, it tests the Standard Model hypothesis in the signal region. In this configuration all signal contamination in the background CRs is taken to be zero. (Note that, if the contamination is actually non zero, this assumption leads to a conservative p -value for discovery, since the background in the SR is overestimated.) The signal strength parameter μ is fixed to one, and the fit is for the number of signal event in the SR. As no model-specific interpretation of the signal excess is made, the nuisance parameters for the signal cross section uncertainty, the luminosity uncertainty, and signal Monte Carlo statistics uncertainty, are fixed to zero in the fit. The discovery fit gives the same prediction for the background in the signal region as the background fit; the difference is that the discovery fit quantifies the level of agreement between the number of events observed in the signal region and the number of events expected from known sources.
- The **exclusion fit** tests for a specific new physics model. Signal predictions are used for both the SR and CRs. A common signal strength parameter μ is left free in the fit, which simultaneously describes the signal expectation in the SR and each CR. As a model-specific interpretation of the signal excess is made, the nuisance parameters for the signal cross section uncertainty, the luminosity uncertainty, and signal Monte Carlo statistics uncertainty are turned on in the fit and left free.

Note that a discovery plane typically shows the reach in discovery sensitivity for a two-dimensional grid of related specific new physics models. An example is the discovery reach in the mSUGRA $m_0 - m_{1/2}$ plane, with fixed values of $\tan\beta$ and A_0 . Since here one tests the discovery against a set of specific models with detailed predictions for the signal expectation in the SR and CRs with associated uncertainties, the fit configuration used to make such figures is the “exclusion fit”, and not the “discovery fit” configuration.

5.6.2 Summary of transfer function values

Table 5.8 lists the transfer function central values from the combined TR and WR control regions (TWR) into the various signal regions for the processes WZ and top . In practice, the transfer functions for signal vary as a function of the $bRPV$ - $mSUGRA$ grid point. Uncertainties on the central value have been calculated on several contributions: b -tagging fraction, jet/ MET energy scale and resolution, lepton scale and resolution, Monte Carlo statistics, theory extrapolation and pile-up. The values in this table and the uncertainties found in Ref. [114] are used as main input to the fit discussed in the next section.

Table 5.8: Transfer function central values between the combined TR and WR control regions (TWR) and the four signal regions considered.

Region	$C_{TWR \rightarrow SR}^{WZ}$	$C_{TWR \rightarrow SR}^{tt}$
3JL	0.048	0.222
3JT	0.015	0.042
4JL	0.011	0.023
4JT	0.001	0.003

5.6.3 Fit results

Tables 5.9 and 5.10 present the fit results per signal region. The results are obtained using the discovery fit, where the fitted signal excess in the signal region is allowed to become negative. The errors shown are the full uncertainties (statistical plus systematics) except for the error on the background estimate in each signal region, which is the systematic uncertainty only.

Some notes on the interpretation of the numbers in these tables: in the rows “Fitted bkg events”, the uncertainties quoted for the TR , WR , and $TR+WR$ equal the square-root of the numbers of observed events in these regions, i.e. they are only statistical in nature. This is by construction as, in each of these regions, the total expected number of events is constrained by a Poisson distribution, and this expected number consists of only top , W/Z , and QCD events (i.e. no signal events). Essentially, these numbers are to be interpreted as a null-check: the fit to the TR and WR exactly reproduces the numbers of observed events. The systematic uncertainties are visible on the individual fitted components, given in the rows underneath the Fitted bkg events entries. Due to negative correlations between the three background components, the uncertainties on the individual background components can be larger than the uncertainty on the total background sum. The individual top and W/Z background estimates obtained from the TR and WR —including systematic uncertainties—are then extrapolated to signal region. In the signal region, the discovery fit also contains a signal component, which is allowed to become negative. For the SR, the “Fitted bkg events” element shows the systematic uncertainties on the total background estimate, including the propagated statistical uncertainties from the control regions, but does not reflect the statistical uncertainty of the signal region.

Going to the actual interpretation of the results, no significant signal excess is observed in any of the signal regions. This is reflected in the fitted number of background events in the signal regions, which is always compatible with the observed number of events. The 3JL, 3JT and 4JL regions show downward fluctuations in the number of observed events compared with the background expectations. The 4JT region shows a minor excess of events. The Monte Carlo QCD estimates are provided for illustration purposes only—they are not used in the fit. When comparing the fitted numbers to the nominal simulation predictions (bottom part of the tables),

one should bear in mind that global scale-level uncertainties (e.g. from the luminosity) do not enter the fit results. When making such a comparison, however, these uncertainties need to be considered for the simulation predictions (non-global uncertainties are part of the fit result errors). Therefore, the predicted simulation numbers have a global uncertainty of at least $\pm 3.7\%$ (luminosity). The fitted number of WZ events are in good agreement with expectations. The estimated number of top events is about 10 to 20% higher in both the WR and TR than the MC expectation. Note that these absolute MC predictions do not contain any theory or luminosity uncertainty. The number of top events is consistent though with the latest ATLAS $t\bar{t}$ cross section measurement of 176 ± 5 (stat.) $^{+14}_{-11}$ (syst.) $^{+8}_{-7}$ (lumi.) pb [134]. This increase is consistent with the small discrepancy seen between data and Monte Carlo in the M_{eff} distributions in Figures 5.6, corresponding to the inclusive 3 and 4 jet channels. The fitted increase in the top contribution is propagated to the signal regions where, within the background uncertainty, the fit prediction is always compatible with (though higher than) the corresponding Monte Carlo estimate. The fitted number of top and WZ events are strongly anti-correlated due to the allowed migration between the WR and TR as introduced by the b -tagging uncertainty. This anti-correlation can be seen from the uncertainties of the combined top+ WZ events (in particular in the TR and WR) in comparison to the individual top and WZ uncertainties. Note that the b -tagging uncertainty is also present in the SR, as the ratio of top to WZ events is different in the SR than in the combined $TR+WR$. In the SR, however, the corresponding top and WZ uncertainties are dominated by uncorrelated extrapolation uncertainties (e.g. the theory uncertainties). Only upper limits are set for the number of QCD events in each signal region. The fit results clearly indicate that the QCD estimates from Monte Carlo are typically insufficient and/or affected by limited Monte Carlo statistics when compared with the data-driven estimates. Finally, a similar under-estimate of the Monte Carlo prediction for the top background is observed as in the tight regions.

5.6.4 Impact of systematic uncertainties

Table 5.11 shows the breakdown of the uncertainties on the background estimates of each signal region into various statistical and systematic components. For all SRs, the full uncertainty is dominated by the systematic uncertainty on the number of events (expected) in the signal region. The dominant systematic uncertainties, similar between the various signal regions, are:

- Jet energy scale and resolution.
- Limited MC statistics, in particular for the W and top sample in the signal region. This uncertainty shows up in the extrapolation of the fitted number of W and top events into the SR.
- Theory uncertainties on the W and top extrapolation into the SR.

5.6.5 Limits on visible cross sections and discovery p -values

The model-independent CL_S upper limits [135] on the observed and expected number of signal events at 95% confidence level (CL) in the various signal regions have been derived using the technique described in Ref. [118]. To test the Standard Model null hypothesis, pseudo-experiments are generated using the background-only expectation. Each pseudo-experiment is fit twice: once with the signal strength parameter fixed to zero ($\mu = 0$) and once with the signal parameter left free, but constrained to be greater than zero. The second fit tests for background fluctuations faking a potential signal. Each pseudo-experiment gets assigned a test statistic

Table 5.9: Signal regions: 3-jets loose and tight. Fit results for an integrated luminosity of 1035 pb^{-1} . The results are obtained from the control regions using the discovery fit (see text for details). Nominal MC expectations (normalised to MC cross sections) are given for comparison. The Monte Carlo QCD estimates are provided for illustrational purposes only, and are not used in the fit. The errors shown are the statistical plus systematic uncertainties, except for the error on the background estimate in the signal region, which is the systematic uncertainty only.

3-jets channels	3JL SR	3JT SR	TR	WR
Observed events	58	11	166	413
Fitted bkg events	64 ± 19	13.9 ± 4.3	166 ± 13	413 ± 20
Fitted top events	47 ± 16	8.9 ± 3.2	142 ± 14	69.7 ± 7.1
Fitted WZ events	16.6 ± 9.4	5.0 ± 3.2	19.0 ± 4.8	322 ± 23
Fitted top+WZ events	64 ± 19	22.8 ± 5.4	161 ± 13	392 ± 21
Fitted QCD events	0.0 ± 0.0	$0.0^{+0.6}_{-0.0}$	5.4 ± 2.2	21.6 ± 5.7
MC exp. SM events	58	13.4	139.1	465
MC exp. top events	38	7.3	115	56.8
MC exp. WZ events	20.1	6.1	23.2	393
MC exp. top+WZ events	58	13.4	138.2	450
MC exp. QCD events	0.0 ± 0.0	0.0 ± 0.0	0.9 ± 0.8	15.1 ± 13.1

Table 5.10: Signal regions: 4-jets loose and tight. Fit results for an integrated luminosity of 1035 pb^{-1} . The results are obtained from the control regions using the discovery fit (see text for details). Nominal MC expectations (normalised to MC cross sections) are given for comparison. The Monte Carlo QCD estimates are provided for illustrational purposes only, and are not used in the fit. The errors shown are the statistical plus systematic uncertainties, except for the error on the background estimate in the signal region, which is the systematic uncertainty only.

4-jets channels	4JL SR	4JT SR	TR	WR
Observed events	50	7	1448	1623
Fitted bkg events	53 ± 16	6.0 ± 2.7	1448 ± 38	1623 ± 40
Fitted top events	39 ± 13	4.7 ± 2.2	1319 ± 45	382 ± 13
Fitted WZ events	14.1 ± 8.5	1.4 ± 1.1	91 ± 19	1169 ± 46
Fitted top+WZ events	53 ± 16	6.1 ± 2.5	1410 ± 40	1552 ± 44
Fitted QCD events	0.0 ± 0.0	$0.0^{+0.6}_{-0.0}$	38 ± 10	72 ± 16
MC exp. SM events	51	5.7	1341	1778
MC exp. top events	36	4.3	1231	357
MC exp. WZ events	14.2	1.4	92	1185
MC exp. top+WZ events	51	5.7	1323	1542
MC exp. QCD events	0.0 ± 0.0	0.0 ± 0.0	18 ± 13	236 ± 170

Table 5.11: Breakdown of the dominant systematic uncertainties on background estimates in the various signal regions. Note that the individual uncertainties can be correlated, and do not necessarily add up quadratically to the total background uncertainty.

Muon channel	SR3jL	SR3jT	SR4jL	SR4jT
Total statistical ($\sqrt{N_{\text{obs}}}$)	± 7.62	± 3.32	± 7.07	± 2.65
Total background systematic	+19.27 -19.27	+4.35 -4.31	+15.79 -15.80	+2.71 -2.66
Jet/MET energy resolution	± 8.99	± 1.06	± 0.92	± 0.52
Jet/MET energy scale	± 6.99	± 0.18	± 9.06	± 1.61
Lepton energy resolution	± 0.00	± 0.00	± 0.00	± 0.00
Lepton energy scale	± 0.75	± 0.26	± 1.42	± 0.54
b -tagging	± 1.00	± 0.19	± 0.87	± 0.12
MC stat top	± 5.39	± 2.12	± 4.01	± 1.40
MC stat W	± 2.52	± 1.37	± 2.57	± 0.65
QCD fake rate	< 0.1	< 0.1	< 0.1	< 0.1
QCD real rate	± 0.53	± 0.14	± 0.44	< 0.1
Theory top	± 12.87	± 2.44	± 9.99	± 1.19
Theory W	± 8.80	± 2.66	± 7.28	± 0.70
Pile-up	± 3.45	± 0.75	± 2.73	± 0.31

defined from the difference in likelihoods between the two fits. This fit procedure is also applied to the data sample. The discovery p -value is defined as the fraction of pseudo-experiments with a test statistic value greater than the one found in data.

The CL_S upper limit on the observed (S_{obs}^{95}) and expected (S_{exp}^{95}) number of events are given in Table 5.12. The same table also shows the 95% CL upper limits on the visible cross section, $\langle \epsilon\sigma \rangle^{95}$, which equal the limits on the observed number of signal events divided by the luminosity. The last two columns of this table indicate the CL_B values and discovery p -values ($p(\mu = 0)$). The CL_B values indicate the amount of (possible) downward fluctuation of the background, and are needed for the calculation of CL_S limits. See Ref. [114] for CL_S limits on mSUGRA/CMSSM models.

The signal regions are all consistent with the Standard Model-only hypothesis.

5.6.5.1 Limits on MSUGRA/CMSSM

The procedure used here follows the ATLAS Statistics Forum recommendations to set limits [136], and is explained in detail in Ref. [118].

Summary of signal systematics

When computing exclusion limits, systematic uncertainties on the cross section and acceptance are taken into account. Bear in mind that global scale-level uncertainties (e.g. from the luminosity and the trigger) do not affect the background evaluation, which is data-driven, but do affect the signal interpretation, which requires an explicit signal event prediction obtained from Monte Carlo. Theoretical uncertainties on the NLO cross section are determined by fluctuating the renormalisation/factorisation scale up and down by a factor of 2, and by varying the α_S and PDF choice. The effects of detector systematics are studied by scaling the jet four-

Table 5.12: First three columns: CL_S upper limits on the visible cross section ($\langle\epsilon\sigma\rangle^{95}$) and on the observed (S_{obs}^{95}) and expected (S_{exp}^{95}) number of events. The last two columns indicate the CL_B value, needed for a CL_S calculation, and discovery p -value ($p(\mu = 0)$).

Signal Region	$\langle\epsilon\sigma\rangle^{95}$ [fb]	S_{obs}^{95}	S_{exp}^{95}	CL_B	$p(\mu = 0)$
SR3jL	36.3	37.6	$41.1^{+16.1}_{-7.2}$	0.39	0.60
SR3jT	9.6	9.9	$11.4^{+4.5}_{-2.0}$	0.31	0.70
SR4jL	31.3	32.4	$34.4^{+13.8}_{-6.5}$	0.42	0.58
SR4jT	8.6	8.9	$8.0^{+3.0}_{-1.6}$	0.63	0.39

momenta coherently by the uncertainty on the JES, as well as smearing the jets independently by the JER, as is done on Standard Model MC samples. Typical magnitudes of the signal uncertainties are 10 – 20%. Due to large variation in signal efficiency across the MSUGRA ($m_0 - m_{1/2}$) plane, the uncertainty due to limited MC statistics for each grid point varies between 15 – 50%. Finally, a flat 1% systematic uncertainty is applied to account for the effect of jet cleaning cuts on the signal events. These cuts are not applied to Monte Carlo data sets. It is estimated that such cuts applied to 20 GeV fail 0.1% of simulated jets, hence for signal points that typically have 10 such jets, the difference will be no greater than 1%. Trigger uncertainties of 3% are assigned. A common 3.7% uncertainty is assigned for the luminosity estimate.

Exclusion limits on bilinear RPV model

By applying the four selections, exclusion regions for the bRPV-mSUGRA model are obtained in all but one SR, the 4jL. Figures 5.25, 5.26 and 5.27 show the observed and expected 95% CL limits in the ($m_0 - m_{1/2}$) plane for the 3jL, 3jT and 4jT selection. For the 4jL selection no exclusion was obtained due to the low sensitivity for the signal in this region. The plots also show the evolution of the LSP decay length, $c\tau$, in the ($m_0, m_{1/2}$) plane. With increasing $c\tau$ the efficiency of this analysis decreases rapidly due to the drop in the acceptance mainly of the cosmic veto and to a lesser extend of the $E_{\text{T}}^{\text{miss}}$ cut. The focus is instead on signal points with sufficiently prompt LSP decays. We thus do not consider low $m_{1/2}$ values around $m_{1/2} \simeq 200$ GeV if they lead to significant decay lengths. The exclusion limits set by the tight cuts are much stricter than the ones obtained by the loose selection, as is the case for the bounds acquired for R -parity conserving CMSSM (see Ref. [114]). The exclusion limits set here are relevant for other RPV supersymmetric models with bilinear R -parity breaking terms in the superpotential such as the μ SUSM [?], where similar neutralino LSP decay modes are predicted [?].

5.7 Conclusions

In this chapter, a search for bilinear R -parity violating supersymmetry is presented in final states containing one isolated muon, jets and missing transverse momentum from $\sqrt{s} = 7$ TeV proton-proton collisions at the LHC, with a luminosity of 1.04 fb^{-1} recorded by ATLAS in 2011.

Good agreement is obtained between the observed number of events in the signal regions and the Standard Model expectations. Hence, limits are set on contributions of new physics to the signal regions. The result is interpreted in the bilinear RPV scenario, for which limits have not been shown before at hadron colliders. The expected and observed exclusion limits set in the bRPV-mSUGRA/CMSSM $m_0 - m_{1/2}$ plane can be found in Figure 5.27, discarding this model at 95% confidence level for squark masses lower than 760 GeV ($m_{\tilde{g}} = m_{\tilde{q}}$; $c\tau_{\text{LSP}} < 15$ mm, remind

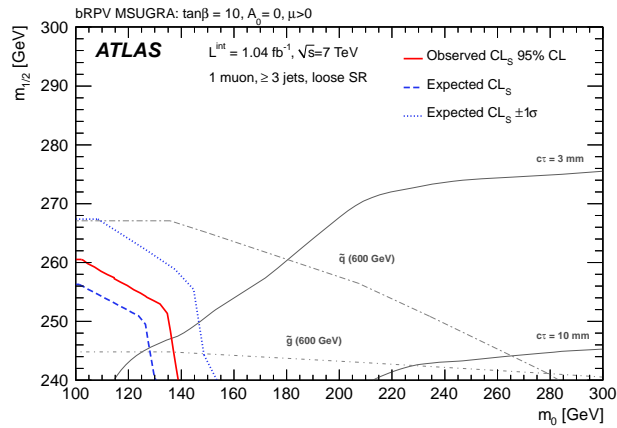


Figure 5.25: Exclusion plots for the bilinear RPV model in $mSUGRA$ parameter space applying the 3-jets loose (3JL) selection. The contours for the LSP decay length of 3 mm and 10 mm are also shown.

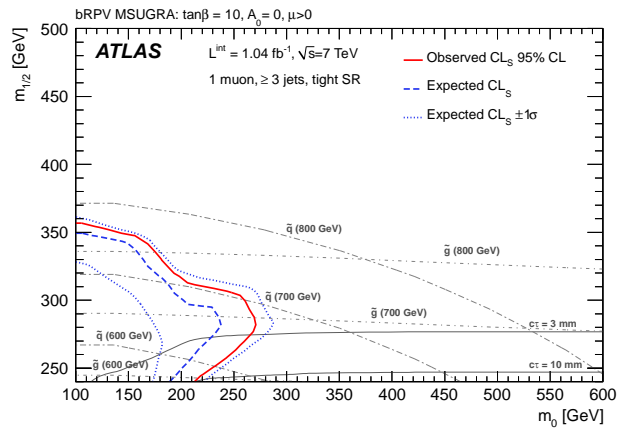


Figure 5.26: Exclusion plots for the bilinear RPV model in $mSUGRA$ parameter space applying the 3-jets tight (3JT) selection. The contours for the LSP decay length of 3 mm and 10 mm are also shown.

that this analysis does not explore the $m_{1/2} < 200$ GeV area).

In addition to the $bRPV$ interpretation, two further models are used to interpret the results. In the R -parity conserving $MSUGRA/CMSM$ model, the exclusion limits significantly improve with respect to the previous result [112]. The results are also used to set cross section limits in the simplified models for gluino-gluino and squark-squark production with subsequent one cascade decays. The limits are also used to present exclusion planes in the gluino (squark) LSP mass plane. More information about these exclusion limits can be found in Ref. [113, 114].

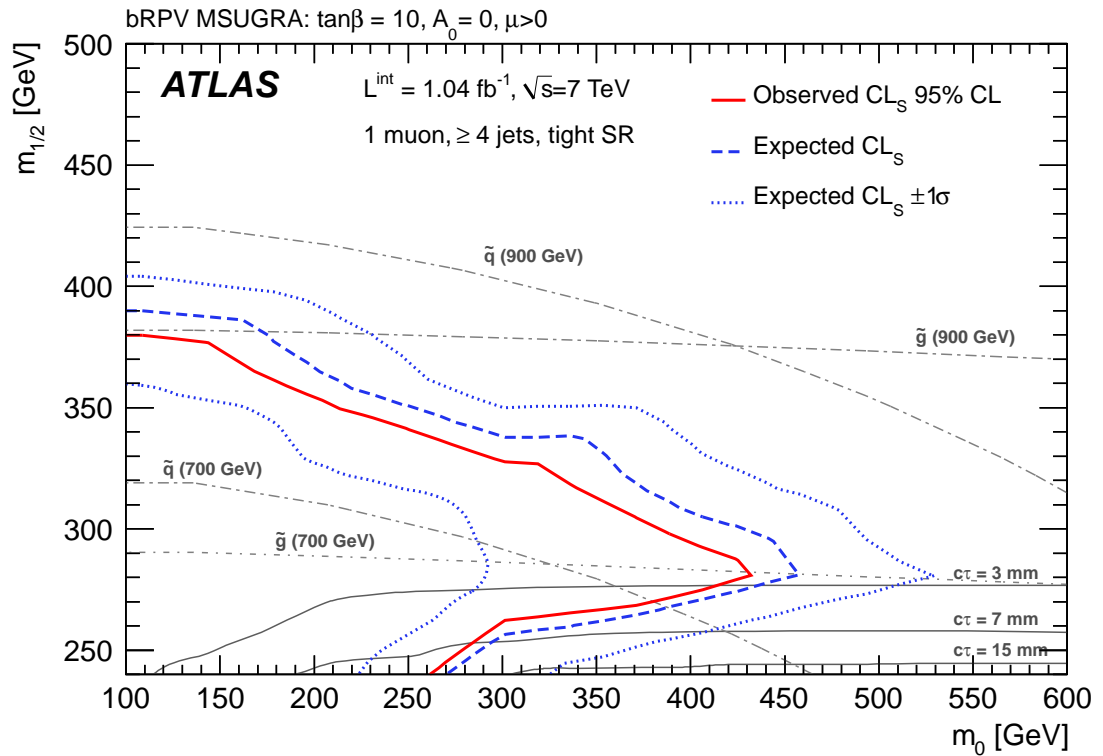


Figure 5.27: Exclusion plot for the bilinear *RPV* model in *mSUGRA* parameter space applying the 4-jets tight (4JT) selection. The expectation for the $m_{1/2} = 240$ GeV points that were not simulated is based on efficiency interpolation. The relative uncertainty for these points is assumed to be 30%. The contours for the LSP decay length of 3, 7 and 15 mm are also shown.

Chapter 6

AtlFast-II validation for SUSY

6.1 Introduction

ATLAS searched for supersymmetric signatures in several models with the 2010 data set [115, 116, 137] finding no evidence for physics beyond the SM and extending significantly the constraints to different types of SUSY models. This situation imposed new challenges, giving rise to a large number of Monte Carlo (MC) sample production requests by the SUSY Working Group. First, there is the need of pursuing the analyses available at that time with more data to become more sensitive to higher mass scales. Second, there is also the need of extending those analyses to increase the sensitivity to more challenging topologies predicted by different SUSY models. Finally, negative results are interpreted in terms of exclusion limits on particular theoretical scenarios. This is usually presented in 2-dimensional grids, where each point is a combination of parameters in a particular model and where relatively large statistics and granularity are needed for precise estimations.

The simulation of the effect that the ATLAS detector has on such MC generated events requires a huge amount of computing resources in terms of CPU time and storage capabilities. In order to accelerate the simulation process and to save resources as much as possible, an alternative to the standard full simulation of events by the ATLAS framework has been developed: AtlFast-II (AF-II) [138] simulation. When simulating events with AF-II, a not-so-detailed description of the ATLAS detector is implemented in Geant-4, introducing a simplified version of the particles behaviour in their pass through the calorimeter, thus making the simulation process faster although less precise.

Since the SUSY processes have relatively large theoretical uncertainties (typically of the order of 20 – 25%) mainly due to the limited knowledge of the proton PDFs as well as renormalisation and factorisation scales, SUSY analysers considered the usage of the AF-II package, provided that the accuracy in describing the objects and the event yields are significantly better. The usage of AF-II reduces the simulation time and allows for more flexibility to the analysers.

A dedicated effort was made in order to evaluate the performance of the new AF-II package in the context of the SUSY needs. In this chapter these results are given, after which a summary and a proposal, which ended up in the usage of AF-II for actual analyses, is outlined. This results were presented in several meetings with the simulation and performance groups [139–142] and resumed in an ATLAS Communication Physics Note [143].

6.2 AtlFast-II description

ATLAS has implemented a detector simulation within the Athena software framework [92] based on Geant-4 [99], the standard simulation “full Geant-4”. However, due to the complexity of the ATLAS detector geometry, the full Geant-4 simulation can take very long times to simulate single physics events. Almost 80% of the full simulation time is spent simulating particles traversing the calorimetry, and about 75% of the full simulation time is spent simulating electromagnetic particles. The Fast G4 Simulation aims to speed up this slowest part of the full simulation by removing low energy electromagnetic particles from the calorimeter and replacing them with pre-simulated showers stored in memory. AtlFast-I [144] was developed for physics parameter space scans and studies that require very large statistics but do not require the level of detail contained in the full simulation. It only provides momenta for the reconstructed objects, without any detailed simulation of efficiencies and fakes. AtlFast-II aims at simulating events as fast as possible while still being able to run the standard ATLAS reconstruction. Hence, its output includes all the properties associated with a reconstructed object.

AF-II is a combination of full simulation and fast simulation:

- The simulation of the **Inner Detector** uses the full Geant-4 simulation, but only with the Inner Detector enabled.
- The **calorimeter** is simulated using FastCaloSim [145], replacing the calorimeter simulation with per-particle average shower-shapes. FastCaloSim uses the truth information of all interacting particles at the end of the inner detector volume as input to the calorimeter simulation. Instead of simulating the particle interactions with the detector material, the energy of single particle showers is calculated by FastCaloSim directly using parametrizations of the longitudinal and lateral energy profile. The parametrizations are based on a 30 million event sample of fully-simulated (i.e. simulated with Geant-4) single photons and charged pions in an energy range between 200 MeV and 500 GeV. All electron and photon showers are approximated by the photon parametrization and all hadronic showers are approximated by the charged pion parametrization.
- The **Muon System** uses full simulation, together with the inner detector. All particles run through Inner Detector full simulation, at the end of which all particles but muons are killed. Muons are simulated as in full simulation in the calorimeter and muon system.
- All necessary information for the **trigger** simulation is available in digitization, so the normal trigger simulation is applied.

For details on the full Geant-4 and AF-II descriptions see Ref. [128].

6.3 Validation setup

For this study, 18 different mSUGRA points were used. Both sets of samples, with AF-II and full Geant-4 simulations, were officially requested. The full Geant-4 samples are part of the central $mc10b$ production and add up a total of 329505 events. The AF-II samples amount to a total of 340000 events. Each of the full Geant-4 samples were normalised such that the number of events was the same as in the corresponding AF-II sample.

Both AF-II and full Geant-4 samples were generated using the same generator. They only differ in the simulation process, in which either AF-II or full Geant-4 simulation was used in order to produce the files. Then, these files were digitised and reconstructed identically in both cases.

Table 6.1: Description of the software used to produce the full Geant-4 and AF-II samples used for this study.

Production tag	Release	full/fast sim	Comment
e598	15.6.12.5	both	event generation with Herwig++
e757	15.6.14.4	both	event generation with Herwig++
s1213	15.6.12.9	fast	EVNT→HITS
s933	15.6.12.9	full	EVNT→HITS (50 evts/job)
s946	15.6.12.9	full	merging of HITS files
d544	16.6.4.3	fast	HITS→RDO
r2366	16.6.4.3	fast	RDO→AOD
r2302	16.6.4.3	full	HITS→RDO→AOD
r2300	16.6.4.2	full	AOD merging
p543	16.6.4.2	both	AOD→NTUP_SUSY

The specific data sets used for this study are listed below:

AtlFast-II:

```
mc10_valid.106484.SU4_herwigpp_susy.merge.NTUP_SUSY.e598_s1213_d544_r2366_p543/
mc10_valid.123301.SU_100_60_0_10_P_herwigpp_susy.merge.NTUP_SUSY.e757_s1213_d544_r2366_p543/
mc10_valid.123302.SU_100_90_0_10_P_herwigpp_susy.merge.NTUP_SUSY.e757_s1213_d544_r2366_p543/
mc10_valid.123320.SU_180_60_0_10_P_herwigpp_susy.merge.NTUP_SUSY.e757_s1213_d544_r2366_p543/
mc10_valid.123321.SU_180_90_0_10_P_herwigpp_susy.merge.NTUP_SUSY.e757_s1213_d544_r2366_p543/
mc10_valid.123605.SU_1380_60_0_10_P_herwigpp_susy.merge.NTUP_SUSY.e757_s1213_d544_r2366_p543/
mc10_valid.123606.SU_1380_90_0_10_P_herwigpp_susy.merge.NTUP_SUSY.e757_s1213_d544_r2366_p543/
mc10_valid.123624.SU_1460_60_0_10_P_herwigpp_susy.merge.NTUP_SUSY.e757_s1213_d544_r2366_p543/
mc10_valid.123625.SU_1460_90_0_10_P_herwigpp_susy.merge.NTUP_SUSY.e757_s1213_d544_r2366_p543/
mc10_valid.123337.SU_180_570_0_10_P_herwigpp_susy.merge.NTUP_SUSY.e757_s1213_d544_r2366_p543/
mc10_valid.123338.SU_180_600_0_10_P_herwigpp_susy.merge.NTUP_SUSY.e757_s1213_d544_r2366_p543/
mc10_valid.123423.SU_580_300_0_10_P_herwigpp_susy.merge.NTUP_SUSY.e757_s1213_d544_r2366_p543/
mc10_valid.123424.SU_580_330_0_10_P_herwigpp_susy.merge.NTUP_SUSY.e757_s1213_d544_r2366_p543/
mc10_valid.123622.SU_1380_570_0_10_P_herwigpp_susy.merge.NTUP_SUSY.e757_s1213_d544_r2366_p543/
mc10_valid.123623.SU_1380_600_0_10_P_herwigpp_susy.merge.NTUP_SUSY.e757_s1213_d544_r2366_p543/
mc10_valid.123641.SU_1460_570_0_10_P_herwigpp_susy.merge.NTUP_SUSY.e757_s1213_d544_r2366_p543/
mc10_valid.123642.SU_1460_600_0_10_P_herwigpp_susy.merge.NTUP_SUSY.e757_s1213_d544_r2366_p543/
mc10_valid.123443.SU_660_330_0_10_P_herwigpp_susy.merge.NTUP_SUSY.e757_s1213_d544_r2366_p543/
```

full sim MC10b:

```
mc10_7TeV.106484.SU4_herwigpp_susy.merge.NTUP_SUSY.e598_s933_s946_r2302_r2300_p543/
mc10_7TeV.123301.SU_100_60_0_10_P_herwigpp_susy.merge.NTUP_SUSY.e757_s933_s946_r2302_r2300_p543/
mc10_7TeV.123302.SU_100_90_0_10_P_herwigpp_susy.merge.NTUP_SUSY.e757_s933_s946_r2302_r2300_p543/
mc10_7TeV.123320.SU_180_60_0_10_P_herwigpp_susy.merge.NTUP_SUSY.e757_s933_s946_r2302_r2300_p543/
mc10_7TeV.123321.SU_180_90_0_10_P_herwigpp_susy.merge.NTUP_SUSY.e757_s933_s946_r2302_r2300_p543/
mc10_7TeV.123605.SU_1380_60_0_10_P_herwigpp_susy.merge.NTUP_SUSY.e757_s933_s946_r2302_r2300_p543/
mc10_7TeV.123606.SU_1380_90_0_10_P_herwigpp_susy.merge.NTUP_SUSY.e757_s933_s946_r2302_r2300_p543/
mc10_7TeV.123622.SU_1460_60_0_10_P_herwigpp_susy.merge.NTUP_SUSY.e757_s933_s946_r2302_r2300_p543/
mc10_7TeV.123623.SU_1460_90_0_10_P_herwigpp_susy.merge.NTUP_SUSY.e757_s933_s946_r2302_r2300_p543/
mc10_7TeV.123337.SU_180_570_0_10_P_herwigpp_susy.merge.NTUP_SUSY.e757_s933_s946_r2302_r2300_p543/
mc10_7TeV.123338.SU_180_600_0_10_P_herwigpp_susy.merge.NTUP_SUSY.e757_s933_s946_r2302_r2300_p543/
mc10_7TeV.123423.SU_580_300_0_10_P_herwigpp_susy.merge.NTUP_SUSY.e757_s933_s946_r2302_r2300_p543/
mc10_7TeV.123424.SU_580_330_0_10_P_herwigpp_susy.merge.NTUP_SUSY.e757_s933_s946_r2302_r2300_p543/
mc10_7TeV.123622.SU_1380_570_0_10_P_herwigpp_susy.merge.NTUP_SUSY.e757_s933_s946_r2302_r2300_p543/
mc10_7TeV.123623.SU_1380_600_0_10_P_herwigpp_susy.merge.NTUP_SUSY.e757_s933_s946_r2302_r2300_p543/
mc10_7TeV.123641.SU_1460_570_0_10_P_herwigpp_susy.merge.NTUP_SUSY.e757_s933_s946_r2302_r2300_p543/
mc10_7TeV.123642.SU_1460_600_0_10_P_herwigpp_susy.merge.NTUP_SUSY.e757_s933_s946_r2302_r2300_p543/
mc10_7TeV.123443.SU_660_330_0_10_P_herwigpp_susy.merge.NTUP_SUSY.e757_s933_s946_r2302_r2300_p543/
```

Details of the software releases used for the entire processing chain are given in Table 6.1.

Physics-wise, the samples were all generated within the mSUGRA SUSY framework. The first sample, SU4, is one of the main reference samples for the E_T^{miss} -based searches. The other samples were picked from one of the existing SUSY signal grids. The mSUGRA parameters of

each sample can be found from the actual name. For instance, the sample SU_660_330_0_10_P was generated with mSUGRA parameters $m_0=660$, $m_{1/2}=330$, $A_0=0$, $\tan\beta=10$ and $\mu > 0$, where P stands for a positive value of μ .

The different samples were all used together in the comparisons, hence mixing different SUSY final state configurations. In this way, a larger statistic sample was obtained and, in addition, a wide variety of SUSY signatures could be explored at the same time: at large m_0 , they are dominated by gluino-gluino production, which gives longer decay chains with more jets, whereas at large $m_{1/2}$, the squark-gluino and squark-squark production processes dominate, which tend to produce shorter decay chains with more energetic objects.

In order to estimate the gain that AF-II offers in simulation time with respect to full Geant-4 for these complex final states, two of the samples were examined. Table 6.2 shows a summary of the results. These were obtained averaging only the execution times (pilot Timing) of different jobs and they are subject to possible different machine performances on the grid. This is the reason of the differences between times in processes that should be approximately the same (for example, the reconstruction time). Thus, it could be interpreted as an estimation of the uncertainty. Overall, AF-II provides a gain of 8-9 in simulation time, which is reduced to 4-6 when considering the whole process. In addition, in this summary it is not taken into account the fact that the fast simulation jobs can skip the merging steps since they contain more events per job already. This is another factor that reduces the total time it takes from the submission of the job until it is converted to a SUSY ntuple.

Table 6.2: Time spent in each of the different steps followed in full Geant-4 and AF-II for two different SUSY samples. Last two rows show the factor in speed gain by using AF-II considering only the simulation time (sim) or considering the total amount of time (tot). The numbers take only into account the execution time (pilot Timing) and have been approximately averaged for the different jobs.

Step	$m_0 = 1460$ $m_{1/2} = 90$ [GeV]		$m_0 = 180$ $m_{1/2} = 570$ [GeV]	
	full Geant-4 (min/ev)	AF-II (min/ev)	full Geant-4 (min/ev)	AF-II (min/ev)
evgen	0.004	0.004	0.004	0.004
simulation	11.1	1.4	12.2	1.4
merging	0.03	–	0.03	–
digit	–	0.34	–	1.1
recon	0.67	0.31	0.73	0.49
merging	0.01	–	0.01	–
D3PD	0.03	0.03	0.03	0.03
AF-II/full (sim)		7.9		8.9
AF-II/full (tot)		5.7		4.4

6.4 Object definition

The different object definitions follow the Combined Performance group recommendations and are the ones used in the current SUSY analyses:

jets

- AntiKt4 Topo
- $p_T > 20$ GeV
- $|\eta| < 2.8$

b-jets

- AntiKt4 Topo
- $p_T > 20$ GeV
- $|\eta| < 2.8$
- $SV0 > 5.85$ (def. in Section 2.3.6.6)

electrons

- $p_T > 20$ GeV
- $|\eta| < 2.47$
- author = 1 or 3
- "IsEM" & ElectronMedium = 0
- "el_LOQ" & BADCLUSELECTRON = 0

signal electrons

- To be used by the 1 electron channel selection
- $p_T > 25$ GeV
- $|\eta| < 2.47$
- author = 1 or 3
- "IsEM" & ElectronTight_WithTrackMatch = 0
- "el_LOQ" & BADCLUSELECTRON = 0
- $\text{IsoPtCone02}/p_T < 0.1$ GeV

muons

- $p_T > 10$ GeV
- $|\eta| < 2.4$
- IsCombined OR
IsLowPtReconstructed = 1
- mu_staco_tight = 1

signal muons

- To be used by the 1 muon channel selection
- $p_T > 10$ GeV
- $|\eta| < 2.4$
- IsCombined OR
IsLowPtReconstructed = 1
- mu_staco_tight = 1
- IsoPtCone02 < 1.8 GeV
- z0_exPV < 10

photons

- $p_T > 20$ GeV
- $|\eta| < 2.5$
- PhotonTight

taus

- ¹⁾
- $p_T > 15$ GeV
 - $|\eta| < 2.5$

H_T

- $H_T = \sum_{i,j,k} p_T(\text{jet}^i) + p_T(\text{muon}^j) + p_T(\text{electron}^k)$
i = 3 leading jets,
j = all selected muons,
k = all selected electrons;

missing transverse energy

- $E_T^{\text{miss}} = E_{T,\text{RefFinal}}^{\text{miss}}$ (def. in Section 2.3.6.7)

transverse mass

- $m_T = \sqrt{2 \cdot p_T^l \cdot E_T^{\text{miss}} \cdot (1 - \cos(\Delta\phi(l, E_T^{\text{miss}})))}$

effective mass

- $M_{\text{eff}} = E_T^{\text{miss}} + H_T$

¹⁾Due to a bug in producing the files, the neural network discriminator for taus was always set to dummy values and a check on this variable was not possible. Thus, all the taus in the tau container have been considered here and further checks will be performed in the future.

6.5 Results

The comparison between AF-II and full Geant-4 is performed over the samples listed in Section 6.3 at two different levels: description of the objects and quantities used in SUSY analyses and the performance in baseline event selections.

6.5.1 Description of objects

In SUSY searches, many different physical objects and quantities are used covering different range in p_T and η . Comparisons between full Geant-4 and AF-II simulations are performed on each of them, leading to the following results:

Jets Kinematic distributions for AF-II jets are in good agreement with respect to those generated using full Geant-4, except for a small deficit of AF-II jets, specially at lower p_T ($\sim 3\%$ when selecting jets with $p_T > 20$ GeV, dropping to $\sim 1.5\%$ at $p_T > 30$ GeV). Other distributions such as LArQuality, jet timing, electromagnetic fraction and EMJES show good agreement. Figure 6.1, shows the comparison of the inclusive jet p_T distributions for full Geant-4 and AF-II simulations with the corresponding jet energy scale (JES) uncertainties. The differences between the simulations account for approximately half the uncertainty from JES in the first bin, dropping rapidly to a negligible difference in the rest of the distribution.

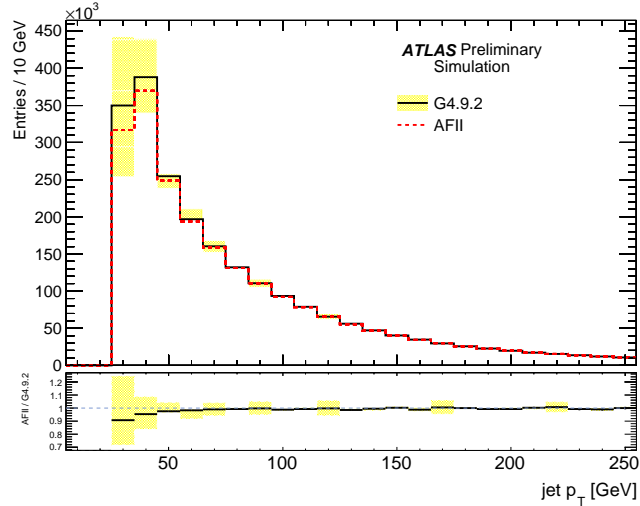


Figure 6.1: Comparison of the inclusive jet p_T distribution for full Geant-4 and AF-II, the yellow band corresponding to the jet energy scale uncertainty variations.

***b*-tagging** Since the inner detector is simulated using full Geant-4, no significant differences are observed when *b*-tagging is applied to the jets. Comparisons were made after requiring SV0 tagger (see Section 2.3.6.6) to be above 5.85 and showing separately the jets matched to a *b*-quark (labelled with a *pdgId* of 5 or -5, using the standard tool from the *b*-tagging group) and those which do not match. Deviations are below 1%.

Electrons The number of AF-II electrons after applying the selection cuts except for the isolation is $\sim 1.4\%$ lower than in full Geant-4. The agreement is at the 1% level when the

electron is found by the cluster based egamma algorithm (author= 1). Thus, the main differences come from the electrons found by both the cluster based and track based egamma algorithms (author= 3). These differences are lower for electrons associated to true electrons. The matching is performed using the egamma standard truth matching tool, after removing hadrons and conversions²⁾. The difference is higher for fake electrons, $\sim 10\%$, but depends on the p_T . These deviations are most probably due to inaccuracies in shower description, which are currently being corrected. However, they are well below the theoretical uncertainties in SUSY signals and the impact in 0-lepton or 1-lepton final states should be small. In Figure 6.2 the p_T of electrons is shown for truth matched and fake electrons. Deviations in the kinematic region of p_T between 20 and 25 GeV have been investigated since they affect some of the 2-lepton final states as will be discussed in Appendix E.

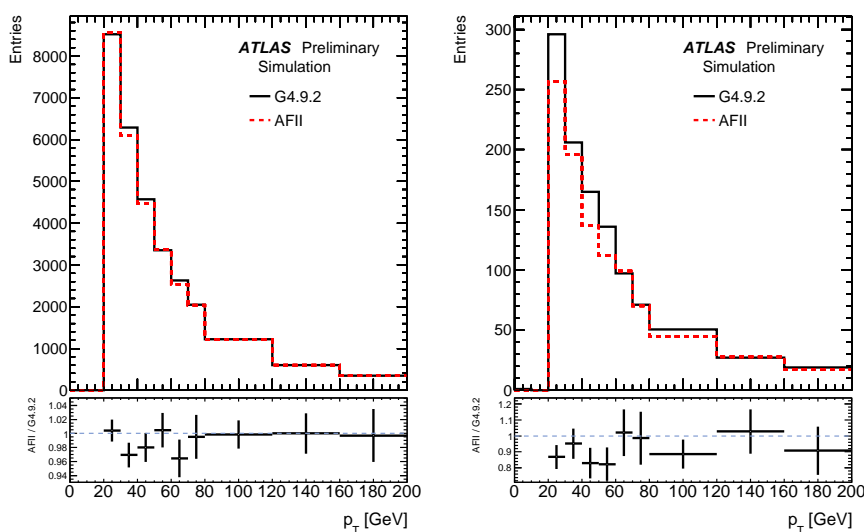


Figure 6.2: Comparison of electron p_T distributions for full Geant-4 and AF-II, for truth matched electrons (left) and fakes (right). No isolation criteria to the electrons have been imposed and details of the matching are given in the text.

Muons Good agreement is expected in muons because they are simulated using full Geant-4. Differences could only arise from energy depositions in the calorimeter, affecting the isolation condition and punch-through muons. Distributions of the isolation energy in a cone of 0.2, p_T , η , ϕ , charge and number of TRT hits show that deviations are lower than 0.1%. Figure 6.3 shows the muon p_T and isolation variable distributions for the two simulations.

Taus Good agreement is observed for taus in p_T , η and ϕ distributions. There is also a good agreement for all the tau reconstruction algorithms and also for the electron and muon veto terms. In complex distributions such as the Boosted Decision Tree (BDT) output a small shift towards higher values of the AF-II distribution with respect to full Geant-4 is observed ($\sim 7\%$ shift in the mean value of the distribution). The difference is smaller ($\sim 3\%$) in the interesting region where the cut above 0.2 is implemented, which is the loose

²⁾`el_truth_matched && el_truth_barcode < 200000 && abs(el_truth_type) == 11 && el_truth_status == 1`

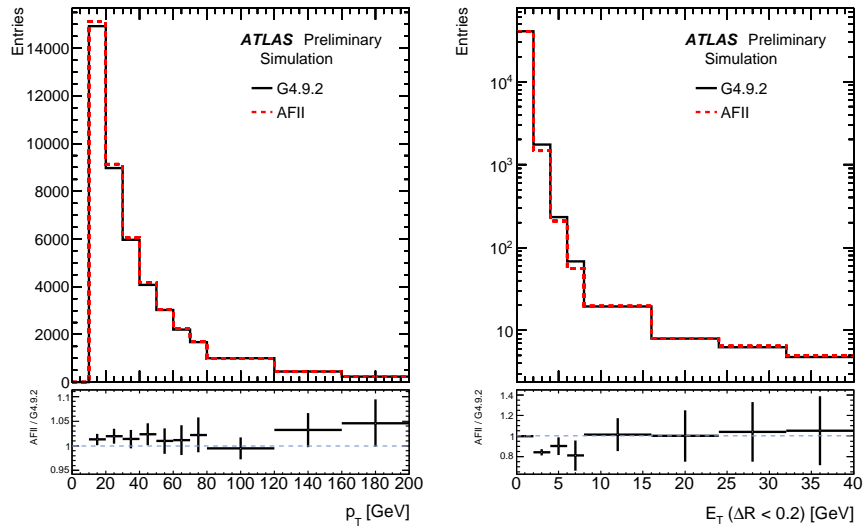


Figure 6.3: Comparison of muon p_T and isolation distributions for full Geant-4 and AF-II.

identification cut. This translates into a good description on the number of taus passing the loose or medium criteria. After applying the medium BDT requirement, deviations in the number of reconstructed taus above 20 (25) GeV matched to true taus are of the order of 4% (1.5%). Figure 6.4 shows the comparison of the different tau p_T distribution for reconstructed taus matched to true taus (left), using the official matching criteria from the Tau Working Group, and the fakes (right).

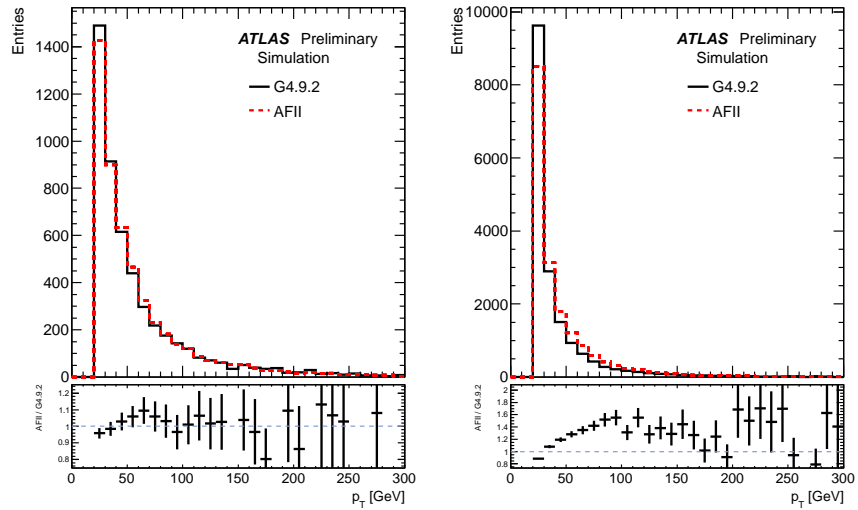


Figure 6.4: Comparison of tau p_T distributions for full Geant-4 and AF-II in the case of reconstructed taus matched to true taus (left) and fake taus (right), as described in the text.

Photons Kinematic distributions for photons and the different author definitions from egamma algorithms show excellent agreement with no appreciable differences. When considering photons passing the tight egamma criteria the difference goes to $\sim 2\%$. Photon p_T distribution for both simulations is shown in Figure 6.5 after applying the selection criteria.

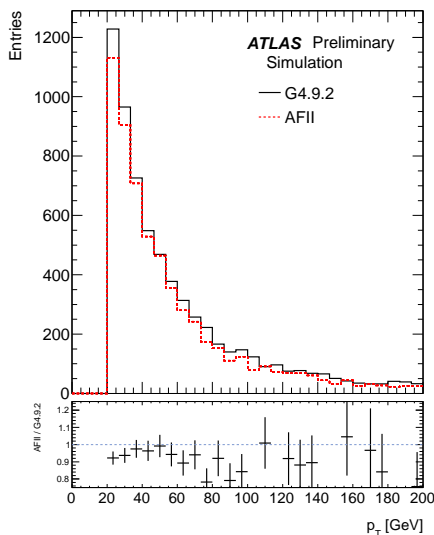


Figure 6.5: Comparison of tight photon p_T distribution for full Geant-4 and AF-II.

m_T The transverse mass between the E_T^{miss} and the electron or the muon can be observed in Figures 6.6. There is an overall good agreement, slightly better for the muon case, as expected.

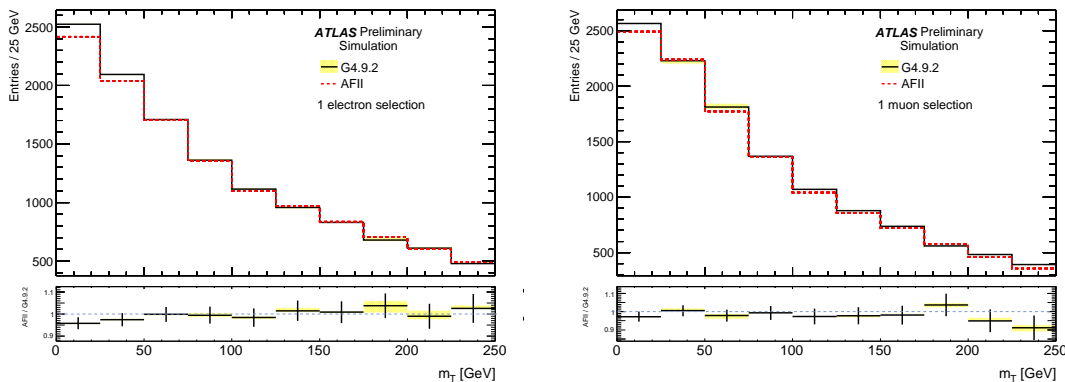


Figure 6.6: Comparisons of the distributions of the transverse mass between the E_T^{miss} and the electron (left) and muon (right) for full Geant-4 and AF-II, as well as the ratio between the two.

H_T The H_T distribution, as defined in Section 6.4, predicted by AF-II is slightly shifted to lower values (1.5%). This small shift can be attributed the description of the three leading jet p_T . The scalar p_T sum of only electrons or muons show excellent agreement.

E_T^{miss} The E_T^{miss} distribution predicted by AF-II presents a deviation of less than 5% to the full Geant-4 prediction, as shown in Figure 6.7. The overall mean shift is $\sim 2\%$ but when electrons or muons are present in the event, the differences are reduced to 1%. The distribution is well described, being the lowest E_T^{miss} region the one with larger differences. This region is more sensitive to lower p_T jet modelling and the unclustered energy (cell-out term). In fact, as shown in Figure 6.8, the AF-II prediction of this term is significantly shifted towards lower values (the mean of the distribution has a 5% shift). However, the effect of this term in the SUSY phase space is usually negligible and the shift represents only half the uncertainty associated to this term.

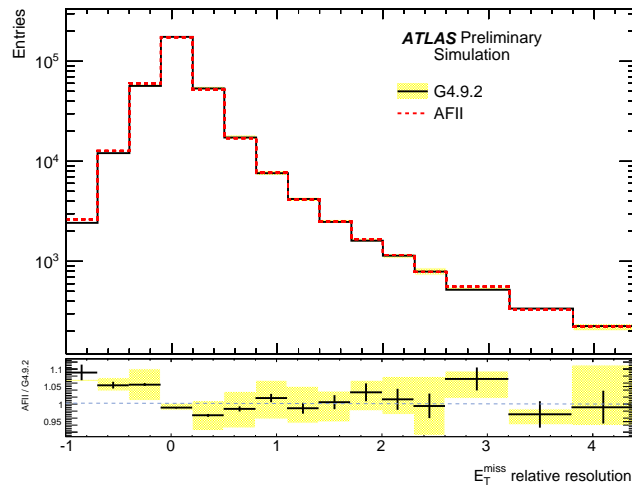


Figure 6.7: Comparison of the E_T^{miss} resolution defined as $(E_T^{\text{miss}} [\text{reco}] - E_T^{\text{miss}} [\text{truth}]) / E_T^{\text{miss}} [\text{truth}]$ for full Geant-4 and AF-II, as well as the ratio between the two.

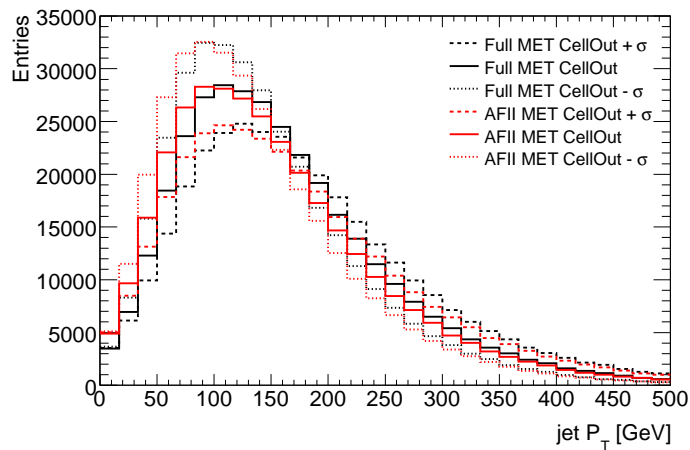


Figure 6.8: Comparison of the unclustered energy distribution for full Geant-4 and AF-II and the corresponding topocluster energy uncertainties.

M_{eff} The M_{eff} quantity is generally the most powerful discriminator in SUSY analyses since it is a complex variable which accounts for most of the calibrated cluster energy in the event as well as the $E_{\text{T}}^{\text{miss}}$. Figure 6.9 shows the differences between AF-II and full Geant-4 simulations, which are well within 5%, basically due to the accumulated differences in the $E_{\text{T}}^{\text{miss}}$ and H_{T} terms already discussed. The highest deviations are observed at the low M_{eff} region ($M_{\text{eff}} < 400$ GeV).

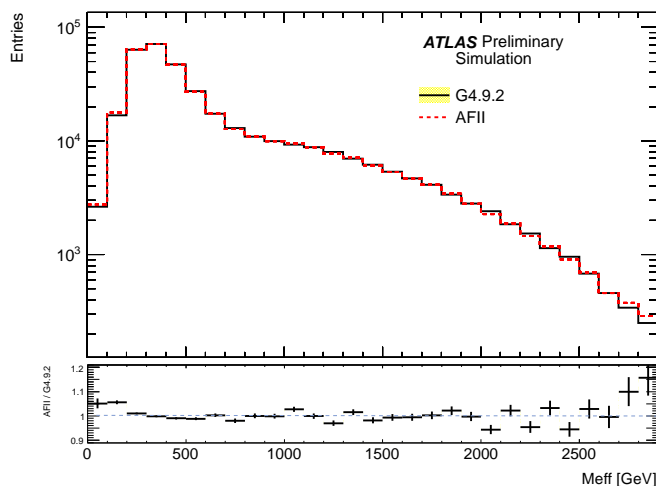


Figure 6.9: Comparison of the M_{eff} distribution for full Geant-4 and AF-II, as well as the ratio between the two.

6.5.2 Description of event selection efficiencies

In order to estimate in more detail the effect of the AF-II usage in SUSY analyses, the different baseline selections adopted by 0-, 1- and 2-lepton analyses have been examined. After each cut, the relative difference of the efficiencies between AF-II and full Geant-4 are quoted with respect to the initial number of events and with respect to the number of events before the cut under investigation. The details of this comparison can be found in the talks [139–142] and here just a summary of the most relevant information is given. Table 6.3 shows the total difference in efficiencies before the last cut is applied ($|\Delta\epsilon_{\text{T}}^{\text{BefLast}}|$)³⁾, after the last cut is applied ($|\Delta\epsilon_{\text{T}}^{\text{Last}}|$), the maximum relative difference in the event selection ($|\Delta\epsilon_{\text{R}}^{\text{max}}|$) and the corresponding cut. As it can be seen, in most of the cases differences are below 2%. However, differences are larger in some of the cases where 2 leptons are required. These event selections are particularly challenging due to the small p_{T} window imposed to the electrons in order to avoid overlapping with other channels⁴⁾. A detailed comparison of the cause of the differences at the event-by-event level was performed and can be found in the Appendix E. The conclusion was that the effect is due

³⁾The last cut applied is the tightest one and it corresponds to $M_{\text{eff}} > 1000$ GeV for 0-lepton final states, $M_{\text{eff}} > 500$ GeV for 1-lepton final states and $E_{\text{T}}^{\text{miss}} > 250$ GeV for 2-lepton final states.

⁴⁾The event selections named “1-muon and 1-elec (low p_{T}) opp. sign” correspond to selections where a muon is required to fulfil the trigger requirement and an electron should also be present. In order to avoid the overlapping with the opposite situation, in which the electron is required to pass the trigger (hence, it should be with a p_{T} above 25 GeV) and an extra muon should also be present in the event, in this case the electron is imposed to be between 20 and 25 GeV.

to a small bias in the p_T description of the electrons at low p_T that become important when the acceptance is extremely small (at the per mill level).

Table 6.3: Event selections for different final states and the difference in efficiency between full Geant-4 and AF-II predictions. $|\Delta\epsilon_T^{\text{BefLast}}|$ is the total difference in efficiencies before the last cut is applied, $|\Delta\epsilon_T^{\text{Last}}|$ is the same quantity but calculated after the last cut is applied, $|\Delta\epsilon_R^{\text{max}}|$ is the maximum relative difference in efficiencies throughout the event selection and last column is the cut producing this maximum difference.

Event selection	$ \Delta\epsilon_T^{\text{BefLast}} $	$ \Delta\epsilon_T^{\text{Last}} $	$ \Delta\epsilon_R^{\text{max}} $	Cut with $ \Delta\epsilon_R^{\text{max}} $
0-lepton, ≥ 2 jets	0.97%	1.27%	0.30%	$M_{\text{eff}} > 1000$ GeV
0-lepton, ≥ 3 jets	1.50%	0.45%	1.06%	$M_{\text{eff}} > 1000$ GeV
1-electron	0.54%	0.50%	1.20%	$m_T > 100$ GeV
1-muon	0.11%	0.06%	1.88%	Lepton cut
2-electron opposite sign	1.65%	1.09%	2.78%	$E_T^{\text{miss}} > 250$ GeV
2-muon opposite sign	1.52%	2.87%	1.65%	$E_T^{\text{miss}} > 80$ GeV
1-elec and 1-muon opp. sign	2.84%	4.97%	2.19%	$E_T^{\text{miss}} > 250$ GeV
1-muon and 1-elec (low p_T) opp. sign	5.33%	25.9%	19.6%	$E_T^{\text{miss}} > 250$ GeV
2-electron same sign	6.68%	2.58%	6.23%	Tight iso electrons
2-muon same sign	4.18%	8.49%	4.14%	$E_T^{\text{miss}} > 250$ GeV
1-elec and 1-muon same sign	5.14%	5.37%	3.03%	Tight iso electrons
1-muon and 1-elec (low p_T) same sign	0%	13.0%	13.0%	$E_T^{\text{miss}} > 250$ GeV

6.6 Summary and proposal

The performance of AF-II was evaluated in different SUSY signal scenarios of a mSUGRA model with different final state topologies and jet p_T spectra. The description of the different objects was found to be very accurate (deviations well below 5%). Distributions of basic quantities for SUSY searches have been also examined and a similar level of agreement was observed. This maximum 5% deviation in some cases was also found to be well within the JES uncertainties. In addition, the baseline event selections performed in different SUSY searches, such as 0-lepton search (with two jets and three jets), one lepton search (both electron and muon separately) and two lepton searches (both opposite sign and same sign with different flavour combinations), were tested. Deviations in the total signal efficiencies or individual cuts were found to be $\sim 1 - 2\%$, except in cases where an electron with $p_T < 25$ GeV is required.

Given this excellent performance of the AF-II package for SUSY signal studies, the following proposal was given:

- New signal grids for SUSY analyses could be simulated using the current AF-II package, when appropriate.
- As a cross check and continuous monitoring of the AF-II performances in the different SUSY models, some full Geant-4 points could be interleaved. These could be in the form of coarser grids and represent around 10 – 20% of the overall phase space covered by the grid.
- Due to the excellent agreement between full Geant-4 and AF-II compared to the current theoretical uncertainties in the signal estimation, the application of the current recommendations from the Combined Performance Groups to define the different physical objects

and to estimate the uncertainties for the full Geant-4 simulated samples could also be applied in the same way to the AF-II SUSY signal samples. As soon as new recommendations are provided, these would be applied to cover the possible cases in which the full Geant-4 recommendations are not accurate enough for AF-II. In addition, longer term tunings of AF-II to data would also minimise the differences and will be beneficial to improve this approach.

In this way, the SusyWG could benefit from the long-standing dedicated efforts of ATLAS to develop and validate fast detector simulations. The factor of 8-9 gain in simulation time would allow more detailed studies of the SUSY parameter space and more accurate results. In addition, the group would also benefit from a faster turn-on in the availability of the samples, which is an important feature to improve the quality of the results when time constraints are present.

This proposal was accepted by the SusyWG and after this work SUSY MC requests used AF-II whenever possible. In several of the SUSY analysis papers published during the summer 2011 and 2012, AF-II has been used for the production of the (total or partial) SUSY signal grids involved. Also other ATLAS groups different from SUSY are using AF-II to simulate different types of processes. All the results from these analyses can be found in Ref. [146].

Chapter 7

Conclusions

This thesis has been devoted to the search for Supersymmetry in an mSUGRA scenario where the R -parity is broken through the bilinear term (bRPV). The bulk of the work carried out has been divided into two main analyses, both of them inclusive, based in the selection of final states containing one muon and several jets. This final state has been proved to be favoured by the bRPV scenario thanks to the lightest supersymmetric particle decay channels involving muons and jets.

In the first part of the thesis, presented in Chapter 4, a Monte Carlo (MC) study has been performed, analysing the possibility to observe bilinear R -parity violation in supersymmetry in ATLAS at the LHC for three different energy configurations: the LHC nominal energy (14 TeV), an intermediate energy (10 TeV) and the energy at which the LHC started to work at the end of 2010, and during 2011 (7 TeV). All possible sources of SM background have been properly taken into account, together with the combinatorial background arising from the high lepton and jet multiplicity environment characterising SUSY events.

The requirements applied in this analysis select events containing at least one high- p_T muon, two high- p_T jets and a set of thresholds on global variables such as E_T^{miss} , M_{eff} or S_T , defined in Chapter 4. Another set of requirements is applied in order to disentangle the signal decay channel ($\tilde{\chi}_1^0 \rightarrow \mu\bar{q}q'$) from the combinatorial background coming from the SUSY sample itself.

After the event selection, when inspecting the number of SUSY inclusive signal and SM background events surviving the SM cuts applied, a ratio $S_{\text{SUSY}}/\sqrt{B} > 30$ is expected for both the 7 TeV and 10 TeV samples, giving rise to a significance of $Z_n = 1.28$ ($Z_n = 0.60$) for the 7 TeV sample (10 TeV sample) for a luminosity of 2 fb^{-1} , with Z_n defined as in Ref. [9]. In this definition of Z_n an uncertainty of 50% is assumed for the background from QCD multijet events and 20% for the background from $t\bar{t}$, W + jets, Z + jets and W/Z pairs. In the 14 TeV sample and for the same selection $S_{\text{SUSY}}/\sqrt{B} > 95$ is seen, although not all sources of background were included in this case, so it should be understood only as an approximation.

Looking at the invariant mass distribution of one muon and two jets and after applying an extra selection in the object combination resembling that expected for the neutralino decay to a muon and a hadronic W , a signal of $S_{\text{SUSY}}/\sqrt{B} > 30$ ($S_{\text{SUSY}}/\sqrt{B} > 50$) can be observed for the 7 TeV sample (10 TeV sample). From this distribution it is possible to reconstruct the neutralino mass, obtaining a mass peak on $114.8 \pm 1.1 \text{ GeV}$ ($115.9 \pm 0.8 \text{ GeV}$), where the theoretical value for the $\tilde{\chi}_1^0$ mass is 109.8 GeV (118 GeV), only statistical errors taken into account. This distribution leads to a significance of $Z_n = 7.22$ ($Z_n = 3.55$) and even better significance of $Z_n = 7.74$ ($Z_n = 5.37$) in the mass window 90 to 140 GeV for a luminosity of 2 fb^{-1} .

This feasibility study was performed assuming a bRPV-mSUGRA point (SU3-like) with a

rather low m_0 and $m_{1/2}$ parameter values (100 GeV and ~ 300 GeV, respectively) characterised by a high SUSY cross section ($\sigma \sim O(10 \text{ pb})$) and a low neutralino mass ($M_{\tilde{\chi}_1^0} \simeq 120 \text{ GeV}$). In higher values of $m_{1/2}$, although the production cross section is lower, the LSP mass migrates to higher values of $M_{\tilde{\mu}_j}$ and hence the mass peak should become more prominent over the background. The branching ratio $BR(\tilde{\chi}_1^0 \rightarrow \mu W)$, on the other hand, as evident from Figure 2 of Ref. [88], is expected to increase with m_0 from $\sim 10\%$ in SU3 up to $\gtrsim 25\%$ for $m_0 \gtrsim 500 \text{ GeV}$, depending also on the other mSUGRA parameters and the atmospheric neutrino mixing angle. In order to generalise the results, a systematic study involving the production of fast simulation (ATLFAST II) samples in a grid of mSUGRA parameters may be performed in the future to determine the exclusion and discovery reach for this model. Moreover, the assumed R -parity violating couplings may be embedded in other supersymmetric frameworks, distinct from mSUGRA, such as the phenomenological MSSM (pMSSM) [105] or the minimal Anomaly Mediated Supersymmetry Breaking (mAMSB) [106].

Even though this analysis is performed and the selection criteria are chosen and optimised for a specific RPV model where the breaking occurs through bilinear terms, it may be generalised to investigate trilinear RPV, such as when $\lambda'_{2,jk} \neq 0$. By relaxing, for instance, the W -mass constraint on the two jets, the decay $\tilde{\chi}_1^0 \rightarrow \mu \bar{q} q'$ may be probed.

The significance can be increased if the delayed decay of the neutralino, having a decay length of $\sim 300 \mu\text{m}$, is exploited. This is a generic feature not only of the specific scenario (bilinear RPV) we studied, where the LSP decay length ranges from 0.1 to 100 mm [88, 102], but of other trilinear RPV scenarios with $\lambda' \sim 10^{-3}$ [107]. Such an analysis, however, addresses the issue of distinguishing the LSP from B -mesons — since they have comparable lifetimes — which requires dedicated studies.

RPV SUSY signals may be characterised, in certain models, by a fairly high missing energy though lower than the corresponding RPC case. This means that if evidence of SUSY should be observed in a similar conventional E_T^{miss} -based inclusive search at the LHC, the case of R -parity violation should not be excluded.

This motivates the second part of the thesis, in which an analysis with real ATLAS data taken from LHC collisions at $\sqrt{s} = 7 \text{ TeV}$ has been performed, searching for a final state containing one high- p_T muon and at least 3 high- p_T jets. This analysis was originally designed for the search of standard SUSY (conserving R -parity, RPC) and thus a rather strong E_T^{miss} requirement is applied. Nevertheless, as stated above, bRPV can have similar features as those of RPC and an interpretation of the analysis in terms of bRPV is feasible.

The analysis, presented in Chapter 5, considers four different signal regions (SR) in which the SUSY signal is expected to dominate over the SM background. The SRs are defined in terms of the minimal jet multiplicity per event, the minimal E_T^{miss} and M_{eff} content and its ratio, while all of them share the defining requirement of the analysis: the content of exactly one muon. A set of control regions (CR) are also defined in terms of the same variables, in which a particular type of SM background is expected to dominate over the others. These CRs are meant to clarify the SM background behaviour, verifying its understanding and ensuring the correct interpretation of data in the SRs.

After performing a combined fit of every CRs and extrapolating the results to each of the SRs, no excess of events is observed in data with respect to the expected SM content. These leads to an interpretation in terms of the bRPV model, giving rise to the first exclusion limits for the bRPV-mSUGRA model ever set. In three out of the four SRs defined, the bRPV model is sensitive enough to derive in exclusion limit plots, which can be found in Figures 5.25 to 5.27. The SR selecting at least 4 high- p_T jets and tighter cuts on the global variables is the one with the highest sensitivity for the bRPV model. It leads to the exclusion plot shown in Figure 5.27, the most stringent one, discarding this model at 95% confidence level for squark masses lower

than 760 GeV ($m_{\tilde{g}} = m_{\tilde{q}}; c\tau_{\text{LSP}} < 15 \text{ mm}$).

As a complement to the physics analyses that have been the main objective of this thesis, a simulation performance study has been carried out. After the first 2010 ATLAS searches found no evidence for physics beyond the SM and significantly extended the constraints to different types of SUSY models, new challenges rose up requiring a large number of new Monte Carlo (MC) samples. The final analyses are followed up with more data to reach higher mass scales and more challenging topologies predicted by different SUSY models needed to be included in the analysis menu. These analyses are usually performed by studying 2-dimensional grids, where each point is a combination of SUSY parameters in a particular model and where relatively large statistics and granularity are needed for precise estimations.

The simulation of the effect that the ATLAS detector has on such MC generated events requires a huge amount of computing resources in terms of CPU time and storage capabilities. In order to accelerate the simulation process and to minimise the required resources, the faster although not-so-precise ATLFAST-II (AF-II) [138] simulation has been developed. A dedicated effort has been done in order to evaluate the performance of the new AF-II package in the context of the SUSY needs.

The work done here consists of the validation of the ATLAS fast simulation framework ATLFAST-II by the comparison of its efficiencies with the standard ATLAS full simulation (full Geant-4) of events. The performance of AF-II has been evaluated in different SUSY signal scenarios in an mSUGRA model with different final state topologies and jet p_T spectra. The description of the different objects has been found to be very accurate (deviations well below 5%). Distributions of basic quantities for SUSY searches have also been examined and a similar level of agreement has been observed. This maximum 5% deviation in some cases was also found to be well within the jet energy scale (JES) uncertainties. In addition, the baseline event selections performed in different SUSY searches, such as 0-lepton search (with two jets and three jets), one lepton search (both electron and muon separately) and two lepton searches (both opposite sign and same sign with different flavour combinations), have been tested. Deviations in the total signal efficiencies or individual cuts are found to be $\sim 1 - 2\%$, except in cases where an electron with $p_T < 25 \text{ GeV}$ is required in which deviations are slightly larger.

After the AF-II validation accomplished here, the ATLAS SUSY Working Group decided to request the SUSY MC production using AF-II whenever possible. This production was used as a key ingredient in several published analysis papers in different SUSY searches [117, 147–149], based in AF-II.

Chapter 8

Epilogue

8.1 Analysis follow up.

Following the results presented in Chapter 5 one further analysis has been performed using higher ATLAS luminosity from $\sqrt{s} = 7$ TeV pp collisions at the LHC. This analysis has been carried out in SRs involving multijets final states, with an important increase of the analysed luminosity (4.7 fb^{-1}) and an update in the pile-up treatment optimised for higher beam intensities. In addition to the muon channel, an electron channel has been added with the signal lepton definition as specified in [150]. The lepton p_T requirements are exactly the same as in the previous case, the difference being the minimum number of jets in the event, which in this case is seven. Also the cuts on the global variables such as E_T^{miss} , M_{eff} or m_T applied in the SRs are updated to the higher luminosity condition. Full description of the SRs can be found in Table 8.1. Similar CRs as in the analysis in Chapter 5 are used and, in addition, extra CRs are adapted to the SRs jet multiplicity required and in the global variables (details in the same table).

Table 8.1: Overview of the selection criteria for the signal and control regions (CR) in this analysis. The p_T selections for leptons are given for electrons (muons). All mass and momentum requirements are in units of GeV.

	Signal region	3-jet W CR	3-jet $t\bar{t}$ CR	7-jet W CR	7-jet $t\bar{t}$ CR	Z+jets CR	dileptonic $t\bar{t}$ CR
Trigger		Single electron or muon (+jet)					
N_{lep}	1	1	1	1	1	≥ 2	≥ 2
p_T^ℓ	> 25 (20)	> 25 (20)	> 25 (20)	> 25 (20)	> 25 (20)	> 25 (20)	> 25 (20)
$p_T^{\ell 2}$	< 10	< 10	< 10	< 10	< 10	> 10	> 10
N_{jet}	≥ 7	≥ 3	≥ 3	≥ 7	≥ 7	≥ 2	≥ 2
p_T^{jet}	$> 80 \dots 25$	$> 80, 25, 25$	$> 80, 25, 25$	$> 80 \dots 25$	$> 80 \dots 25$	$> 80, 50$ or $50, 50, 50, 50$	$> 80, 50$ or $50, 50, 50, 50$
$N_{b\text{-jet}}$	—	0	≥ 1	0	≥ 1	—	≥ 1
E_T^{miss}	> 180	40 to 150	40 to 150	40 to 120	40 to 120	< 50	30 to 80
m_T	> 120	40 to 80	40 to 80	40 to 80	40 to 80	—	—
$m_{\text{eff}}^{\text{inc}}$	> 750	> 500	> 500	> 400	> 400	—	—
$m_{\ell\ell}$	—	—	—	—	—	[81,101]	< 81 or > 101

A complete description of this analysis can be found in [150] and [151].

In a first approximation to this new setup it was observed that the sensitivity within higher luminosity covered a wider area in the bRPV-mSUGRA ($m_{1/2}, m_0$) plane than in the previous setup. Therefore, an extension of the bRPV-mSUGRA signal grid has been simulated covering the range $m_0 < 2000$ GeV and $m_{1/2} < 1000$ GeV and the same fixed values $A_0 = 0$ GeV, $\text{sgn}(\mu) = +1$ and $\tan\beta = 10$. The simulation of new points where the $\tilde{\chi}_1^0$ decay length is short enough not to generate displaced vertices has been done using AF-II.

For this analysis, information is combined into a global likelihood simultaneous fit in all CRs, performed taking into account the background shape. After taking into account all possible sources of systematic uncertainties, no significant discrepancy is seen between the expected number of SM events in the SRs and the observed data. Final numbers for the electron and muon channels are shown in Table 8.2. The deviation in the muon (electron) channel has a p -value of 0.019 (0.13), amounting to approximately a 2.1σ (1.1σ) effect. Combining the two channels, the deviation has again a p -value of 0.019.

Table 8.2: The observed numbers of events in the electron and muon signal regions, and the background expectations from the fit. The inputs to the fit are also shown; these consist of the data-driven multijet background estimate and the nominal expectations from simulation (MC), normalised to theoretical cross sections. The errors shown are the statistical plus systematic uncertainties on the mean background.

Number of events	Electron	Muon
Observed	7	7
Fitted background	4.3 ± 1.2	2.2 ± 1.1
Fitted top	3.1 ± 0.7	1.9 ± 1.0
Fitted W/Z +jets	0.3 ± 0.5	0.3 ± 0.5
Fitted other background	0.2 ± 0.2	< 0.05
Fitted multijet	0.6 ± 0.7	< 0.05
MC expectation SM	6.0 ± 2.4	3.7 ± 2.4
MC expectation top	4.5 ± 1.8	3.4 ± 2.2
MC expectation W/Z +jets	0.3 ± 0.4	0.3 ± 0.4
MC expectation other bkg	0.5 ± 0.7	0.0 ± 0.2
Data-driven multijet	0.6 ± 0.7	< 0.05

The statistically independent electron and muon channels are combined to set limits in the bRPV-mSUGRA model, using the CL_s [135] prescription. The limit in the plane ($m_{1/2}, m_0$) is shown in Figure 8.1. The uncertainty band around the expected limit includes all uncertainties except theoretical uncertainties on the signal while the band on the observed limit indicates the sensitivity to the theoretical uncertainties on the signal. A significant improvement in the limit can be seen over the previous ATLAS result [113] also presented in Chapter 5 and shown as a blue line. For $m_{1/2} \lesssim 250$ GeV the increasing LSP lifetime results in a loss of acceptance from the requirements on the muon impact parameter. This region is not considered in the analysis.

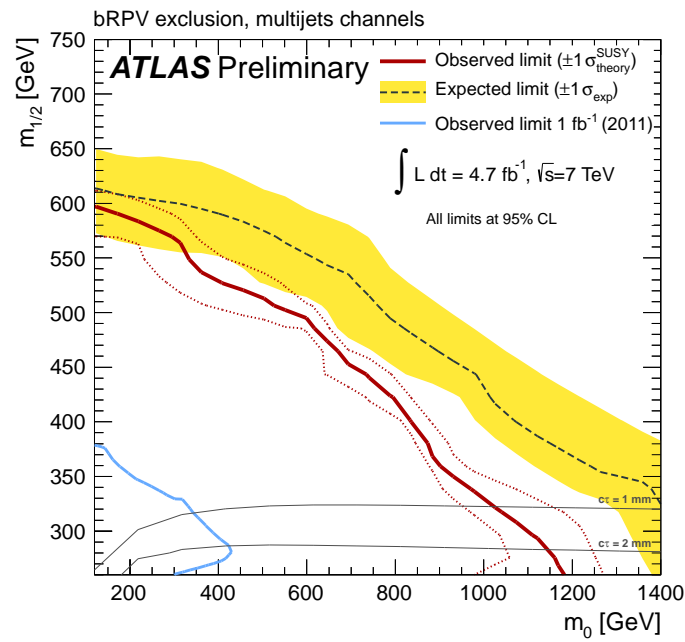


Figure 8.1: Expected and observed 95% CL exclusion limits in the bRPV model. The results are obtained by combining the electron and muon channels. The band around the median expected limit shows the $\pm 1\sigma$ variations on the median expected limit, including all uncertainties except theoretical uncertainties on the signal. The dotted lines around the observed limit indicate the sensitivity to $\pm 1\sigma$ variations on these theoretical uncertainties. The thin solid black contours show the LSP lifetime. The result from the previous ATLAS measurement presented in Chapter 5 for this model is also shown.

Chapter 9

Resumen en castellano

9.1 Introducción

Supersimetría (SUSY) [1] es una de las teorías más prometedoras que da solución a muchas de las cuestiones abiertas del Model Estándar (SM, por sus siglas en inglés) de física de Altas Energías. Éste proporciona la descripción más precisa de la fenomenología conocida en Física de Partículas Elementales. Aunque ha sido probado experimentalmente hasta la escala del TeV con excelentes resultados (LEP [5], Tevatron [6]), hay evidencias claras que apuntan hacia la existencia de Nueva Física más allá del SM.

Entre todos los posibles escenarios que se pueden dar en SUSY, hay uno particularmente interesante en el que, gracias a la rotura de la paridad- R mediante el término bilineal (bRPV, ver Sección 9.1.2), los neutrinos adquieren masa de manera natural a la vez que la partícula supersimétrica más ligera (LSP) deja de ser estable.

En esta tesis se presentan básicamente dos análisis para la búsqueda bRPV-SUSY en la Naturaleza. La primera parte de la tesis está dedicada a la determinación del potencial de descubrimiento del modelo bRPV y a la medida de la masa del neutralino-LSP a través del canal de desintegración $\tilde{\chi}_1^0 \rightarrow \mu W$, en el detector ATLAS instalado en el Gran Colisionador de Hadrones (LHC, por sus siglas en inglés) [3,4] del CERN. El estudio se ha realizado para tres energías de funcionamiento del LHC: $\sqrt{s} = 7, 10$ y 14 TeV. En la segunda parte de la tesis se lleva a cabo una búsqueda inclusiva de bRPV utilizando $\sim 1 \text{ fb}^{-1}$ de datos de ATLAS tomados en colisiones del LHC durante 2011. Para ello se considera estados finales que contengan un muón y tres o más jets. En este análisis no se observa ningún exceso significativo de datos en relación al número esperado de fondo del SM. Este resultado se interpreta como una prueba negativa de la existencia de bRPV-mSUGRA en la región del espacio de parámetros estudiada y consecuentemente, se fijan límites de exclusión para este modelo por primera vez.

9.1.1 El LHC y el detector ATLAS

El Gran Colisionador de Hadrones (LHC) [3,4] es un acelerador y colisionador de partículas situado en el CERN. Sus objetivos principales son el descubrimiento del bosón de Higgs, medidas de precisión de los parámetros del SM y la clarificación de la física más allá del SM, a través del estudio de colisiones protón-protón (pp) a energías de hasta 14 TeV. Además cuenta con un programa para el estudio del plasma quark-gluón a través de interacciones con iones pesados (Pb) a energías de hasta 2.8 TeV por nucleón.

Instalados en el LHC hay varios experimentos. ATLAS [7–9] y CMS [10] son detectores de propósito general, diseñados para explorar la física mencionada arriba. TOTEM [42], integrado en CMS, y LHCf [44], situado a ± 140 m del punto de interacción de ATLAS, estudian sucesos a ángulos muy pequeños. LHCb [41] está diseñado para estudiar la física del quark- b y ALICE [43] está especializado en el estudio de colisiones con iones pesados. Finalmente, se está desarrollando el experimento MoEDAL [45], cuya motivación principal es la búsqueda directa de monopolos magnéticos.

ATLAS es el experimento más grande del LHC. Estructurado en capas cilíndricas con tapas a ambos lados y de propósito general, su diseño ha sido optimizado para ser sensible a un amplio rango de procesos físicos. Comprende varios subdetectores, cada uno de ellos especializado en la identificación de un tipo específico de partícula. El Detector Interno asegura un reconocimiento robusto de trazas, del vértice primario y, con ayuda de un imán solenoide, la medida de momentos. El Calorímetro Electromagnético permite la identificación de electrones y fotones y la medida de sus energías. El Calorímetro Hadrónico sirve para la medida de la energía de jets así como la energía faltante. Finalmente, el Espectrómetro de Muones está diseñado para la identificación de muones y su momento. El detector completo está embebido en un imán toroidal que asegura una medida adecuada de todas las características de las partículas. Todos los detalles sobre el diseño y funcionamiento del detector ATLAS se pueden encontrar en Ref. [8].

El LHC empezó a funcionar de manera estable a finales de 2010 y hasta ahora ha proporcionado una luminosidad integrada de 5.61 fb^{-1} a una energía de $\sqrt{s} = 7 \text{ TeV}$ y alrededor de 19 fb^{-1} en colisiones a $\sqrt{s} = 8 \text{ TeV}$. El detector ATLAS está teniendo una respuesta magnífica, habiendo recolectado más del 90% de la luminosidad proporcionada por el LHC con condiciones excelentes del detector.

9.1.2 Supersimetría

Supersimetría (SUSY) [1] predice una masa del Higgs libre de correcciones cuadráticamente divergentes, es una teoría de gran unificación (GUT) e incluye candidatos a materia oscura [29]. Además en el caso que se estudia en esta tesis, confiere masa a los neutrinos de forma natural. SUSY se define como la invariancia de la teoría bajo intercambio de fermiones y bosones de forma que a cada partícula del SM se le asigna un compañero supersimétrico (spartícula) con exactamente los mismos números cuánticos excepto por el spin, que varía en $\pm 1/2$.

En caso de existir, SUSY debe ser una simetría rota. Actualmente no se sabe con certeza cuál es el mecanismo de rotura de SUSY por lo cual y con el objetivo de obtener observables fenomenológicos, se añade al lagrangiano supersimétrico, L_{inv} , una parte que rompa SUSY explícitamente a bajas energías, L_{soft} .

$$L_{\text{SUSY}} = L_{\text{inv}} + L_{\text{soft}}. \quad (9.1)$$

El L_{soft} más simple que reproduce toda la fenomenología conocida es el Modelo Supersimétrico Mínimo (MSSM). Este lagrangiano introduce 105 parámetros nuevos [81] aunque muchos de ellos están acotados experimentalmente [82]. Este número se reduce notablemente si se acepta algún modo de rotura espontánea de la simetría a altas escalas de energía. En el modelo considerado en esta tesis, Supergravedad Mínima (mSUGRA) [83], el número de parámetros se simplifica drásticamente, quedando reducido a cinco: la masa de los bosones a escala GUT, m_0 ; la masa de los fermiones a escala GUT, $m_{1/2}$; el cociente entre valores esperados en el vacío de los dos bosones de Higgs neutros, $\tan\beta = v_u/v_d$; el acoplo trilinear a escala GUT, A_0 y el signo del parámetro del potencial de Higgs, $\text{sgn}(\mu)$.

En el MSSM se asume conservación de la paridad- R (RPC), un número cuántico definido a partir del número leptónico, el número bariónico y el spin en la forma $P_R = (-1)^{3(B-L)+2s}$. Sin embargo, dicha conservación no se apoya en ninguna motivación fundamental. La rotura de la paridad- R mediante el término bilineal [87–89], construye el modelo efectivo más simple que contiene las características más importantes de la rotura espontánea de la paridad- R a bajas energías y que además proporciona masa a los neutrinos de manera natural y acorde a los datos de oscilaciones de neutrinos [16].

La desintegración de la partícula supersimétrica más ligera (LSP) en el canal $\tilde{\chi}_1^0 \rightarrow \mu W (\rightarrow q\bar{q}')$ es especialmente interesante para búsqueda de bRPV ya que permite la reconstrucción completa del $\tilde{\chi}_1^0$ y por tanto la medida de su masa. Por este motivo, el trabajo realizado en esta tesis se centra en el análisis de este modo de desintegración con dos objetivos principales. Primero, el descubrimiento / exclusión del modelo bRPV-mSUGRA en un cierto rango del espacio de parámetros y segundo, la reconstrucción de la masa del $\tilde{\chi}_1^0$ -LSP.

La búsqueda de Supersimetría es uno de los objetivos principales del experimento ATLAS. Las búsquedas estándar implican conservación de la paridad- R caracterizadas por una alta energía transversa perdida (E_T^{miss}). Con el objetivo de simplificar la estrategia de búsquedas, los análisis realizados en ATLAS se clasifican según el número de leptones (electrones y muones) en el estado final:

- Análisis con cero leptones, una multiplicidad mínima de jets y cierta cantidad de E_T^{miss} .
- Análisis con exactamente un leptón más cierta multiplicidad de jets y E_T^{miss} .
- Análisis con dos leptones en las combinaciones: dos electrones, dos muones, un electrón y un muón, además subdivididos en dos clases (leptones con el mismo signo o con signo opuesto de la carga eléctrica).
- Análisis con tres leptones.
- Análisis sin exigencias en el número de leptones: con dos fotones, con uno o más b-jets o con uno o más leptones tau.

Complementando estas búsquedas, existe un programa de búsquedas no-estándar de modelos con violación de la paridad- R (RPV) o modelos en los que existen partículas de vida media larga.

Varios experimentos de altas energías anteriores al LHC han dado lugar a resultados de exclusión en señales de SUSY con RPV , (LEP [31], Tevatron [32], HERA [33], Belle/Babar [34]). También laboratorios de neutrinos o datos de astrofísica [35] han dado lugar a restricciones en SUSY con RPV . Los experimentos ATLAS [36–38] y CMS [39] también han dado ya varios resultados en este sentido. Sin embargo, todos estos resultados están basados en asunciones diferentes a las tomadas en el modelo considerado en esta tesis y por tanto no tienen un impacto directo en el análisis aquí realizado.

9.2 Análisis con muestras de Monte Carlo

El objetivo de este análisis es probar si el descurrimiento / exclusión del modelo bRPV-SUSY es factible en ATLAS y la reconstrucción de la masa de la LSP mediante su modo de desintegración $\tilde{\chi}_1^0 \rightarrow \mu^\pm W^\mp (\rightarrow q\bar{q}')$. Todas las posibles fuentes de fondo del SM han sido tenidas en cuenta a lo largo del análisis. Se presenta un estudio para tres energías de trabajo del LHC diferentes: su energía nominal (14 TeV), una energía intermedia (10 TeV) y la energía a la cual el LHC empezó a funcionar a finales de 2010 y durante todo 2011 (7 TeV). Este análisis está concebido como un experimento de contaje pretendiendo la distinción de la señal de SUSY, sucesos en los que se da la desintegración $\tilde{\chi}_1^0 \rightarrow \mu^\pm W^\mp (\rightarrow q\bar{q}')$, sobre el fondo, en tres pasos:

- Aplicación de un **trigger de muones y preselección**, exigiendo que el muón esté aislado y que el suceso contenga dos o más jets.
- **Estudio del fondo del SM** para la eliminación de la mayor parte de fondo del SM conservando gran parte de la señal. Se utilizan variables globales con distinto comportamiento en bRPV-mSUGRA y en el SM.
- **Estudio del fondo combinatorio**. Reducción del fondo combinatorio de SUSY, entendido como las combinaciones de jets y muones que no proceden originalmente de una desintegración de la LSP.

Después de estos tres pasos, se construye la masa invariante del muon y par de jets seleccionados para la obtención de la masa de la LSP.

9.2.1 Definición de la señal

Para el desarrollo del análisis se ha simulado tanto la señal de bRPV-mSUGRA como el SM a las tres energías estudiadas, utilizando el software de ATLAS, Athena [92]. Todos los modos posibles de desintegración del $\tilde{\chi}_1^0$ así como todos los subprocesos que contribuyen a la producción de SUSY se permiten durante la generación.

La comparación entre las tres energías no es directa, ya que los puntos en el espacio de parámetros de bRPV-mSUGRA son ligeramente diferentes. Una característica importante de RPV es que su distribución de E_T^{miss} está desplazada hacia valores más bajos comparada con el caso de RPC. Sin embargo, en el caso particular aquí estudiado, se espera una cierta cantidad de E_T^{miss} debido a la presencia de neutrinos en la mayoría de modos de desintegración de la LSP. Como ejemplo se puede ver en la Figura 9.1 cómo la distribución de E_T^{miss} se desplaza hacia valores más altos en los casos en los que una o las dos LSPs de desintegran mediante canales que contienen neutrinos, para la muestra a 7 TeV.

Otro punto importante para el desarrollo del análisis es la presencia de muones procedentes de desintegraciones de la LSP. En las Tablas 4.1 y 4.2 se detallan los valores seleccionados para los parámetros de bRPV-mSUGRA así como los porcentajes de sucesos que contienen neutrinos (sobre un 95%) y muones (sobre un 50%) procedentes de la desintegración de la LSP. En adelante, nos referiremos a la producción completa de SUSY como “SUSY-inclusiva” y a la submuestra en la que al menos un $\tilde{\chi}_1^0$ se desintegra en el modo $\tilde{\chi}_1^0 \rightarrow \mu\bar{q}q'$, como “canal-de-senal”.

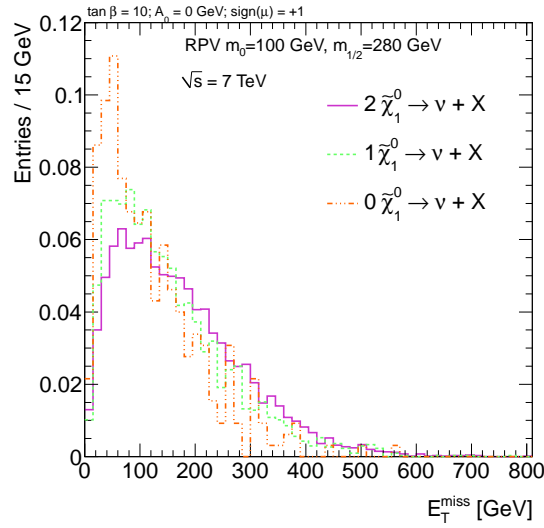


Figure 9.1: Distribución de E_T^{miss} para la señal de SUSY inclusiva a 7 TeV para sucesos que contienen ninguna, una o dos LSPs con neutrinos en su modo de desintegración, normalizadas a área 1.

9.2.2 Trigger y preselección

Dado el estado final que se busca ($\tilde{\chi}_1^0 \rightarrow \mu W (\rightarrow q\bar{q}')$), el primer paso en el análisis corresponde a la aplicación de un trigger que implique un muón de alto p_T , el cual reduce significativamente el fondo del SM.

En un segundo paso se requiere que el muón que disparó el trigger esté aislado y que el suceso contenga al menos dos jets con $p_T > 20$ GeV. El muón se considera aislado cuando la energía transversa en un cono de radio $\Delta R = 0.2^1$ alrededor del muón, está por debajo de cierto límite. En estos análisis las dos opciones que dieron mejor resultado fueron $E[\Delta R_\mu < 0.2] < 40$ GeV, selección denominada como “loose” y $E[\Delta R_\mu < 0.2] < 20$ GeV, denominada como “tight”. Los resultados de la aplicación del trigger así como la de las distintas opciones de preselección se muestran en la Tabla 9.1 para las tres energías estudiadas.

En lo sucesivo, se asumirá la aplicación de la preselección mu18i_loose_2j20 al análisis a 7 TeV, mu10i_loose_2j20 al análisis a 10 TeV y mu10_2j20 al de 14 TeV.

¹⁾ R es una invariante Lorentz definida en términos de la pseudorapidez (η) y del ángulo polar (ϕ) en la forma $\Delta R = \sqrt{\Delta\eta^2 + \Delta\phi^2}$

Table 9.1: Eficiencias en SUSY y el fondo del SM a 7, 10 y 14 TeV para diversas opciones de trigger preselección.

Proceso	Eficiencia (%)			
	EF_mu10	EF_mu18	EF_mu20	mu18i_loose_2j20
muestra 7 TeV				
SUSY-canal-de-señal	94.8	88.9	86.7	91.3
SUSY-inclusivo	70.6	62.6	60.4	59.6
Fondo total SM	0.036	6.8×10^{-3}	5.6×10^{-3}	2.2×10^{-3}
muestra 10 TeV	mu10	mu20	mu10i_loose_2j20	mu10i_tight_2j20
SUSY-canal-de-señal	97.9	90.7	97.4	90.2
SUSY-inclusivo	69.9	58.9	66.7	65.1
Fondo total SM	0.119	0.118	0.047	0.046
muestra 14 TeV	mu10	mu20		mu10_2j20
SUSY-canal-de-señal	92.3	79.3		89.9
SUSY-inclusivo	67.5	54.7		64.7
Fondo total SM	0.10	0.09		0.08

9.2.3 Supresión del fondo del SM

Para poder discriminar la señal inclusiva de SUSY del fondo del SM, se consideran las siguientes variables:

Energía transversa faltante (E_T^{miss}): Suma vectorial del \mathbf{p}_T de leptones y jets.

Masa efectiva (M_{eff}): Suma escalar de la E_T^{miss} , del p_T de todos los electrones y muones y del p_T de los cuatro jets más energéticos:

$$M_{\text{eff}} = E_T^{\text{miss}} + \sum p_T^{\text{electrons}} + \sum p_T^{\text{muons}} + \sum_{1..4} p_T^{\text{jet}} \quad (9.2)$$

Esfericidad transversa (S_T): El tensor de esfericidad transversa se define como:

$$S_T^{\alpha\beta} = \frac{\sum_i p_i^\alpha p_i^\beta}{\sum_i \|\mathbf{p}_i\|^2} \quad (9.3)$$

donde α y β corren sobre los ejes x e y para todos los jets, electrones, muones y taus en el suceso. Por diagonalización de $S_T^{\alpha\beta}$ se encuentran dos autovalores $\lambda_1 \geq \lambda_2$, con $\lambda_1 + \lambda_2 = 1$. La esfericidad transversa (S_T) se define entonces como:

$$S_T = \frac{2\lambda_2}{\lambda_1 + \lambda_2} \quad (9.4)$$

tomando valores $0 \geq S_T \geq 1$.

Con el objetivo de obtener una fracción óptima de señal sobre fondo (S_{SUSY}/B), se ha realizado un estudio sistemático para cada una de las tres energías, probando varios umbrales en las variables anteriormente definidas y relaciones entre ellas. Se requiere que un número de sucesos de señal relativamente alto pase la selección, de forma que se pueda construir una distribución de masa invariante de un muón y dos jets, después de aplicar la selección contra el fondo combinatorio, con suficiente estadística como para poder hacer un ajuste sobre la masa del $\tilde{\chi}_1^0$. Las posibles correlaciones entre variables se han tenido en cuenta en este estudio.

Aunque para cada energía se encontró conjuntos de cortes ligeramente diferentes, se ha decidido tomar el siguiente conjunto para los tres escenarios, al que nos referiremos como *cortes-SM*:

$$\begin{aligned} M_{\text{eff}} &> 1.2 \text{ TeV}, \\ E_{\text{T}}^{\text{miss}} &> 40 \text{ GeV}, \\ S_{\text{T}} &> 0.2. \end{aligned} \quad (9.5)$$

Las eficiencias y flujo de cortes para esta combinación de *cortes-SM* se puede ver en la Tabla 9.2. Los sucesos en *SUSY-canal-de-señal* se refieren a aquellos en los que al menos unos de los $\tilde{\chi}_1^0$ se desintegra a un muón y un W hadrónico. La submuestra *fondo-de-SUSY* corresponde a todos los demás sucesos de SUSY.

Table 9.2: Eficiencias y flujo de cortes para los *cortes-SM* después de la preselección con respecto al número inicial de sucesos para la muestra de 7, 10 y 14 TeV. Los números de sucesos están normalizados a 2 fb^{-1} .

	$M_{\text{eff}} > 1.2 \text{ TeV}$		$M_{\text{eff}} > 1.2 \text{ TeV}$ $S_{\text{T}} > 0.2$		$M_{\text{eff}} > 1.2 \text{ TeV}$ $S_{\text{T}} > 0.2$ $E_{\text{T}}^{\text{miss}} > 40 \text{ GeV}$	
	# sucesos	ef (%)	# sucesos	ef (%)	# sucesos	ef (%)
muestra 7 TeV						
SUSY-canal-señal	706.3	62.8	468.8	41.7	437.1	38.6
SUSY-inclusivo	2586.6	37.0	1691.0	24.2	1615.1	23.1
Fondo total SM	36637.3	3.0×10^{-7}	3569.4	7.0×10^{-8}	2200.9	1.3×10^{-8}
S_{SUSY}/B	0.071	–	0.47	–	0.74	–
S_{SUSY}/\sqrt{B}	13.5	–	28.3	–	34.4	–
muestra 10 TeV						
SUSY-canal-señal	760	81.5	534	57.2	486	50.1
SUSY-inclusivo	4947	52.1	3318	34.9	3191	33.6
Fondo total SM	142556	3.5×10^{-6}	41188	1.0×10^{-6}	7302	1.8×10^{-7}
S_{SUSY}/B	0.03	–	0.08	–	0.44	–
S_{SUSY}/\sqrt{B}	13.1	–	16.4	–	37.3	–
muestra 14 TeV						
SUSY-canal-señal						41.2
SUSY-inclusivo						28.0
Fondo total SM						1.5×10^{-7}
S_{SUSY}/B					0.40	–
S_{SUSY}/\sqrt{B}					95.3	–

La distribución final de $E_{\text{T}}^{\text{miss}}$ después de aplicar los *cortes-SM* se puede ver en las Figuras 9.2. Estos cortes no pueden eliminar completamente la contaminación por el fondo del SM aunque la señal de SUSY aparece muy por encima del fondo de SM para valores altos de $E_{\text{T}}^{\text{miss}}$. Como se verá más adelante, esta situación mejora significativamente después de aplicar cortes adicionales dedicados a reducir el fondo combinatorial.

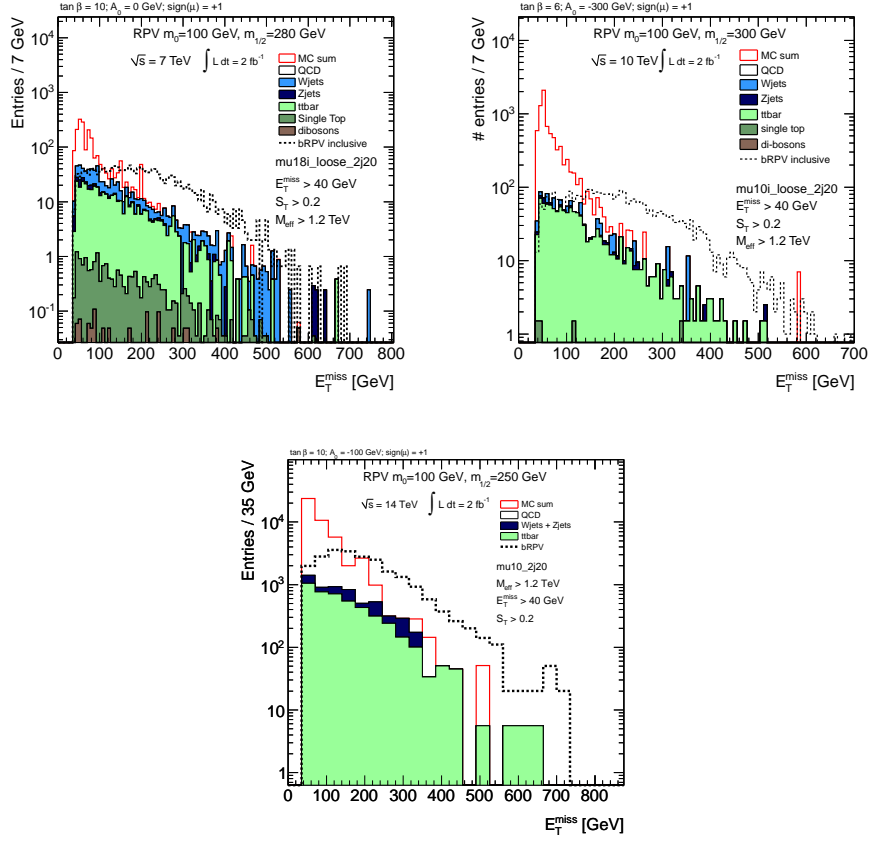


Figure 9.2: Distribuciones de E_T^{miss} para la señal SUSY inclusiva y para los fondos del SM a 7 TeV (arriba izquierda), a 10 TeV (arriba derecha) y a 14 TeV (abajo), después de los *cortes-SM*, normalizada a 2 fb^{-1} . *MC sum* se refiere a la suma normalizada de todas las fuentes de fondo del SM.

9.2.4 Estudio sobre el fondo combinatorio

En esta sección se establecen criterios de selección adicionales para la extracción del modo de desintegración $\tilde{\chi}_1^0 \rightarrow \mu W (\rightarrow \bar{q}q')$ de entre el fondo combinatorio de SUSY. En sucesos de SUSY se generan varios bosones W y muones durante la cascada de desintegración. Esto se ve en la Figura 9.3, donde se representa el número de muones por suceso (izquierda) en función del número de canales-de-sígnal, y el número de bosones W por suceso (derecha) en función de cuántos $\tilde{\chi}_1^0$ se desintegran en canales que contienen bosones W . El reto es seleccionar aquellos jets procedentes de un W , que además procede de un $\tilde{\chi}_1^0$, junto con el muón que procede del mismo $\tilde{\chi}_1^0$. El resto de combinaciones son denominadas *fondo-de-SUSY*.

Se define un candidato-a- W como un par de jets con masa invariante $m_{jj} \in \{M_W \pm 5 \text{ GeV}\}$. Teniendo en cuenta que el $\tilde{\chi}_1^0$ es un objeto "boostado", se espera que la distancia angular entre los dos jets que forman el W , ΔR_{jj} y entre el candidato-a- W y el muón, $\Delta R_{\mu W}$, sean pequeñas para las canales-de-sígnal. Esto se demuestra en los paneles superiores de las Figuras 4.18, en la que se presenta la correlación entre el momento del W (izquierda) y el $\tilde{\chi}_1^0$ (derecha) con la distancia angular entre sus productos de desintegración para las canales-de-sígnal. Las mismas

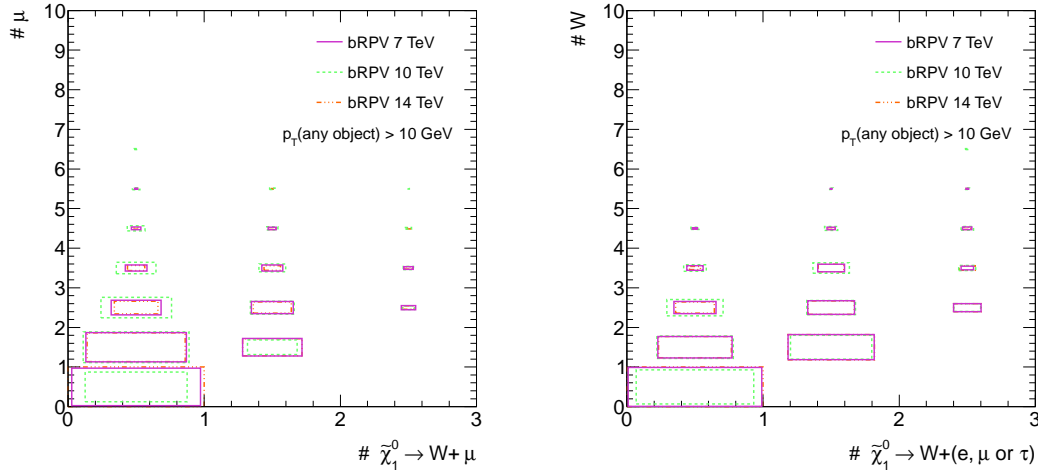


Figure 9.3: *Izquierda:* Número de muones por suceso en función del número de canales-de-síñal en ese suceso. *Derecha:* Número de bosones W por suceso en función del número de $\tilde{\chi}_1^0$ que se desintegran a W .

cantidades se representan en los paneles inferiores para la síñal inclusiva de SUSY. Tras estudiar la correlación observada, así como la existente entre ΔR_{jj} y $\Delta R_{\mu W}$, se concluye que la aplicación de cortes correlacionados es menos efectiva que los siguientes cortes independientes, denominados *cortes-combinatorias*:

$$\begin{aligned} p_T(\mu) &> 25 \text{ GeV} \\ \Delta R_{\mu W} &< 1.5 \\ \Delta R_{jj} &< 2.5 \end{aligned} \quad (9.6)$$

El flujo de cortes para los *cortes-combinatorias* se muestra en la Tabla 9.3 para la muestra de 7 y 10 TeV. En estas tablas se muestra el número de sucesos que, después de pasar los *cortes-SM*, contienen al menos un candidato-a- $\tilde{\chi}_1^0$ con la definición dada por los *cortes-combinatorias* aplicados en cada paso. El fondo de SM en su conjunto global se reduce en un orden de magnitud.

9.2.5 Masa invariante muón+jets y conclusión

Finalmente se presenta la distribución de la masa invariante de un muón y dos jets, tras pasar todos los criterios de selección en la Figura 9.4 (izquierda para 7 TeV, derecha para 10 TeV). La mayoría del fondo del SM ha sido eliminado. La línea discontinua, *bRPV inclusive*, corresponde a todas las combinaciones posibles de muones y candidatos-a- W que cumplen los requisitos en la muestra de SUSY. El área gris, *bRPV background*, muestra el fondo combinatorio de SUSY. El pico en la masa de la LSP destaca claramente sobre el fondo del SM y su ajuste a una gaussiana en el rango 90 - 140 GeV da un valor de (114.8 ± 1.1) GeV para el caso de 7 TeV y (115.9 ± 0.8) GeV para el de 10 TeV, donde el error es sólo estadístico. La discrepancia entre los valores obtenidos y los generados (109.8 GeV para 7 TeV; 118.0 GeV para 10 TeV) se podría deber a errores sistemáticos. Si se mira al número de sucesos de síñal inclusiva de SUSY y del SM que pasan los *cortes-SM*, se obtiene una significancia de $Z_n = 1.28$ ($Z_n = 0.60$) para el caso de 7 TeV (10 TeV) para una luminosidad de 2 fb^{-1} , con Z_n definido como en Ref. [9].

Table 9.3: Flujo de cortes para la muestra de SUSY a 7 y 10 TeV y para el fondo del SM para los *cortes-combinatoriales* después de haber aplicado los *cortes-SM*. Las eficiencias están calculadas respecto al número inicial de sucesos. Los números de sucesos están normalizados a 2 fb^{-1} .

	$\Delta R_{jj} < 2.5$		$\Delta R_{jj} < 2.5$ $p_T^\mu > 25 \text{ GeV}$		$\Delta R_{jj} < 2.5$ $p_T^\mu > 25 \text{ GeV}$ $\Delta R_{\mu W} < 1.5$	
	# sucesos	ef (%)	# sucesos	ef (%)	# sucesos	ef (%)
muestra 7 TeV						
SUSY-canal-de-señal	245.8	21.8	229.5	20.4	158.2	14.2
fondo-de-SUSY	566.5	10.3	523.2	9.5	291.7	5.3
Fondo total SM	399.4	3.3×10^{-9}	340.9	2.8×10^{-9}	140.4	1.2×10^{-9}
$S_{\text{SUSY inclusive}}/B_{\text{SM}}$	2.0	–	2.2	–	3.2	–
muestra 10 TeV						
SUSY-canal-de-señal	430	46.1	380	40.7	314	33.6
fondo-de-SUSY	1774	18.7	1361	14.3	616	6.5
Fondo total SM	4229	1.0×10^{-7}	1313	3.2×10^{-8}	324	7.9×10^{-9}
$S_{\text{SUSY inclusive}}/B_{\text{SM}}$	0.52	–	1.33	–	2.89	–

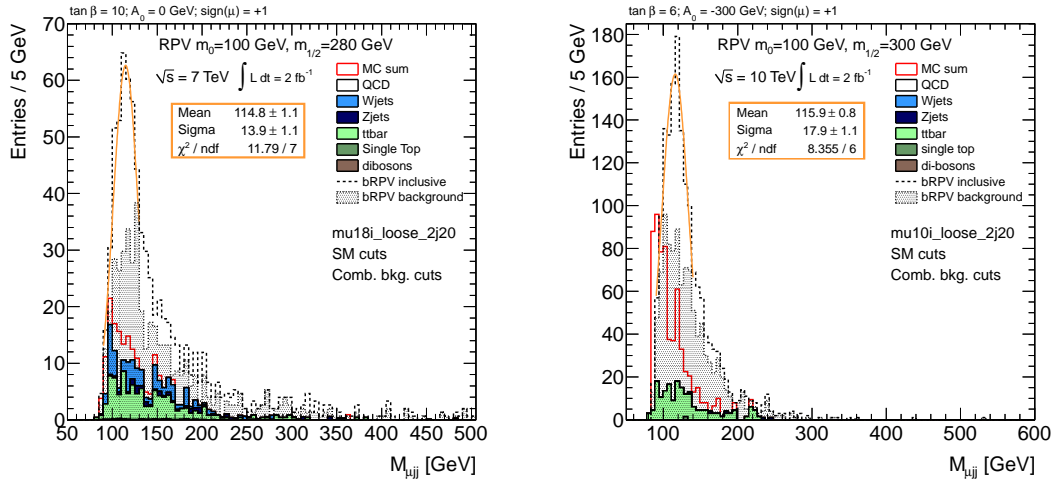


Figure 9.4: Distribución de la masa invariante $M_{\mu ij}$ para el fondo del SM y para la muestra de SUSY a 7 TeV (izquierda) y a 10 TeV (derecha), después de aplicar los *cortes-SM* y *cortes-combinatoriales*, para una luminosidad integrada de 2 fb^{-1} . *MC sum* es la suma normalizada de todas las fuentes de fondo del SM.

9.3 Búsqueda de bRPV-SUSY con datos de ATLAS de 2011

El experimento ATLAS tiene un programa muy completo para la búsqueda de Supersimetría. Tras considerar todos los análisis llevados a cabo en el ATLAS SUSY Working Group, se ha comprobado que una búsqueda en bRPV con estados finales que contengan exactamente un muón, al menos tres jets y cierta cantidad de E_T^{miss} , el llamado “análisis de 1-muón”, es eficiente.

bRPV-mSUGRA comparte varias características con RPC-mSUGRA, haciendo este análisis aplicable a ambos casos. Por ejemplo, el análisis basado en trigger de muones es eficiente para ambos casos, en los dos escenarios hay alta multiplicidad de jets y cascadas de desintegración largas y ambos modelos contienen alta E_T^{miss} .

Ésta es la primera vez que se aplica un análisis de este tipo al caso de bRPV, proporcionando por primera vez límites de exclusión en el espacio de parámetros de bRPV-mSUGRA que acotan este modelo. Este resultado ha sido publicado en la revista Physical Review D [113]. Una descripción más detallada se puede encontrar en la Nota Interna de ATLAS [114].

9.3.1 Regiones de señal y de control

Este análisis se aplica a un extenso conjunto de señales de SUSY incluyendo cuadrículas de puntos del espacio de parámetros de RPC, bRPV y de los llamados modelos simplificados (ver Ref. [113] para detalles). Para cubrir este amplio rango de señales, el análisis incluye cuatro regiones de señal en las que ésta domina sobre el fondo del SM. Estas regiones incluyen la presencia de E_T^{miss} , un muón y al menos tres jets en un canal o cuatro jets en el otro. Para cada uno de estos canales se define a su vez una región llamada “loose”, con restricciones suaves y otra llamada “tight” con restricciones más severas, basadas en tres variables globales:

- E_T^{miss} , como ya se definió en 9.2.3,
- masa transversa $m_T = \sqrt{2 \cdot p_T^\ell \cdot E_T^{\text{miss}} \cdot (1 - \cos(\Delta\phi[\ell, E_T^{\text{miss}}]))}$, donde p_T^ℓ es el p_T del leptón seleccionado,
- masa efectiva: $M_{\text{eff}} = p_T^\ell + \sum_{i=1}^{3(4)} p_T^{\text{jet}_i} + E_T^{\text{miss}}$.

Todos los objetos utilizados en el análisis deben cumplir unos requisitos de calidad:

Jets. Sólo los jets con $p_T > 25$ GeV y $|\eta| < 2.8$ son considerados. Si un jet se solapa con un electrón ($\Delta R(\text{jet}, e) < 0.2$) el objeto se clasifica como electrón. Además se descartan los “bad jets”, objetos mal clasificados como jets.

Electrones. Se selecciona únicamente los electrones con $p_T > 20$ GeV y $|\eta_{\text{clust}}| < 2.47$. Los electrones que se solapan con un jet en la región $0.2 < \Delta R(e, \text{jet}) < 0.4$, se eliminan.

Muones. Sólo los que tengan $p_T > 10$ GeV, $|\eta| < 2.4$, $\Delta R(\mu, \text{jet}) > 0.4$ y $\Delta R(\mu, \text{jet}) < 0.4$ son seleccionados. Para el análisis también se utiliza una selección más estricta de muones, llamados muones de señal, los cuales deben cumplir además $p_T > 20$ GeV y estar aislados: $p_T[\Delta R_\mu < 0.2] < 1.8$ GeV.

E_T^{miss} . Suma vectorial del momento transverso de todos los objetos seleccionados, más cualquier otra actividad en el calorímetro.

Para reducir las incertidumbres asociadas a la estimación del fondo del SM en las regiones de señal, se define una región de control (CRs, Sección 5.1.2) para cada tipo de fondo, otrogonales

a las de señal. En cada una de las regiones de control se realiza una normalización del fondo de MC sobre los datos reales. Asumiendo que la forma de las distribuciones está correctamente descrita por las simulaciones de MC se definen factores de extrapolación desde las regiones de control a las regiones de señal.

Así, se define una región de control para W +jets (WR), una para sucesos con quarks top (TR), y una para QCD (QR), utilizada únicamente para el cálculo del *lepton fake rate* (objetos mal reconstruidos como leptones) ya que este fondo se estudia principalmente por un método derivado de los datos (ver Sección 5.5.2).

9.3.2 Muestras: datos, fondos del SM y bRPV

Todos los datos utilizados en este análisis fueron recogidos por el detector ATLAS en colisiones pp a una energía de centro de masas de 7 TeV en el LHC, resultando en una luminosidad integrada de $\int Ldt = (1035 \pm 38) \text{ pb}^{-1}$.

Todas las muestras de Monte Carlo han sido pesadas de acuerdo con el número de interacciones esperadas por choque de paquetes de protones (*pile-up*) en cada periodo de toma de datos.

Este análisis incluye la búsqueda de bRPV-mSUGRA en una cuadrícula de 88 puntos en el espacio de parámetros, motivada por el análisis en Ref. [129]. Para tres de los parámetros de mSUGRA se toma un valor constante ($\tan\beta = 10$, $A_0 = 0 \text{ GeV}$ y $\text{sgn}(\mu) = +1$) mientras que los otros dos toman distintos valores en los rangos $m_0 \in (100, 800) \text{ GeV}$ y $m_{1/2} \in (200, 600) \text{ GeV}$.

Teniendo en cuenta los datos experimentales de física de neutrinos, se calculan las masas y fracciones de desintegración (BR) utilizando SPheno [94] y son posteriormente incluidas en el generador de sucesos PYTHIA [93] a través del formato de datos SLHA [95,96].

En el modelo bRPV el neutralino-LSP no es estable sino que se desintegra a partículas del SM. En las Figuras 9.5 se puede ver la distancia de desintegración (izquierda) para el neutralino en reposo así como el BR del modo de desintegración que nos ocupa, $\tilde{\chi}_1^0 \rightarrow \mu^\pm W^\mp$ (derecha) en función de m_0 y $m_{1/2}$.

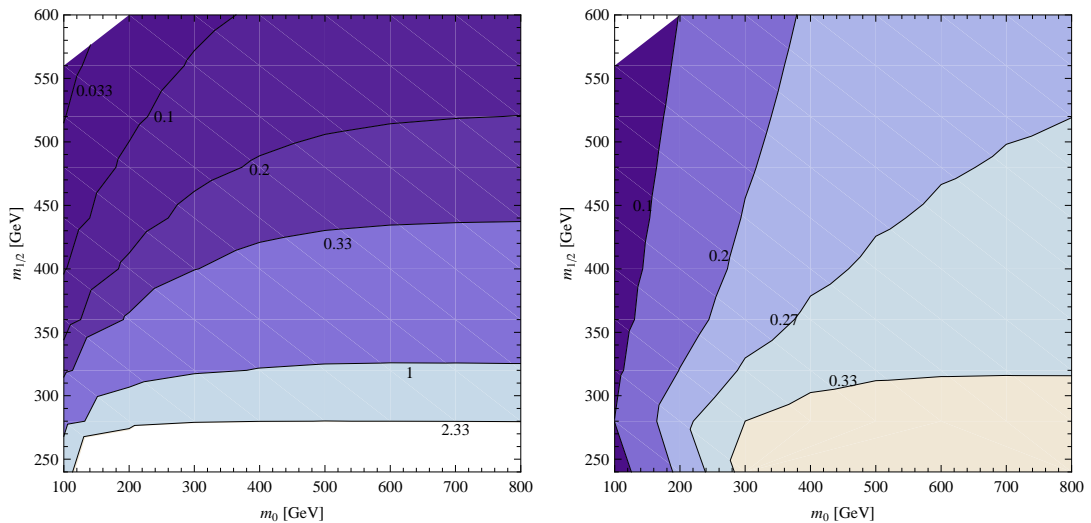


Figure 9.5: *Izquierda:* Distancia de desintegración del $\tilde{\chi}_1^0$ en reposo. Las líneas de contorno están en unidades de mm. *Derecha:* Distribución del $BR(\tilde{\chi}_1^0 \rightarrow \mu^\pm W^\mp)$ como función de m_0 y $m_{1/2}$.

9.3.3 Trigger y preselección

El primer paso del análisis consiste en la aplicación del trigger de muones más bajo no preescalado, tanto para las muestras de MC como para los datos. Después se seleccionan los sucesos que tengan un vértice primario y exactamente un muón de señal cumpliendo la definición dada en la Sección 9.3.1. También se requiere que el suceso tenga tres (cuatro) jets con las condiciones descritas en 9.3.1, según la región de señal. El jet más energético debe cumplir $p_T > 60$ (80) GeV y los siguientes jets $p_T > 25$ (40) GeV. Por último se requiere la condición de que ningún jet esté alineado con la E_T^{miss} : $\Delta\phi(\vec{j}_i, E_T^{\text{miss}}) > 0.2$. En la Figura 9.6 se muestra la distribución de M_{eff} para datos y MC tras aplicar la preselección en varias regiones. La banda amarilla muestra la suma del error estadístico y el sistemático. Todas las distribuciones muestran muy buen acuerdo entre datos y simulaciones de MC.

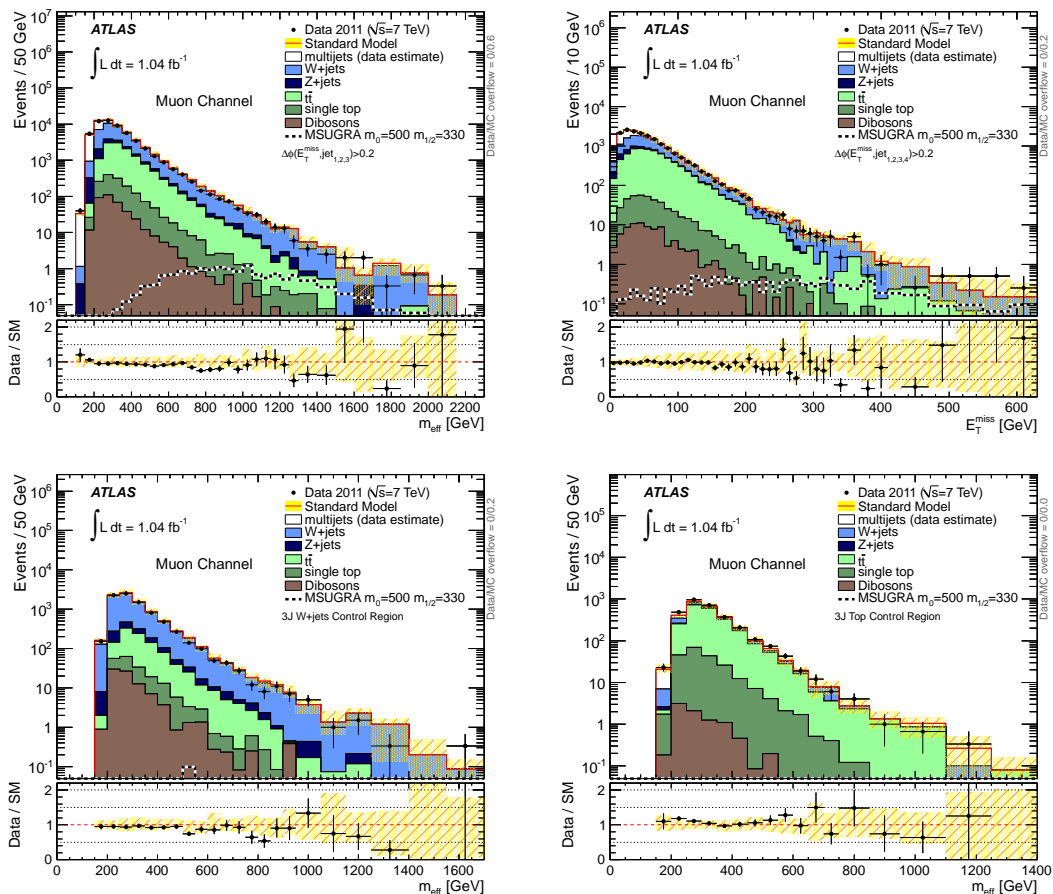


Figure 9.6: Distribución de M_{eff} para datos y muestras de MC tras aplicar la preselección en la región de señal de 3-jets (arriba izquierda), la de 4-jets (arriba derecha), la región de control WR con 3-jets (abajo izquierda) y región de control TR con 3-jets (abajo derecha).

9.3.4 Selección de sucesos

Para eliminar el fondo del SM se seleccionan cortes en las variables discutidas anteriormente, definiendo cuatro regiones óptimas que cubren toda la cuadrícula de señal. Estas regiones se dividen en función del número de jets mínimo exigido (3 ó 4) y la severidad de los cortes: 3JL (tres jets loose), 3JT (tres jets tight), 4JL (cuatro jets loose) y 4JT (cuatro jets tight). Se pueden encontrar las definiciones de estas cuatro regiones en la Tabla 9.4, junto con las de las regiones de control.

Table 9.4: Definición de las cuatro regiones de señal seleccionadas 3JL, 3JT, 4JL y 4JT junto con las regiones de control W y top.

Selección	Regiones de Señal				Regions de Control	
	3JL	3JT	4JL	4JT	3J	4J
Número de muones	= 1					
p_T Muón (GeV)	> 20					
p_T veto leptones adicionales (GeV)	> 20(10) para electrones (muones)					
Número de jets	≥ 3		≥ 4		≥ 3	≥ 4
p_T jet dominante (GeV)	60	80	60	60	60	60
p_T jets subdominantes (GeV)	25	25	25	40	25	25
$\Delta\phi(\vec{jet}_i, \vec{E}_T^{\text{miss}})$	[> 0.2 (mod. π)] for all 3 (4) jets					
m_T (GeV)	> 100				$40 < m_T < 80$	
E_T^{miss} (GeV)	> 125	> 240	> 140	> 200	$30 < E_T^{\text{miss}} < 80$	
$E_T^{\text{miss}} / M_{\text{eff}}$	> 0.25	> 0.15	> 0.30	> 0.15	–	–
M_{eff} (GeV)	> 500	> 600	> 300	> 500	> 500	> 300

Contaminación debida a rayos cósmicos

Los muones procedentes de la radiación cósmica son una fuente potencial de fondo. Los procesos de colisiones de protones se concentran en valores bajos del parámetro de impacto transversal y longitudinal respecto del PV, $|z_0^{\text{PV}}|$ y $|d_0^{\text{PV}}|$, mientras que los muones cósmicos toman valores más altos [112]. Para acotarlos se ha estudiado una opción con cortes severos (tight):

$$|z_0^{\text{PV}}| > 1 \text{ mm} \quad \text{y/o} \quad |d_0^{\text{PV}}| > 0.2 \text{ mm} \quad (9.7)$$

y otra con cortes más suaves (soft):

$$|z_0^{\text{PV}}| > 5 \text{ mm} \quad \text{y/o} \quad |d_0^{\text{PV}}| > 1 \text{ mm} \quad (9.8)$$

En el caso de RPC ambas opciones tienen una eficiencia similar. En bRPV hay que tener en cuenta que el neutralino-LSP puede tener una vida media larga dando lugar a muones desplazados respecto del PV. Aplicando la opción tight estos sucesos son eliminados de forma drástica, como se puede apreciar en la Figura 9.7, donde se muestra la eficiencia de los dos cortes. En ambas figuras se reconoce la forma de la distribución de la distancia de desintegración, haciéndose evidente que la selección tight elimina una cantidad inasumible de señal. Por tanto se selecciona la opción soft. La contribución del fondo de muones cósmicos sobre el análisis es despreciable [112].

En la Tabla 9.5 se muestra el número de sucesos esperado para el MC y el observado en los datos para las cuatro regiones de señal y las regiones de control W +top, después de todos los criterios de selección. No se observa ningún exceso de sucesos en ninguna de las regiones de señal.

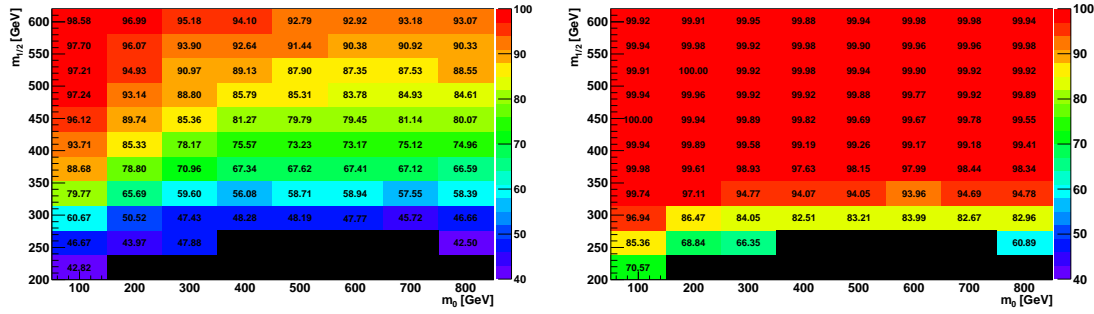


Figure 9.7: Eficiencia del veto a cósmicos con respecto al corte anterior para la selección tight (izquierda) y para la soft (derecha). Las áreas negras corresponden a puntos donde la LSP tiene vida media larga.

Table 9.5: Número de sucesos esperado para el MC y el observado en los datos para las cuatro regiones de señal y las regiones de control $W+top$.

	3JL	3JT	4JL	4JT	3J WT CR	4J WT CR
Datos	58	11	50	7	579	3071
MC	58.3	13.4	50.5	5.7	604	3119

Señal de bRPV

En esta sección se estudia el efecto de la selección sobre bRPV. La eficiencias y flujo de cortes para la combinación final de cortes en el punto ($m_0 = 100$ GeV, $m_{1/2} = 280$ GeV) de bRPV se muestran como ejemplo en la Tabla 9.6 para las regiones 3JL y 3JT.

Para la obtención del número esperado de sucesos de bRPV en cada una de las regiones de señal, se necesita definir algunas cantidades.

- La **aceptancia** da el número de sucesos que pasan todos los criterios de selección a nivel de generación (*truth*), normalizados por el número inicial de sucesos. Esta cantidad se calcula independientemente para cada subproceso de generación i , pesado por su sección eficaz. Se define la aceptación en la región SR como:

$$Acc(SR) = \frac{1}{\sigma} \sum_i \sigma_i \cdot \frac{n_i^{\text{truth}}(SR)}{n_i^{\text{initial}}} \quad (9.9)$$

donde σ_i es la sección eficaz a NLO del subproceso i y σ la total: $\sigma = \sum_i \sigma_i$
 n_i^{initial} es el número inicial de sucesos generados por el subproceso i y $n_i^{\text{truth}}(SR)$ el número de los que pasan la selección SR a nivel de generación (*truth*).

- La **eficiencia** es una medida de lo bien que se reconstruyen los objetos. Da el número de sucesos reconstruidos que pasan la selección, normalizado por el número de sucesos que pasan todos los criterios de selección a nivel *truth*. Se define la eficiencia en la región SR como:

$$Eff(SR) = \frac{1}{\sigma} \sum_i \sigma_i \cdot \frac{n_i^{\text{reco}}(SR)}{n_i^{\text{truth}}(SR)} \quad (9.10)$$

Table 9.6: Eficiencia y flujo de cortes para el punto ($m_0 = 100$ GeV, $m_{1/2} = 280$ GeV) de bRPV para las regiones 3JL y 3JT. Los umbrales de 3JT se dan entre paréntesis. El número de sucesos ha sido pesado por la eficiencia del trigger y por el efecto del *pile-up*.

bRPV 100_280 trigger + PU reweighting	Events		Eff. (%) wrt previous cut		Eff. (%) wrt initial	
	3JL	3JT	3JL	3JT	3JL	3JT
GRL	9953.21			100.00		100.00
Trigger (EF mu18)	5055.07			50.79		50.79
Event cleaning	4828.76			95.52		48.51
Cosmic muon veto	4670.86			96.73		46.93
Lepton cut	1263.08			27.04		12.69
≥ 1 jet $p_T \geq 60$ GeV (80 GeV)	1215.75	1144.65	96.25	90.62	12.21	11.50
≥ 3 jets $p_T \geq 25$ GeV	1164.41	1113.70	95.78	97.30	11.70	11.19
$\Delta\phi(\text{jet}, E_T^{\text{miss}}) > 0.2$	920.18	885.39	79.03	79.50	9.25	8.90
$E_T^{\text{miss}} > 125$ GeV (240 GeV)	574.60	242.15	62.44	27.35	5.77	2.43
$m_T > 100$ GeV	250.99	116.12	43.68	47.95	2.52	1.17
$E_T^{\text{miss}} / M_{\text{eff}} > 0.25$ (0.15)	122.31	115.99	48.73	99.89	1.23	1.17
$M_{\text{eff}} > 500$ GeV (600 GeV)	115.98	115.99	94.82	100.00	1.17	1.17

donde $n_i^{\text{reco}}(\text{SR})$ es el número de sucesos generados por el subproceso i , que pasan la selección SR a nivel de reconstrucción (reco).

Como se observa en las Figuras 5.14 y 5.15, tanto aceptación como eficiencia se reducen en la zona de bajo $m_{1/2}$ debido básicamente al veto en muones cósmicos y la mayor vida media del $\tilde{\chi}_1^0$ en esta zona.

- El **número esperado de sucesos** y su error se definen en términos de estas dos variables:

$$N_{\text{exp}}(\text{SR}) = \sigma \cdot L \cdot \text{Acc}(\text{SR}) \times \text{Eff}(\text{SR}) = L \cdot \sum_i \sigma_i \cdot \frac{n_i^{\text{reco}}(\text{SR})}{n_i^{\text{initial}}} \quad (9.11)$$

$$\varepsilon(N_{\text{exp}}(\text{SR})) = \frac{1}{N_{\text{exp}}(\text{SR})} \cdot L \cdot \sqrt{\sum_i \frac{\sigma_i^2 \cdot n_i^{\text{reco}}(\text{SR})}{n_i^{\text{initial},2}} \cdot \left(1 - \frac{n_i^{\text{reco}}(\text{SR})}{n_i^{\text{initial}}}\right)} \quad (9.12)$$

Este número se presenta en la Figura 5.16 (derecha) para una luminosidad de 1.035 fb^{-1} para la cuadrícula de bRPV junto con su incertidumbre para las cuatro SRs.

La sección eficaz total, calculada con Prospino 2.1 [97,98] se muestra en la Figura 5.17 y sus incertidumbres en las Figuras 5.18.

9.3.5 Resultados

En esta sección se presentan los principales resultados del análisis de 1-muón sobre bRPV. Los resultados se obtienen en los siguientes tres pasos:

- **Ajuste al fondo (*background fit*):** Se ajusta simultáneamente todos los fondos en todas las regiones de control sin tener en cuenta la señal.

- **Ajuste de descubrimiento (*discovery fit*):** El número de sucesos de fondo en las SRs, determinado mediante el ajuste simultáneo en las CRs adecuadamente extrapolado, se compara con el número de sucesos observado. Ésta es la llamada hipótesis de “sólo Modelo Estándar”, que se utilizaría para proclamar un descubrimiento en caso de un exceso significativo.
- **Ajuste de exclusión (*exclusion fit*):** Se proclama una exclusión en un modelo de SUSY en caso de que el número de sucesos observado sea significativamente menor que el número esperado de fondo más señal.

En las Tablas 5.9 y 5.10 se encuentran los resultados del ajuste de descubrimiento por región de señal. En ninguna de las regiones de señal se observa un exceso significativo de sucesos. Se ha utilizado la técnica descrita en Ref. [118] para extraer los límites superiores CL_S [135] al 95% de nivel de confianza en las cuatro regiones de señal estudiadas. Los resultados en todas las regiones de señal (ver Tabla 5.12) son consistentes con la hipótesis de “sólo Modelo Estándar”. Con esto se obtiene regiones de exclusión para el modelo bRPV-mSUGRA. La Figura 9.8 muestra los límites observado y esperado al 95% CL en el plano $(m_0, m_{1/2})$ para la selección 4JT, que proporciona la exclusión más extensa. En el gráfico también se puede ver la distancia de desintegración de la LSP, $c\tau$. Como se aprecia, la eficiencia de análisis decrece rápidamente conforme $c\tau$ aumenta, debido principalmente a la caída de la aceptación por el veto a los muones cósmicos.

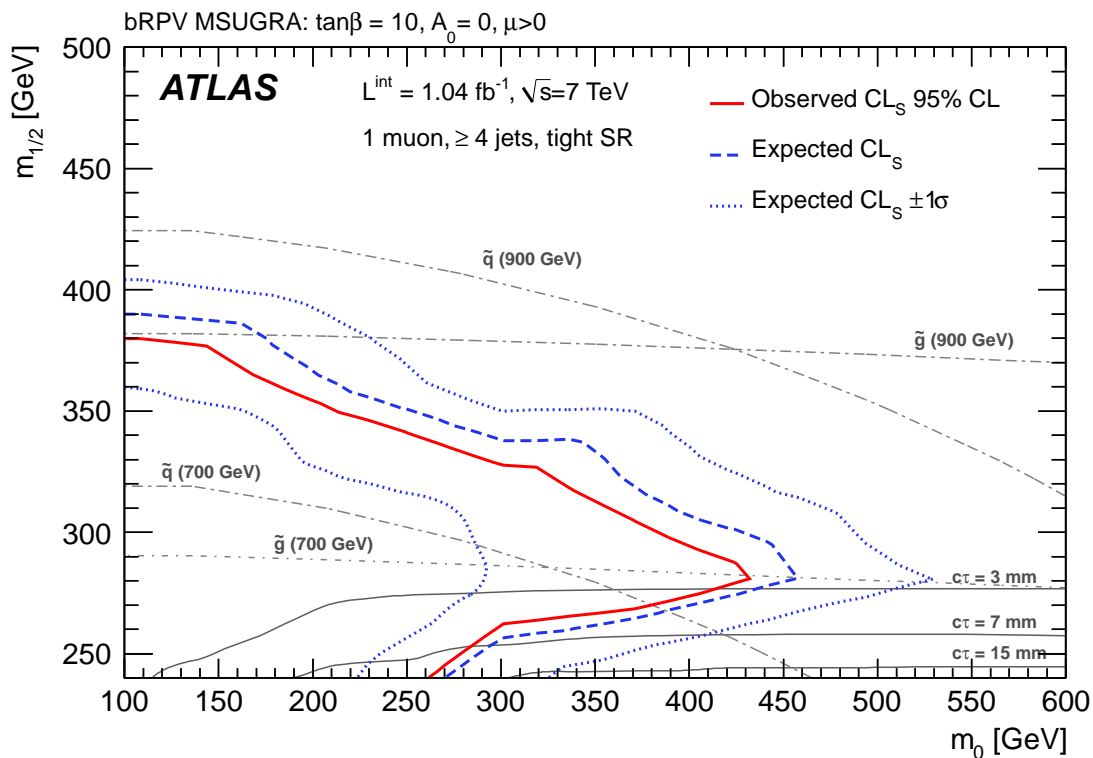


Figure 9.8: Gráfico de exclusión para el modelo bRPV-mSUGRA en la región de señal 4JT.

9.3.6 Conclusiones

En este capítulo se presenta una búsqueda de supersimetría con violación de la paridad- R mediante el término bilineal (bRPV) en estados finales que contengan exactamente un muón y al menos tres jets, con datos de colisiones protón-protón en 2011 a una energía de centro de masas de $\sqrt{s} = 7$ TeV, para una luminosidad integrada de 1.04 fb^{-1} .

En todas las regiones estudiadas se observa un buen acuerdo entre datos y números esperados para el fondo del Modelo Estándar (SM). Este resultado se ha interpretado en términos del modelo bRPV, procediendo al establecimiento de límites de exclusión de este modelo como se puede ver en la Figura 9.8. La existencia de este modelo se ha descartado con un nivel de confianza del 95% para masas de squarks por debajo de 760 GeV ($m_{\tilde{q}} = m_{\tilde{q}}$; $c\tau_{\text{LSP}} < 15$ mm). Es importante mencionar que esta es la primera vez que se pone límites de exclusión experimentales a este modelo concreto de supersimetría con violación de la paridad- R mediante el término bilineal.

La información detallada referente a este análisis se puede encontrar en Ref. [113, 114].

9.4 Validación de AF-II para SUSY

La simulación del efecto que tiene el detector ATLAS sobre sucesos generados con MC requiere gran cantidad de recursos computacionales. Para acelerar el proceso de simulación se ha desarrollado una herramienta alternativa a la simulación completa (full Geant-4): la simulación AtlFast-II (AF-II) [138]. Ésta combina la simulación completa del detector interno y sistema de muones con una simplificación del calorímetro, en la que el depósito de energía de cascadas electromagnéticas se parametriza en función del perfil de energía de la partícula que la provoca.

Teniendo en cuenta las incertidumbres teóricas en sucesos de SUSY (20 – 25%), se considera el paquete AF-II adecuado para la simulación en estos modelos. En este capítulo se presenta la evaluación del buen funcionamiento de AF-II en el contexto de SUSY. Se compara el comportamiento de todo tipo de objetos así como la eficiencia en la selección de sucesos para diferentes muestras de mSUGRA simuladas tanto en full Geant-4 como en AF-II. Como parte del estudio se ha estimado un factor 4–6 de ganancia en tiempo de AF-II sobre la simulación completa.

9.4.1 Resultados

Después de hacer una selección de objetos acorde con la utilizada en los principales análisis de SUSY se obtiene los siguientes resultados en la comparación de AF-II con full Geant-4:

Jets Todas las distribuciones muestran buen acuerdo entre AF-II y full Geant-4. Sólo en el caso de p_T hay una ligera discrepancia en todo caso menor que la mitad de la incertidumbre asociada a la escala de energía de los jets. El tagging de los jets se hace en el detector interno, que se simula completamente en AF-II y las desviaciones son menores que el 1%.

Electrones El número de electrones en AF-II es un $\sim 1.4\%$ menor que en full Geant-4, error muy por debajo de las incertidumbres teóricas de SUSY.

Muones Las desviaciones son menores que el 0.1%. Esto era de esperar ya que los muones se reconstruyen en el detector interno.

Taus Se observa un buen acuerdo en variables como p_T , η y ϕ en todos los algoritmos de reconstrucción. Las diferencias en taus que pasan el criterio de selección *loose* o *medium* son de alrededor del 1.5% para taus con $p_T > 25$ GeV.

Fotones Las distribuciones cinemáticas para fotones no muestran diferencias apreciables. Para fotones que pasan el criterio más severo de selección hay una pequeña diferencia de $\sim 2\%$.

m_T Hay buen acuerdo en todos los casos con resultados ligeramente mejores cuando el leptón seleccionado es un muón, como se esperaba.

H_T Esta distribución está ligeramente (1.5%) desplazada hacia valores más bajos en el caso de AF-II debido íntegramente a la descripción de los jets que entran en su definición.

E_T^{miss} Se observa una desviación de $\sim 2\%$ entre AF-II y full Geant-4, sobre todo en la región de valores más bajos. Esta desviación se reduce al 1% en sucesos en los que hay electrones o muones presentes.

M_{eff} La desviación entre AF-II y full Geant-4 para este término es de $\sim 5\%$, básicamente debida a las diferencias acumuladas en E_T^{miss} y H_T .

Para una estimación más detallada del efecto de la utilización de AF-II en SUSY, se ha examinado la selección básica de análisis basados en búsquedas con 0, 1 ó 2 leptones. La máxima diferencia entre eficiencias relativas entre cada paso de las selecciones está por debajo del 2%.

9.4.2 Propuesta

Dado el comportamiento extraordinario de AF-II (desviaciones menores del 5% en la descripción de objetos y del orden del $\sim 1 - 2\%$ de las eficiencias de selección), se propone lo siguiente:

- La simulación de nuevas señales de SUSY con AF-II, siempre que sea apropiado.
- Una comprobación continua del funcionamiento de AF-II en diferentes análisis de SUSY, simulando algunos puntos con full Geant-4 y comparándolos con AF-II.
- Se recomienda que se apliquen las mismas prescripciones en cuanto a descripción de objetos en AF-II que en full Geant-4.

Esta propuesta fue aceptada por el SUSY Working Group y, tras la realización de este trabajo, AF-II se utilizó en diferentes análisis que dieron lugar a varias publicaciones [117,147–149]. Los detalles de esta comparación se pueden encontrar en la nota de ATLAS [143] y en las charlas [139–142].

9.5 Conclusiones

Esta tesis se ha dedicado a la búsqueda de Supersimetría en un escenario de mSUGRA en el cual la paridad- R se rompe mediante el término bilineal (bRPV-mSUGRA). El grueso del trabajo se divide en dos análisis inclusivos, basados en la selección de estados finales con un muón y varios jets, favorecido en el caso de bRPV gracias a la desintegración de la partícula supersimétrica más ligera (LSP) a estas partículas en varios de sus canales.

En la primera parte de la tesis, expuesta en el Capítulo 4, se presenta un estudio con muestras de Monte Carlo (MC) sobre la posibilidad de observar bRPV en el experimento ATLAS para tres energías de funcionamiento del LHC: 14 TeV, 10 TeV y 7 TeV. Se han tenido en cuenta todas las posibles fuentes de fondo del Modelo Estándar (SM) y también el fondo combinatorial de SUSY. Tras la selección de sucesos, se obtiene una fracción $S_{\text{SUSY}}/\sqrt{B} > 30$ que da lugar a una significancia de $Z_n = 1.28$ ($Z_n = 0.60$) para la muestra de 7 TeV (10 TeV) y una luminosidad de 2 fb^{-1} , con Z_n definido como en Ref. [9]. En la muestra de 14 TeV se obtiene un cociente $S_{\text{SUSY}}/\sqrt{B} > 95$, aunque no se han tenido en cuenta todas las fuentes de fondo y por tanto este análisis debe tomarse como una aproximación. A partir de la distribución de la masa invariante de un muón y dos jets se puede reconstruir la masa del neutralino, el ajuste de la cual da un valor de $114.8 \pm 1.1 \text{ GeV}$ ($115.9 \pm 0.8 \text{ GeV}$), cuando el valor teórico es 109.8 GeV (118.0 GeV). Únicamente se ha tenido en cuenta el error estadístico, con lo cual la discrepancia observada se puede deber a errores sistemáticos.

Las señales de SUSY con violación de la paridad- R (RPV) suelen contener cierta cantidad $E_{\text{T}}^{\text{miss}}$. Por ello, si se observase una evidencia de la existencia de SUSY en una búsqueda inclusiva basada en $E_{\text{T}}^{\text{miss}}$, no se podría descartar el caso de RPV directamente. Ésta es la razón para el desarrollo de la segunda parte de la tesis, la cual está dedicada a la interpretación en el modelo bRPV de una búsqueda con datos reales de ATLAS procedentes de colisiones a $\sqrt{s} = 7 \text{ TeV}$ en el LHC. La búsqueda, basada en estados finales con exactamente un muón, varios jets y una cantidad mínima de $E_{\text{T}}^{\text{miss}}$, da lugar a los primeros límites de exclusión que se ha puesto a bRPV.

Tras realizar un fit combinado de las muestras de MC a los datos no se observa ningún exceso significativo de datos sobre las predicciones del SM. Este resultado se interpreta como una evidencia negativa de la existencia de bRPV-SUSY y, consecuentemente, se definen límites

de exclusión que se pueden ver en la Figura 5.27. Este modelo se puede descartar a un 95% de nivel de confianza para masas de los squarks mayores que 760 GeV ($m_{\tilde{g}} = m_{\tilde{q}}$; $c\tau_{\text{LSP}} < 15$ mm).

Como complemento a estos dos análisis de física, se ha realizado un estudio sobre el buen funcionamiento de la herramienta de simulación AF-II. El trabajo, presentado en el Capítulo 6, consiste en la validación de esta herramienta para varios análisis en SUSY, comparando su funcionamiento con el de la herramienta usual, full Geant-4. Tras la obtención de resultados muy positivos, el ATLAS SUSY Working Group decidió adoptar el uso de AF-II para la simulación de varias muestras de SUSY, que dieron lugar a varias publicaciones sobre búsquedas de SUSY [117,147–149]

9.6 Seguimiento del análisis

Viendo los resultados presentados en el Capítulo 5 se ha realizado un seguimiento del análisis para una luminosidad de 4.7 fb^{-1} con datos de ATLAS de colisiones pp a $\sqrt{s} = 7 \text{ TeV}$ en el LHC. El análisis considera estados finales con exactamente un leptón (electrón o muón) de alto- p_T y al menos 7 jets. Teniendo en cuenta todas las fuentes de fondo del SM, no se observa una discrepancia significativa entre el número esperado de sucesos en el SM (6.0 ± 2.4 en el canal de 1-electrón, 3.7 ± 2.4 en el de 1-muón) y el número observado de sucesos (7 en ambos canales).

Los canales de electrón y muón, estadísticamente independientes, se combinan para dar lugar a los límites de exclusión para el modelo bRPV-mSUGRA mostrados en la Figura 9.9. La banda de incertidumbre alrededor del límite incluye todas las incertidumbres posibles excepto la teórica de SUSY, la cual está representada por las bandas en el límite observado. Se puede ver una mejora significativa en la sensibilidad con respecto a la presentada en la tesis, que se muestra en la línea azul. La región de bajo $m_{1/2}$ corresponde a LSP con largas vidas medias y no está considerada en este análisis.

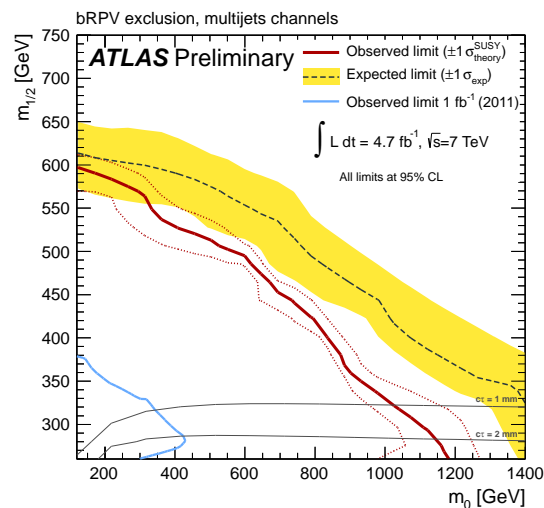


Figure 9.9: Límites de exclusión al 95% CL esperados y observados para el modelo bRPV. La banda alrededor del valor medio muestra las variaciones $\pm 1\sigma$ incluyendo todas las incertidumbres excepto la teórica de la señal. Ésta está representada por las líneas punteadas. La fina línea negra continua muestra la longitud de desintegración de la LSP. El resultado del análisis anterior de ATLAS presentado en el Capítulo 5 para este modelo se muestra como una línea azul.

Appendix A

Monte Carlo sample details

A.1 SUSY production processes

Table A.1: NLO Cross sections for all possible SUSY production processes in a proton-proton collider at 7 TeV for bRPV-mSUGRA point defined in Table 4.1 with $m_0 = 100$ GeV, $m_{1/2} = 280$ GeV. The cross sections have been calculated by PYTHIA at LO and by Prospino at NLO.

subProcess	σ [pb]	
$q q \rightarrow \tilde{q} \tilde{g}$	1.107	$\tilde{q} \tilde{g} = \tilde{q} \tilde{g} + \tilde{\bar{q}} \tilde{g}$
$q q \rightarrow \tilde{q} \tilde{q}$	0.825	$\tilde{q} \tilde{q} = \tilde{q} \tilde{q} + \tilde{\bar{q}} \tilde{\bar{q}}$
$q q \rightarrow \tilde{\chi} \tilde{\chi}$	0.434	$\tilde{b} \tilde{b} = \tilde{b}_1 \tilde{b}_1 + \tilde{b}_2 \tilde{b}_2 + \tilde{b}_1 \tilde{\chi}_1^0 + \tilde{b}_2 \tilde{\chi}_1^0$
$q q \rightarrow \tilde{q} \tilde{\bar{q}}$	0.343	$\tilde{t} \tilde{\bar{t}} = \tilde{t}_1 \tilde{\bar{t}}_1 + \tilde{t}_2 \tilde{\bar{t}}_2 + \tilde{t}_1 \tilde{\chi}_1^0 + \tilde{t}_2 \tilde{\chi}_1^0$
$q q \rightarrow \tilde{g} \tilde{g}$	0.169	$\tilde{\chi}^0 = \tilde{\chi}_1^0, \tilde{\chi}_2^0, \tilde{\chi}_3^0, \tilde{\chi}_4^0$
$q q \rightarrow \tilde{\ell} \tilde{\ell}$	0.146	$\tilde{\chi}^\pm = \tilde{\chi}_1^\pm, \tilde{\chi}_2^\pm$
$q q \rightarrow \tilde{t} \tilde{\bar{t}}$	0.088	$\tilde{\chi} = \tilde{\chi}^0 + \tilde{\chi}^\pm$
$q q \rightarrow \tilde{q} \tilde{\chi}^\pm$	0.059	$\tilde{\ell} \tilde{\ell} = \tilde{e}_L \tilde{e}_L + \tilde{e}_R \tilde{e}_R + \tilde{\nu}_{eL} \tilde{\nu}_{eL} + \tilde{e}^+ \tilde{\nu}_{eL} + \tilde{e}^- \tilde{\nu}_{eL} +$
$q q \rightarrow \tilde{q} \tilde{\chi}^0$	0.052	$\tilde{\mu}_L \tilde{\mu}_L + \tilde{\mu}_R \tilde{\mu}_R + \tilde{\nu}_{\mu L} \tilde{\nu}_{\mu L} + \tilde{\mu}^+ \tilde{\nu}_{\mu L} + \tilde{\mu}^- \tilde{\nu}_{\mu L} +$
$q q \rightarrow \tilde{b} \tilde{b}$	0.029	$\tilde{\tau}_1 \tilde{\tau}_1 + \tilde{\tau}_2 \tilde{\tau}_2 + \tilde{\tau}_1 \tilde{\tau}_2 + \tilde{\nu}_\tau \tilde{\nu}_\tau + \tilde{\tau}_1^+ \tilde{\nu}_\tau + \tilde{\tau}_1^- \tilde{\nu}_\tau + \tilde{\tau}_2^+ \tilde{\nu}_\tau + \tilde{\tau}_2^- \tilde{\nu}_\tau$
$q q \rightarrow \tilde{g} \tilde{\chi}^\pm$	0.025	
$q q \rightarrow \tilde{g} \tilde{\chi}^0$	0.020	
Total	3.296	

A.2 Monte Carlo signal samples for the 1muon+2jets analyses

Full details on the generation and simulation conditions are provided in Table A.2 for the three-energy scenarios.

Table A.2: Simulation details for the signal samples in the three-energy scenarios.

LHC c.m.s. energy	Athena release	PYTHIA version	SPheno version	# of simulated events
7 TeV	16.0.3	6.4.20	3.1.0	10000
10 TeV	14.2.20	6.4.20	v3beta20	10000
14 TeV	12.0.7	6.4.20	v3beta20	10000

The parameter values taken in each case, including the mSUGRA point, neutrino physics experimental constraints and bRPV parameters can be found in Table A.3 for the 7, 10 and 14 TeV signal samples.

Table A.3: Parameters for the mSUGRA point, neutrino physics experimental constraints, bRPV parameters and $\tilde{\chi}_1^0$ -LSP characteristics for the signal samples in the three-energy scenarios.

mSUGRA point	neutrino mixing parameters	bRPV parameters
7 TeV sample		
$m_0 = 100$ GeV	$\Delta m_{\text{atm}}^2 = 2.35 \times 10^{-3} \text{eV}^2$	$\epsilon_1 = 198$ MeV;
$m_{1/2} = 280$ GeV	$\Delta m_{\text{sol}}^2 = 7.58 \times 10^{-5} \text{eV}^2$	$\epsilon_2 = -373$ MeV;
$\tan\beta = 10$	$\tan^2\theta_{\text{atm}} = 1.26$	$\epsilon_3 = 383$ MeV
$A_0 = 0$ GeV	$\tan^2\theta_{\text{sol}} = 0.47$	$v_1 = -17.5$ MeV
$\text{sgn}\mu = +1$		$v_2 = 33.0$ MeV
		$v_3 = 33.8$ MeV
LSP mass	LSP lifetime	cross section
$m_{\tilde{\chi}_1^0} = 109.8$ GeV	$c\tau(\tilde{\chi}_1^0) = 677$ μm	3.3 pb
10 TeV sample		
$m_0 = 100$ GeV; $m_{1/2} = 300$ GeV	$\Delta m_{\text{atm}}^2 = 2.2 \times 10^{-3} \text{eV}^2$	$\epsilon_1 = -\epsilon_2 = \epsilon_3 = 102$ MeV
$\tan\beta = 6$	$\Delta m_{\text{sol}}^2 = 2.8 \times 10^{-5} \text{eV}^2$	$v_1 = -8.8$ MeV
$A_0 = -300$ GeV	$\tan^2\theta_{\text{atm}} = 0.96$	$v_2 = 9.0$ MeV
$\text{sgn}\mu = +1$	$\tan^2\theta_{\text{sol}} = 0.64$	$v_3 = -8.6$ MeV
LSP mass	LSP lifetime	cross section
$m_{\tilde{\chi}_1^0} = 118.0$ GeV	$c\tau(\tilde{\chi}_1^0) = 290$ μm	4.8 pb
14 TeV sample		
$m_0 = 100$ GeV; $m_{1/2} = 250$ GeV	$\Delta m_{\text{atm}}^2 = 2.2 \times 10^{-3} \text{eV}^2$	$\epsilon_1 = -\epsilon_2 = \epsilon_3 = 40$ MeV
$\tan\beta = 10$	$\Delta m_{\text{sol}}^2 = 3.4 \times 10^{-5} \text{eV}^2$	$v_1 = -2.7$ MeV
$A_0 = -100$ GeV	$\tan^2\theta_{\text{atm}} = 0.97$	$v_2 = 2.9$ MeV
$\text{sgn}\mu = +1$	$\tan^2\theta_{\text{sol}} = 0.64$	$v_3 = -2.6$ MeV
LSP mass	LSP lifetime	cross section
$m_{\tilde{\chi}_1^0} = 97.1$ GeV	$c\tau(\tilde{\chi}_1^0) = 1.6$ mm	41 pb

A.3 Monte Carlo SM samples for the one-lepton analysis

All Monte Carlo samples used in the one-lepton analysis defined in Chapter 5 are taken from the official mc10a Monte Carlo production. Table A.4 lists all top, multijet and diboson samples used in this analysis together with the data set number, the generator, the corresponding cross sections. Similar numbers, as well as the k-factor applied, are summarised in Tables A.5 and A.6 for W - and Z -samples.

Table A.4: top and diboson-Monte Carlo samples with sample ID, generator and cross section.

Sample ID	Name	Generator	$\sigma \times \text{BR}$ [pb]
105200	T1	MC@NLO Jimmy	8.9
105204	TTbar FullHad	MC@NLO Jimmy	7.1
105860	TTbar	PowHeg Jimmy	7.9
105861	TTbar	PowHeg PYTHIA	7.9
108340	st tchan enu	MC@NLO Jimmy	7.0
108341	st tchan munu	MC@NLO Jimmy	7.0
108342	st tchan taunu	MC@NLO Jimmy	7.0
108343	st schan enu	MC@NLO Jimmy	4.7
108344	st schan munu	MC@NLO Jimmy	4.7
108345	st schan taunu	MC@NLO Jimmy	4.7
108346	st Wt	MC@NLO Jimmy	1.3
105985	WW	Herwig	1.7
105986	ZZ	Herwig	1.3
105987	WZ	Herwig	5.5

Table A.5: *W*-Monte Carlo samples with sample ID, generator, cross section and k-factor.

Sample ID	Name	Generator	$\sigma \times \text{BR}$ [pb]	k-factor
107680	WenuNp0 pt20	AlpgenJimmy	$6.9 \cdot 10^3$	1.20
107681	WenuNp1 pt20	AlpgenJimmy	$1.3 \cdot 10^3$	1.20
107682	WenuNp2 pt20	AlpgenJimmy	$3.8 \cdot 10^2$	1.20
107683	WenuNp3 pt20	AlpgenJimmy	$1.0 \cdot 10^2$	1.20
107684	WenuNp4 pt20	AlpgenJimmy	$2.5 \cdot 10^1$	1.20
107685	WenuNp5 pt20	AlpgenJimmy	6.9	1.20
107690	WmunuNp0 pt20	AlpgenJimmy	$6.9 \cdot 10^3$	1.20
107691	WmunuNp1 pt20	AlpgenJimmy	$1.3 \cdot 10^3$	1.20
107692	WmunuNp2 pt20	AlpgenJimmy	$3.8 \cdot 10^2$	1.20
107693	WmunuNp3 pt20	AlpgenJimmy	$1.0 \cdot 10^2$	1.20
107694	WmunuNp4 pt20	AlpgenJimmy	$2.5 \cdot 10^1$	1.20
107695	WmunuNp5 pt20	AlpgenJimmy	6.9	1.20
107700	WtaunuNp0 pt20	AlpgenJimmy	$6.9 \cdot 10^3$	1.20
107701	WtaunuNp1 pt20	AlpgenJimmy	$1.3 \cdot 10^3$	1.20
107702	WtaunuNp2 pt20	AlpgenJimmy	$3.8 \cdot 10^2$	1.20
107703	WtaunuNp3 pt20	AlpgenJimmy	$1.0 \cdot 10^2$	1.20
107704	WtaunuNp4 pt20	AlpgenJimmy	$2.5 \cdot 10^1$	1.20
107705	WtaunuNp5 pt20	AlpgenJimmy	6.9	1.20
106280	WbbNp0 pt20	AlpgenJimmy	3.2	1.20
106281	WbbNp1 pt20	AlpgenJimmy	2.6	1.20
106282	WbbNp2 pt20	AlpgenJimmy	1.4	1.20
106283	WbbNp3 pt20	AlpgenJimmy	0.6	1.20

Table A.6: *Z*- and Drell Yan Monte Carlo samples with sample ID, generator, cross section and k-factor.

Sample ID	Name	Generator	$\sigma \times \text{BR}$ [pb]	k-factor
107650	ZeeNp0 pt20	AlpgenJimmy	$6.6 \cdot 10^2$	1.25
107651	ZeeNp1 pt20	AlpgenJimmy	$1.3 \cdot 10^2$	1.25
107652	ZeeNp2 pt20	AlpgenJimmy	$4.0 \cdot 10^1$	1.25
107653	ZeeNp3 pt20	AlpgenJimmy	$1.1 \cdot 10^1$	1.25
107654	ZeeNp4 pt20	AlpgenJimmy	2.9	1.25
107655	ZeeNp5 pt20	AlpgenJimmy	$7.5 \cdot 10^{-1}$	1.25
107660	ZmumuNp0 pt20	AlpgenJimmy	$6.6 \cdot 10^2$	1.25
107661	ZmumuNp1 pt20	AlpgenJimmy	$1.3 \cdot 10^2$	1.25
107662	ZmumuNp2 pt20	AlpgenJimmy	$4.0 \cdot 10^1$	1.25
107663	ZmumuNp3 pt20	AlpgenJimmy	$1.1 \cdot 10^1$	1.25
107664	ZmumuNp4 pt20	AlpgenJimmy	2.9	1.25
107665	ZmumuNp5 pt20	AlpgenJimmy	$7.5 \cdot 10^{-1}$	1.25
107670	ZtautauNp0 pt20	AlpgenJimmy	$6.6 \cdot 10^2$	1.25
107671	ZtautauNp1 pt20	AlpgenJimmy	$1.3 \cdot 10^2$	1.25
107672	ZtautauNp2 pt20	AlpgenJimmy	$4.0 \cdot 10^1$	1.25
107673	ZtautauNp3 pt20	AlpgenJimmy	$1.1 \cdot 10^1$	1.25
107674	ZtautauNp4 pt20	AlpgenJimmy	2.9	1.25
107675	ZtautauNp5 pt20	AlpgenJimmy	$7.5 \cdot 10^{-1}$	1.25

Appendix B

Backup plots for the 10 TeV and 14 TeV analyses

B.1 Event selection: SM background for the 10 TeV analysis

As a part of the SM background study for the 10 TeV sample, correlations between the variables E_T^{miss} , M_{eff} and S_T have been checked. In Figure B.1 an example of these plots is presented, showing that no significant correlation between them is observed.

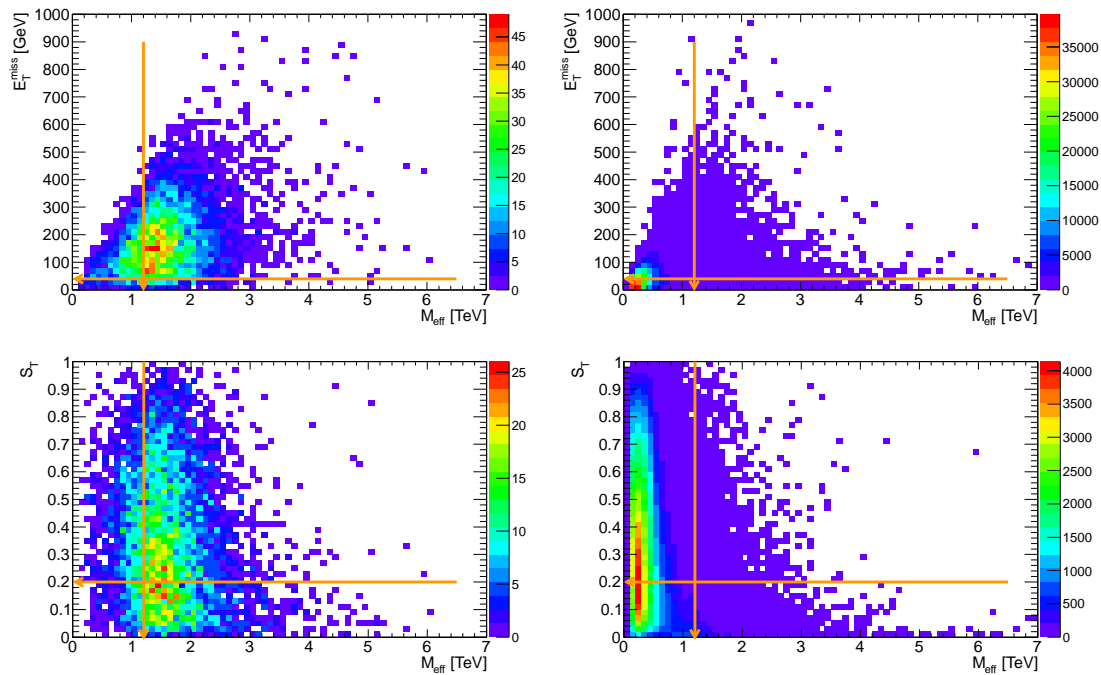


Figure B.1: M_{eff} vs. E_T^{miss} (top) and M_{eff} vs. S_T (bottom) distributions for the SUSY inclusive signal (left) and for all SM backgrounds (right) at 10 TeV after the `mu10i_loose_2j20` selection, normalised to 2 fb^{-1} . The arrows show the cut values.

B.2 Event selection: SM background for the 14 TeV analysis

Analogous to the 7 TeV analysis, S_T plots for the bRPV signal and for all SM background sources under consideration in the 14 TeV analysis are shown in Figures B.2 before any selection or cuts applied (left) and after the preselection μ_{10_2j20} (right). Similar to the 7 TeV case, the QCD distribution peaks at very low S_T values (< 0.01). W +jets distribution is also dominant at low S_T values while top backgrounds and bRPV signal have a flatter distribution. The right panel of the figure shows how the preselection strongly reduces the QCD background in three orders of magnitude. The spikes seen in the low S_T region are caused by large normalisation factors applied to these samples, due to the huge QCD cross section.

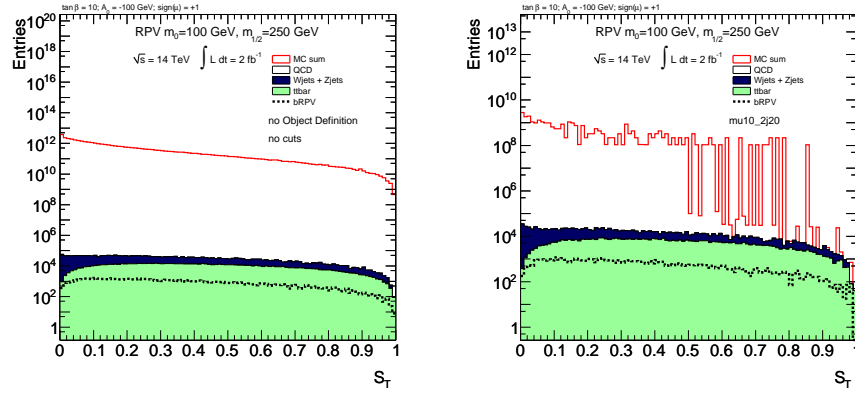


Figure B.2: S_T distributions for the SUSY inclusive signal and for all SM backgrounds under consideration at 14 TeV before applying any object definition (left) and after the preselection μ_{10_2j20} (right), normalised to 2 fb^{-1} .

B.3 Combinatorial background study for the 10 TeV analysis

Analogous plots to those shown in the 7 TeV analysis for the correlations over several variables in the combinatorial background study are shown here for the 10 TeV analysis.

In Figure B.3, 2-dimensional plots are shown for p_T - ΔR correlations for the SUSY sample: the correlation for the W (left) and $\tilde{\chi}_1^0$ (right) momentum and the separation angle between their decay products is plotted for truth particles (top) and for reconstructed candidates (bottom). In the truth (top) plots and as expected, higher momenta of the decaying particle imply smaller separation angles for the decay products. On the contrary, reconstructed (bottom) plots are more evenly spread over the p_T - ΔR plane. Bear in mind that the reconstructed W -candidate is selected only if $m_{jj} \subset \{M_W \pm 5 \text{ GeV}\}$.

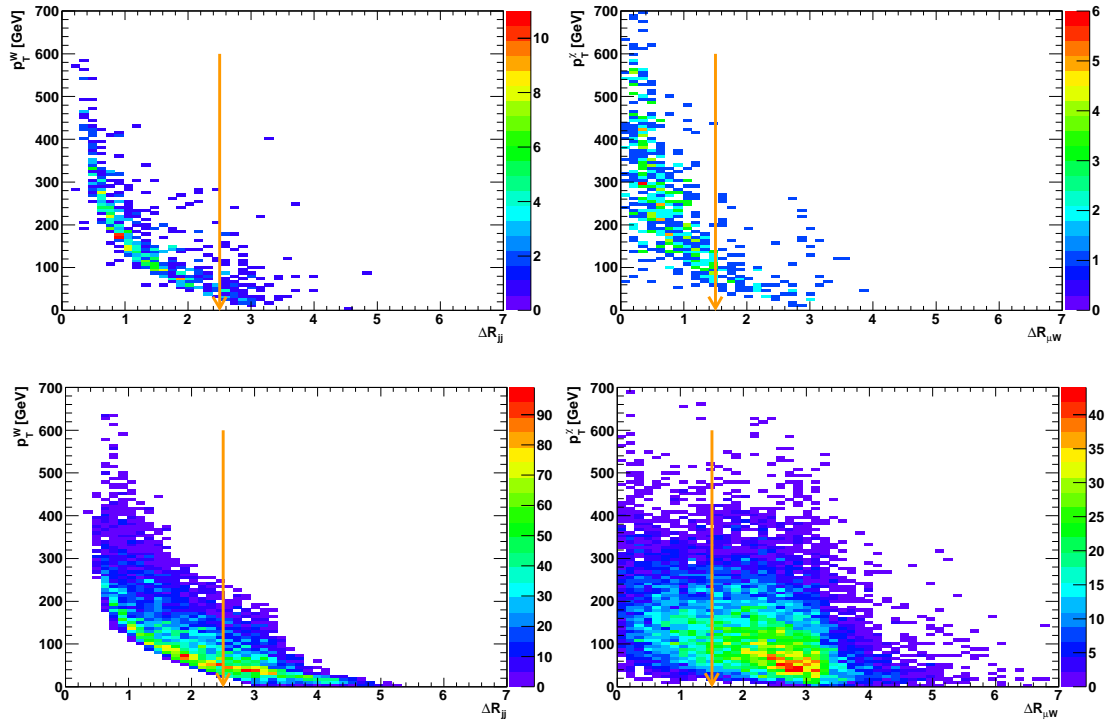


Figure B.3: p_T - ΔR correlations for the SUSY sample at 10 TeV. *Top left*: p_T of truth W bosons coming from LSPs vs. the angle between their decay products: two jets. *Top right*: p_T of truth $\tilde{\chi}_1^0$ vs. the angle between its decay products: a muon and a W . *Bottom left*: p_T of all W candidates (with $m_{jj} \subset \{M_W \pm 5 \text{ GeV}\}$) vs. the angle between the pair of reconstructed jets used to form it. *Bottom right*: Neutralino-candidate p_T vs. the angle between the reconstructed muon and the W -candidate (with $m_{jj} \subset \{M_W \pm 5 \text{ GeV}\}$) used to identify it. The arrows show the cut values.

Several combined cuts on the variables $p_T(W) - \Delta R_{jj}$ and $p_T(\tilde{\chi}_1^0) - \Delta R_{\mu W}$ have been checked following the study in the 7 TeV sample. Similar results as in that case are found so no combined cut on any of these variables is finally applied.

Correlation between ΔR_{jj} and $\Delta R_{\mu W}$ is checked in Figure B.4 for both the truth signal decay (left) and the inclusive reconstructed sample (right), with negative result.

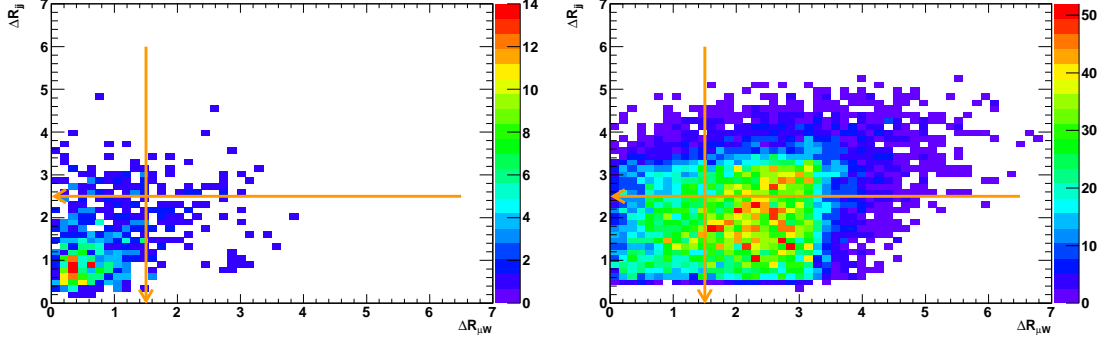


Figure B.4: Correlation of angular distances for the SUSY sample at 10 TeV. *Left*: Angle between true jets coming from an LSP-originating W vs. the angle between a true muon and a true W both coming from an LSP. *Right*: Angle between all reconstructed jets to form a W -candidate as a function of the angle of all reconstructed muons and all W -candidates. The arrows show the cut values.

Finally, correlation between $p_T(W)$ and $p_T(\tilde{\chi}_1^0)$ has been studied similar as in the 7 TeV case, with the same result.

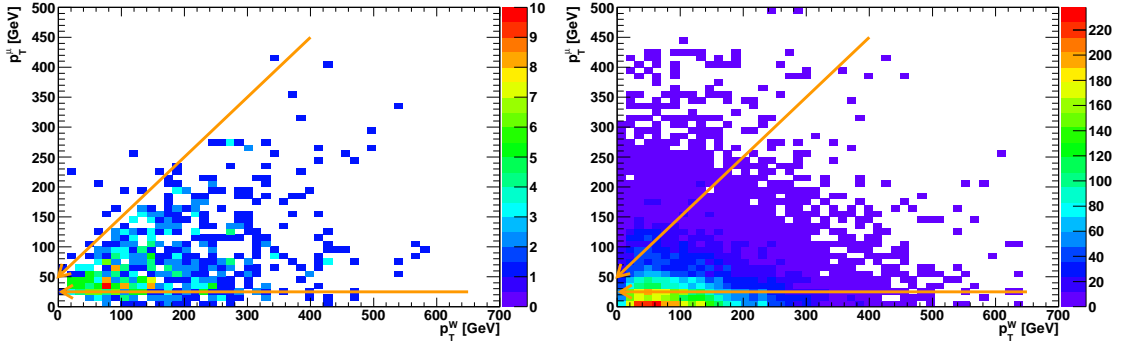


Figure B.5: Transverse momenta correlations for the SUSY sample at 10 TeV. *Left*: True-muon p_T coming from an LSP vs. true- $W p_T$ coming from the same LSP. *Right*: Reconstructed-muon p_T vs. W -candidate p_T to be combined with it to form a $\tilde{\chi}_1^0$ -candidate. The arrows show the cut values.

After all these checks, it has been decided that only independent cuts on $p_T(\mu)$, ΔR_{jj} and $\Delta R_{\mu W}$ will be applied in order to discriminate the combinatorial background from the muon and pair of jets originating from a $\tilde{\chi}_1^0$.

Appendix C

Combinatorial background study for different p_T^μ thresholds

In Figure 4.25, the $M_{\mu jj}$ distribution was shown for the whole SUSY sample applying, among other selection criteria, the cut $p_T^\mu > 25$ GeV. In this appendix, the shape of this distribution for the signal decay and for the SUSY combinatorial background applying various thresholds on the muon transverse momentum is studied for the 10 TeV sample. Analogous tests have been performed for the 7 TeV case.

A subsample of the SUSY inclusive signal containing at least one true neutralino decaying to a muon and a hadronic W is identified, henceforth called “signal-subsample”. The preselection and *SM cuts* are now applied to this signal-subsample, obtaining the contribution to the μjj invariant mass of events involving at least one such neutralino. This distribution is drawn in Figure C.1, the four panels corresponding to different p_T^μ thresholds: 10, 25, 60 and 100 GeV. In this figure the signal-subsample peak (black area) remains clearly visible and fixed around the lightest neutralino mass independently of the p_T^μ selection, with only a decrease in the acceptance as the cut becomes tighter. Unlike signal, the distribution shape of the rest of events not included in the signal-subsample (green dashed line) is strongly dependent on the p_T^μ cut value. This can be seen in the successive plots of Figure C.1, where a displacement of the combinatorial background peak can be seen as the p_T^μ cut increases. The edge at ~ 90 GeV seen at the combinatorial background for $p_T^\mu > 10$ GeV disappears at thresholds higher than 20 GeV. Even though a tighter cut would act as a better discriminant for the signal-subsample, the $p_T^\mu > 25$ GeV is selected so that a considerable statistics remains available.

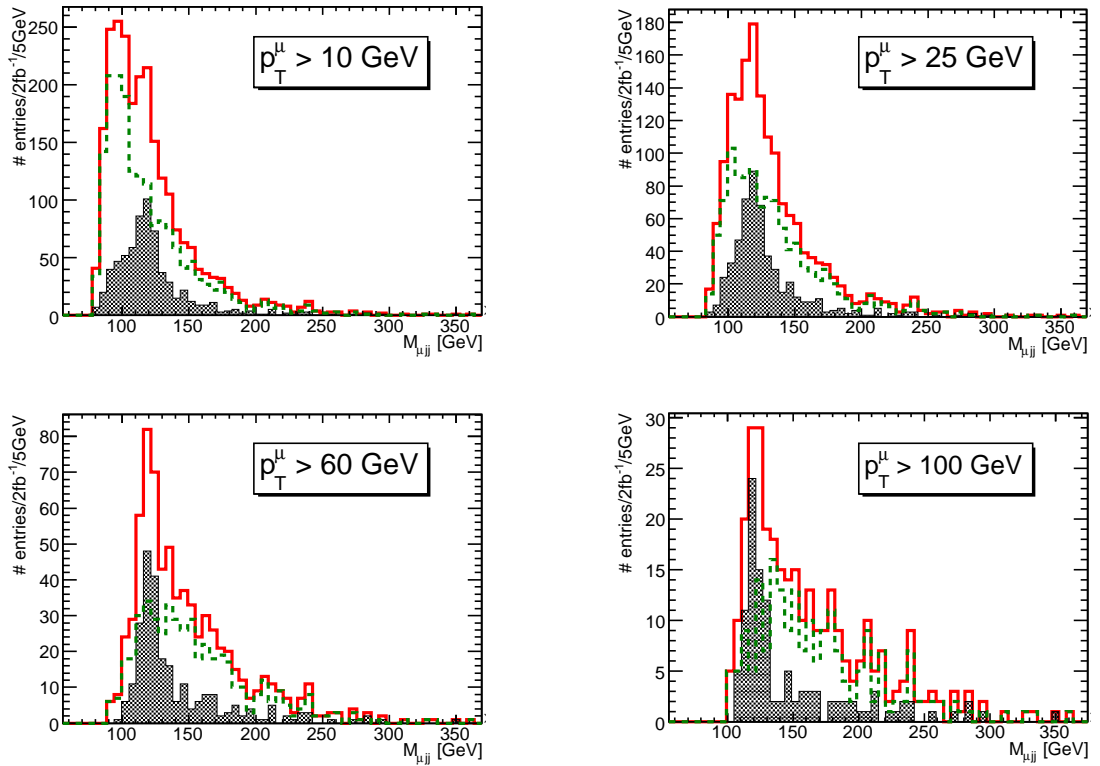


Figure C.1: Invariant mass $M_{\mu_{ij}}$ for various p_T cuts on the selected muons after applying the preselection and SM cuts. The whole SUSY inclusive sample (red-continuous line), the signal subsample (black area) and their difference (green-dashed line), corresponding to the combinatorial background, are shown. The p_T^μ thresholds from top-left to bottom-right are 10, 25, 60 and 100 GeV, respectively.

Appendix D

Further details on the comparison RPC versus bRPV

In Figures D.1 to D.5, a comparison between RPC and bRPV distributions on the variables involved in the 1-muon analysis is shown for 5 different mSUGRA points: $(m_0 = 100 \text{ GeV}, m_{1/2} = 200 \text{ GeV})$, $(m_0 = 100 \text{ GeV}, m_{1/2} = 280 \text{ GeV})$, $(m_0 = 100 \text{ GeV}, m_{1/2} = 360 \text{ GeV})$, $(m_0 = 200 \text{ GeV}, m_{1/2} = 280 \text{ GeV})$, $(m_0 = 400 \text{ GeV}, m_{1/2} = 320 \text{ GeV})$.

In every case nearby grid points are compared. Comparison is shown after the 1-muon selection and after the m_T cut (but before applying the E_T^{miss} and M_{eff} cuts) for the four signal regions selections considered in the analysis, for the following variables:

- E_T^{miss} : The E_T^{miss} spectrum for bRPV is softer than that of RPC in all of the signal region selections throughout the grid. The difference between RPC and bRPV becomes more important at high m_0 , having an effect on the final acceptance of this mSUGRA area to be decreased with respect to the low m_0 area, yet remaining significantly higher than the expected from SM processes.
- M_{eff} : The M_{eff} distribution is similar in both RPC and bRPV cases, with its shape slightly shifted towards higher values in bRPV in the low m_0 - low $m_{1/2}$ region. This cut does not have a major impact on the final selection and thus the acceptances are not very much affected by it.
- m_T : This distributions is also similar in both cases, giving rise to slightly lower values for bRPV at high m_0 . Since the cut value on m_T is maintained in the four signal regions, no differences on acceptances are appreciated due to this cut.
- $E_T^{\text{miss}} - M_{\text{eff}}$ plane: As already mentioned in Section 5.5.1, the cut on this combination of variables becomes the dominant selection in the loose regions, leading to higher number of surviving events in the tight selections better than in the loose ones. This effect is more important in the high m_0 , giving a better acceptance for this points in the tight regions. This can be seen in the exclusion plots shown in Figures 5.26 and 5.27, where a larger area is excluded in the tight selections.

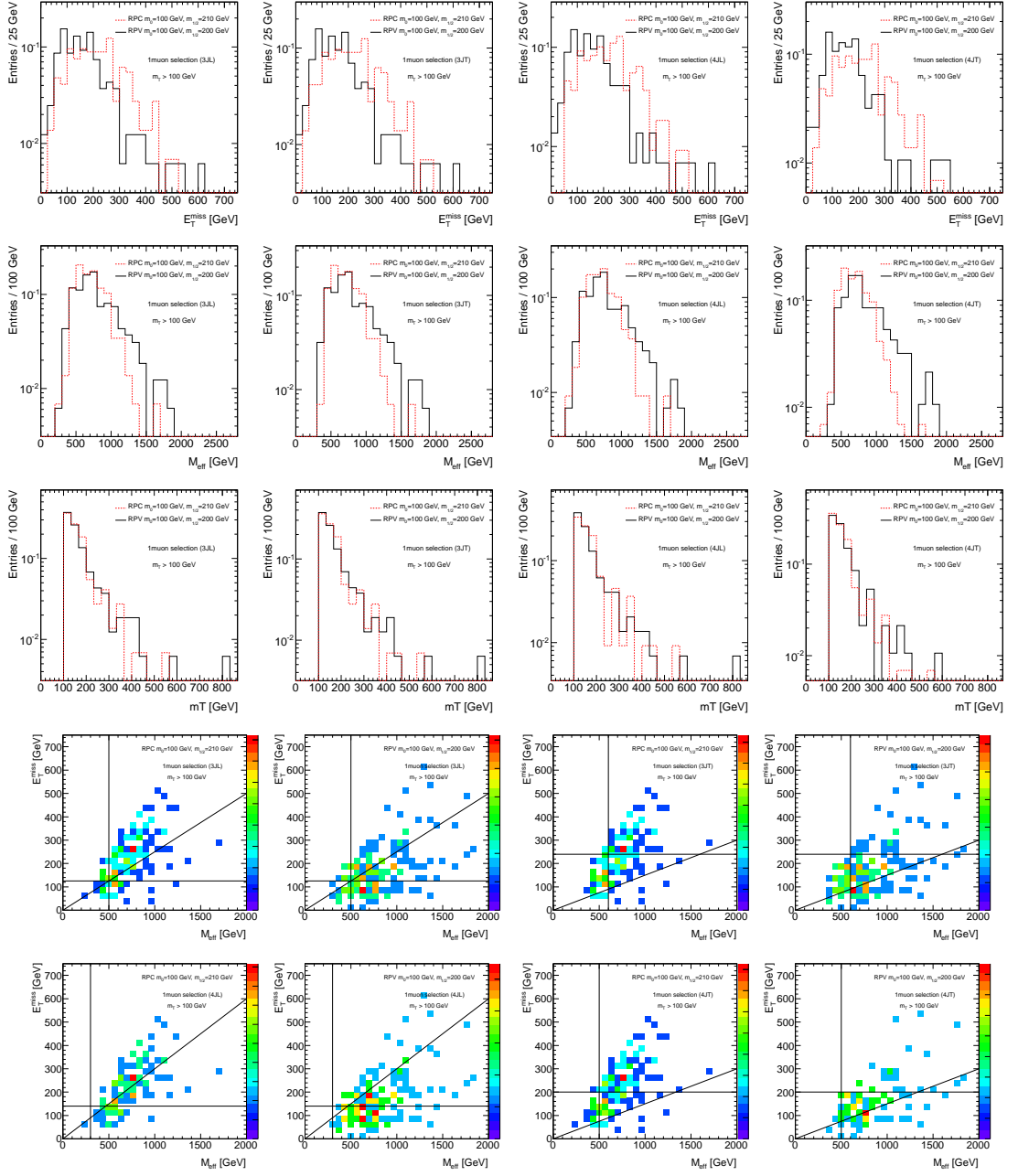


Figure D.1: E_T^{miss} (first row), M_{eff} (second row) and m_T (third row) distributions comparison in the signal point (100, 200) for bRPV SUSY (black continuous line) and nearby point (100, 210) R -parity conserving SUSY (red dashed line) after 1-muon 3JL (first column), 3JT (second column), 4JL (third column) and 4JT (last column) selections and after the m_T cut common to all SRs. Bottom plots show a comparison between RPC and bRPV in the E_T^{miss} vs. M_{eff} plane for the four signal region selections after applying the $m_T > 100$ GeV cut. The distributions are normalised to unity.

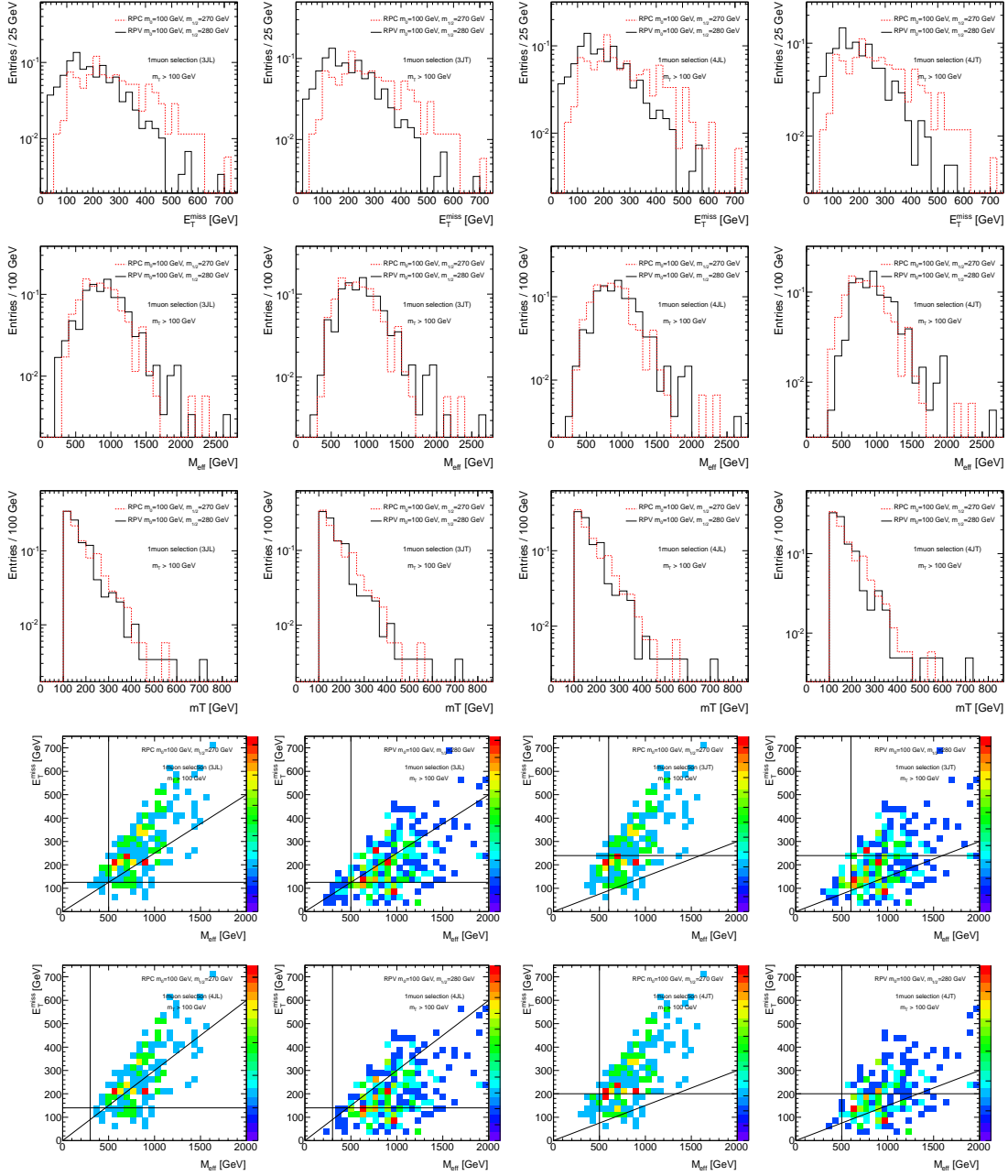


Figure D.2: E_T^{miss} (first row), M_{eff} (second row) and m_T (third row) distributions comparison in the signal point (100, 280) for bRPV SUSY (black continuous line) and nearby point (100, 270) R -parity conserving SUSY (red dashed line) after 1-muon 3JL (first column), 3JT (second column), 4JL (third column) and 4JT (last column) selections and after the m_T cut common to all SRs. Bottom plots show a comparison between RPC and bRPV in the E_T^{miss} vs. M_{eff} plane for the four signal region selections after applying the $m_T > 100$ GeV cut. The distributions are normalised to unity.

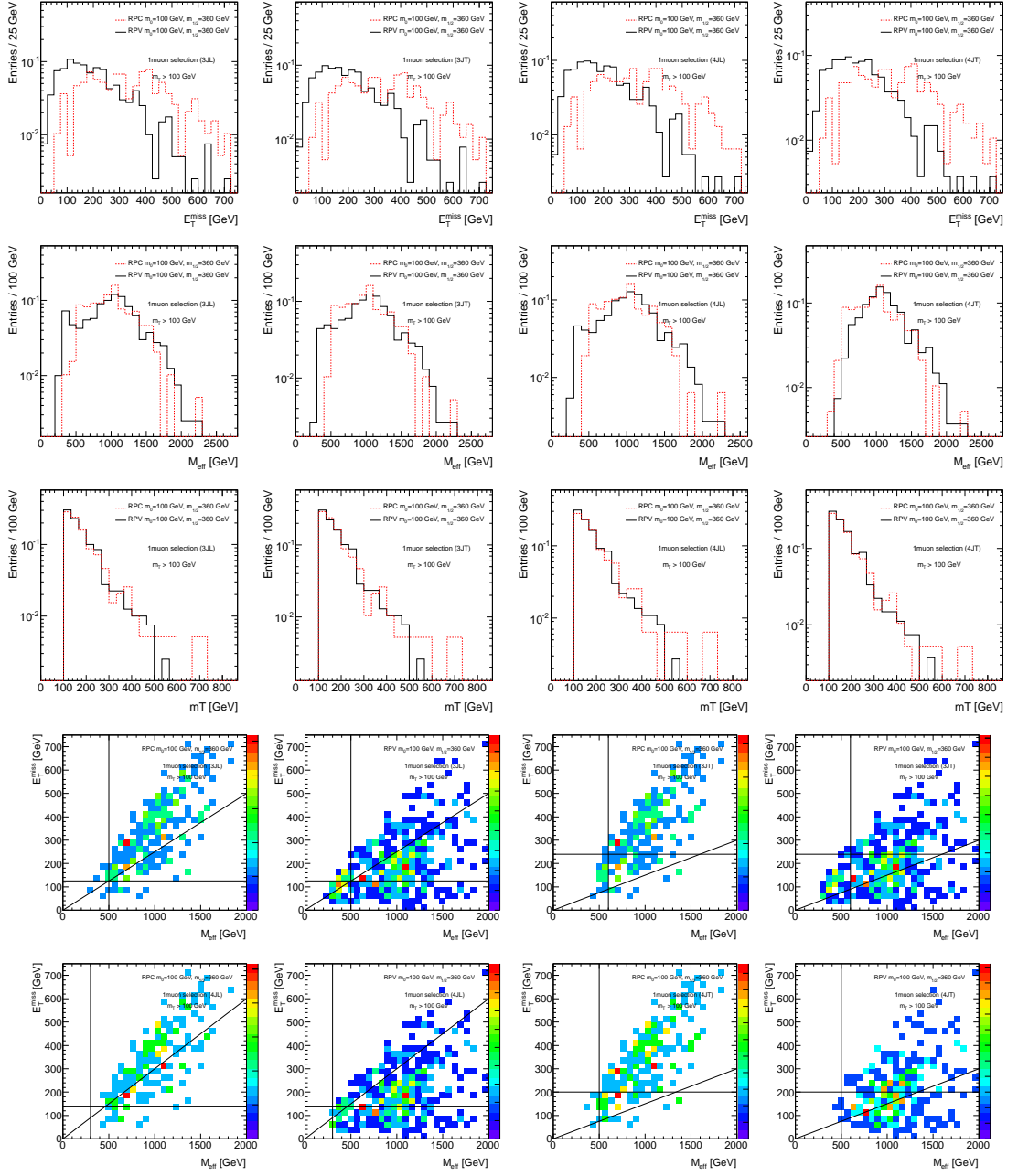


Figure D.3: E_T^{miss} (first row), M_{eff} (second row) and m_T (third row) distributions comparison in the signal point (100, 360) for bRPV SUSY (black continuous line) and same point (100, 360) R -parity conserving SUSY (red dashed line) after 1-muon 3JL (first column), 3JT (second column), 4JL (third column) and 4JT (last column) selections and after the m_T cut common to all SRs. Bottom plots show a comparison between RPC and bRPV in the E_T^{miss} vs. M_{eff} plane for the four signal region selections after applying the $m_T > 100$ GeV cut. The distributions are normalised to unity.

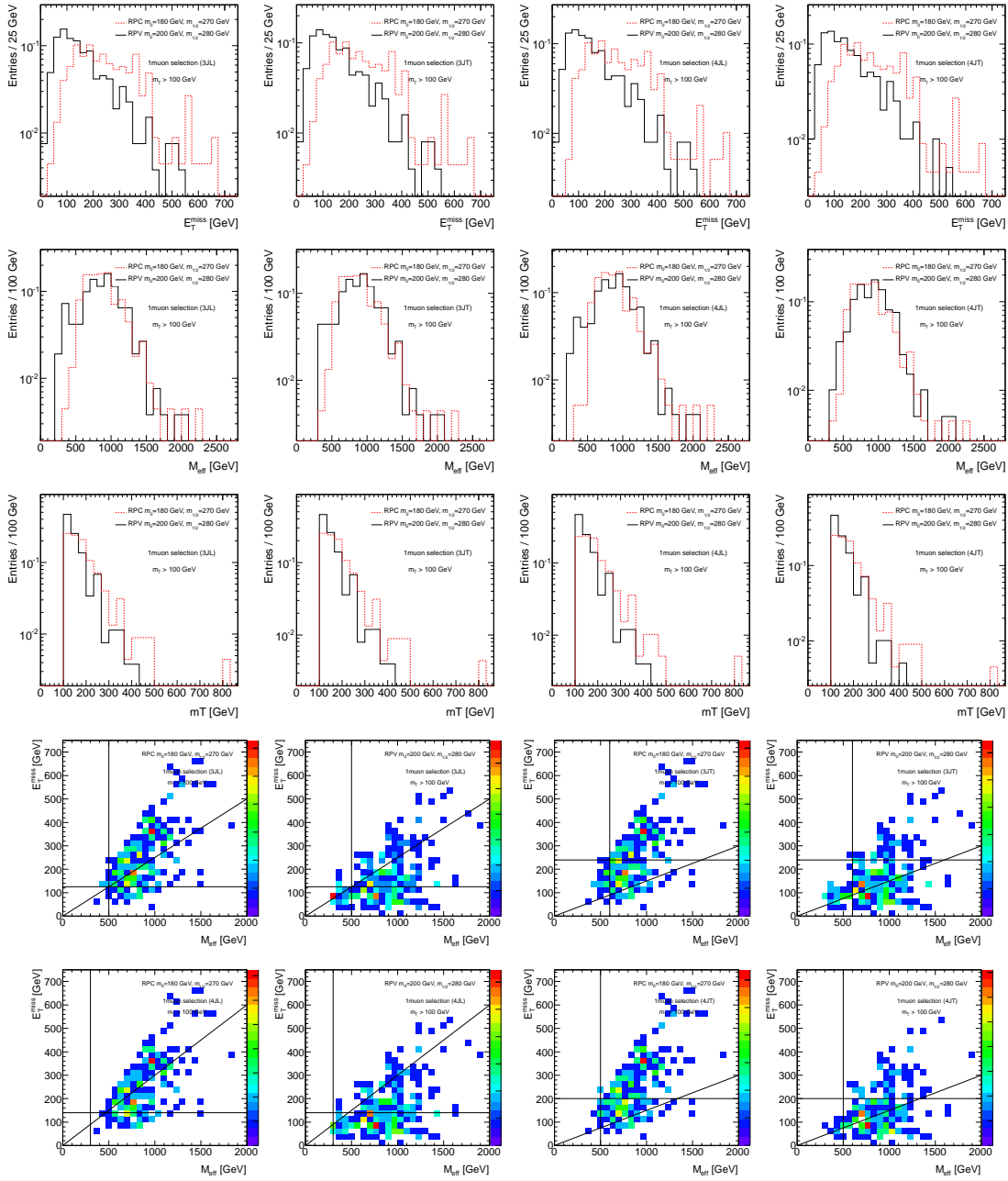


Figure D.4: E_T^{miss} (first row), M_{eff} (second row) and m_T (third row) distributions comparison in the signal point (200, 280) for bRPV SUSY (black continuous line) and nearby point (180, 270) R -parity conserving SUSY (red dashed line) after 1-muon 3JL (first column), 3JT (second column), 4JL (third column) and 4JT (last column) selections and after the m_T cut common to all SRs. Bottom plots show a comparison between RPC and bRPV in the E_T^{miss} vs. M_{eff} plane for the four signal region selections after applying the $m_T > 100$ GeV cut. The distributions are normalised to unity.

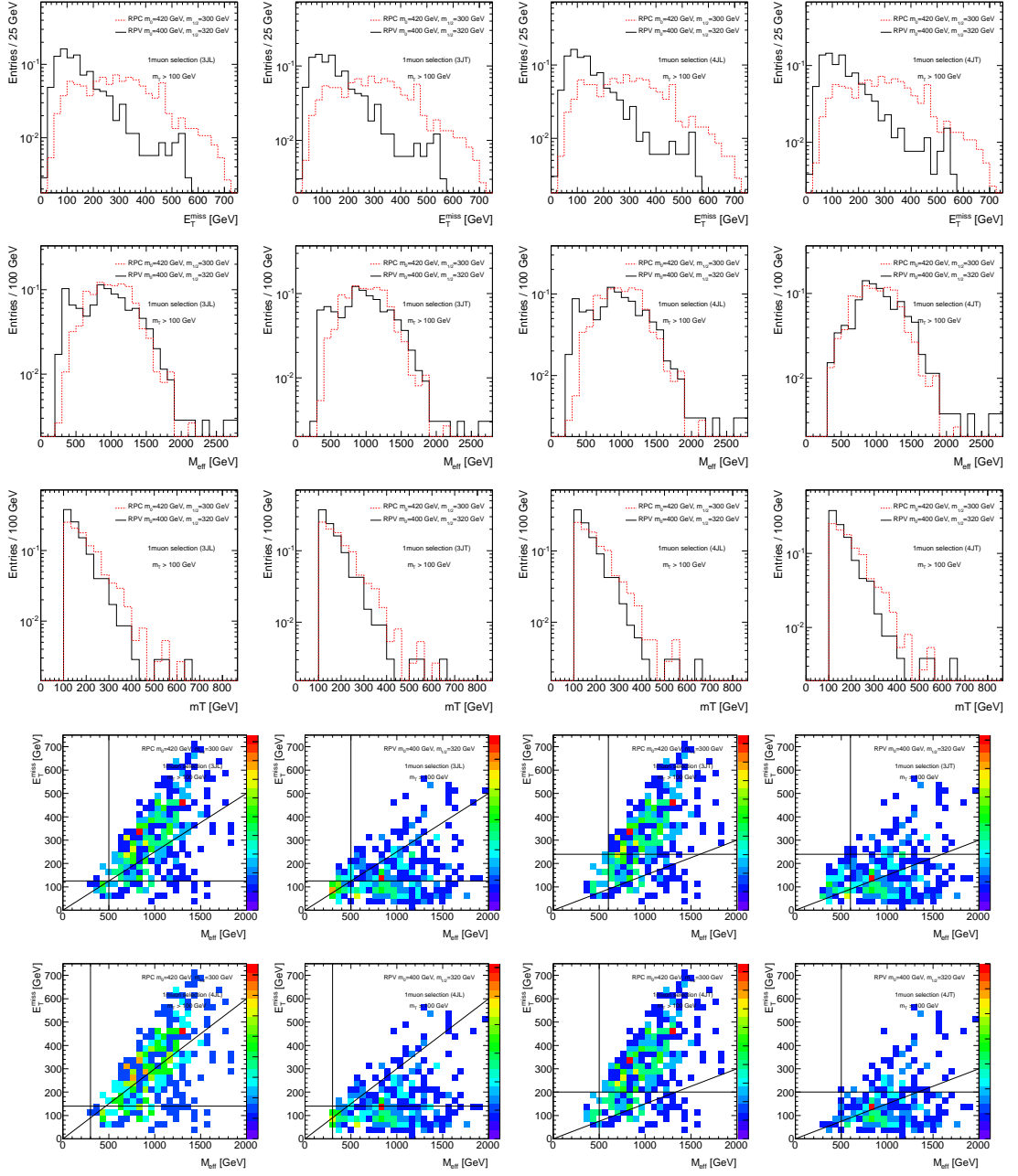


Figure D.5: E_T^{miss} (first row), M_{eff} (second row) and m_T (third row) distributions comparison in the signal point (400, 320) for bRPV SUSY (black continuous line) and nearby point (420, 300) R -parity conserving SUSY (red dashed line) after 1-muon 3JL (first column), 3JT (second column), 4JL (third column) and 4JT (last column) selections and after the m_T cut common to all SRs. Bottom plots show a comparison between RPC and bRPV in the E_T^{miss} vs. M_{eff} plane for the four signal region selections after applying the $m_T > 100$ GeV cut. The distributions are normalised to unity.

Appendix E

OS muon + electron cut flow details

This channel is challenging since the p_T window for the electrons in order to pass the cuts, avoiding the overlapping with the other channel is very small. The preselection cuts for this channel are the following:

1. GRL.
2. Muon Trigger EF_mu18.
3. Jet/MET Cleaning.
4. Primary vertex cut.
5. Electron crack removal.
6. Cosmic muon veto.
7. Dilepton requirement:
 - 7.1 1 signal muon
 - 7.2 1 good electron
 - 7.3 electron $p_T > 25$ GeV OR not EF_e20_medium

Event by event comparison for this cut flow was performed for sample 106484. Among 49449 full Geant-4 and 50000 AF-II initial events, 54 full Geant-4 events and 61 AF-II events (difference of less than 2 per mill) pass the preselection cuts and are named “signal events” in the following. Studying the events in detail, it was found that 22 of them are common for the two simulations and the rest of them are classified in Table E.1 according to the reason of the difference. In addition, a breakdown of these events and the cause of the difference is shown in Table E.2.

Table E.1: Source of differences between events present in full Geant-4 or in AF-II, only

Reason for the cut failure	Events in full Geant-4 not in AF-II	Events in AF-II not in full Geant-4	% of events in category
EF_mu18 = 0	10	3	18%
Num μ signal = 0	4	5	13%
Num electron medium = 0	13	6	27%
signal electron $p_T < 20$ GeV	8	10	27%
signal electron $p_T > 25$ GeV	3	5	13%
EF_e20_medium = 1	1	3	6%
Total	39	32	–

In around 18% of cases, the cause of difference is due to events failing the trigger cut, being AF-II the one failing more often this cut. This can be most probably due to small differences in low p_T muons. A similar number of events in both simulations fail the muon signal cuts and the medium electron trigger veto. There are also more events simulated using AF-II that fail the medium electron criteria but the main source of discrepancies are due to fluctuations in the p_T description of the electrons. As expected, the differences are larger, the lower the p_T cut. As it can be observed in Table E.2, the individual p_T difference from the electron candidates that fail the p_T window cut 7.3 for only one of the simulation types is relatively small (less than 20%) with some tails predominantly at the region in which AF-II is higher than full Geant-4. Thus, it is concluded that the main reason for the differences observed in this event selection is the individual fluctuations of the p_T of the electrons in acceptances that are at the per mill level.

Table E.2: Details on the electron conditions for events passing up to the cut 7.1 on the OS muon + electron cut flow either for full Geant-4 or for AF-II but not for both. In cases where a good electron is not found in the event, the reason is specified in the last column: ElectronMedium meaning the fourth requirement detailed in the Object Definition Section 6.4 for electrons, is not fulfilled or p_T outside the window between 20 and 25 GeV.

Event Number		signal electron p_T [GeV]	Reason of failure
227	full Geant-4	–	ElectronMedium
	AF-II	20.8	–
3433	full Geant-4	23.3	–
	AF-II	–	ElectronMedium
4009	full Geant-4	–	ElectronMedium
	AF-II	22.4	–
5032	full Geant-4	–	ElectronMedium
	AF-II	21.6	–
7753	full Geant-4	–	ElectronMedium
	AF-II	23.5	–
8973	full Geant-4	22.0	–
	AF-II	–	19.1
9476	full Geant-4	–	ElectronMedium
	AF-II	23.0	–
9801	full Geant-4	20.3	–
	AF-II	–	18.5
9877	full Geant-4	21.8	–
	AF-II	–	14.9
10443	full Geant-4	20.0	–
	AF-II	–	19.8
11473	full Geant-4	–	ElectronMedium
	AF-II	21.0	–
13197	full Geant-4	42.0	–
	AF-II	–	ElectronMedium
13920	full Geant-4	24.2	–
	AF-II	–	ElectronMedium
15081	full Geant-4	–	19.4
	AF-II	21.6	–

Event Number		signal electron p_T [GeV]	Reason of failure
15958	full Geant-4	39.0	–
	AF-II	–	ElectronMedium
16259	full Geant-4	–	ElectronMedium
	AF-II	23.8	–
18400	full Geant-4	–	14.8
	AF-II	22.5	–
18895	full Geant-4	20.7	–
	AF-II	–	19.3
20080	full Geant-4	–	14.5
	AF-II	21.9	–
20670	full Geant-4	–	ElectronMedium
	AF-II	22.7	–
20850	full Geant-4	22.0	–
	AF-II	–	26.0
21594	full Geant-4	21.6	–
	AF-II	–	ElectronMedium
21676	full Geant-4	24.7	–
	AF-II	–	25.5
22040	full Geant-4	22.5	–
	AF-II	–	19.3
24323	full Geant-4	–	ElectronMedium
	AF-II	49.1	–
25337	full Geant-4	–	ElectronMedium
	AF-II	21.9	–
26997	full Geant-4	23.9	–
	AF-II	–	15.1
27507	full Geant-4	20.9	–
	AF-II	–	16.2
28148	full Geant-4	–	15.5
	AF-II	20.3	–
30857	full Geant-4	23.1	–
	AF-II	–	16.7
30965	full Geant-4	24.6	–
	AF-II	–	25.5
31170	full Geant-4	–	12.2
	AF-II	20.3	–
33344	full Geant-4	–	18.8
	AF-II	20.8	–
34793	full Geant-4	–	25.8
	AF-II	24.3	–
37173	full Geant-4	–	19.7
	AF-II	20.2	–

Event Number		signal electron p_T [GeV]	Reason of failure
37300	full Geant-4	24.6	–
	AF-II	–	25.4
39421	full Geant-4	–	ElectronMedium
	AF-II	23.7	–
41808	full Geant-4	–	ElectronMedium
	AF-II	46.2	–
44170	full Geant-4	24.1	–
	AF-II	–	25.4
44344	full Geant-4	–	25.4
	AF-II	25.0	–
44403	full Geant-4	23.4	–
	AF-II	–	25.1
44737	full Geant-4	23.9	–
	AF-II	–	19.7
45495	full Geant-4	24.9	–
	AF-II	–	26.6
46784	full Geant-4	24.7	–
	AF-II	–	ElectronMedium
47428	full Geant-4	–	ElectronMedium
	AF-II	20.8	–
48237	full Geant-4	–	10.2
	AF-II	26.6	–

Bibliography

- [1] For a review on SUSY see for example:
S.P. Martin. *A supersymmetry Primer*. [hep-ph/9709356], 1997.
I. J. R. Aitchison. *Supersymmetry in particle physics: An elementary introduction*. SLAC-R-865, 2007.
- [2] For a review on the SM see:
D. Perkins. *Introduction to High Energy Physics*. Cambridge University Press, 4th edition, 2000.
- [3] The LHC Study Group. *The Large Hadron Collider: Conceptual Design*. CERN/AC/95-05(LHC), 1995.
- [4] Lyndon Evans and Philip Bryant. *LHC Machine. (Part of The CERN Large Hadron Collider: Accelerator and Experiments)*. JINST **3** (S08001), 2008.
- [5] S. Myers. *The LEP collider, from design to approval and commissioning, Nov 26, 1990*. CERN-91-08 Presented at CERN Accelerator School: The LEP Collider from Design to Approval and Commissioning, Geneva, Switzerland, Nov 26, 1990, CAS: CERN accelerator school, 6th John Adams Memorial lecture, 1990.
- [6] See for example:
Wilson, Robert Rathbun. *The Tevatron*. Phys. Today **30N10** (23-30), 1977.
- [7] ATLAS Collaboration. *ATLAS: technical proposal for a general purpose pp experiment at the Large Hadron Collider at CERN*. CERN-LHCC-94-43, 1994.
- [8] G. Aad *et al.* [ATLAS Collaboration]. *The ATLAS Experiment at the CERN Large Hadron Collider*. JINST **3** (S08003), 2008.
- [9] G. Aad *et al.* [ATLAS Collaboration]. *Expected Performance of the ATLAS Experiment - Detector, Trigger and Physics*. [arXiv:0901.0512/hep-ex], 2009.
- [10] The CMS Collaboration. *CMS technical proposal*. CERN-LHCC-94-38, 1994.
The CMS Collaboration. *The CMS Experiment at the CERN LHC*. JINST **3** (S08004), 2008.
- [11] ATLAS Collaboration. *Observation of a new particle in the search for the Standard Model Higgs boson with the ATLAS detector at the LHC*. Phys. Lett. **B10** (1016); [arXiv:1207.7214/hep-ex], 2012.
- [12] CMS Collaboration. *Observation of a new boson at a mass of 125 GeV with the CMS experiment at the LHC*. Phys. Lett. **B10** (1016); [arXiv:1207.7235/hep-ex], 2012.

- [13] D.I. Kazakov. *Beyond the Standard Model (In Search of Supersymmetry)*. hep-ph/0012288v2, 2001.
- [14] K. Nakamura et al. (Particle Data Group). *The Review of Particle Physics*. J. Phys. **G37** (075021), 2010.
- [15] Forero, D.V. and Tortola, M. and Valle, J.W.F. *Global status of neutrino oscillation parameters after Neutrino-2012*. [arXiv:1205.4018], 2012.
- [16] M. Maltoni, T. Schwetz, M. A. Tortola and J. W. F. Valle. *Status of global fits to neutrino oscillations*. New J. Phys. **6** (122); [hep-ph/0405172], 2004.
- Y. Takeuchi [for the Super-Kamiokande Collaboration]. *Results from Super-Kamiokande*. [arXiv:1112.3425/hep-ex], 2011.
- A. Izmaylov [for the T2K Collaboration]. *New Oscillation Results from the T2K experiment*. [arXiv:1112.0273/hep-ex], 2011.
- Y. Abe et al. [DOUBLE-CHOOZ Collaboration]. *Indication for the disappearance of reactor electron antineutrinos in the Double Chooz experiment*. [arXiv:1112.6353/hep-ex], 2011.
- A. Habig [MINOS Collaboration]. *MINOS neutrino oscillation results*. Nucl. Phys. Proc. Suppl. **218** (320), 2011.
- A. Gando et al. [The KamLAND Collaboration]. *Constraints on θ_{13} from A Three-Flavor Oscillation Analysis of Reactor Antineutrinos at KamLAND*. Phys. Rev. **D83** (052002); [arXiv:1009.4771/hep-ex], 2011.
- M. Wurm et al. [Borexino Collaboration]. *The solar neutrino results of Borexino*. Conf. Proc. **C100901** (341), 2010.
- N. D'Ambrosio [OPERA Collaboration]. *The OPERA neutrino oscillation experiment: Results of the first year of data tracking*. INSPIRE-849369, 2008.
- R. Terri [K2K Collaboration]. *Results of the K2K oscillation analysis*. AIP Conf. Proc. **981** (169), 2008.
- [17] Komatsu, E. and others. *Seven-Year Wilkinson Microwave Anisotropy Probe (WMAP) Observations: Cosmological Interpretation*. Astrophys. J. Suppl. **192** (18); [arXiv:1001.4538], 2011.
- E. Komatsu et al. [WMAP Collaboration]. *Five-year Wilkinson Microwave Anisotropy Probe (WMAP) Observations: Cosmological Interpretation*. Astrophys. J. Suppl. **180** (330); [arXiv:0803.0547/astro-ph], 2009.
- [18] U. Amaldi, W. de Boer and H. Furstenau. *Comparison of grand unified theories with electroweak and strong coupling constants measured at LEP*. Phys. Lett. **B260** (447), 1991.
- [19] H. Georgi and S. Glashow. *Unity of All Elementary-Particle Forces*. Phys. Lett. **B32** (438), 1974.
- J. R. Ellis, S. Kelley and D. V. Nanopoulos. *Precision Lep Data, Supersymmetric Guts And String Unification*. Phys. Lett. **B249** (441), 1990.
- J. R. Ellis, S. Kelley and D. V. Nanopoulos. *Probing the desert using gauge coupling unification*. Phys. Lett. **B260** (131), 1991.
- C. Giunti, C. W. Kim and U. W. Lee. *Running coupling constants and grand unification models*. Mod. Phys. Lett. **A6** (1745), 1991.
- P. Langacker and M. x. Luo. *Implications of precision electroweak experiments for $M(t)$, $\rho(0)$, $\sin^2 \Theta(W)$ and grand unification*. Phys. Rev. **D44** (817), 1991.

- [20] B. R. Greene, K. H. Kirklin, P. J. Miron and G. G. Ross. *A Three Generation Superstring Model. 1. Compactification And Discrete Symmetries*. Nucl. Phys. **B278** (667), 1986.
- B. R. Greene, K. H. Kirklin, P. J. Miron and G. G. Ross. *A Three Generation Superstring Model. 2. Symmetry Breaking and the Low-Energy Theory*. Nucl. Phys. **B292** (606), 1987.
- B. R. Greene, C. A. Lutken and G. G. Ross. *Couplings In The Heterotic Superconformal Three Generation Model*. Nucl. Phys. **B325** (101), 1989.
- [21] For an introduction and reviews in technicolor, see for example:
S. Weinberg. *Implications of Dynamical Symmetry Breaking*. Phys. Rev. **D13** (974), 1976.
- L. Susskind. *Dynamics of Spontaneous Symmetry Breaking in the Weinberg-Salam Theory*. Phys. Rev. **D20** (2619), 1979.
- S. Dimopoulos and L. Susskind. *Mass Without Scalars*. Nucl. Phys. **B155** (237), 1979.
- C. T. Hill and E. H. Simmons. *Strong dynamics and electroweak symmetry breaking*. Phys. Rept. **381** (235); [hep-ph/0203079], 2003.
- F. Sannino. *Conformal Dynamics for TeV Physics and Cosmology*. Acta Phys. Polon. **B402** (3533); [arXiv:0911.0931], 2009.
- [22] S. Borgani, A. Masiero and M. Yamaguchi. *Light gravitinos as mixed dark matter*. Phys. Lett. **B386** (189); [hep-ph/9605222], 1996.
- F. Takayama and M. Yamaguchi. *Gravitino dark matter without R-parity*. Phys. Lett. **B485** (388); [hep-ph/0005214], 2000.
- M. Hirsch, W. Porod and D. Restrepo. *Collider signals of gravitino dark matter in bilinearly broken R-parity*. JHEP **0503** (062); [hep-ph/0503059], 2005.
- [23] E. J. Chun and H. B. Kim. *Axino Light Dark Matter and Neutrino Masses with R-parity Violation*. JHEP **0610** (082); [hep-ph/0607076], 2006.
- K. Choi, E. J. Chun and K. Hwang. *Axino as a sterile neutrino and R-parity violation*. Phys. Rev. **D64** (033006); [hep-ph/0101026], 2001.
- E. J. Chun and H. B. Kim. *Nonthermal axino as cool dark matter in supersymmetric standard model without R-parity*. Phys. Rev. **D60** (095006); [hep-ph/9906392], 1999.
- [24] I. Antoniadis et al. *Direct collider signatures of large extra-dimensions*. Phys. Lett. **B460** (176); [hep-ph/9905311], 1999.
- [25] N. Brett et al. *Black hole production at the LHC: the Discovery reach of the ATLAS experiment*. ATL-COM-PHYS-2008-034, 2008.
- [26] For a review on Little Higgs theories see:
Schmaltz, Martin and Tucker-Smith, David. *Little Higgs review*. Ann. Rev. Nucl. Part. Sci. **55** (229-270), 2005.
- S. Weinberg. *Approximate symmetries and pseudoGoldstone bosons*. Phys. Rev. Lett. **29** (1698), 1972.
- H. Georgi and A. Pais. *Vacuum Symmetry and the PseudoGoldstone Phenomenon*. Phys. Rev. **D12** (508), 1975.
- [27] K. Inoue, A. Kakuto, H. Komatsu, and S. Takeshita. *Aspects of Grand Unified Models with Softly Broken Supersymmetry*. Prog. Theor. Phys. **68** (927), 1982.

- R. Flores and M. Sher. *Higgs masses in the standard, multi-Higgs and supersymmetric models.* *Annals Phys.* **148** (95), 1983.
- J.F. Gunion and H.E. Haber. *Higgs bosons in supersymmetric models (I).* *Nucl. Phys.* **B272** 567-568), 1986.
- [28] Gunion, John F. and Haber, Howard E. *The CP conserving two Higgs doublet model: The Approach to the decoupling limit.* *Phys.Rev.* **D67** (075019); [hep-ph/0207010], 2003.
- [29] J. R. Ellis, J. S. Hagelin, D. V. Nanopoulos, K. A. Olive and M. Srednicki. *Supersymmetric relics from the big bang.* *Nucl. Phys.* **B238** (453), 1984.
- [30] <https://twiki.cern.ch/twiki/bin/view/AtlasPublic/SupersymmetryPublicResults>.
- [31] ALEPH Collaboration, A. Heister et al. *Search for supersymmetric particles with R-parity violating decays in e^+e^- collisions at \sqrt{s} up to 209 GeV.* *Eur. Phys. J.* **C31** (1-16); [hep-ex/0210014], 2003.
- DELPHI Collaboration, J. Abdallah et al. *Search for supersymmetric particles assuming R-parity non-conservation in e^+e^- collisions at $\sqrt{s} = 192$ GeV to 208 GeV.* *Eur. Phys. J.* **C36** (1-23); [hep-ex/0406009], 2004.
- OPAL Collaboration, G. Abbiendi et al. *Search for R parity violating decays of scalar fermions at LEP.* *Eur. Phys. J.* **C33** (149-172); [hep-ex/0310054], 2004.
- [32] CDF Collaboration, F. Abe et al. *Search for R-parity violating supersymmetry using like-sign dielectrons in $p\bar{p}$ collisions at $\sqrt{s} = 1.8$ TeV.* *Phys. Rev. Lett.* **83** (2133-2138); [hep-ex/9908063], 1999.
- D0 Collaboration, B. Abbott et al. *Search for R-parity violation in multilepton final states in $p\bar{p}$ collisions at $\sqrt{s} = 1.8$ TeV.* *Phys. Rev.* **D62** (071701); [hep-ex/0005034], 2000.
- D0 Collaboration, V. M. Abazov et al. *Search for R-parity violating supersymmetry in dimuon and four-jets channel.* *Phys. Rev. Lett.* **89** (171801); [hep-ex/0111053], 2002.
- D0 Collaboration, V. M. Abazov et al. *Search for R-parity violating supersymmetry via the LL anti-E couplings λ_{121} , λ_{122} or λ_{133} in $p\bar{p}$ collisions at $\sqrt{s} = 1.96$ TeV.* *Phys. Lett.* **B638** (441-449); [hep-ex/0605005], 2006.
- [33] ZEUS Collaboration, S. Chekanov et al. *Search for stop production in R-parity-violating supersymmetry at HERA.* *Eur. Phys. J.* **C50** (269-281); [hep-ex/0611018], 2007.
- [34] Y. Kao and T. Takeuchi. *Constraints on R-parity violation from recent Belle/Babar data.* [arXiv:0909.0042/hep-ph], 2009.
- [35] A. Abada and M. Losada. *Constraints on both bilinear and trilinear R-parity violating couplings from neutrino laboratories and astrophysics data.* *Phys. Lett.* **B492** (310-320); [hep-ph/0007041], 2000.
- [36] ATLAS Collaboration, Aad, Georges and others. *Search for a heavy neutral particle decaying into an electron and a muon using 1 fb⁻¹ of ATLAS data.* *Eur. Phys.* **C71** (1809); [arXiv:1109.3089], 2011.
- ATLAS Collaboration, Aad, Georges and others. *Search for lepton flavour violation in the $\mu\mu$ continuum with the ATLAS detector in $\sqrt{s} = 7$ TeV pp collisions at the LHC.* *Eur. Phys. J.* **C72** (2040); [arXiv:1205.0725], 2012.

- [37] ATLAS Collaboration. *Search for long-lived, heavy particles in final states with a muon and multi-track displaced vertex in proton-proton collisions at a centre-of-mass energy of 7 TeV with the ATLAS detector*. ATLAS-CONF-2012-113, 2012.
- [38] ATLAS Collaboration. *Constraining R-parity violating Minimal Supergravity with stau₁ LSP in a four lepton final state with missing transverse momentum*. ATLAS-CONF-2012-035, 2012.
- [39] CMS Collaboration, S. Chatrchyan et al. *Search for Physics Beyond the Standard Model Using Multilepton Signatures in pp Collisions at $\sqrt{s} = 7$ TeV*. [arXiv:1106.0933/hep-ex], 2011.
CMS Collaboration, S. Chatrchyan et al. *Search for anomalous production of multilepton events in pp collisions at $\sqrt{s} = 7$ TeV*. JHEP **1206** (169); [arXiv:1204.5341], 2012.
- [40] Report of the task force on SSC operations. SCC-SR-1005(1985).
- [41] LHCb Collaboration. *LHCb technical proposal*. CERN-LHCC-98-004, 1998.
- [42] W.Kienzle et al. [TOTEM Collaboration]. *TOTEM, Total cross section, elastic scattering and diffractive dissociation at the LHC: Technical Proposal*. CERN-LHCC-99-007, 1999.
- [43] ALICE Collaboration. *ALICE: Technical proposal for a Large Ion Collider Experiment at the CERN LHC*. CERN-LHCC-95-71, 1995.
- [44] Adriani, O. and others. *The LHCf detector at the CERN Large Hadron Collider*. JINST **3** (S08006), 2008.
- [45] The MoEDAL Collaboration. *Technical Design Report of the MoEDAL experiment*. CERN-LHC-2009-006. MoEDAL-TDR-1.1, 2012.
The LHCb Collaboration. *The LHCb Detector at the LHC*. JINST **3** (S08005), 2008.
- [46] ATLAS Collaboration. *The ATLAS Inner Detector commissioning and calibration*. Eur. Phys. J. **C70** (787-821), 2010.
- [47] ATLAS Collaboration. *Alignment of the ATLAS Inner Detector Tracking System with 2010 LHC proton-proton collisions at $\sqrt{s} = 7$ TeV*. ATLAS-CONF-2011-012, 2011.
- [48] ATLAS Collaboration. *A study of the material in the ATLAS inner detector using secondary hadronic interactions*. [arXiv:1110.6191v2/hep-ex], 2011.
- [49] ATLAS Collaboration. *ATLAS pixel detector electronics and sensors*. JINST **3** (P07007), 2008.
- [50] A. Abdesselan et al. *The Barrel Modules of the ATLAS Semiconductor Tracker*. Nucl. Instr. and Meth. **A568** (642-671), 2006.
- [51] A. Abdesselan et al. *The ATLAS Semiconductor Tracker end-cap module*. Nucl. Instr. and Meth. **A575** (353-389), 2007.
- [52] T. Akesson et al. *Status of design and construction of the Transition Radiation Tracker (TRT) for the ATLAS experiment at the LHC*. Nucl. Instr. and Meth. **A522** (131-145), 2004.
- [53] ATLAS Collaboration. *ATLAS Liquid Argon Calorimeter: Technical Design Report*. CERN-LHCC-96-041, 1996.
- [54] ATLAS Collaboration. *ATLAS Tile Calorimeter: Technical Design Report*. CERN-LHCC-96-042, 1996.

- [55] ATLAS Collaboration. *ATLAS Muon Spectrometer: Technical Design Report*. CERN-LHCC-97-022, 1997.
- [56] ATLAS Collaboration. *ATLAS Magnet System: Technical Design Report*. CERN-LHCC-97-018, 1997.
- [57] ATLAS Collaboration. *ATLAS Level-1 Trigger: Technical Design Report*. CERN-LHCC-98-014, 1998.
- [58] P. Jenni et al., ATLAS Collaboration. *ATLAS high-level trigger, data-acquisition and controls: Technical Design Report*. CERN-LHCC-2003-022, 2003.
- [59] ATLAS Collaboration. *Tracking Results and Comparison to Monte Carlo simulation at $\sqrt{s} = 900$ GeV*. ATLAS-CONF-2010-01, 2010.
- ATLAS Collaboration. *Performance of the ATLAS Silicon Pattern Recognition Algorithm in Data and Simulation at $\sqrt{s} = 7$ TeV*. ATLAS-CONF-2010-072, 2010.
- T. Cornelissen et al. *Concepts, Design and Implementation of the ATLAS New Tracking (NEWT)*. ATL-SOFT-PUB-2007-007, 2007.
- [60] ATLAS Collaboration. *Performance of primary vertex reconstruction in proton-proton collisions at $\sqrt{s} = 7$ TeV in the ATLAS experiment*. ATLAS-CONF-2010-069, 2010.
- [61] S. Hassani et al. *A muon identification and combined reconstruction procedure for the ATLAS detector at the LHC using the (MUONBOY, STACO, MuTag) reconstruction packages*. Nuclear Instruments and Methods in Physics Research **A572** (77-79), 2007.
- [62] Lagouri, Th and others. *A muon identification and combined reconstruction procedure for the ATLAS detector at the LHC at CERN*. IEEE Trans. Nucl. Sci. **51**, 2004.
- N. van Eldik. *The ATLAS muon spectrometer: calibration and pattern recognition*. PhD thesis.
- [63] Tarem, S. and Tarem, Z. and Panikashvili, N. and Belkind, O. *MuGirl – Muon identification in the ATLAS detector from the inside out*. Nuclear Science Symposium Conference Record **1**. IEEE, 2006.
- [64] M. Cacciari, G. P. Salam, and G. Soyez. *The anti-kt jet clustering algorithm*. JHEP **04** (063), 2008.
- [65] ATLAS Collaboration. *Calorimeter clustering algorithms: Description and performance*. ATL-LARG-PUB-2008-002, 2008.
- [66] L. Breiman, J. Friedman, C. Stone, and R. Olshen. *Classification and Regression Trees*. Chapman & Hall, 1984.
- Y. Freund and R. Shapire. *Experiments with a New Boosting Algorithm*. Proceedings 13th International Conference on Machine Learning, 1996.
- [67] ATLAS Collaboration. *Performance of the Reconstruction and Identification of Hadronic Tau Decays with ATLAS*. ATLAS-CONF-2011-152, 2011.
- [68] ATLAS Collaboration. *Impact parameter-based b-tagging algorithms in the 7 TeV collision data with the ATLAS detector: the TrackCounting and JetProb algorithms*. ATLAS Note ATLAS-CONF-2010-041, 2010.

- [69] ATLAS Collaboration. *Commissioning of the ATLAS high-performance b-tagging algorithms in the 7 TeV collision data*. ATLAS-CONF-2011-102, 2011.
- [70] ATLAS Collaboration. *Performance of the ATLAS Secondary Vertex b-tagging Algorithm in 7 TeV Collision Data*. ATLAS Note ATLAS-CONF-2010-042, 2010.
- [71] G. Piacquadio, C. Weiser. *A new inclusive secondary vertex algorithm for b-jet tagging in ATLAS*. J. Phys. Conf. Ser. **119** (032032), 2008.
- [72] I. Bird, K. Bos, N. Brook, D. Duellmann, C. Eck, I. Fisk, D. Foster, B. Gibbard, C. Grandi, F. Grey, J. Harvey, A. Heiss, F. Hemmer, S. Jarp, R. Jones, D. Kelsey, J. Knobloch, M. Lamanna, H. Marten, P. Mato Vila, F. Ould-Saada, B. Panzer-Steindel, L. Perini, L. Robertson, Y. Schutz, U. Schwickerath, J. Shiers, T. Wenaus. *LHC computing Grid: Technical Design Report. Version 1.06 (20 Jun 2005)*. ISBN 92-9083-253-3. Technical Design Report LCG (<https://lcg-archive.web.cern.ch/lcg-archive/TDR/>), 2005.
- [73] M. Ellert, A. Konstantinov, B. Kónyacs, O. Smirnov, A. Wäänänen. *The NorduGrid project: using Globus toolkit for building GRID infrastructure*. Nucl. Instr. Meth. **A502** (407-410), 2003.
- [74] R. Pordes, D. Petravick, B. Kramer, D. Olson, M. Livny, A. Roy, P. Avery, K. Blackburn, T. Wenaus, F. Wrthwein, I. Foster, R. Gardner, M. Wilde, A. Blatecky, J. McGee, R. Quick. *The open science grid*. J. Phys.: Conf. Ser. **78** (012057), 2007.
- [75] S. L. Glashow. *Partial symmetries of weak interactions*. Nucl. Phys. **B 22** (579), 1961.
S. Weinberg. *A model of leptons*. Phys. Rev. Lett. **19** (1264), 1967.
A. Salam. *Elementary particle theory*. Almqvist and Wiksells, Stockholm, 1968.
- [76] S. Coleman and J. Mandula. *All Possible Symmetries Of The S Matrix*. Phys. Rev. **159** (1251), 1967.
- [77] R. Haag, J. Lopuszanski, and M. Sohnius. *All Possible Generators of Supersymmetries of the s Matrix*. Nucl. Phys. **B88** (257), 1975.
- [78] J. Wess and B. Zumino. *Supergauge Transformations in Four-Dimensions*. Nucl. Phys. **B70** (39), 1974.
- [79] Higgs, P. W. *Broken symmetries, massless particles and gauge fields*. Phys. Lett. **12** (132-133), 1964.
Englert F.; Brout, R. *Broken symmetry and the mass of gauge vector mesons*. Phys. Rev. Lett. **13** (321-322), 1964.
Guralnik, G. S.; Hagen, C. R.; Kibble, T. W. B. *Global conservation laws and massless particles*. Phys. Rev. Lett. **13** (585-587), 1964.
H. Goldberg. *Constraint on the photino mass from cosmology*. Phys. Rev. Lett. **50** (1419), 1983.
- [80] J. R. Ellis and D. Ross. *A light Higgs boson would invite supersymmetry*. Phys. Lett. **B506** (331), (2001).
- [81] S. Dimopoulos and D. W. Sutter. *The Supersymmetric Flavor Problem*. Nucl. Phys. **B452** (496), 1995.

- [82] B. A. Campbell. *Supersymmetry And Neutral Flavor Nonconservation*. Phys. Rev. **D28** (209), 1983.
- R. Barbieri, L.J. Hall and A. Strumia. *Violations of lepton flavour and CP in supersymmetric unified theories*. Nucl. Phys. **B445**, 1995.
- F. Gabbiani, E. Gabrielli, A. Masiero and L. Silvestrini. *A complete analysis of FCNC and CP constraints in general SUSY extensions of the standard model*. Nucl. Phys. **B477** (321), 1996.
- S. Pokorski, J. Rosiek and C. A. Savoy. *Constraints on Phases of Supersymmetric Flavour Conserving Couplings*. Nucl. Phys. **B570**, 2000.
- S. Abel, S. Khalil and O. Lebedev. *EDM Constraints in Supersymmetric Theories*. Nucl. Phys. **B606** (151), 2001.
- T. Besmer, C. Greub and T. Hurth. *Bounds on flavour violating parameters in supersymmetry*. Nucl. Phys. **B609** (359), 2001.
- G. Burdman, E. Golowich, J. Hewett and S. Pakvasa . *Rare Charm Decays in the Standard Model and Beyond*. Phys. Rev. **D66** (014009), 2002.
- A.J. Buras, P.H. Chankowski, J. Rosiek and L. Slawianowska. $\Delta M_{d,s}$, $B_{d,s}^0 \rightarrow \mu^+ \mu^-$ and $B \rightarrow X_s \gamma$ in Supersymmetry at Large $\tan \beta$. Nucl. Phys. **B659** (3), 2003.
- M. Ciuchini, E. Franco, A. Masiero and L. Silvestrini. *$b \rightarrow s$ Transitions: A New Frontier for Indirect SUSY Searches*. Phys. Rev. **D67** (075016), 2003.
- [83] P. Van Nieuwenhuizen. *Supergravity*. Phys. Rept. **68** (189), 1981.
- A. H. Chamseddine, R. L. Arnowitt and P. Nath. *Locally Supersymmetric Grand Unification*. Phys. Rev. Lett. **49** (970), 1982.
- H. P. Nilles. *Supersymmetry, Supergravity and Particle Physics*. Phys. Rept. **110** (1), 1984.
- [84] G. G. Ross and R. G. Roberts. *Minimal supersymmetric unification predictions*. Nucl. Phys. **B377** (571), 1992.
- [85] Searches for heavy bound states:
 Smith, P.F. and Bennett, J.R.J. *A search for heavy stable particles*. Nucl.Phys. **B149** (525-533), 1979.
- Smith, P.F. and Bennett, J.R.J. and Homer, G.J. and Lewin, J.D. and Walford, H.E. and others. *A search for anomalous hydrogen in enriched D-2 O, using a time-of-flight spectrometer*. Nucl. Phys. **B206** (333-348), 1982.
- Norman, E.B. and Gazes, S.B. and Bennett, D.A. *Searches for supermassive X- particles in iron*. Phys. Rev. Lett. **58** (1403-1406), 1987.
- [86] Cosmological constraints on heavy stable particles:
 Wolfram, Stephen. *Abundances of Stable Particles Produced in the Early Universe*. Phys. Lett. **B82** (65), 1979.
- Dover, C.B. and Gaisser, T.K. and Steigman, Gary. *Cosmological constraints on new stable hadrons*. Phys. Rev. Lett. **42** (1117), 1979.
- [87] W. Porod and P. Z. Skands. *Measuring neutrino mixing angles at LHC*. [hep-ph/0401077], 2006.
- [88] F. de Campos, O. J. P. Eboli, M. B. Magro, W. Porod, D. Restrepo, M. Hirsch and J. W. F. Valle. *Probing bilinear R-parity violating supergravity at the LHC*. JHEP **0805** (048); [arXiv:0712.2156/hep-ph], 2008.

- [89] J. C. Romao, M. A. Diaz, M. Hirsch, W. Porod and J. W. F. Valle. *A supersymmetric solution to the solar and atmospheric neutrino problems*. Phys. Rev. **D61** (071703); [hep-ph/9907499], 2000.
M. Hirsch and J. W. F. Valle. *Supersymmetric origin of neutrino mass*. New J. Phys. **6** (76); [hep-ph/0405015], 2004.
- [90] M. Hirsch, M. A. Diaz, W. Porod, J. C. Romao and J. W. F. Valle. *Neutrino masses and mixings from supersymmetry with bilinear R parity violation: A Theory for solar and atmospheric neutrino oscillations*. Phys. Rev. **D62** (113008); [hep-ph/0004115], 2002.
- [91] E. Torró, V. Mitsou, C. García. *Probing Bilinear R-Parity Violating Supersymmetry in the Muon plus Jets Channel*. ATL-PHYS-INT-2010-042, 2010.
- [92] G. Aad *et al.* [ATLAS Collaboration]. *ATHENA: The ATLAS Common Framework Developer Guide*. [online] Available: <http://ATLAS.web.cern.ch/ATLAS/GROUPS/SOFTWARE/OO/architecture/General/Documentation/AthenaDeveloperGuide-8.0.0-draft.pdf>, 2004.
- [93] T. Sjostrand, S. Mrenna and P. Skands. *PYTHIA 6.4 Physics and Manual*. JHEP **05** (026); [hep-ph/0603175], 2006.
- [94] Thanks to Werner Porod for his help and his interest in the improvement of SPheno. W. Porod. *SPheno, a program for calculating supersymmetric spectra, SUSY particle decays and SUSY particle production at e^+e^- colliders*. Comput. Phys. Commun. **153** (275); [hep-ph/0301101], 2003.
- [95] P. Skands *et al.* *SUSY Les Houches accord: Interfacing SUSY spectrum calculators, decay packages, and event generators*. JHEP **0407** (036); [hep-ph/0311123], 2004.
- [96] B. C. Allanach *et al.* *SUSY Les Houches Accord 2*. Comp. Phys. Commun. **180** (8-25); [arXiv:0801.0045/hep-ph], 2009.
- [97] W. Beenakker and R. Hoepker and M. Spira. *PROSPINO: A Program for the Production of Supersymmetric Particles in Next-to-leading Order QCD*. <http://www.citebase.org/abstract?id=oai:arXiv.org:hep-ph/9611232>, 1996.
- [98] W. Beenakker, R. Hopker, M. Spira, P.M. Zerwas. *Squark and gluino production at hadron colliders*. Nucl. Phys. **B492** (51), 1997.
- [99] Geant4 Collaboration. *Geant4, a simulation toolkit*. Nuclear Instruments and Methods in Physics Research Section A: Accelerators, Spectrometers, Detectors and Associated Equipment, 2003.
J. Allison *et al.* *GEANT4 developments and applications*. IEEE Transactions on Nuclear Science **53** (270-278), 2006.
- [100] M. Hirsch and J. W. F. Valle. *Neutrinoless double beta decay in supersymmetry with bilinear R-parity breaking*. Nucl. Phys. **B557** (60-78); [hep-ph/9812463], 1999.
- [101] D. F. Carvalho, M. E. Gomez, and J. C. Romao. *Charged lepton flavor violation in supersymmetry with bilinear R-parity violation*. Phys. Rev. **D65** (093013); [arXiv:hep-ph/0202054], 2002.

- [102] F. de Campos, O. J. P. Eboli, M. B. Magro, W. Porod, D. Restrepo and J. W. F. Valle. *Probing neutrino mass with displaced vertices at the Tevatron*. Phys. Rev. **D71** (075001); [hep-ph/0501153], 2005.
- [103] ATLAS Collaboration, Combined muon working group, <https://twiki.cern.ch/twiki/bin/view/AtlasProtected/MCPAnalysisGuidelin%esEPS2011>.
- [104] S. Gadatsch. *Template morphing in many dimensions with several t parameters*. Talk given at ATLAS Statistics Forum, <http://indico.cern.ch/conferenceDisplay.py?confId=74940>, 2 December 2009.
- [105] Berger, Carola F. and Gainer, James S. and Hewett, JoAnne L. and Rizzo, Thomas G. *Supersymmetry Without Prejudice*. JHEP **0902** (023); [arXiv:0812.0980/hep-ph], 2009.
- [106] de Campos, F. and Diaz, M.A. and Eboli, O.J.P. and Magro, M.B. and Porod, W. and others. *CERN LHC signals for neutrino mass model in bilinear R -parity violating m_{AMSB}* . Phys. Rev. **D77** (115025); [arXiv:0803.4405/hep-ph], 2008.
- [107] S. Dawson. *R -Parity Breaking In Supersymmetric Theories*. Nucl. Phys. **B261** (297), 1985.
- [108] CDF Collaboration, T. Aaltonen et al. *Inclusive Search for Squark and Gluino Production in $p\bar{p}$ Collisions at $\sqrt{s} = 1.96$ TeV*. Phys. Rev. Lett. **102** (121801); [arXiv:0811.2512/hep-ex], (2009).
- [109] D0 Collaboration, V. M. Abazov et al. *Search for squarks and gluinos in events with jets and missing transverse energy using 2.1 fb^{-1} of $p\bar{p}$ collision data at $\sqrt{s} = 1.96$ TeV*. Phys. Lett. **B660** (449-457); [arXiv:0712.3805/hep-ex], 2008.
- [110] D0 Collaboration, V. M. Abazov et al. *Search for associated production of charginos and neutralinos in the trilepton final state using 2.3 fb^{-1} of data*. Phys. Lett. **B680** (34-43); [arXiv:0901.0646/hep-ex], 2009.
- [111] ATLAS Collaboration, G. Aad et al. *Search for supersymmetry using final states with one lepton, jets, and missing transverse momentum with the ATLAS detector in $\sqrt{s} = 7$ TeV pp* . Phys. Rev. Lett. **102** (131802); [arXiv:1102.2357/hep-ex], 2011.
- [112] ATLAS Collaboration, G. Aad et al. *Search for supersymmetry with jets, missing transverse momentum and one lepton at $\sqrt{s} = 7$ TeV (supporting INT note)*. ATLAS-CONF-2011-090, 2011.
- [113] ATLAS Collaboration, G. Aad et al. *Search for supersymmetry in final states with jets, missing transverse momentum and one isolated lepton in $\sqrt{s} = 7$ TeV pp collisions using 1 fb^{-1} of ATLAS data*. Phys. Rev. **D85**; [arXiv:1109.6606/hep-ex], 2011.
- [114] Asai, S; Baak, M; Beale, S; Becker, S; Bianco, M; Boyd, J; Bruneliere, R; Caron, S; Castaneda, A; Clement, C; Consorti, V; Cote, D; Dietrich, J; de Jong, P; Edmonds, K; Eifert, T; Flowerdew, M; Genest, M-H; Gorini, A; Hoecker, A; Hohlfield, M; Horner, S; Kanaya, N; Lari, T; Lorenz, J; Lundberg, J; Makovec, N; Marshall, Z; Meyer, C; Mitsou, V; Muller, T; Pataraiia, S; Petersen, B; Portell, X; Poveda, J; Primavera, M; Rave, T; Redelbach, A; Romero, E; Sarangi, T; Sasaki, Y; Short, D; Sundermann, J-E; Torro, E; Tuan, VA; vd Leeuw, R; Ventura, A; Wu, SL; Zhuang, X. *Search for Supersymmetry with jets and missing transverse momentum and one lepton at $\sqrt{s} = 7$ TeV pp collisions (supporting INT note)*. ATL-PHYS-INT-2011-082, 2011.

- [115] ATLAS Collaboration. *Search for squarks and gluinos using final states with jets and missing transverse momentum with the ATLAS detector in $\sqrt{s} = 7$ TeV proton-proton collisions.* [arXiv:1012.5290], submitted to Phys. Lett. **B**, 2011.
- [116] ATLAS Collaboration. *Search for supersymmetric particles in events with lepton pairs and large missing transverse momentum in $\sqrt{s} = 7$ TeV proton-proton collisions at the ATLAS detector.* [arXiv:1103.6208v1], submitted to EPJC Letters, 2011.
- [117] ATLAS Collaboration. *Search for supersymmetry in pp collisions at $\sqrt{s} = 7$ TeV in final states with missing transverse momentum and b-jets with the ATLAS detector.* Phys. Rev. **D85** (112006); [arXiv:1203.6193], 2012.
- [118] ATLAS Collaboration, R. Brunelière et al. *Setting exclusion limits in ATLAS supersymmetry searches via a likelihood ratio based method.* Tech. Rep. ATL-COM-PHYS-2011-004, 2011.
- [119] U. Langenfeld, S. Moch, and P. Uwer. *Measuring the running top-quark mass.* Phys. Rev. **D80** (054009); [arXiv:0906.5273/hep-ph], 2009.
- [120] J. M. Campbell, R. K. Ellis, and D. L. Rainwater. *Next-to-leading order QCD predictions for W+2jet and Z+2jet production at the CERN LHC.* Phys. Rev. **D68** (094021); [hep-ph/0308195], 2003.
- [121] C. F. Berger et al. *Vector Boson + Jets with BlackHat and Sherpa.* Nucl. Phys. Proc. Suppl. 205-206 92-97; [arXiv:1005.3728/hep-ph], 2010.
- [122] M. L. Mangano, M. Moretti, F. Piccinini, R. Pittau, and A. Polosa. *ALPGEN, a generator for hard multiparton processes in hadronic collisions.* JHEP **07** (001); [hep-ph/0206293], 2003.
- [123] F. Krauss, A. Schalicke, S. Schumann, and G. Soff. *Simulating W/Z+jets production at the CERN LHC.* Phys. Rev. **D72** (2054017); [hep-ph/0503280], 2005.
- [124] ATLAS Collaboration. *Measurement of the production cross section for W bosons in association with jets in pp collisions at $\sqrt{s} = 7$ TeV with the ATLAS detector.* Tech. Rep. CERN-PH-EP-2010-081; [arXiv:1012.5382], 2010.
- [125] ATLAS Collaboration. *Measurement of the top quark-pair production cross section with ATLAS in pp collisions at $\sqrt{s} = 7$ TeV.* Tech. Rep. CERN-PH-EP-2010-064; [arXiv:1012.1792], 2010.
- [126] http://atlasdqm.web.cern.ch/atlasdqm/grlgen/Susy/Susy_v01/.
- [127] <https://indico.cern.ch/getFile.py/access?contribId=7&resId=0&materialId=s%lides&confId=106717>.
- [128] ATLAS Collaboration. *The ATLAS Simulation Infrastructure.* Eur. Phys. J. **C70** (823-874); [arXiv:1005.4568], 2010.
- [129] F. De Campos et al. *Probing Neutrino Oscillations in Supersymmetric Models at the Large Hadron Collider.* Phys. Rev. **D82** (075002); [arXiv:1006.5075/hep-ph], 2012.
- [130] ATLAS Collaboration, Heavy Flavour Working Group, b-tagging performance, https://twiki.cern.ch/twiki/bin/view/AtlasProtected/BTaggingBenchmarks#%JetFitterCOMBNN_AN1.
- [131] ATLAS Collaboration. *Electron and photon reconstruction and identification in ATLAS: expected performance at high energy and results at $\sqrt{s} = 900$ GeV.* Tech. Rep. ATLAS-CONF-2010-0052, 2010.

- [132] ATLAS Collaboration. *Measurement of the $W \rightarrow \ell\nu$ and $Z/\gamma \rightarrow \ell\ell$ production cross sections in proton-proton collisions at $\sqrt{s} = 7$ TeV with the ATLAS detector*. [arXiv:1010.2130/hep-ex].
- [133] ATLAS Collaboration, Egamma combined performance group, <https://twiki.cern.ch/twiki/bin/view/AtlasProtected/EfficiencyMeasurements>.
- [134] ATLAS Collaboration. *Measurement of the cross section for top-quark pair production in pp collisions at $\sqrt{s} = 7$ TeV with the ATLAS detector using final states with two high- p_T leptons*. JHEP **1205** (059); [arXiv:1202.4892/hep-ex], 2012.
- [135] A. Read. *Presentation of search results: the CLs technique*. Journal of Physics G: Nucl. Part. Phys. **28** (26932704), 2002.
- [136] G. Cowan, K. Cranmer, E. Gross, and O. Vitells. *Asymptotic formulae for likelihood-based tests of new physics*. Eur. Phys. J. **C71** (1554); [arXiv:1007.1727], 2011.
- [137] Aad, G *et al.* *Search for supersymmetry using final states with one lepton, jets, and missing transverse momentum with the ATLAS detector in $\sqrt{s} = 7$ TeV pp collisions*. Phys. Rev. Lett. **102** (131802); [arXiv:1102.2357/hep-ex], 2011.
- [138] <https://twiki.cern.ch/twiki/bin/viewauth/Atlas/AtlfastDocumentation>.
- [139] X. Portell Bueso. *SUSY requirements for fast simulation*, <https://indico.cern.ch/contributionDisplay.py?contribId=1&confId=133590>.
- [140] E. Torr . *Final decision on using AF-II for SUSY signal grids*, <https://indico.cern.ch/getFile.py/access?contribId=0&resId=0&materialId=slides&confId=130447>.
- [141] X. Portell Bueso. *Sign-off on AF-II simulation for SUSY at EPS*, <https://indico.cern.ch/getFile.py/access?contribId=2&resId=0&materialId=slides&confId=136687>.
- [142] E. Torr . *AF-II validation for SUSY results for EPS*, <https://indico.cern.ch/getFile.py/access?contribId=9&resId=3&materialId=slides&confId=141119>.
- [143] Torr Pastor, E ; Ct, D ; Portell Bueso, X. *Validation of the ATLEFAST-II package for the simulation of supersymmetry events*. ATL-COM-PHYS-2011-1181, 2011.
- [144] <http://www.hep.ucl.ac.uk/atlas/atlfast/>.
- [145] <https://twiki.cern.ch/twiki/bin/viewauth/Atlas/FastCaloSim>.
- [146] <https://twiki.cern.ch/twiki/bin/view/AtlasPublic>.
- [147] ATLAS Collaboration. *Search for squarks and gluinos using final states with jets and missing transverse momentum with the ATLAS detector in $\sqrt{s} = 7$ TeV proton-proton collisions*. Phys. Lett. **B710** (67-85); [arXiv:1109.6572], 2012.
- [148] ATLAS Collaboration. *Search for new phenomena in final states with large jet multiplicities and missing transverse momentum using $\sqrt{s} = 7$ TeV pp collisions with the ATLAS detector*. JHEP **1111** (099); [arXiv:1110.2299], 2011.
- [149] ATLAS Collaboration. *Searches for supersymmetry with the ATLAS detector using final states with two leptons and missing transverse momentum in $\sqrt{s} = 7$ TeV proton-proton collisions*. Phys. Lett. **B709** (137-157); [arXiv:1110.6189], 2012.

- [150] ATLAS Collaboration. *Search for supersymmetry at $\sqrt{s} = 7$ TeV in final states with large jet multiplicity, missing transverse momentum and one isolated lepton with the ATLAS detector.* ATLAS-CONF-2012-140 / ATLAS-COM-CONF-2012-150, 2012.
- [151] ATLAS Collaboration. *Search for supersymmetry at $\sqrt{s} = 7$ TeV in final states with large jet multiplicity, missing transverse momentum and one isolated lepton with the ATLAS detector (supporting INT note).* ATL-COM-PHYS-2012-839, 2012.